EXPERIMENTAL INVESTIGATION OF THE EFFECTS OF FLUID ELASTIC PROPERTIES, SAND PARTICLE SIZE AND SURFACE PROPERTIES ON THE BED EROSION DYNAMICS OF THE SAND BED DEPOSITED IN HORIZONTAL PIPELINE

by

Mehmet Meric Hirpa

A thesis submitted in partial fulfilment of the requirements for the degree of

Master of Science

in

Petroleum Engineering

Department of Civil and Environmental Engineering
University of Alberta

ABSTRACT

A large-scale 9 m long horizontal flow loop equipped with a non-intrusive laser-based particle image velocimetry (PIV) system was used to carry out bed erosion experiments with water and viscoelastic fluids. Also, pipe flow experiments with viscoelastic fluids were carried out in this horizontal flow loop.

Effect of sand particle surface characteristics on the critical velocity and the near wall turbulence characteristics of water flow in the horizontal loop were investigated by using surface-treated and untreated industrial sands of four different mesh size. The PIV technique was used to determine instantaneous local velocity distribution near the stationary sand bed-water interface under sub-critical and critical flow conditions. The near wall velocity distributions determined with the measured frictional pressure loss values were then used for the evaluation of the Reynolds shear stresses, axial and radial turbulent intensities acting at the bed/water interface. Critical velocity for the onset of particle removal from the sand bed increased with the increasing particle size. When sand particles with special surface treatment were used, it was observed that the critical velocity required for the onset of the bed erosion was significantly lower than that of required for the untreated sand particles. The degree of reduction in critical velocity varied between 14 to 40% depending on the particle size. The effect of surface treatment on the transport efficiency became more significant with the decreasing particle size.

Effects of sand particle size and sand surface properties on the critical velocity required for the onset of the bed erosion and the near-wall turbulence characteristics of the polymer fluid flow over the sand bed in the horizontal pipeline were studied experimentally. Industrial sand particles having three different size ranges with and without special surface treatment were used in this experimental study. The instantaneous local velocity distributions and near wall turbulence characteristics (such as Reynolds stress, axial and turbulence intensity profiles) of dilute polymer fluid flow over the stationary sand bed under turbulent flow conditions were determined by PIV technique. The critical velocity for the onset of the particle removal from a stationary sand bed using a polymer fluid flow is affected by the sand particle size and the surface characteristics, however, the

effect was not straightforward, and it was varied depending on the relative comparison of the sand particle size with respect to the thickness of the viscous sublayer under turbulent flow condition.

An experimental study was conducted to investigate how the fluid elastic properties would influence, the frictional pressure drops, the critical velocity for the onset of the bed erosion, and turbulent flow characteristics (i.e. Reynolds stress, axial and radial turbulence intensity profiles) of the polymer fluid flow over the stationary sand bed deposited in horizontal pipeline. Polymer fluids were prepared by mixing three different grades (i.e. $5x10^5$, $8x10^6$, $20x10^6$ g/gmol) of partially hydrolyzed polyacrylamide (HPAM) polymer. These polymer fluids, which had almost identical shear viscosity characteristics while showing significantly different elastic properties, were used together with 30/50 mesh size industrial sands in the bed erosion experiments. After determining the critical velocities for the onset of the bed erosion using both fluids, the frictional pressure drops at critical and several subcritical velocities were recorded for both fluids. Results showed that the fluid elasticity affects the bed erosion dynamics significantly. Generally, frictional pressure drops, and critical velocities for the bed erosion all increased with the increasing fluid elasticity.

Three polymer fluids were prepared by mixing three different grades of HPAM polymer and these fluids, having the same shear viscosity but different elasticity, were used for the experiments. By using these fluids, we were able to investigate the direct effect of the fluid elasticity on drag reduction and the onset of the turbulence in horizontal pipe flow.

Results showed that that drag reduction associated with the pipe flow of a dilute polymer fluid was enhanced by the increasing the fluid elasticity. Moreover, the fluid elasticity was effective in controlling the onset of the turbulent flow. An earlier transition to turbulent flow regime (as compared to water flow) was only observed during the flow of the most elastic fluid. Drag reduction started to be effective at a Weissenberg number around 2 and it increased with increasing Weissenberg number.

PREFACE

Chapter 3, Chapter 4, Chapter 5 and Chapter 6 present the research done in the scope of this thesis. These four chapters are completely based on four separate papers. I and Sumanth Kumar Arnipally conducted all the experiments in Chapter 3 and Chapter 4. However, I conducted the analyses of the data and prepared all the content for two papers related to these chapters. The paper constituting Chapter 3 was submitted to SPE Journal for publication and that paper is now under review. The paper constituting Chapter 4 will be submitted to a relevant journal for publication as well. I executed all experimental work in Chapter 5 and Chapter 6 by myself. Also, I prepared two separate papers from this experimental work. Those two papers will be submitted to relevant journals for publication. In total four separate papers were produced from this experimental work. The titles of these four papers presented in Chapter 3, Chapter 4, Chapter 5 and Chapter 6 are respectively; "Effect of particle size and surface properties on the near wall turbulence characteristics and the critical velocity required for the particles removal from the sand bed deposited in horizontal pipelines", "Effect of sand particle size and surface properties on the near wall turbulence characteristics of the polymer fluid flow and the critical velocity required for the particle removal from the sand bed deposited in horizontal pipelines", "Effect of polymer fluid viscoelastic properties on the early transition to turbulent flow and the drag reduction in the flow through horizontal pipe", "Effect of fluid elastic properties on the bed erosion dynamics of a sand bed deposited in a horizontal pipeline".

ACKNOWLEDEGMENTS

First, I would like to thank my supervisor Dr. Ergun Kuru for his support and guidance in my thesis. In past 2 years, he helped me a lot at each stage of this research. Involving in his research group and working under his supervision was certainly a great chance for me and having this opportunity contributed me a lot both academically and personally.

Also, I want to give my special thanks to Majid Bizhani, Sumanth Kumar Arnipally and Todd Kinnee. In past 2 years, I was always together with them as friends and colleagues and I learnt a lot from them while I was initially mastering the experimental setup, equipment and the experimental procedure involved in my research.

I am also beholden to my mother Aynur Hirpa, my father Ayhan Hirpa and my brother Merih Hirpa in Turkey. They have always stood my side in good or bad days with their endless support, love and motivation. Without them no achievement in my life would be possible. I would like to also thank my greatest friend Najia Nuha Mehdi and Feridun Mumcuoglu, who has always been a source of inspiration for me as a great petroleum engineer.

This research is financially supported through the funds available from Natural Sciences and Engineering Research Council of Canada (NSERC EGP 515333-17 KURU and NSERC RGPIN-2016-04647 KURU). I would also like to thank 3M Company for supporting this study by collaborating through NSERC-Engage funding program and also providing us treated and untreated sand particles used in our experiments.

TABLE OF CONTENTS

ABSTRACT ii

PREFACE iv

ACKNOWLEDEGMENTS v

TABLE OF CONTENTS vi

LIST OF TABLES xiv

LIST OF FIGURES xv

1. INTRODUCTION 1

1.1. OVERVIEW 1

1.2. PROBLEM STATEMENT 2

1.3. OBJECTIVES AND SCOPE OF THE CURRENT STUDY 7

1.4. CONTRIBUTIONS OF THE CURRENT STUDY 8

1.5. STRUCTURE OF THE THESIS 9

1.6. REFERENCES 11

2. EXPERIMENTAL SETUP AND METHODOLOGY 14

2.1. EXPERIMENTAL SETUP 14

2.2. METHODOLOGY 18

2.2.1. Rheology of Fluids Tested and Fluid Preparation 19

2.2.2. Pipe Flow Experiments 25

2.2.3. Bed Erosion Experiments 25

2.2.4. PIV Measurements 26

2.2.5. PIV Image Calibration 27

2.2.6. PIV Data Processing 29

2.3. REFERENCES 31

3. EFFECT OF PARTICLE SIZE AND SURFACE PROPERTIES ON THE NEAR WALL TURBULENCE CHARACTERISTICS AND THE CRITICAL VELOCITY REQUIRED FOR THE PARTICLES REMOVAL FROM THE SAND BED DEPOSITED IN HORIZONTAL PIPELINES 32

3.1. ABSTRACT 32

3.2. INTRODUCTION 33

3.3. MATERIALS AND METHODS 35

3.3.1. Sand Particles 35

3.3.2. Experimental Flow Loop 36

3.3.3. Experimental Procedure 38

3.3.3.1. Sand Bed Establishment 38

3.3.3.2. Water Circulation, Calibration of Pressure Loss Measurements and Determination of Critical Flow Rate 39

3.3.3.3. PIV Measurements 40

3.3.4. Data Processing and Analysis 41

3.4. RESULTS AND DISCUSSIONS – TURBULENT FLOW OF WATER OVER THE UNTREATED SAND ……43

3.4.1. Frictional Pressure Loss Measurements for the Flow of Water over the Untreated Sand Beds of Three Different Particle Size Range at Subcritical Velocity of 0.25 m/s. 43

3.4.2. Results of PIV Measurements at the Subcritical Flow Velocity of 0.25 m/s..... 46

3.4.3. Critical Flow Rate Required for the Onset of Particle Removal..... 52

3.5. RESULTS AND DISCUSSIONS – TURBULENT FLOW OF WATER OVER THE SURFACE TREATED SAND BED 55

3.5.1. Frictional Pressure Loss Measurements for the Flow of Water over the Treated Sand Beds of 4 Different Particle Size Range at Various Subcritical Flow Rates. 55

3.5.2. Results of PIV Measurements at the Subcritical Flow Velocity of 0.16 m/s..... 57

3.5.3. Critical Flow Rate Required for the Onset of Particle Removal from Treated Sand Bed Deposits…… .. 62

3.6. COMPARISON OF THE RESULTS OF TREATED VS. UNTREATED SAND BED EROSION TESTS……..... 65

3.6.1. Comparison of Frictional Pressure Drop - Treated versus Untreated Sand Bed Erosion Tests..... 65

3.6.2. Comparison of PIV Data Measured Over the Treated and the Untreated Sand Beds 68

3.6.3. Comparison of Critical Velocities Required for the Onset of Particle Removal from Treated and Untreated Sand Beds..... 74

3.7. CONCLUSIONS..... 75

3.8. ACKNOWLEDGEMENTS..... 77

3.9. REFERENCES 77

4. EFFECT OF SAND PARTICLE SIZE AND SURFACE PROPERTIES ON THE NEAR WALL TURBULENCE CHARACTERISTICS OF THE POLYMER FLUID FLOW AND THE CRITICAL VELOCITY REQUIRED FOR THE PARTICLE REMOVAL FROM THE SAND BED DEPOSITED IN HORIZONTAL PIPELINES 80

4.1. ABSTRACT 80

4.2. INTRODUCTION 80

4.3. MATERIALS AND METHODS 82

4.3.1. Sand Particles 82

4.3.2. Experimental Flow Loop 83

4.3.3. Experimental Procedure 85

4.3.3.1. Verification of the Accuracy of the Frictional Pressure Loss Measurements 86

4.3.3.2. Sand Bed Establishment 87

4.3.3.3. Polymer Fluid Circulation and Measurement of Critical Flow Rate 87

4.3.3.4. PIV Measurements 87

4.3.4. Data Processing and Analysis 88

4.4. RESULTS AND DISCUSSIONS – BED EROSION EXPERIMENTS USING UNTREATED SANDS 92

4.4.1. Frictional Pressure Drops Measured for the Polymer Fluid Flow over the Untreated Sand Bed 92

4.4.2. Turbulent Flow Characteristics of Polymer Fluid Flow over the Untreated Sand Bed 93

4.4.3. Critical Velocity Required for the Particle Removal from Untreated Sand Bed 98

4.5. RESULTS AND DISCUSSIONS – BED EROSION TESTS WITH TREATED SANDS 105

4.5.1. Frictional Pressure Drops Measured for the Polymer Fluid Flow over the Treated Sand Bed..... 105

4.5.2. Turbulent Flow Characteristics of Polymer Fluid Flow over the Treated Sand Bed. 106

4.5.3. Critical Velocities for Particle Removal from the Treated Sand Beds 110

4.6. RESULTS AND DISCUSSIONS – COMPARISON OF THE RESULTS FOR THE FLOW OF POLYMER FLUID OVER THE TREATED AND UNTREATED SAND BED..... 116

4.6.1. Comparison of Frictional Pressure Drops Measured for the Polymer Fluid Flow over the Treated and Untreated Sand Bed 116

4.6.2. Comparison of the Turbulence Characteristics of Polymer Fluid Flow over the Treated and Untreated Sand Bed 118

4.6.3. Comparison of Critical Velocities Required for Particle Removal from the Treated and Untreated Sand Bed..... 127

4.7. CONCLUSIONS..... 128

4.8. ACKNOWLEDGEMENTS..... 131

4.9. REFERENCES 131

5. EFFECT OF POLYMER FLUID VISCOELASTIC PROPERTIES ON THE EARLY TRANSITION TO TURBULENT FLOW AND THE DRAG REDUCTION IN THE FLOW THROUGH HORIZONTAL PIPE 133

5.1. ABSTRACT..... 133

5.2. INTRODUCTION 134
5.3. MATERIALS AND METHODS 136
5.3.1. Polymer Fluids 136
5.3.2. Experimental Flow Loop 139
5.3.3. Experimental Procedure 140
5.3.4. Data Processing and Analysis 142
5.4. RESULTS AND DISCUSSIONS 145
5.4.1. Rheology of Fluid Mixtures 145
5.4.2. Frictional Pressure Drops and PIV Analysis 148
5.4.3. Analyses of the Turbulent Flow Characteristics Using Data Obtained by PIV Measurements ... 152
5.4.4. Analyses of the Early Onset of the Turbulence 158
5.4.5. Critical Conditions for the Onset Drag Reduction and the Maximum Drag Reduction 164
5.5. CONCLUSIONS 165
5.6. ACKNOWLEDGEMENTS 168
5.7. REFERENCES 168
6. EFFECT OF FLUID ELASTIC PROPERTIES ON THE BED EROSION DYNAMICS OF A SAND BED DEPOSITED IN A HORIZONTAL PIPELINE 172
6.1. ABSTRACT 172
6.2. INTRODUCTION 173
6.3. MATERIALS AND METHODS 175

6.3.1. Sand Particles 175
6.3.2. Polymer Fluids 175
6.3.3. Experimental Setup 178
6.3.4. Experimental Procedure 180
6.3.4.1. Sand Bed Establishment 180
6.3.4.2. Polymer Fluid Circulation, Calibration of Pressure Transducer, and Measurement of Critical Flow Rates 180
6.3.4.3. PIV Measurements 181
6.3.5. Data Processing and Analysis 182
6.4. RESULTS AND DISCUSSIONS 185
6.4.1. Rheological Properties of Polymer Fluids 185
6.4.2. Critical Velocities for 30/50 Mesh Size of Sand Particles in Fluid A and Fluid B 188
6.4.3. Frictional Pressure Drop Due to Flow Polymer Fluids in Pipe 193
6.4.4. Frictional Pressure Losses Due to Flow of Polymer Fluids Over the 30/50 Mesh Size Sand Bed 194
6.4.5. PIV Data for 30/50 Mesh Size of Sand Particles in Fluid A and Fluid B 195
6.5. CONCLUSIONS 202
6.6. ACKNOWLEDGEMENTS 204
6.7. REFERENCES 204
7. CONCLUSIONS AND RECOMMENDATIONS FOR FUTURE WORK 208
7.1. Conclusions 208

7.1.1. Major conclusions 208

7.1.2. Conclusions from individual chapters 210

7.1.2.1. Chapter 3 - Effect of particle size and surface properties on the near wall turbulence characteristics and the critical velocity required for the particles removal from the sand bed deposited in horizontal pipelines 210

7.1.2.2. Chapter 4 - Effect of sand particle size and surface properties on the near wall turbulence characteristics of the polymer fluid flow and the critical velocity required for the particle removal from the sand bed deposited in horizontal pipelines 211

7.1.2.3. Chapter 5 - Effect of polymer fluid viscoelastic properties on the early transition to turbulent flow and the drag reduction in the flow through horizontal pipe 213

7.1.2.4. Chapter 6 - Effect of fluid elastic properties on the bed erosion dynamics of a sand deposited in a horizontal pipeline 214

7.2. RECOMMENDATIONS FOR FUTURE WORK 216

BIBLIOGRAPHY 219

LIST OF TABLES

Table 2-1 Compositions and concentrations for Fluid A, Fluid B and Fluid C. 24

Table 3-1 Size Ranges of Sand Particles Used in the Experiments 35

Table 3-2 Frictional Pressure Drop vs Untreated Sand Particle Size Range Measured at 0.25 m/s. 44

Table 3-3 Summary of the test results at the onset of the untreated sand bed erosion 52

Table 3-4 Frictional Pressure Drop vs Treated Sand Particle Size Range Measured at 0.16 m/s. 56

Table 3-5 Summary of the results of treated sand bed erosion experiments 62

Table 3-6 Comparison of the critical velocity required for the onset of the particle removal from treated 74

Table 4-1 Size Ranges of Sand Particles Used in the Experiments 82

Table 4-2 Frictional Pressure Drop Over Untreated Sand Bed Measured at 0.25 m/s. 92

Table 4-3 Results of untreated sand bed erosion experiments using polymer fluid. 98

Table 4-4 Forces acting on a single untreated sand particle at critical velocity 101

Table 4-5 Forces acting on a single untreated sand particle at sub-critical velocity 102

Table 4-6 Viscous sublayer thickness for polymer fluid flow over the untreated sand bed at their 103

Table 4-7 Frictional Pressure Drop vs Mesh Size of Treated Sand Measured at 0.25 m/s. 105

Table 4-8 Results of treated sand bed erosion experiments using polymer fluid. 111

Table 4-9 Forces acting on a single treated sand particle at critical velocity 111

Table 4-10 Forces acting on a single treated sand particle at sub-critical velocity 112

Table 4-11 Viscous sublayer thickness for polymer fluid flow over the treated sand bed at critical flow 113

Table 4-12 Comparisons of the critical velocities - Treated vs Untreated sand 128

Table 5-1 HPAM different grades molecular weight data 137

Table 5-2 Compositions and concentrations of Fluids A, B and C 138

Table 5-3 Summary of the rheological properties of Fluids A, B and C 148

Table 6-1 Molecular weight of different HPAM polymer grades 176

Table 6-2 Polymer compositions and concentrations of Fluid A and Fluid B 177

Table 6-3 Summary of the rheological properties of Fluid A and Fluid B 187

Table 6-4 Details of bed erosion experiments for Fluid A and Fluid B 189

LIST OF FIGURES

Figure 2-1 Schematic of the horizontal flow loop [1]. 14
Figure 2-2 Suction tank and the centrifugal pump. 15
Figure 2-3 The air mixer installed on the suction tank. 16
Figure 2-4 VFD unit controlling the electric motor. 16
Figure 2-5 The differential pressure transducer. 17
Figure 2-6 The magnetic flow meter in the horizontal loop. 18
Figure 2-7 Stress and strain plot for a typical frequency test [3]. 21
Figure 2-8 Bohlin C-VOR 150 rheometer. 22
Figure 2-9 A typical PIV image. 27
Figure 2-10 The calibration target. 28
Figure 2-11 An example for a calibrated field of view. 28
Figure 2-12 Peak search and cross correlation process [6]. 30
Figure 3-1 Contact angle measurement for 20/40 mesh size sands: a-) Non-treated sand b-) Surface 36
Figure 3-2 Schematic diagram of the experimental flow loop [9]. 36
Figure 3-3 Image of the PIV setup and the test section 37
Figure 3-4 Comparison of experimental friction factor values estimated from water only flow tests 40
Figure 3-5 a) Typical PIV image acquired during the tests, b) resultant velocity field. 42
Figure 3-6 Frictional pressure drop data for different mesh size of untreated sand particles. 45
Figure 3-7 Comparison of the near wall velocity profiles for the flow of water over the sand beds of three 47
Figure 3-8 Normalized Reynolds stress profiles for the flow of water over the sand beds of three 48
Figure 3-9 Axial turbulence intensity profiles for the flow of water over the sand beds of three. 49
Figure 3-10 Radial turbulence intensity profiles for the flow of water over the sand beds of three different 50
Figure 3-11 Friction velocity vs particle mesh size for experiments conducted at sub-critical velocity of. 51
Figure 3-12 Critical velocity required for the onset of the untreated sand bed erosion versus the particle 53
Figure 3-13 Critical pressure drop versus the particle mesh size measured at the onset of the untreated 54
Figure 3-14 Friction velocity vs particle mesh size for experiments conducted at the critical velocity. 55

Figure 3-15 Frictional pressure drop measured for the flow of water over the treated sand beds at....57
Figure 3-16 Dimensionless velocity profiles for 20/40, 30/50 and 40/70 mesh size of treated sand particles 58
Figure 3-17 Reynolds stress profiles for the turbulent flow of water over the treated sand beds of 20/40, ...59
Figure 3-18 Axial turbulence intensity profiles for the turbulent flow of water over 20/40, 30/50 and 40/70....60
Figure 3-19 Radial turbulence intensity profiles for 20/40, 30/50 and 40/70 mesh size of treated sand....61
Figure 3-20 Frictional velocities for 20/40, 30/50 and 40/70 mesh size of treated sand particles at the....62
Figure 3-21 Critical velocities for treated sand particles. 63
Figure 3-22 Critical pressure drop measured at the onset of the treated sand bed erosion with water.....64
Figure 3-23 Frictional velocities obtained from PIV data measured at the onset of the treated sand bed....64
Figure 3-24 Comparison of the frictional pressure drop data measured at various velocities of water Flow....66
Figure 3-25 Comparison of the frictional pressure drop data measured at various velocities of water flow....66
Figure 3-26 Comparison of the frictional pressure drop data measured at various velocities of water flow....67
Figure 3-27 Comparison of the frictional pressure drop data measured at various velocities of water flow....67
Figure 3-28 The near wall velocity profiles for 0.25 m/s water flow over the treated and untreated sand....68
Figure 3-29 The near wall velocity profiles for 0.22 m/s water flow over the treated and untreated sand....69
Figure 3-30 Reynolds shear stress profiles for 0.25 m/s water flow over the treated and untreated sand....70
Figure 3-31 Comparison of the Reynolds shear stress profiles for 0.22 m/s water flow over the treated and....70
Figure 3-32 Comparison of the axial turbulence intensity profiles for 0.25 m/s water flow over the treated 71
Figure 3-33 Comparison of the axial turbulence intensity profiles for 0.22 m/s water flow over the treated 72
Figure 3-34 Radial turbulence intensity profiles for the flow of water over the treated and untreated....73
Figure 3-35 Radial turbulence intensity profiles for the flow of water over the treated and untreated sand....73
Figure 3-36 Comparison of the critical velocity required for the onset of the particle removal from....75
Figure 4-1 Contact angle measurement for 20/40 mesh size sands: a-) Non-treated sand b-) Surface 83
Figure 4-2 Rheogram of the polymer fluid used in the study....83
Figure 4-3 Schematic diagram of the experimental flow loop [9]....84
Figure 4-4 Image of the PIV setup and the test section 85
Figure 4-5 Comparison of experimental friction factor values estimated from water only flow tests 86
Figure 4-6 Typical PIV image acquired during the tests, b) resultant velocity field. 90

Figure 4-7 Frictional pressure drop measured for the flow of polymer fluid over the untreated sand bed.....93
Figure 4-8 Dimensionless velocity profiles for flow of polymer fluid over untreated sand bed at the 95
Figure 4-9 Reynolds stress profiles for flow of polymer fluid over untreated sand bed at the superficial.....95
Figure 4-10 Axial turbulence intensity profiles for flow of polymer fluid over untreated sand bed at the 96
Figure 4-11 The radial turbulence intensity profile for the flow of polymer fluid over the untreated sand 97
Figure 4-12 Friction velocity vs particle mesh size for experiments conducted at sub-critical velocity of.....98
Figure 4-13 Critical velocity for the onset of the particle removal from untreated sand bed using polymer 99
Figure 4-14 Critical velocity for the onset of the particle removal from untreated sand bed using polymer 104
Figure 4-15 Friction velocity vs particle mesh size for experiments conducted at the critical velocity. 105
Figure 4-16 Frictional pressure drop for the flow of polymer fluid over the treated sand bed. 106
Figure 4-17 Dimensionless velocity profiles for polymer fluid flow over the treated sand bed at the.....107
Figure 4-18 Reynolds stress profiles for polymer fluid flow over the treated sand bed at the superficial 108
Figure 4-19 Axial turbulence intensity profiles for polymer fluid flow over the treated sand bed at the.....109
Figure 4-20 Radial turbulence intensity profiles for polymer fluid flow over the treated sand bed at the 109
Figure 4-21 Friction velocity vs treated sand particle mesh size for experiments conducted at sub-critical.....110
Figure 4-22 Critical velocity for the onset of the particle removal from the treated sand bed using 111
Figure 4-23 Critical pressure drop versus the treated sand particle mesh size 115
Figure 4-24 Friction velocity vs treated sand particle mesh size for the experiments conducted at the.....115
Figure 4-25 Comparison of frictional pressure drop data for the polymer fluid flow over the 20/40 mesh 116
Figure 4-26 Comparison of frictional pressure drop data for the polymer fluid flow over the 30/50 mesh 117
Figure 4-27 Comparison of frictional pressure drop data for the polymer fluid flow over the 40/70 mesh 117
Figure 4-28 Dimensionless near wall velocity profiles for the flow of polymer fluid over the 20/40 mesh 118
Figure 4-29 Dimensionless near wall velocity profiles for the flow of polymer fluid over the 30/50 mesh 119
Figure 4-30 Dimensionless near wall velocity profiles for the flow of polymer fluid over the 40/70 mesh 120
Figure 4-31 Reynolds stress profiles for the flow of polymer fluid over the 20/40 mesh size treated and 121
Figure 4-32 Reynolds stress profile for the flow of polymer fluid over the 30/50 mesh size treated and.....122
Figure 4-33 Reynolds stress profiles for the flow of polymer fluid over the 40/70 mesh size treated and 123
Figure 4-34 Axial turbulence intensity profiles for the flow of polymer fluid over the 20/40 mesh size 124

Figure 4-35 Axial turbulence intensity profiles for the flow of polymer fluid over 30/50 mesh size treated 124
Figure 4-36 Axial turbulence intensity profiles for the flow of polymer fluid over 40/70 mesh size treated 125
Figure 4-37 Radial turbulence intensity profiles for the flow of polymer fluid over 20/40 mesh size. 126
Figure 4-38 Radial turbulence intensity profiles for the flow of polymer fluid over 30/50 mesh size treated 126
Figure 4-39 Radial turbulence intensity profiles for the flow of polymer fluid over 40/70 mesh size treated 127
Figure 4-40 Comparisons of the critical velocities - Treated vs Untreated sand. 128
Figure 5-1 Schematic diagram of the experimental flow loop [20]. 139
Figure 5-2 Image of the PIV setup and the test section 140
Figure 5-3 Comparison of experimental friction factor values estimated from water only flow tests 141
Figure 5-4 Shear stress vs. shear rate plots for Fluids A, B and C 146
Figure 5-5 Frequency sweep test data for Fluid A 147
Figure 5-6 Frequency sweep test data for Fluid B 147
Figure 5-7 Frequency sweep test data for Fluid C 148
Figure 5-8 Frictional pressure drop measured during the flow of Fluids A, B and C in the horizontal pipe 150
Figure 5-9 Friction factors vs. Reynolds number for the flow of Fluids A, B and C in horizontal pipe. 150
Figure 5-10 First normal stress differences of Fluids A, B and C 152
Figure 5-11 Full velocity profiles at the flow rate of 221.5 lpm 153
Figure 5-12 Full velocity profiles at the flow rate of 316 lpm. 153
Figure 5-13 Dimensionless velocity profiles of Fluids A, B, and C at the flowrate of 221.5 lpm 154
Figure 5-14 Dimensionless velocity profiles of Fluids A and Fluid B at the flowrate of 316 lpm. 154
Figure 5-15 Reynolds stress profiles at the flowrate of 221.5 lpm. 155
Figure 5-16 Reynolds stress profiles at the flowrate of 316 lpm. 156
Figure 5-17 Axial turbulence intensity profiles at the flowrate of 221.5 lpm. 157
Figure 5-18 Axial turbulence intensity profiles at the flowrate of 316 lpm. 157
Figure 5-19 Radial turbulence intensity profiles at the flowrate of 221.5 lpm. 158
Figure 5-20 Radial turbulence intensity profiles at the flowrate of 316 lpm. 158
Figure 5-21 Friction factor vs Reynolds number plot of Fluid A. 160
Figure 5-22 Friction factor vs. Reynolds number plot of Fluid B. 160

Figure 5-23 Friction factor vs. Reynolds number plot of Fluid C 161
Figure 5-24 Flowrate vs. wall shear stress plot for Fluid A. 162
Figure 5-25 Flowrate vs. wall shear stress plot for Fluid B. 163
Figure 5-26 Flowrate vs. wall shear stress plot for Fluid C. 163
Figure 5-27 Drag reduction in percentage vs Weissenberg number. 164
Figure 6-1 Schematic diagram of the experimental flow loop [17]. 178
Figure 6-2 Image of the PIV setup and the test section 179
Figure 6-3 Comparison of experimental friction factor values estimated from water only flow tests against the ones calculated from Dodge and Metzner equation [18] 181
Figure 6-4 a) Typical PIV image acquired during the tests, b) resultant velocity field. 183
Figure 6-5 Shear stress vs. shear rate diagram of Fluid A and Fluid B 186
Figure 6-6 Frequency sweep test data for Fluid A 188
Figure 6-7 Frequency sweep test data for Fluid B 188
Figure 6-8 First normal stress differences measured for Fluid A and Fluid B. 190
Figure 6-9 Normal forces calculated from measured first normal stress differences. 191
Figure 6-10 Frictional pressure drops for Fluid A and Fluid B without a sand bed. 193
Figure 6-11 Frictional pressure drops for Fluid A and fluid B over the sand bed. 195
Figure 6-12 Velocity profiles in the annulus between the sand bed and the pipe wall measured at flow rate 196
Figure 6-13 Velocity profiles in the annulus between the sand bed and the pipe wall measured at flow rate 196
Figure 6-14 Dimensionless velocity profiles for Fluid A and Fluid B at 225 lpm 197
Figure 6-15 Dimensionless velocity profiles of Fluid A and Fluid B at 274 lpm 197
Figure 6-16 Reynolds stress profiles for Fluid A and Fluid B at 225 lpm 199
Figure 6-17 Reynolds stress profiles for Fluid A and Fluid B at 274 lpm 199
Figure 6-18 Axial turbulence intensity profiles for Fluid A and Fluid B at 225 lpm 200
Figure 6-19 Axial turbulence intensity profiles for Fluid A and Fluid B at 274 lpm 200
Figure 6-20 Radial turbulence intensity profiles for Fluid A and Fluid B at 225 lpm. 201
Figure 6-21 Radial turbulence intensity profile for Fluid A and Fluid B at 274 lpm. 202

1. INTRODUCTION

1.1. OVERVIEW

Flow of fluids through circular pipes or passages in different geometric shapes and the interaction of fluids with the surrounding have been focused greatly by researchers for many years as most engineering problems require a deep understanding of dynamics of fluid flow in various flow mediums. In oil well drilling, the circulating fluid is the main tool establishing the sole communication between the surface and hundreds of meters deep subsurface formations being drilled. By examining the content of the drilling fluid or the cuttings transported to surface, the exact story of what is happening at the bottom of the well during drilling can be revealed. However, in addition to bringing immediate information about the formations being drilled, a fluid must have low annular frictional pressure losses and excellent solids transport abilities in order to be considered as the circulating fluid for drilling oil and gas wells. More recently, drilling long horizontal and extended reach wells has been becoming the industry standard. The nature of horizontal wells dictates the drilled cuttings to settle down to the lower side of the wellbore. Drilled cuttings deposited on the lower side under the effect of gravitational forces form a continuous cuttings bed along the horizontal section of the well. If this situation cannot be handled properly and excessive cuttings deposition is allowed, operational problems such as slow drilling rates, damage to the downhole equipment, high drag, high torque and most seriously a stuck pipe might arise and as the worst-case scenario all these might cause losing the drilled well [1,2,3]. Therefore, the circulating fluid must be capable of preventing the cuttings bed deposition and it must also be able to remove the deposited cuttings efficiently.

The horizontal and extended reach wells are commonly preferred to optimize the productivity from a single well by increasing the length of the production zone. Considering the high demand for hydrocarbons in the world today, more wells are being drilled horizontally and the horizontal sections of these wells become longer to further increase the production. However, longer horizontal sections mean higher annular frictional pressure drops or

higher equivalent circulating densities. Drilling through weak formations horizontally, the high equivalent circulating density could cause lost circulation, and this might restrict the maximum drillable horizontal distance. Therefore, annular frictional pressure drops exhibited by the circulating fluid might be crucial when drilling horizontal or extended reach wells and to prevent lost circulation, the frictional pressure gradient in the annulus should not exceed the fracture gradient of the formation being drilled.

Flow dynamics of the circulating fluid through the wellbore is very important in terms of frictional pressure drops and cuttings transport abilities. Therefore, in order to be able to drill longer horizontal sections and problem free holes, flow resistance and solids transport abilities must be the main priorities in designing drilling fluids for horizontal and extended reach wells.

1.2. PROBLEM STATEMENT

Formation of stationary cuttings bed deposits is inevitable when drilling the long horizontal and extended reach wells. Operational problems such as slow drilling rate, excessive torque and drag, bridging, pack-off, hole fill and pipe stuck arise due to these bed deposits [1,2,3]. Occasionally, drilling must stop to clean the well, which costs time and money. The mere act of circulating drilling fluid may not clean the well as the critical flow rate and the shear stress for bed erosion must be reached [2,3]. Despite significant progress made in drilling fluids, tools, and field practices, along with more than 50 years of university and industry research, field experience indicates that hole cleaning is still a major problem on most highly inclined and horizontal wells [2,3].

Brown et al. [4] investigated the performance of different fluids including water and polymers on annular hole cleaning by conducting experiments in a specially designed flow loop. Their work provided a broader picture of the hole cleaning in the drilling operations. Adari et al. [5] conducted extensive experiments to determine the effect of drilling fluid rheological properties and flow rates on the cuttings bed erosion. Martins et al. [6] approached this subject in terms of predicting bed height after circulation and finding out the correlations to

determine the circulation rate to mobilize the bed effectively. The macro scale up work of Rabenjafimanantsoa et al. [7], where the flow through the sand bed was investigated with the aid of PIV (Particle Image Velocimetry) and UVP (Ultrasound Velocity Profile), provided a deeper understanding on the flow structure and its relationship with the sand bed. Bizhani et al. [8], in a recent work, investigated the effect of fluid viscoelasticity on the bed erosion, also with a comparison to water, using PIV in horizontal annuli.

Particle size was considered as an important variable in most of the numerical models used for the predicting critical velocity required for the onset of the bed erosion regardless of the type of fluid and the flow regime. However, in most of the previous experimental studies, the focus of the investigations were the type of fluid and the flow regime required for an efficient hole cleaning operation and its optimization. In order to understand the sand removal phenomenon, the effect of particle size must also be given a detailed look. Therefore, we investigated the effect of particle size on the critical velocity and near wall turbulence characteristics of water and a dilute polymer fluid flow over the sand bed deposited in a horizontal pipeline experimentally. We have also investigated the effect of sand particle surface characteristics on the same. Industrial sands of different mesh sizes with and without special surface treatment were used in these experiments. The particle image velocimetry (PIV) technique was used to determine instantaneous local velocity distribution near the stationary sand bed-fluid interface under flow conditions.

Rabenjafimanantsoa et al. [7] and Bizhani et al. [8] reported the delay in onset of particle movement in bed erosion tests conducted by using polymer fluids. Walker et al. [9], on the other hand, concluded that polymer-based fluids had higher cutting carrying capacity. Based on the field practices from North Sea operations, Saasen and Loklingholm [10] discussed the hole cleaning performance of polymer-based drilling fluids in detail and they concluded that the gel forming as a result of the interaction of cuttings bed and polymer-based drilling fluid is an important factor undermining hole cleaning performance of polymer-based fluids. Therefore, Saasen and Loklingholm [10] suggested the use of high molecular weight polymers only to prevent barite sag [10]. Duan et

al., [11] recommended the use of polymer-based fluids while drilling continues to effectively remove the small particles from the well, but for post-drilling cleanout operations they indicated that use of low viscosity fluids would be more effective. In all these works mainly, viscometric properties of polymer-based fluids were considered and analysed in terms of hole cleaning. However, most of the drilling fluids possess not only viscous but also elastic properties, which might also influence the flow dynamics and interactions of those fluids with the drill cuttings. Powell et al. [12] related the elasticity with the gel-like behaviour and their analysis showed that elasticity enhanced the suspension ability of the biopolymer fluids. Similarly, Zamora et al. [13] mentioned that elasticity enhances the hole cleaning in laminar flow and increases the suspension ability for the biopolymer-based fluids. Cuttings transport experiments conducted by Sayindla et al., [14] and the follow up study by Werner et al. [15] have shown that oil-based fluids had a superior cutting transport ability comparing to water-based fluids despite having the similar viscometric properties. Werner et al. [15] also reported that the water-based drilling fluid used in their study had no yield stress and a 50–100% higher elasticity than the oil-based drilling fluids.

Results from all these previous laboratory tests and field experience indicate that fluid elastic properties play important role in cuttings transport and should be given due consideration together with fluid viscous properties in order to have more realistic assessment of the cuttings transport ability of a drilling fluid. However, there are not many studies in the literature investigating the individual (as well as the combined) effects of drilling fluid viscometric properties (i.e., shear viscosity, yield stress) and the elastic properties on the hole cleaning [15].

Recently, Bizhani and Kuru [8] studied the effect of viscoelasticity on the particle removal from a stationary sand bed deposited in horizontal pipeline. They reported that the delay in particle movement was observed when they used fluid with higher elasticity for bed erosion experiments. Bizhani and Kuru [8] concluded that elastic normal forces arising from the normal stress differences due to the variation of the fluid elastic properties were responsible for this behaviour. One of the limitations in Bizhani and Kuru [8] study was that the fluids used in their study had different elastic properties as well as different shear viscosity values. Therefore, the difference in

hole cleaning performance of these two fluids could be affected by the change in both the elastic properties and shear viscosities. In a similar experimental study, we removed this limitation by formulating two fluids, which had almost identical shear viscosity characteristics while showing significantly different elastic properties (quantified in terms of the longest relaxation time). We then conducted bed erosion experiments using these two fluids under controlled conditions and, for the first time in drilling literature, we were able to quantify the individual effect of the fluid elasticity (independent from shear viscosity) on the critical flow rate for bed erosion and the turbulent flow characteristics of polymer fluid flow over the stationary sand bed.

Drag reducing effect of dilute polymer fluids was first discovered through the experiments conducted by Toms in 1948 [16]. Savins [17] claimed that the drag reduction is directly related to viscoelastic properties of fluids. Savins [17] also highlighted that while all high molecular weight polymer fluids do not have a drag reduction effect, some fluids in colloidal form having viscoelastic properties show drag reduction. Walsh [18] explained that the drag reduction occurs as the energy stored by molecules strained in viscous sublayer is transferred to the center of the flow and he used linear viscoelastic theory of Rouse [19] to calculate the stored strain energy. Based on their experimental work, Elata et al. [20] concluded that for drag reducing polymer fluids, the laminar viscous sublayer thickness increases, and this increase causes the drag reduction. Later, Virk [21] suggested an elastic sublayer model to explain the drag reduction phenomena, his explanations were somehow similar to explanations of Elata et al. [20], however in his model, in addition to viscous sublayer, an elastic sublayer was defined by Virk. Lumley [22] claimed that increasing effective viscosity by the expansion of the molecules in the flow, stabilizes the turbulent eddies by thickening the viscous sublayer and this optimizes the energy transferred in the flow direction. When the optical measurement techniques became available, Achia et al. [23] used such techniques to further analyse the drag reduction of dilute polymer solutions and their experimental results confirmed the existence of a stabilized wall layer (claimed previously in the literature) and this stabilization was linked with elongational viscosities developed during the flow. Massah et al. [24] studied the drag reducing effect of dilute

polymer solutions with FENE-P (Finitely extensible nonlinear elastic) model. Their work showed that the polymer chains deformed by high shear in flow produces some extra stresses and these extra stresses cause the drag reduction by modifying the structure of eddies producing Reynolds stresses [24]. While studying the effect of rheological properties on the drag reduction with direct numerical simulations, Dimitropoulos et al. [25] highlighted the role of elongational viscosities in drag reduction phenomena and they stated that there was a certain Weissenberg number associated with the onset of the drag reduction and elongational viscosity development. Pinho et al. [26] modified the GNF (Generalized Newtonian Fluid) model to include the effect of elongational viscosity and they considered the elongational viscosity among the most important parameters causing the drag reduction. Bonn [27] experimentally showed the direct connection between the elongational viscosity and the drag reduction of dilute polymer solutions. All these works from the literature clearly show the direct relationship between elongational viscosities developed by the polymer chains in solution and the drag reducing effect of dilute polymer solutions.

In addition to the drag reducing effect, dilute polymer solutions might also exhibit early transition to turbulent flow regime. Groisman et al. [28] suggested that polymer fluids with sufficiently high elastic properties would start chaotic flow at low velocities and this might stimulate the effectiveness of mixing polymers by leading an elastic turbulence. Early turbulence phenomena for flow in conduits was initially reported for the flow of dilute polymer solutions in capillary tubes [29]. The occurrence of early turbulence for flow through larger diameter pipes was only a hypothesis until Hansen et al. [30--29] and Forame et al. [31--30] experimentally showed that early turbulence might occur for the flow of dilute polymer fluids in pipes having larger diameters, (i.e. 0.553 cm and 0.660 cm). Early turbulence was also reported by Hoyt [32--31] for flow of dilute polymer solutions in a water tunnel. Hansen et al. [30--29], Forame et al. [31---30] and Hoyt [32--31] related the occurrence of the early turbulence with drag reduction phenomena solely. Dubief et al. [33--32] showed that the elasto-inertial turbulence (EIT) – which occurs as a result of developed elongational viscosities by the stretch of long polymer chains during

the flow - causes earlier transition to turbulent state in channel flow for dilute polymer solutions with the direct numerical simulation method. Samanta et al. [34--33] mentioned that rather than Reynolds number, the elasto-inertial turbulence depends on the shear rate. Their flow experiments in pipes having diameters of 2 mm and 10 mm showed that earlier transition to turbulent regime occurred for 500 ppm polyacrylamide (i.e. molecular weight $5x10^6$ g/gmol) solution. However, they claimed that the early turbulence might not occur for larger diameter pipes as the shear rates will be much lower. In the current study, we have shown that early turbulence might also occur for flow in large diameter pipes (i.e. 9.5 cm) and beside shear rate or drag reduction the elastic properties of the dilute polymer fluids are significant for the early turbulence phenomena. In order to see the direct influence of the fluid viscoelasticity on the drag reduction and the early turbulence phenomena, we have investigated the flow of three dilute polymer fluids having the same shear viscosities but different elastic properties through a 9m long horizontal pipeline with a 95 mm inner diameter. The turbulent characteristics of the flow such as Reynolds stresses, axial and radial turbulence intensity profiles were also determined by analysing the velocity field data collected by using PIV technique. Earlier transition to turbulence was observed only during the flow of fluid with the highest elasticity (among the three tested fluids) while, on the other hand, all the three fluids showed significant drag reducing behaviour. Lowest frictional pressure drops were measured during the flow of the most elastic fluid.

1.3. OBJECTIVES AND SCOPE OF THE CURRENT STUDY

The main objectives of this study were to conduct a comprehensive experimental research study;

- To determine the effects of particle size and surface properties on the bed erosion dynamics and frictional pressure losses when water and dilute polymer fluids are used as a transport
- To determine effect of polymer fluid elasticity on the bed erosion dynamics and frictional pressure losses when the fluid is flowing over a stationary sand bed deposited in horizontal pipeline

- To determine the effect of the fluid elasticity on the frictional pressure losses, critical condition required for the onset of the drag reduction and its magnitude, and critical condition required for the onset of the transition from laminar to turbulent flow when the polymer fluid is flowing through horizontal pipe.

The tasks completed to achieve those targets mentioned above are summarized below;

- Bed erosion experiments with four different mesh size of untreated and treated sand particles were carried out with water. Then, PIV data were recorded for each experiment.
- Bed erosion experiments with three different mesh size of treated and untreated sand particles were carried out with a dilute solution of Alcomer RD 110. Also, PIV data were recorded for each experiment.
- Two dilute polymer solutions having the same shear viscosity, but different elastic properties were prepared by using three different grades ($5x10^5$, $8x10^6$, $20x10^6$ g/gmol) of HPAM (Partially hydrolysed polyacrylamide) and bed erosion experiments with 30/50 mesh size of sand particles were carried out with these solutions. Also, PIV data were recorded for each experiment.
- Three dilute polymer solutions having the same shear viscosity, but different elastic properties were prepared by using three different grades ($5x10^5$, $8x10^6$, $20x10^6$ g/gmol) of HPAM. In the horizontal flow loop, the frictional pressure drops at several flow rates for pipe flow of these fluids were measured and for further analysis the flow of these fluids was recorded by using PIV technique.

1.4. CONTRIBUTIONS OF THE CURRENT STUDY

The main contributions from the current study are summarized below;

- Effects of surface properties on critical flow velocity were found out and this study showed that some surface treatment might advance the onset of particle movement in a stationary sand bed.
- The mechanism of the particle removal from a sand bed was better understood when the transport fluid was a dilute polymer solution. This experimental study showed that beside particle size, the position of

sand particles with respect to viscous sublayer of the dilute polymer solution had a significant role in particle removal.

- The bed erosion experiments in this study revealed out the effects of sand surface properties on frictional pressure drops for flow of water and dilute polymer solutions over a sand bed.
- Effect of viscoelasticity on bed erosion dynamics and frictional pressure drops over a sand bed was investigated in detail. The direct effect of fluid elasticity on bed erosion dynamics and frictional pressure drops over a sand bed was determined first time in the literature with this experimental study.
- The relationship between elastic properties of dilute polymer solutions and the frictional pressure drops they exhibited in pipe flow were revealed out experimentally. Also, the effect of fluid elasticity on onset of drag reduction and early transition to turbulence were discussed in detail.

1.5. STRUCTURE OF THE THESIS

This thesis contains the bed erosion experiments with water and a dilute solution of Alcomer RD-110 over different sizes of treated and untreated sand particle beds and the bed erosion experiments of two dilute solutions of HPAM having the same shear viscosity but different elastic properties over a 30/50 mesh size of sand particle bed. In addition to all these, a detailed experimental study for pipe flow of three dilute solutions of HPAM, having the same shear viscosity but different elastic properties, was included in this thesis and all aspects of the research were covered in seven separate chapters.

In chapter 1, initially an overview on the research subject was given and the problem was stated. Then, the scope of the experimental work and the main objectives for this research were introduced. Mentioning the contributions of this study to the research area was followed up all those. Then, the introduction section was finalized by presenting the plot of the thesis at the end.

In chapter 2, the experimental setup, the main equipment, and the methodology used in all experiments were explained. This section contains the description of each component in the horizontal flow loop together with a detailed explanation for the experimental procedures followed and PIV data acquisition. Also, some basic knowledge on fluid rheology, viscoelasticity and the details of fluid mixing procedure were provided.

In chapter 3, the results of the bed erosion experiments with four different mesh size of treated and untreated sand particles were presented where the transport fluid is water. A detailed discussion about effects of surface properties and sand particle size on bed erosion dynamics of water flow over a stationary sand bed were given.

Chapter 4 presents the results of bed erosion experiments with three different mesh size of treated and untreated sand particles where the transport fluid is a dilute solution of Alcomer RD-110. The effects of surface properties and sand particle size on bed erosion dynamics of a dilute polymer solution flow over a sand bed were discussed in detail.

In chapter 5, the results of pipe flow experiments carried out with three dilute solutions prepared by using three different grades of HPAM having the same shear viscosity, but different viscoelastic properties were discussed in detail in terms of frictional pressure drops, onset of drag reduction and transition to turbulent state.

Chapter 6 provided the results of bed erosion experiments done with two dilute solutions prepared by using three different grades of HPAM having the same shear viscosity, but different viscoelastic properties. The discussion of the experimental results was focused on the effects of elasticity on bed erosion dynamics.

In chapter 7, a short conclusion for each experimental work was given and some recommendations were provided for the future works similar to ours in this research area.

1.6. REFERENCES

1. Nazari, T., Hareland, G., Azar, J. J. (2010, May). Review of Cuttings Transport in Directional Well Drilling: Systematic Approach. SPE Western Regional Meeting Anaheim, California, USA, SPE-132372-MS, doi: 10.2118/132372-MS.
2. Li, J., Luft, B. (2014a, October). Overview of Solids Transport Studies and Applications in Oil and Gas Industry - Experimental Work. SPE Russian Oil and Gas Exploration & Production Technical Conference and Exhibition. Moscow, Russia, SPE-171285-MS, doi: 10.2118/171285-MS.
3. Li, J., Luft, B. (2014b, December). Overview Solids Transport Study and Application in Oil-Gas Industry-Theoretical Work. International Petroleum Technology Conference. Kuala Lumpur, Malaysia, IPTC-17832-MS, doi: 10.2523/IPTC-17832-MS.
4. Brown, N., Bern, P., Weaver, A., (1989). Cleaning Deviated Holes: New Experimental and Theoretical Studies, SPE/IADC Drilling Conf.
5. Adari, R., Miska, S., Kuru, E., Bern, P., and Saasen, A. (2000, February) Cuttings Bed Erosion Curves Help Predict Optimum Circulation Time for Hole Cleaning. ETCE/ OMAE Joint Conference of ASME, New Orleans, LA.
6. Martins, A., Campos, W., Liporace, F., Wei, X., and Van Riet, E. (1997). On the Erosion Velocity of a Cuttings Bed During the Circulation of Horizontal and Highly Inclined Wells. Latin American and Caribbean Petroleum Engineering Conference.
7. Rabenjafimanantsoa, A., Time, R. W., Saasen, A. (2007). Simultaneous Uvp and PIV Measurements Related to Bed Dunes Dynamics and Turbulence Structures in Circular Pipes. 5th International Symposium on Ultrasonic Doppler Methods for Fluid Mechanics and Fluid Engineering, pp. 63-67.
8. Bizhani, M., Kuru, E. (2018). Particle Removal from Sandbed Deposits in Horizontal Annuli Using Viscoelastic Fluids. SPE Journal, Vol.23, Issue.02, pp.256-273, April 2018, doi:10.2118/189443-PA
9. Walker, S., Li, J. (2000, April). The Effects of Particle Size, Fluid Rheology, and Pipe Eccentricity on Cuttings Transport. g2000 SPE/ICoTA Coiled Tubing Roundtable. Houston, TX, SPE-60755-MS, doi: 10.2118/60755-MS.
10. Saasen, A., Løklingholm, G. (2002, February). The Effect of Drilling Fluid Rheological Properties on Hole Cleaning. IADC/SPE Drilling Conference. Dallas, Texas, SPE-74558-MS, doi: 10.2118/74558-MS.

11. Duan, M., Miska, S. Z., Yu, M. et al. (2007, April). Critical Conditions for Effective Sand-Sized Solids Transport in Horizontal and High-Angle Wells. SPE Production and Operations Symposium Oklahoma City, Oklahoma, USA, SPE-106707-MS, doi: 10.2118/106707-MS.

12. Powell, J. W., Parks, C. F., Seheult, J. M. (1991). Xanthan and Welan: The Effects of Critical Polymer Concentration on Rheology and Fluid Performance. Society of Petroleum Engineers. doi:10.2118/22066-MS.

13. Zamora, M., Jefferson, D. T., Powell, J. W. (1993). Hole-Cleaning Study of Polymer-Based Drilling Fluids. Society of Petroleum Engineers. doi:10.2118/26329-MS.

14. Sayindla, S., Lund, B., Ytrehus, J.D., et al., (2017, November). Hole-cleaning performance comparison of oil-based and water-based drilling fluids. J. Pet. Sci. Eng., Volume 159, Pages 49-57. doi.org/ 10.1016/ j.petrol. 2017.08.069.

15. Werner, B., Myrseth, V., Saasen, A. (2017). Viscoelastic properties of drilling fluids and their influence on cuttings transport, Journal of Petroleum Science and Engineering, Volume 156, Pages 845-851, ISSN 0920-4105, https://doi.org/10.1016/j.petrol.2017.06.063.

16. Toms, B. A. (1948). Some observations on the flow of linear polymer solutions through straight tubes at large Reynolds numbers. In Proceedings of the 1st International Congress on Rheology, vol. 2, pp. 135–141. North-Holland.

17. Savins, J. G. (1966). A Stress-Controlled Drag-Reduction Phenomenon. Society of Petroleum Engineers. doi:10.2118/1724-MS

18. Walsh, M. (1967). On the Turbulent Flow of Dilute Polymer Solutions. Ph.D. Thesis, California Inst. Tech., Pasadena, CA.

19. E. Rouse, Prince. (1953). A Theory of the Linear Viscoelastic Properties of Dilute Solution of Coiling Polymers. The Journal of Chemical Physics. 21. 1272-1280. doi:10.1063/1.1699180.

20. Elata, C., J. Lehrer, Kahanovitz, A. (1966). Turbulent Shear Flow of Polymer Solutions. Israel Journal of Technology, Vol. 4, No. 1, 1966, pp. 87-95.

21. Virk, P. (1971). An elastic sublayer model for drag reduction by dilute solutions of linear macromolecules. Journal of Fluid Mechanics, 45(3), 417-440. doi:10.1017/S0022112071000120.

22. Lumley, J. (1973). Drag Reduction in Turbulent Flow by Polymer Additives. Journal of Polymer Science: Macromolecular Reviews. 7. 263 - 290. doi:10.1002/pol.1973.230070104.

23. Achia, B., Thompson, D. (1977). Structure of the turbulent boundary in drag-reducing pipe flow. Journal of Fluid Mechanics, 81(3), 439-464. doi:10.1017/S002211207700216X.

24. Massah, H., & Hanratty, T. (1997). Added stresses because of the presence of FENE-P bead–spring chains in a random velocity field. Journal of Fluid Mechanics, 337, 67-101. doi:10.1017/S0022112097004916

25. Dimitropoulos, C., Sureshkumar, R., Beris, A. (1998). Direct numerical simulation of viscoelastic turbulent channel flow exhibiting drag reduction: Effect of the variation of rheological parameters. Journal of Non-Newtonian Fluid Mechanics. 79. 433-468. doi:10.1016/S0377-0257(98)00115-3.

26. Pinho, F. (2003). A GNF framework for turbulent flow models of drag reducing fluids and proposal for a k-type closure. J. Non-Newtonian Fluid Mech. 114. 149-184. doi:10.1016/S0377-0257(03)00120-4.

27. Bonn, D., Amarouchene, Y., Wagner, C., Douady, S., Cadot, O. (2005). Turbulent drag reduction by polymers. Journal of Physics: Condensed Matter. 17. S1195. doi:10.1088/0953-8984/17/14/008.

28. Groisman, A., Steinberg, V. (2004). Elastic turbulence in curvilinear flows of polymer solutions. New Journal of Physics. 6–29. doi:10.1088/1367-2630/6/1/029.

29. Hansen, R. J., Little R. C. (1974). Early turbulence and drag reduction phenomena in larger pipes, Nature, 10.1038/252690a0, 252, 5485, (690-690).

30. Forame, P. C., Hansen, R. J., Little, R. C. (1972), Observations of early turbulence in the pipe flow of drag reducing polymer solutions. AIChE J., 18: 213-217. doi:10.1002/aic.690180139.

31. W. Hoyt, J. (1977). Laminar-turbulent transition in polymer solutions. Nature. 270. 508-509. doi:10.1038/270508a0.

32. Dubief, Y., Terrapon, E. V., Soria, J. (2013). On the mechanism of elasto-inertial turbulence. Physics of fluids (Woodbury, N.Y.: 1994). 25. 110817. doi:10.1063/1.4820142.

33. Samanta, D., Dubief, Y., Holzner, M., Schäfer, C., Morozov, A., Wagner, C., Hof, B. (2013). Elasto-inertial turbulence. Proceedings of the National Academy of Sciences of the United States of America. 110. doi:10.1073/pnas.1219666110.

2. EXPERIMENTAL SETUP AND METHODOLOGY

This chapter explains the horizontal flow loop, its components and the experimental procedure followed in detail. Also, in this chapter some basic concepts of fluid rheological properties, viscoelasticity and PIV data acquisition were explained briefly.

2.1. EXPERIMENTAL SETUP

The experimental setup in this study is the horizontal flow loop itself and a schematic of the flow loop is given in Figure 2-1, the flow loop mainly comprises of a 500 litres stainless steel tank, a centrifugal pump, a magnetic flow meter, a pressure transducer, glass pipes, steel couplings and five gate valves to control the flow through the loop.

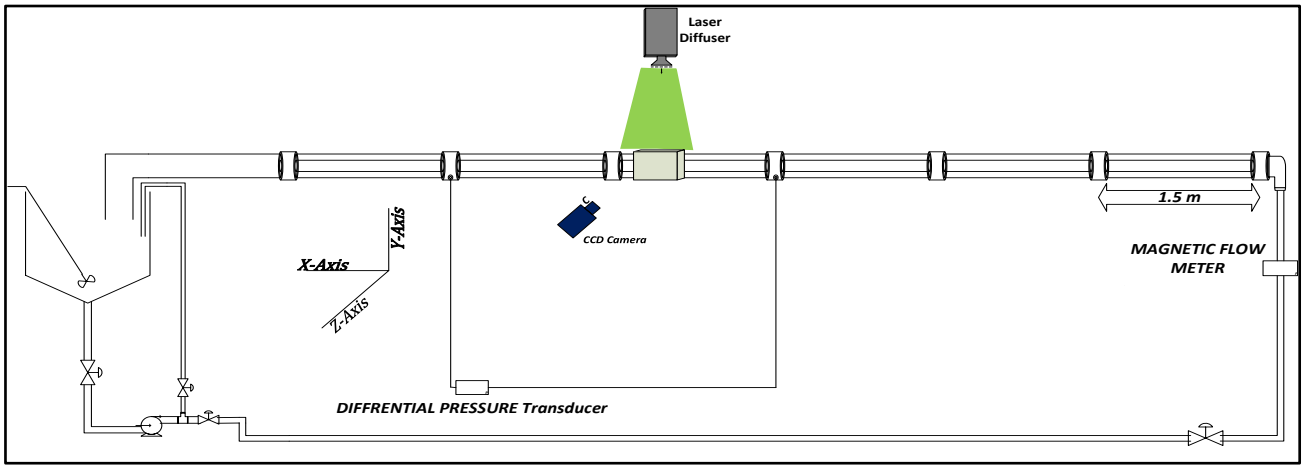

Figure 2-1 Schematic of the horizontal flow loop [1].

The mixing tank can be isolated from the flow loop by closing the gate valve on the bottom and so, the test mixture can be prepared in the isolated tank in a controlled manner. For mechanical agitation of the mixture components, the air operated mixer attached to the tank is used and the rotational speed of the mixer is controlled by adjusting the air flow. There are cooling jackets around the suction tank and by circulating hot/cold water through these jackets, the temperature of the fluid stored inside the tank can be increased or decreased. There are

three weight sensors and two temperature sensors mounted on the tank. One of the temperature sensors measures the temperature of the fluid inside the tank and the other measures the lab temperature.

The centrifugal pump of the system is electric driven. The pump is controlled through a VFD unit (Variable Frequency Drive Unit) by adjusting the rotational speed of the centrifugal pump through a software named as Labview. The flowrate that pump provides depends on a few parameters. The rheological properties of the test fluid, height of the fluid inside the tank and the frictional pressure drops through the system all affects the flowrate provided by the pump. So, the flowrate is measured directly through OMEGA FMG607-R magnetic flow meter. However, approximate maximum and minimum circulation rates in the horizontal loop are 15 lpm and 500 lpm respectively.

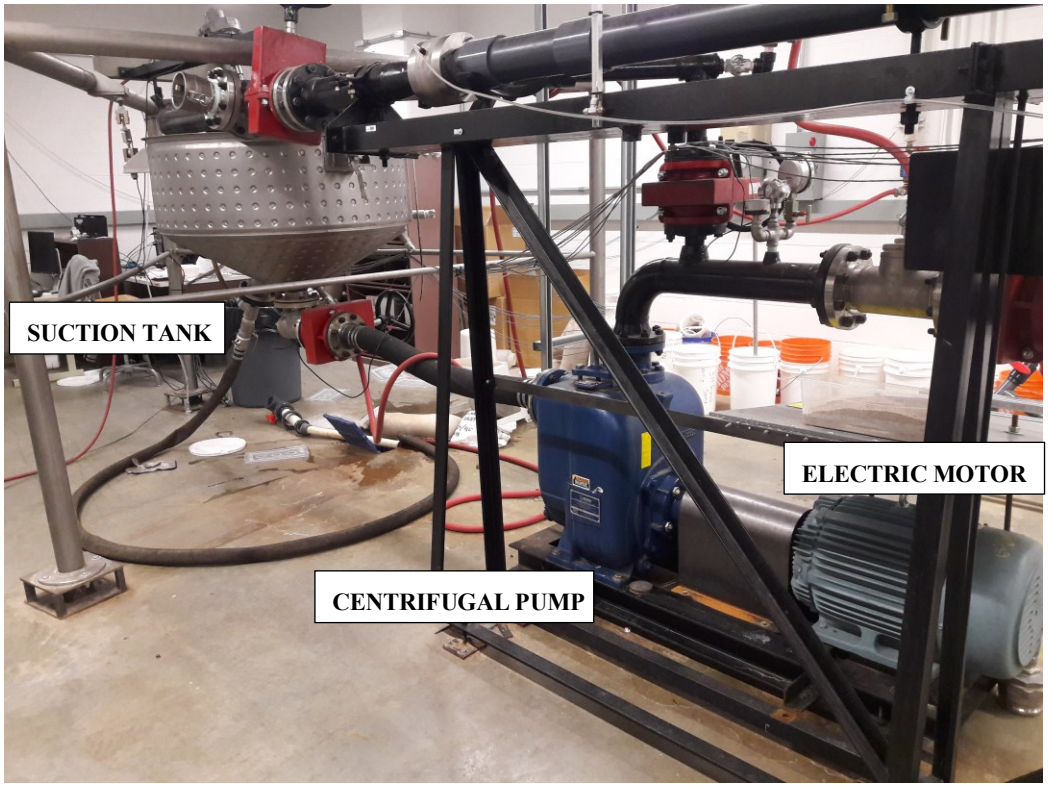

Figure 2-2 Suction tank and the centrifugal pump.

Figure 2-3 The air mixer installed on the suction tank.

Figure 2-4 VFD unit controlling the electric motor.

There is only one suction line from tank to the pump and there is only one discharge line from pump to the flow loop. Also, there is a return line to tank connected to the discharge line. Then, there are two lines connecting the pump and the horizontal section of the flow loop comprising the glass pipes including the main test section. One of those lines is 1-inch diameter and the other one is 2-inch diameter. These two different diameter lines can be preferred depending on the flowrate and pressure requirements of the specific experiments, because higher flowrates and lower pressure drops across the system might be achieved by preferring the bigger diameter connection line or vice versa.

Figure 2-5 The differential pressure transducer.

The magnetic flow meter, OMEGA FMG607-R, is installed on the vertical pipe just before the horizontal section and the accuracy of the flow meter is +/- 0.05 %. Then, the horizontal section starts, and the 9 m long section includes six separate glass pipes, length of each is 1,5 m long and the inner diameter of each is 95 mm. Stainless steel couplings connects each glass pipe. Glass is made up of borosilicate with a refractive index of 1.47. All PIV recordings for the test are measured on the main test section where the pipe is inside a rectangular box filled with glycerol. In order to measure the frictional pressure drops across the flow loop, a pressure transducer OMEGA DPG409 is installed on the flow loop. This pressure transducer measures the pressure drop across a 3.05 m length section with an accuracy of +/- 0.08%.

Figure 2-6 The magnetic flow meter in the horizontal loop.

2.2. METHODOLOGY

In this study there are two main experiments: the first one is the pipe flow experiments and the second one is the bed erosion experiments. For each type of experiments PIV measurements were taken. In this section, fluid preparation, fluid rheology, the procedures for pipe flow and bed erosion experiments and the details of PIV data acquisition are covered separately.

2.2.1. Rheology of Fluids Tested and Fluid Preparation

Both Newtonian and non-Newtonian fluids were used in this experimental study. If the viscosity of a fluid is independent of applied shear stress or shear rate and the shear stress – shear rate relation for that fluid can be described in the form of equation 2-1, then that fluid is defined as Newtonian [2]. However, if the viscosity of a fluid is sensitive to applied shear stress or shear rate and the relation between shear stress and shear rate is not linear, then that fluid is defined as non-Newtonian [2]. Water used in bed erosion tests was the only Newtonian fluid in this study and the dilute polymer solutions used in both bed erosion and pipe flow tests were non-Newtonian. Dilute solutions of both Alcomer RD-110 and HPAM were power law fluids. They were shear thinning in the shear rate range we worked, and they might be defined in the form of a power law equation as shown in equation 2-2.

$$\tau = \mu\gamma \quad \text{(2-1)}$$

$$\tau = K\gamma^{n} \quad \text{(2-2)}$$

In the bed erosion and pipe flow experiments with dilute polymer solutions of HPAM, we investigated the effect of viscoelasticity on bed erosion and pipe flow dynamics. Viscoelastic materials show elastic-like behaviour as well as viscous-like behaviour. For example, the resultant strain would be the same for an elastic material as a result of an applied stress whether the stress is applied fast or slow. However, for viscoelastic materials the resultant strain for an applied stress will also be controlled by time, so applying the same stress fast or slow on a viscoelastic material will result in different strain responses [3]. If a constant stress is applied on a viscoelastic matter, the strain will increase with time and this is called as creep. Similarly, if a constant strain is applied on a viscoelastic matter, the stress will decrease with time, which is called as stress relaxation, or if a cyclic stress is applied on a viscoelastic material, a phase lag will occur, and mechanical energy loss (i.e. heat loss) would be observed.

Viscoelasticity of a material can be tested with three basic methods: creep test, stress relaxation test and cyclic or oscillatory test [3]. Applying the proper test to a material to measure the viscoelasticity depends on the nature of the material and in our study as we were dealing with dilute polymer solutions, we used oscillatory test – more specifically frequency sweep test – to measure the viscoelastic behaviour of the solutions used in this experimental work.

In frequency sweep test, a sinusoidal stress is applied to a material. Applied stress might be defined with equation 2-3, and the strain response of the material to applied stress occurs in the form of equation 2-4. This stress and strain relation can be seen in Figure 2-7 visually. As it is clearly seen from Figure 2-7, there is a shift – phase lag - between stress and strain.

$$\tau(t) = \tau_0 \cos(\omega t + \delta) \quad \text{(2-3)}$$

$$\varepsilon(t) = \varepsilon_0 \cos(\omega t) \quad \text{(2-4)}$$

Where τ is the stress as a function of time, τ_0 is stress amplitude, ω is angular frequency, δ is phase angle, ε is strain as a function of time, ε_0 is strain amplitude and t is time.

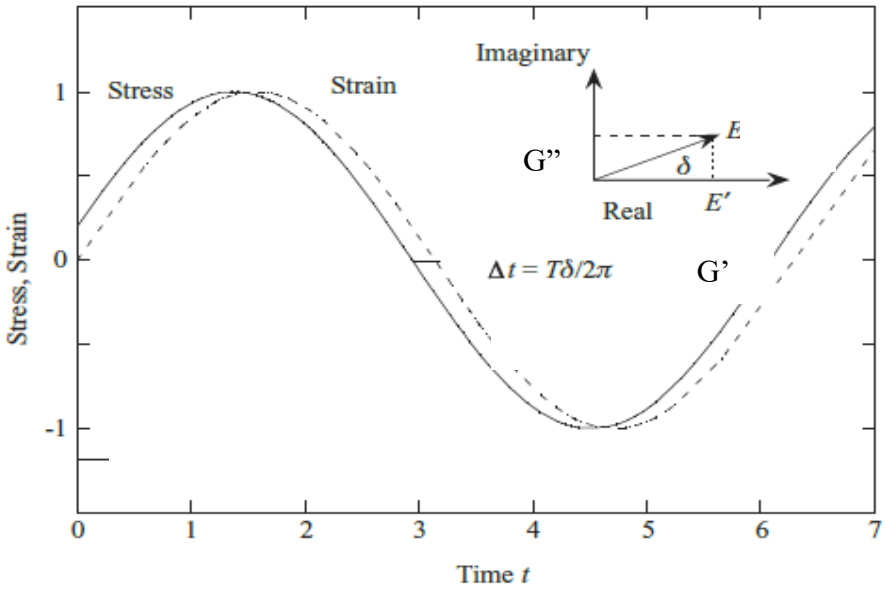

Figure 2-7 Stress and strain plot for a typical frequency test [3].

The stress and strain in the form of sinusoidal function can be rewritten in the form of Euler's equation with imaginary and real parts. This real and imaginary parts can be defined with equation 2-5 and equation 2-6 respectively, where real part stands for in-phase stress and imaginary part stands for out-phase stress.

$$\tau_0' = \tau_o \cos(\delta) \quad \text{(2-5)}$$

$$\tau_0'' = \tau_0 \sin(\delta) \quad \text{(2-6)}$$

Where τ_0' in-phase stress, τ_o is stress amplitude, δ is phase angle, τ_0'' out-phase stress.

So, frequency sweep test measures the storage and loss modulus values of a material at different angular frequencies. The storage modulus (G') is the ratio of in-phase stress to strain and the loss modulus (G") is the ratio of out-phase stress to strain. Storage modulus and loss modulus can be expressed in mathematical form with equation 2-7 and equation 2-8.

$$G' = \frac{\tau_0'}{\varepsilon_0} \quad \text{(2-7)}$$

$$G'' = \frac{\tau_0''}{\varepsilon_0} \quad \text{(2-8)}$$

The loss and storage moduli also represent the extent of irreversible and reversible energy, which is transferred to the material by the applied stress respectively [4]. While the strain caused by in phase stress – defining the storage modulus – can be reversible, the energy transferred to the matter by the out-phase stress – defining the loss modulus – is irreversible as heat loss [4].

Both viscosity and frequency sweep tests were carried out using the high-resolution rheometer Bohlin C-VOR 150.

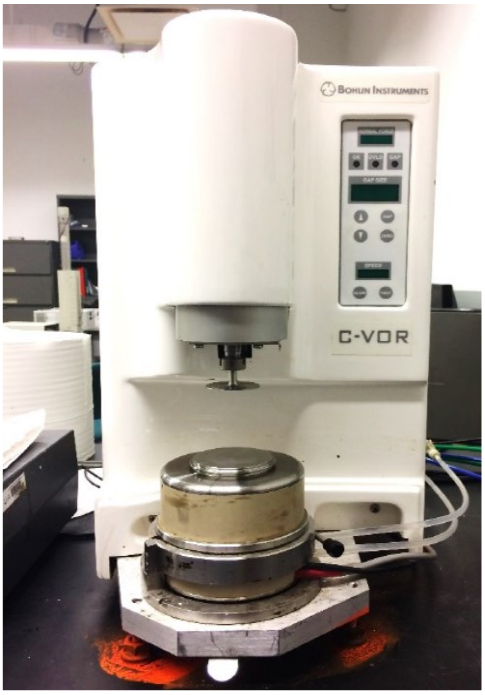

Figure 2-8 Bohlin C-VOR 150 rheometer.

Including both pipe flow and bed erosion tests, five different fluids were used in flow loop experiments in total. These fluids are water, 0.032% w/w dilute solution of Alcomer RD-110 and three dilute polymer solutions of HPAM.

Tap water was used for the bed erosion tests of four different mesh size of treated and untreated sand particles.

Dilute polymer solution of Alcomer RD-110 was used for the bed erosion tests of three different size of treated and untreated sand particles. The concentration for the polymer solution was 0.032% w/w. To prepare this solution:

1) The suction tank was isolated from the rest of the flow loop.
2) The suction tank was filled with 500 litres of water.
3) 160 grams of Alcomer RD-110 was added to the suction tank slowly, while the air mixer is on.
4) The mixture was mixed in the tank till a homogeneous solution was obtained. Mixing speed of the air mixer was kept below 300 rpm.
5) Viscosity of the prepared fluid were measured to verify the rheological properties of the prepared solution.

Three different dilute solutions of HPAM were prepared in this study. Each of these three solutions had the same shear viscosity but different elastic properties. These fluids were prepared by using three different grades (i.e. $5x10^5$, $8x10^6$, $20x10^6$ g/gmol) of HPAM. In order to have the same viscosity for these fluids, it is arranged so that polymer mixtures had the same average molecular weight. This was achieved by using the equation 2-9 [5]. The polydispersity indexes of the compositions were also considered to diverse the viscoelastic properties of these mixtures as much as possible. The polydispersity indexes were calculated based on equation 2-10 [5]. At the end, concentrations and compositions for these dilute solutions were arranged considering polydispersity indexes, average molecular weight of the mixtures and the mixing experience. Table 2-1 shows the determined concentrations and composition for the Fluid A, Fluid B and Fluid C.

$$M_{w,B} = \prod_{i=1}^{n} M_{w,i}^{\omega_i} \quad \text{..... (2-9)}$$

$$I = \frac{M_w}{M_n} = \left(\sum_{i=1}^{n} \omega_i M_{w,i} \right) \times \left(\sum_{i=1}^{n} \frac{\omega_i}{M_{w,i}} \right) \quad \text{..... (2-10)}$$

Where $M_{w,B}$ is the average molecular weight of the polymer blend, ω_i is the weight fraction of the polymer grade i, $M_{w,i}$ is the molecular weight of polymer grade i, M_w is the weighted average molecular weight, M_n is the number average molecular weight and I is the polydispersity index.

Table 2-1 Compositions and concentrations for Fluid A, Fluid B and Fluid C.

Mixture	Concentration	HPAM AB005V (w%)	HPAM 3330S (w%)	HPAM 3630S (w%)	Average Molecular Weight	Polydispersity Index
Fluid A	0.135	24.2	0	75.8	$8x10^6$	8.05
Fluid B	0.095	0	100	0	$8x10^6$	1
Fluid C	0.100	42.95	43.95	13.92	$8x10^6$	4.26

Fluid A and Fluid B were used in bed erosion experiments. Fluid A, Fluid B and Fluid C were used in pipe flow experiments. However, the procedure followed to prepare these fluids was identical. To prepare each fluid;

1) The suction tank was isolated from the rest of the flow loop.
2) The suction tank was filled with 500 litres of water.
3) The required amount of polymer was added to system slowly, while the air mixer is on.
4) The mixture was mixed in the tank till a homogeneous solution was obtained, while the mixing speed of the air mixer was kept below 300 rpm.
5) Viscosity and frequency sweep tests were carried out for the prepared fluid before and after experiments to confirm the rheological properties of the fluid.

2.2.2. Pipe Flow Experiments

Flow dynamics of three dilute polymer solutions having similar viscosity but different viscoelastic properties were compared for pipe flow by conducting flow experiments in horizontal flow loop. Each fluid mixture was prepared by using three different grades of HPAM polymer in predetermined concentrations and compositions as described in section 2.2.1. When the mixture became fully homogenous, then the circulation was started through the flow loop and samples were taken from the return line for rheology tests. Viscosity and oscillatory tests were carried out for each fluid mixture by using Bohlin CVOR-150 rheometer. After validating the rheological properties of the fluid mixture, frictional pressure drops across the test section of the horizontal flow loop were recorded at several flow rates. Finishing recording frictional pressure drops, samples were taken from the return line once again and the rheology tests were carried out once again to check the viscometric and viscoelastic properties of the mixtures. Finally, as the second part of the pipe flow experiments, the fluid mixtures were prepared once again to take the PIV measurements. Near wall and full profile PIV measurements were taken at certain flow rates for each fluid mixture.

2.2.3. Bed Erosion Experiments

Three different bed erosion experiments were involved in this study. The first one was the tests with four different mesh size of treated and untreated sand particles where the transport fluid is water, the second one was the tests with three different mesh size of treated and untreated sand particles where the transport fluid is the dilute solution of Alcomer RD-110 and the third one was the tests with 30/50 mesh size of untreated sand particles where the transport fluids are dilute solutions of three different grades of HPAM having different viscoelastic properties. Even the experiments were done with different fluids, the procedure was the same. The procedure for setting the bed inside the horizontal flow loop was also the same. First, the tank was filled with 500 litres of water and the water circulation through the loop was started at the highest possible flowrate, then the amount of sand required to set the desired sand bed inside the flow loop was added to the suction tank. When a homogenous sand

bed was formed in the horizontal loop, the circulation was stopped and gate valves at the both ends of the flow loop were closed to allow the sand particles to settle down. For the water bed erosion tests, first water was circulated at the minimum rate possible till the circulating fluid became crystal clear. Then, the bed erosion test was carried out for the specific mesh size of sand particles inside the flow loop. If the test was with a polymer solution, initially the water used to set the bed inside the horizontal flow loop was drained by opening draining valves and then the relevant polymer mixture was prepared cautiously in the mixing tank isolated from the flow loop. Finally, after verifying the rheology of the polymer solution prepared in the mixing tank with rheology measurements, the bed erosion test for the sand particles inside the flow loop was carried out.

2.2.4. PIV Measurements

After preparing the mixtures and starting the flow, taking PIV measurements is a straightforward procedure.

1) The aperture and the focus of the camera was adjusted properly to get clear PIV images like the one shown in Figure 2-9.
2) Camera view was calibrated by using the calibration target.
3) Differential time was set to get a particle shift of 10 pixels between two sequential images.
4) At least 1000 images were recorded at each flow rate predetermined for the experiments.
5) Processing and post-processing of the recorded images were done by using the software Davis 8.3.
6) Processed PIV data was exported to excel files for further analysis for each flow rate.

In the next sections the image calibration and processing, which are the most important steps of PIV measurements, were explained in more detail.

Figure 2-9 A typical PIV image.

2.2.5. PIV Image Calibration

The software must recognize the images taken spatially to make some calculations to determine the instantaneous velocities. Therefore, before recording the data the first thing is the calibration of the image space. First, aperture and the focus of the camera is set to be able capture clear images of the flow. Then, before recording any PIV data for the flow, without changing any settings the raw image of the calibration target is taken. As Figure 2-10 shows, the calibration target is a prototype of the flow loop itself. The distance between the dots is already known by the software. So, based on the image taken, the calibration is done by the software and the Field of View (FOV) is configured depending on the calibration. The calibration algorithm automatically removes the image distortions by camera lens errors and projections [6]. An example for the calibrated field of view can be seen in Figure 2-11.

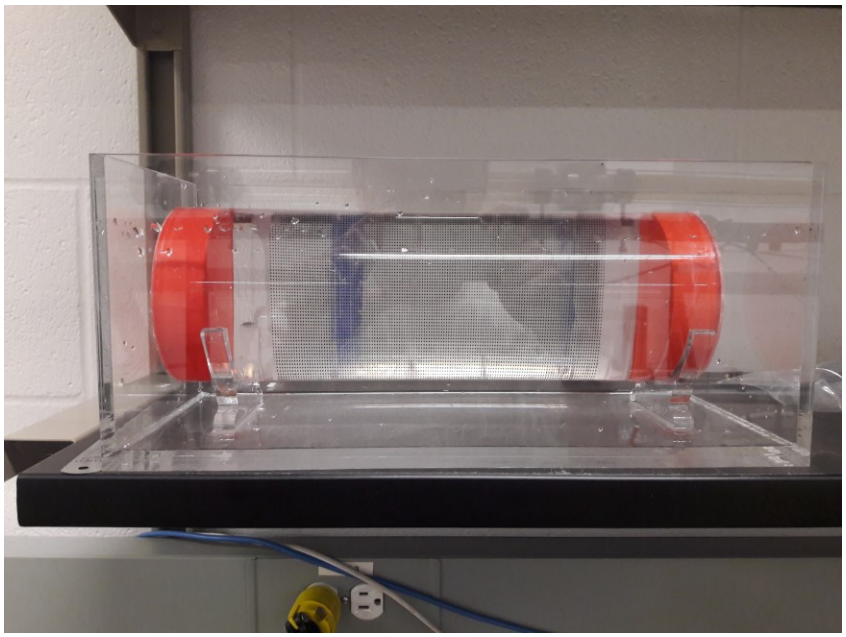

Figure 2-10 The calibration target.

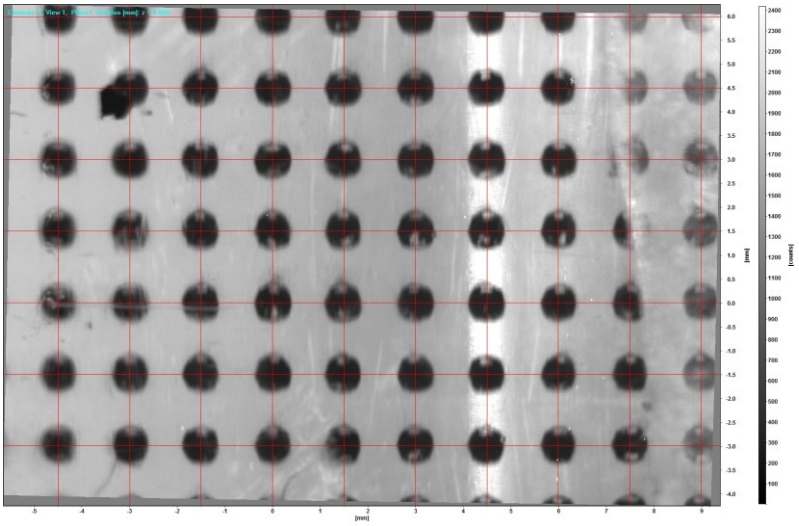

Figure 2-11 An example for a calibrated field of view.

2.2.6. PIV Data Processing

The recorded images are converted to velocity field by processing the images with Davis 8.3. and determining velocity and velocity fluctuations is enough for almost all turbulence analysis. Velocities in x and y direction can be simply estimated with equations presented below;

$$u = \frac{\Delta x}{\Delta t} \quad \text{(2-11)}$$

$$v = \frac{\Delta y}{\Delta t} \quad \text{(2-12)}$$

In above equations, the differential time (Δt) is already known, because it is the delay between two sequential images captured by the camera or the delay between the sequential laser pulses and it is fixed prior to starting PIV measurements. Then, this means that only displacements in x and y directions are required to calculate the velocity. In order to determine the displacement in x and y directions, two sequential images taken are compared segment by segment and movement of particle groups in each segment is determined by this comparison. This comparison is done by an FFT (Fast Fourier Transform) based cross correlation algorithm which the software Davis 8.3. already includes. As shown in Figure 2-12, each sequential image is divided into small windows and then the particle groups as dots in those windows are assessed to a one to one comparison [6]. The software determines the movement of the particle group in each window depending on the highest peak detected as a result of applied cross correlation for each image. Detected particle movement can be converted to distances easily because the image space is already introduced to the software spatially. Then, velocity of the particles is calculated based on the displacement measured and the delay time using the formulas presented in equation 2-11 and 2-12.

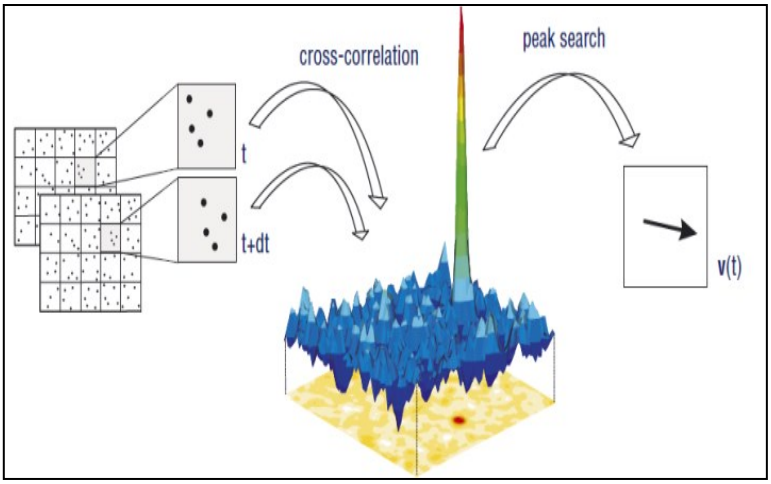

Figure 2-12 Peak search and cross correlation process [6].

We used a multiple pass approach in our analysis to optimize the accuracy of velocity calculations. This multiple pass approach started from a window size of 64x64 and it is finished with a 24x24 window size including 32x32 window size in the between. Also, the overlap was %50 in all these analyses. Then, the velocity fields obtained at the end of this processing was refined with a post processing algorithm and the ultimate velocity field was obtained for the flow. For all these analyses at least 1000 images were captured.

As the flow was turbulent, beside time averaged velocities, fluctuating velocities exist. The average velocities and fluctuating velocities can be shown in equation 2-13 and 2-14 below.

$$u = \bar{u} + u' \quad \text{(2-13)}$$

$$v = \bar{v} + v' \quad \text{(2-14)}$$

In above equations, $\bar{u}$ and $\bar{v}$ are the time average velocities and u' and v' are the fluctuating velocities.

These fluctuating velocities are essential in determining Reynolds stresses, axial and radial turbulent intensity profiles. The equations for Reynolds stresses, axial and radial turbulent intensities were given below.

$$\tau_R = -\rho\overline{u'v'} \quad \text{(2-15)}$$

$$u_{rms} = \sqrt{\overline{u'u'}} \quad \text{(2-16)}$$

$$v_{rms} = \sqrt{\overline{v'v'}} \quad \text{(2-17)}$$

2.3. REFERENCES

1. Bizhani, M. (2017). Experimental and Theoretical Investigations of Particle Removal from Sand Bed Deposits in Horizontal Wells Using Turbulent Flow of Water and Polymer Fluids. PhD Thesis, Civil and Environmental Engineering, University of Alberta, Edmonton, Canada.
2. McCabe, W.L., Smith, J.C. and Harriott, P. (2004). Unit Operations of Chemical Engineering, New York: McGraw-Hill.
3. Lakes, R. (2009). Introduction: Phenomena. In Viscoelastic Materials (pp. 1-13). Cambridge: Cambridge University Press. doi:10.1017/CBO9780511626722.002
4. Roylance, D., (2001) Engineering Viscoelasticity. Department of Materials Science and Engineering Massachusetts Institute of Technology Cambridge, MA 02139

   Retrieved from http://web.mit.edu/course/3/3.11/www/modules/visco.pdf
5. Arnipally, S. K., & Kuru, E. (2018). Settling Velocity of Particles in Viscoelastic Fluids: A Comparison of the Shear-Viscosity and Elasticity Effects. Society of Petroleum Engineers. doi:10.2118/187255-PA
6. LaVision, Davis 8.3 Product Manual. ed, 2015.

3. EFFECT OF PARTICLE SIZE AND SURFACE PROPERTIES ON THE NEAR WALL TURBULENCE CHARACTERISTICS AND THE CRITICAL VELOCITY REQUIRED FOR THE PARTICLES REMOVAL FROM THE SAND BED DEPOSITED IN HORIZONTAL PIPELINES

3.1. ABSTRACT

An experimental study was conducted to investigate the transport of sand particles over the sand bed deposited in a horizontal conduit by using turbulent flow of water. The main objectives were: i-) to determine the near wall turbulence characteristics at the onset of bed erosion (i.e., near wall velocity profile, Reynolds shear stresses, axial and radial turbulent intensities), bed roughness and interfacial friction factor by using particle image velocity (PIV) technique; ii-) to determine critical velocity required for particle removal from the bed deposits; iii-) more specifically, to determine how the sand particle size and surface characteristics would influence the critical velocity required for the onset of bed erosion and the near wall turbulence characteristics.

A large-scale horizontal flow loop equipped with a non-intrusive laser-based particle image velocimetry (PIV) system has been used for the experiments. Effect of sand particle surface characteristics (i.e. wettability) on the critical velocity and the near wall turbulence characteristics were investigated by using treated and untreated industrial sands of four different mesh size (i.e. 20/40, 30/50, 40/70, 100). The PIV technique was used to determine instantaneous local velocity distribution near the stationary sand bed-fluid interface under sub-critical and critical flow conditions. The near wall velocity distribution measured directly at the sand bed/fluid interface together with the measured frictional pressure loss values were then used for the evaluation of the, Reynolds shear stresses, axial and radial turbulent intensities acting at the bed/fluid interface.

The results indicated that near wall velocity profile, Reynolds shear stresses, axial and radial turbulent intensities as well as the critical velocity for the onset of particle removal were all significantly influenced by the

variation in particle size and surface characteristics. Critical velocity for the onset of particle removal from sand beds increased with the increasing particle size.

When sands with special surface treatment were used, it was observed that the critical velocity required for the onset of the bed erosion was significantly lower than that of required for the untreated sands. The degree of reduction in critical velocity varied between 14 to 40% depending on the particle size. The effect of surface treatment on the transport efficiency became more significant with the decreasing particle size.

Knowledge of fluid-particles interaction near the bed interface is indispensable for accurate modelling of numerous industrial operations such as pipeline transport of slurry, sand transport in oil and gas production lines, cuttings transport in oil and gas well drilling and proppant transport in hydraulic fracturing. In this study, by conducting experiments under controlled conditions, we provided much needed fundamental data that can be used for the development of improved solid transport design criteria and suitable mitigation technologies. We have shown the proof of concept that the surface treated sand particles might have great potential for improving the transport efficiency of proppants used for hydraulic fracturing operations.

3.2. INTRODUCTION

Formation of stationary cuttings bed deposits is inevitable when drilling the long horizontal and extended reach wells. Operational problems such as slow drilling rate, excessive torque and drag, bridging, pack-off, hole fill and pipe stuck arise due to these bed deposits [1,2,3]. Occasionally, drilling must stop to clean the well, which costs time and money. The mere act of circulating drilling fluid may not clean the well as the critical flow rate and the shear stress for bed erosion must be reached [2,3]. Despite significant progress made in drilling fluids, tools, and field practices, along with more than 50 years of university and industry research, field experience indicates that hole cleaning is still a major problem on most highly inclined and horizontal wells [2,3].

Brown et al. [4] investigated the performance of different fluids including water and polymers on annular hole cleaning by conducting experiments in a specially designed flow loop. Their work provided a broader picture of the hole cleaning in the drilling operations. Adari et al. [5] conducted extensive experiments to determine the effect of drilling fluid rheological properties and flow rates on the cuttings bed erosion. Martins et al. [6] approached this subject in terms of predicting bed height after circulation and finding out the correlations to determine the circulation rate to mobilize the bed effectively. The macro scale up work of Rabenjafimanantsoa et al. [7], where the flow through the sand bed was investigated with the aid of PIV (Particle Image Velocimetry) and UVP (Ultrasound Velocity Profile), provided a deeper understanding on the flow structure and its relationship with the sand bed. Bizhani et al. [8], in a recent work, investigated the effect of fluid viscoelasticity on the bed erosion, also with a comparison to water, using PIV in horizontal annuli.

Particle size was considered as an important variable in most of the numerical models used for the predicting critical velocity required for the onset of the bed erosion regardless of the type of fluid and the flow regime. However, in most of the previous experimental studies, the focus of the investigations were the type of fluid and the flow regime required for an efficient hole cleaning operation and its optimization. In order to understand the sand removal phenomenon, the effect of particle size must also be given a detailed look. Therefore, an experimental study was conducted to investigate the effect of particle size on the critical velocity and near wall turbulence characteristics of water flow over the sand bed deposited in a horizontal pipeline. We have also investigated the effect of sand particle surface characteristics on the same. Industrial sands of four mesh sizes (20/40, 30/50, 40/70, 100) with and without special surface treatment were used in the study. The particle image velocimetry (PIV) technique was used to determine instantaneous local velocity distribution near the stationary sand bed-fluid interface under flow conditions.

3.3. MATERIALS AND METHODS

3.3.1. Sand Particles

Industrial quartz sand particles (SG =2.65) with and without special surface treatment and in four different mesh sizes (i.e., 20/40, 30/50, 40/70 and 100) were used in the current study. Table 3-1 summarizes the range of sand sizes in microns.

Table 3-1 Size Ranges of Sand Particles Used in the Experiments

Sand Particles Mesh Size	Sand Particles Size Range (microns)
20/40	420-840
30/50	297-590
40/70	210-420
100	149

Surface treated sand particles are strongly hydrophobic as shown in Figure 3-1. The measured contact angle was 139 degrees for 20/40 mesh size sands.

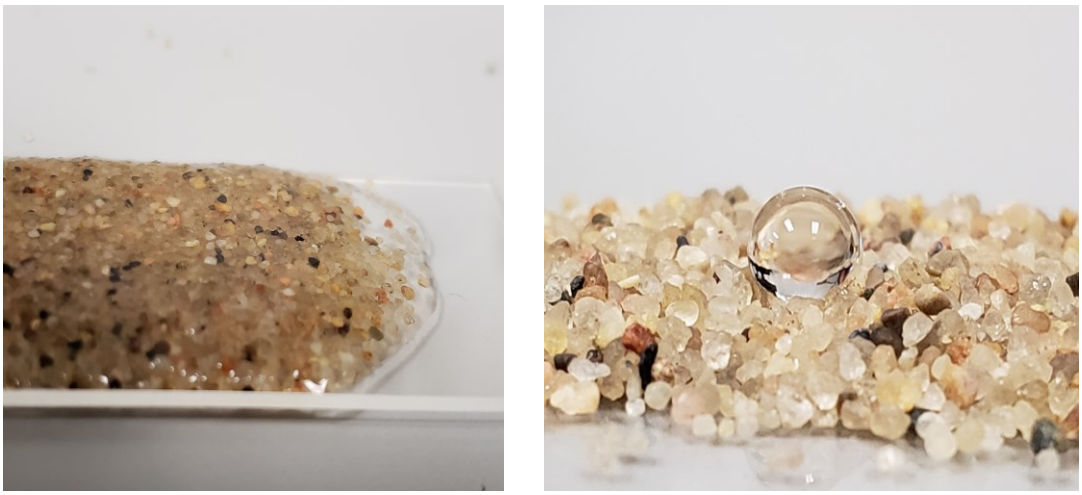

Figure 3-1 Contact angle measurement for 20/40 mesh size sands: a-) Non-treated sand b-) Surface treated sand

3.3.2. Experimental Flow Loop

A schematic diagram of the horizontal flow loop used in the current experimental study is shown in Figure 3-2. The flow loop was comprised of 500 litres capacity mixing tank, a centrifugal pump, suction and discharge lines, a differential pressure transducer, a magnetic flow meter, and several gate valves to control the fluid flow through the system and glass tubes.

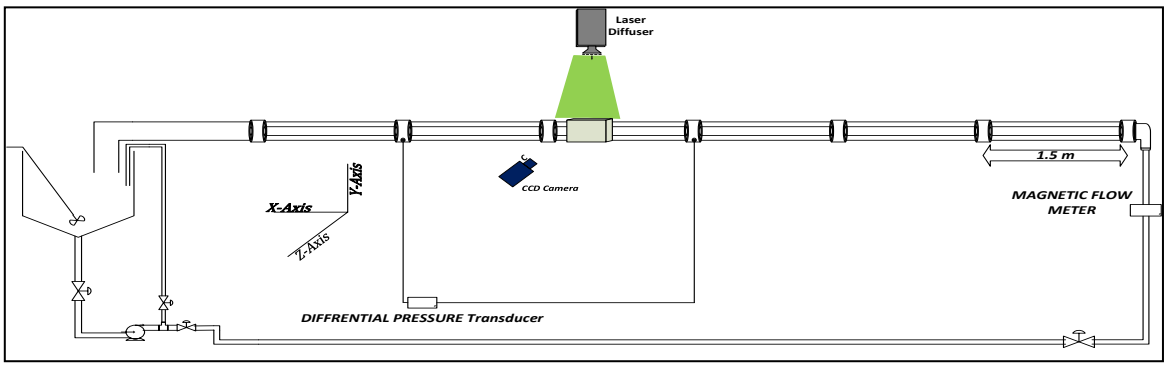

Figure 3-2 Schematic diagram of the experimental flow loop [9].

The total length of the horizontal flow loop was 9 m long. The test section was made from 95 mm ID borosilicate glass pipes. The pump flow rate was controlled by the variable frequency drive (VFD) system. The flow rate was measured by a magnetic flow meter (OMEGA FMG607-R) with accuracy of ±0.5% that was installed at the test section inlet. Frictional pressure drop across 3.08 m long pipe section was measured by using OMEGA DPG409 differential pressure transducer, with an accuracy of ±0.08%, which was installed. All the data were collected by using the data acquisition system powered by the LabView software.

Figure 3-3 illustrates the test section, where all the Particle Image Velocimetry (PIV) measurements were taken. In this section, the borosilicate glass pipe was kept inside a rectangular glass box, which was filled with glycerol. Since glycerol and the glass pipe have similar refractive index, with this arrangement it was possible to manage the laser light was incident directly on the fluid and reduce the light refraction due to the circular surface of the glass pipe and minimize the associated measurement errors.

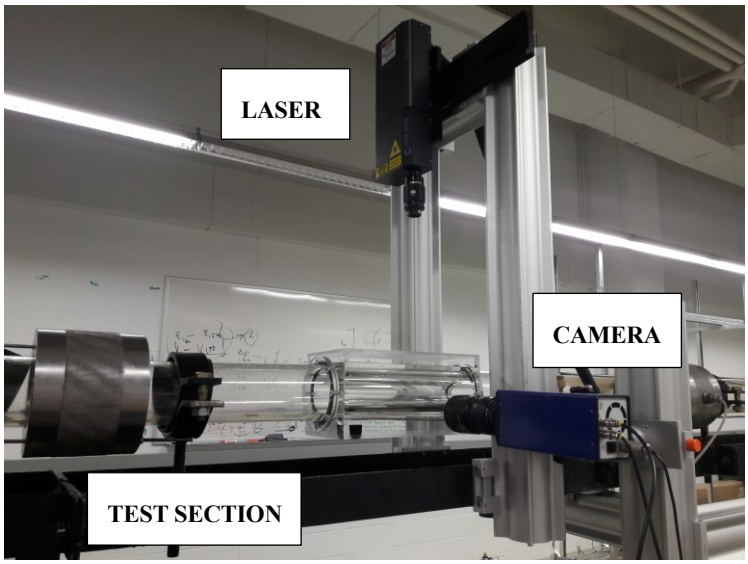

Figure 3-3 Image of the PIV setup and the test section

PIV measurements were performed using a New Wave Research Solo III Nd: YAG laser, a Lavision Imager Intense CCD camera, Nikon 50 mm AF Nikkor lens of 1.4 mm aperture and a commercial processing software, Davis 8.3. The wavelength of the green laser was 532 nm and the Imager Intense was a double framed camera with a 12-bit CCD sensor of having 1376 x 1040 pixels. Both the laser and the camera were synchronized and controlled through a computer using Davis 8.3 software.

In addition, a Samsung digital camera (8 MP, f/2.4, 31 mm, AF, 1080p @ 30fps) was used to record videos of flow loop experiments of the sand bed. These videos were recorded to determine the critical flow rates required for the onset of the sand particle movements.

3.3.3. Experimental Procedure

The experimental procedure consisted of three main stages. The first stage was establishment of the sand particle bed; the second stage was water circulation over the sand particle bed and the critical flow rate determination; and the third stage was PIV measurements at critical flow rate and at a particular subcritical flow rate. All the three stages are briefly explained below.

3.3.3.1. Sand Bed Establishment

Firstly, the suction tank was filled with 500 litres of water. Then, circulation was started at the highest possible flow rate through the loop and keeping water circulated, the required amount of sand depending on the sand particle size (amount of sand is important to get the same bed height for different sands) was added slowly to the tank. When the sand bed was uniform along the flow loop, circulation was stopped and valves on the both end of pipe section were closed. We have kept fluid in the flow loop under static condition over the night to make sure all sand particles in suspension to settle down and form a continuous bed.

3.3.3.2.Water Circulation, Calibration of Pressure Loss Measurements and Determination of Critical Flow Rate

After allowing all the sand particles to settle down and establishing the uniform bed, water was circulated through the flow loop by gradually increasing the flow rate from low to high values. When the movement of the sand particles were observed for the first time (i.e., onset of the bed erosion), then the respective flow rate was recorded as the critical flow rate for that particular sand size. Using the Lab view software, flow rates and the associated frictional pressure drop were recorded.

The accuracy of the frictional pressure loss measurements was confirmed by comparing experimental friction factor values estimated from water only (no sand bed) flow tests against the ones calculated from using conventional pipe flow correlation [10] given for water flow as shown in Figure 3-4. Friction factors based on the experimental pressure loss measurement were calculated by using the Fanning friction equation (Eq.3-1).

$$\Delta P = f\frac{\rho u^2}{d_e}\Delta L \quad \text{(3-1)}$$

Where ΔP is the frictional pressure drop, ΔL is the length of the pipe section over which the friction pressure loss was measured (3m), ρ is the fluid density, u is the bulk velocity, f is the friction factor and, d_e is the equivalent diameter.

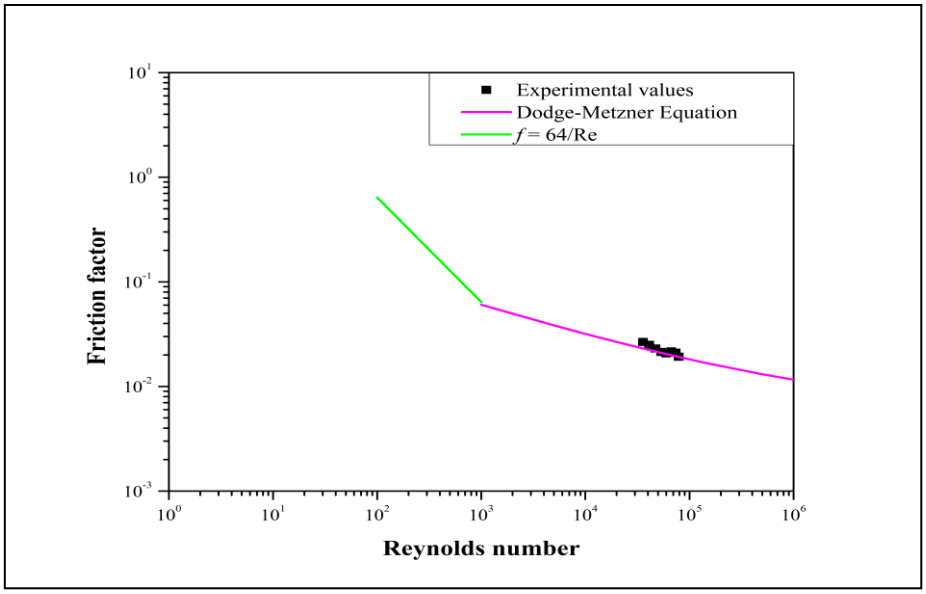

Figure 3-4 Comparison of experimental friction factor values estimated from water only flow tests against the ones calculated from Dodge and Metzner equation [10].

3.3.3.3. PIV Measurements

PIV is a non-intrusive optical measurement technique commonly used to measure and analyse instantaneous velocities of different fluid flow phenomena [11]. In this technique, tracer particles sensitive to the light are exposed to the laser beam and their movement – its velocity and direction - is recorded by a double frame high speed CCD camera and images taken are converted to flow fields via a computer analysis commonly done with a commercial software or with other simple FFT codes [11]. The main assumption in this technique is that those particles, in any condition, will follow the fluid flow, so their movement or behaviour can be assumed as the fluid movement [11].

The PIV setup consisted of a light source and a recording device. A double pulse laser was used as the light source and double frame camera was used as the recording device. The camera view plane must be orthogonal to the laser light as shown in Figure 3-3. The tracer particles were added to the suction tank while maintaining the water circulation for a while to obtain a homogenous tracer distribution in the system. Hollow glass spheres with

mean diameter of 10 microns were used as the tracer particles in the current study. These tracer particles were nearly neutral in water ($1.1 \pm 0.05 \frac{g}{cc}$) to keep them suspended in the flow. Since the flow was seeded with tracer particles, these tracer particles reflect the light when the laser light was thrown on them. This reflected light was then detected by the camera. Two successive images were captured by the camera. Figure 3-5a shows a typical PIV images acquired during the experiments. In this image, the cuttings bed is located at the bottom while the drilling fluid (water), seeded with tracer particles (bright white dots), is flowing over the top. These pictures were processed with appropriate algorithm to determine the instantaneous velocity field of the flow. PIV measurements at critical and subcritical flow rates were recorded using the Davis 8.3 software. At least 1000 pair of images were acquired for each flow experiment, and velocity values were averaged out to ensure higher accuracy in the measurements.

3.3.4. Data Processing and Analysis

Data processing and analysis consisted of two parts. The first and the straightforward one was determination of the critical flow rate. Flow at various flow rates were recorded by the handy cam and then depending on the sand bed and its particles movement, the critical flow rate was determined visually.

The second part was the PIV data processing and analysis. The initially added light sensitive tracer particles following the fluid flow were seen as the bright spots in each pair of captured PIV images and they were detected by the Davis 8.3 software.

By cross correlating these pair of images, the displacement of particles between the two images was determined [12]. Since the time interval between the images was known, the instantaneous velocities were calculated for all detected points by using the particle displacement (Δx and Δy) and time interval (Δt) as follows:

$$\begin{cases} \hat{u} = \frac{\Delta x}{\Delta t} \\ \hat{v} = \frac{\Delta y}{\Delta t} \end{cases} \qquad \text{..... (3-2)}$$

In order to find out the displacement of detected bright spots in x and y direction, Davis 8.3 software applied an FFT based cross correlation method [12]. First, both the images were segmented into small interrogation windows and those windows in two images were compared to recognize the cross correlation [12]. The exact displacement was determined by identification of the highest peak of correlation. A multi-pass approach starting from window size of 64 x 64 down to 24 x 24 including 32 x 32 size in between was used in PIV image processing with overlap of 50%. The obtained data with those settings was exported to excel files for further data analysis. Figure 3-5b shows the final velocity vector field for the flow over the cuttings bed.

Four main features, Reynolds stresses, axial turbulence intensities, radial turbulence intensities and the near wall dimensionless velocities were further analysed and compared for all cases to detect the difference in the turbulent characteristics of the fluid flow over the sand bed. The software, Davis 8.3, calculates all these features based on the governing equations for those using the velocities and velocity fluctuations measured in x and y directions for each pair of images taken.

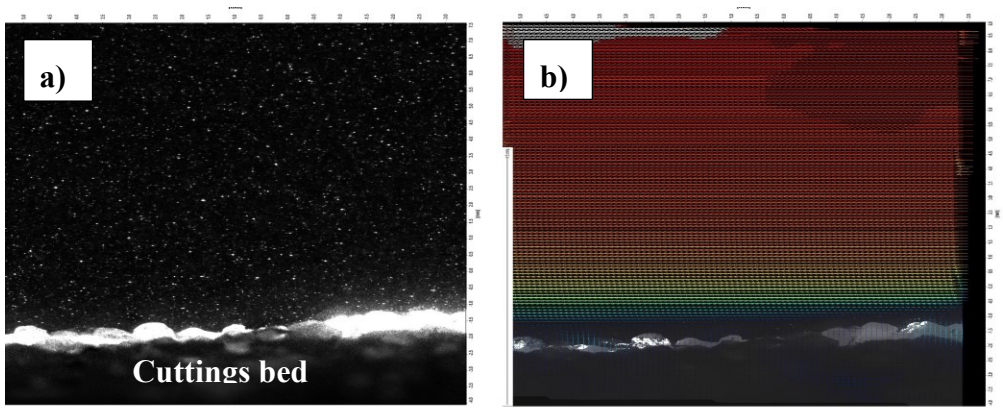

Figure 3-5 a) Typical PIV image acquired during the tests, b) resultant velocity field.

3.4. RESULTS AND DISCUSSIONS – TURBULENT FLOW OF WATER OVER THE UNTREATED SAND

3.4.1. Frictional Pressure Loss Measurements for the Flow of Water over the Untreated Sand Beds of Three Different Particle Size Range at Subcritical Velocity of 0.25 m/s.

Table 3-2 summarizes the results of frictional pressure loss measurements for the flow of water over the sand beds of 3 different particle size ranges (i.e. 20/40, 30/50, 40/70 mesh sizes) at the sub-critical velocity of 0.25 m/s. We tried to keep the initial sand bed height constant in all three experiments. This was not a trivial task, nevertheless we were able to keep the bed height variation within 3-10% range. The slight variation in bed height would possibly influence the frictional pressure losses. In order to minimize the effect of the bed height variation on the frictional pressure losses, we have adjusted the flow rate considering the area above the bed open for flow such that the bulk fluid velocity would be 0.25 m/s in each test. Note that the Reynolds number was around 24,000 for these tests, indicating that flow was most likely under fully turbulent regime. The frictional pressure loss for turbulent flow of water over the sand bed deposited in a horizontal pipe was measured over the 3m long section.

Although care was taken as much as possible to establish the same bed height for all the experiments, there were still some minor differences in the bed heights, which might have slight impact on the measured frictional pressure losses. In order to take the effect of initial bed height variation (i.e. variation of the area open for flow initially), we have determined normalized frictional pressure loss values by multiplying the measured frictional loss values with the corresponding equivalent diameter. The equivalent diameter was estimated by assuming the area open for flow above the cuttings bed as a circle. The measured frictional pressure loss, equivalent diameter and the normalized frictional pressure loss data are all listed in the Table 3-2.

The results shown in Table 3-2 indicate that frictional pressure loss varies depending on the particle size range. The frictional pressure loss for the flow of water over the 30/50 sand bed was higher than that of the case

for 40/70 sand bed, indicating that frictional pressure loss decreases with the decreasing sand size. However, the trend was the opposite, when we used 20/40 mesh size (largest size sand particles within the group tested). The measured frictional pressure loss for the flow over the bed with 20/40 mesh size sands was lower than that of the flow over the beds with 30/50 and 40/70 mesh size sands. Comparison of the frictional pressure losses at various other velocities (Fig.6) also indicates that pressure loss for the flow of water over the 30/50 mesh size sand bed is distinctly higher than that of the cases with 20/40 and 40/70 mesh size sand bed. Frictional pressure loss due to the flow of water over the 20/40 and 40/70 mesh size sand beds do not show significant difference from each other.

Table 3-2 Frictional Pressure Drop vs Untreated Sand Particle Size Range Measured at 0.25 m/s.

Sand Particle Mesh Size	Bed Height (cm)	Flow Rate (lpm)	Frictional Pressure Loss (Pa)	Equivalent Diameter (m)	Normalized Frictional Pressure loss (Pa-m)
20/40	3.4	70.7	50.0	0.0775	3.88
30/50	3.1	75.5	64.5	0.0802	5.17
40/70	3.5	70.0	54.2	0.0771	4.18

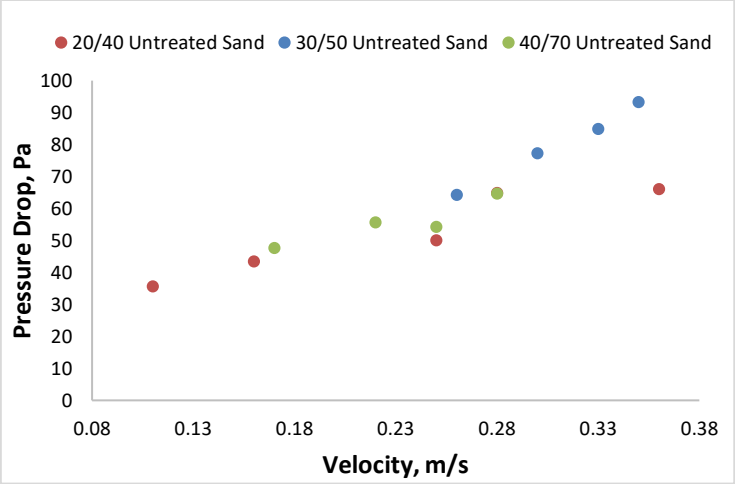

Figure 3-6 Frictional pressure drop data for different mesh size of untreated sand particles.

The relatively high Reynolds number (≈ 24,000) indicates that flow was in turbulent regime in all tests. As we tried to eliminate the effects of the most other parameters, which affect the frictional pressure loss (Eq.3-1), the difference in normalized friction pressure losses, therefore, is most likely due to the differences in friction factors. Relatively high Reynolds numbers suggest that friction factors may be the function of the bed roughness. However, how the bed roughness is related to the particle size (and perhaps to the irregular shape of the sand particles) needs further explanation. In particular, why the largest particle size (20/40) results into the lowest frictional pressure losses (creating almost like a drag reduction effect) or the intermediate sand size (30/50 mesh size) results the highest frictional pressure loss poses a very interesting question.

The PIV data, which we presented later on (Figure 3-7) indicated that the flow regime was hydrodynamically smooth in all three cases. Therefore, contribution from roughness effect is expected to be minimal. The conventional approach, which commonly assumes that the equivalent sand grain roughness height to be equal to the mean or a constant multiple of particle size [13,14] is not sufficient to explain the data presented here. Other factors might contribute to variation of pressure losses are the irregular shape of the sand particles as well as the particle size distribution within the group. We did not have any control on neither of these factors. Nevertheless, the "drag reducing" behaviour of the 20/40 range of sands was notable in our experiments.

3.4.2. Results of PIV Measurements at the Subcritical Flow Velocity of 0.25 m/s

For all the three sand beds tested in this case (i.e., 20/40, 30/50, 40/70), the data acquisition for the PIV measurements was started at their respective subcritical and critical flow rates. It was essential to confirm that the particles were not suspended in the main flow at the subcritical flow rate. For all the figures of PIV measurements, the origin was set at the sand bed-water interface. The y-coordinate in the figures represents the distance from the bed in vertical direction (i.e. perpendicular to the flow direction) and y=0 represents the sand bed-water interface.

Figure 3-7 presents the near wall velocity profiles for the flow of water over the sand beds of three different particle size ranges (i.e. 20/40, 30/50, 40/70 mesh sizes) at the sub-critical velocity of 0.25 m/s. The near wall velocity profiles were presented in terms of dimensionless distance (y^+) and dimensionless velocity units (u^+) as defined by equations 3-3 and 3-4, respectively.

$$y^+ = \frac{\rho y u_\tau}{\mu} \quad \text{(3-3)}$$

$$u^+ = \frac{u}{u_\tau} \quad \text{(3-4)}$$

$$u_\tau = \sqrt{\frac{\tau_b}{\rho}} \quad \text{(3-5)}$$

Where u_τ is the friction (shear) velocity, τ_b is the interfacial bed shear stress (i.e. shear stress at the fluid/sand bed interface), and ρ is the fluid density. The interfacial bed shear stress, τ_b, cannot be deduced accurately from frictional pressure loss data because more than one surface is involved in the flow (i.e. pipe wall and the bed surface). Therefore, the friction velocity, u_τ, cannot be directly estimated by using the bed shear stress. In this study, we have determined the friction velocity, u_τ, by using the plot of velocity versus vertical distance from the surface of the sand bed. These data were obtained directly from PIV measurements. The detailed procedure for determining the friction velocity from the PIV measured velocity data is given elsewhere [9].

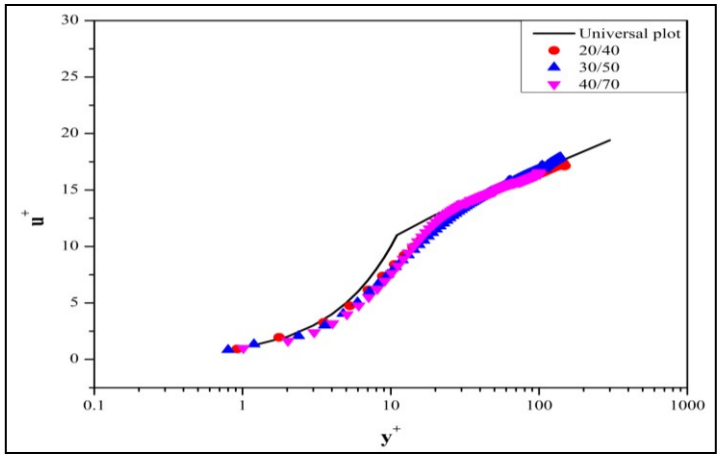

Figure 3-7 Comparison of the near wall velocity profiles for the flow of water over the sand beds of three different particle size range at sub-critical velocity of 0.25 m/s.

The universal law of the wall states that the near wall velocity profiles generally consists of three regions depending upon the dimensionless distance from the bed: Viscous sub-layer y^+ <5, the buffer region 5< y^+<30 and the log-law region y^+> 30. The universal plot of a velocity profile for a hydrodynamically smooth flow condition is defined by Equation 3-6. [15].

$$u^+ = \begin{cases} y^+ & y^+ < 10 \\ 2.44ln(y^+) + 5.5 & y^+ > 30 \end{cases} \quad \text{..... (3-6)}$$

As seen in Figure 3-7, the velocity profiles for the flow of water over the sand beds of 3 different particle size ranges (i.e. 20/40, 30/50, 40/70 mesh sizes) at the sub-critical velocity of 0.25 m/s all follow the universal law within the log-law region (y^+> 30), confirming that the flow in all these cases are hydrodynamically smooth. However, slight downshifts are observed in the viscous sub-layer region. The highest downshift is observed for 40/70 followed by 30/50 then 20/40.

Figure 8 presents comparison of the normalized Reynolds shear stress profiles for the flow of water over the sand beds of three different particle size ranges at the sub-critical velocity of 0.25 m/s. The Reynolds shear stress (or turbulent stress) arises due to velocity fluctuations (u' and v') in the flow and is defined according to Equation 3-7:

$$\tau_R = -\rho\overline{u'v'} \quad \text{..... (3-7)}$$

As shown in Figure 3-8, increasing Reynolds stress was observed when the particle mesh size changed from 40/70 to 30/50, indicating that higher turbulence was registered near the wall with the increasing particle size. However, this trend was reversed for the flow over the bed composed of particles with 20/40 size range. With the 20/40 mesh size, which covers the largest particle size range within the group tested, we registered the lowest turbulence activity levels, again indicating like drag reduction type of behaviour

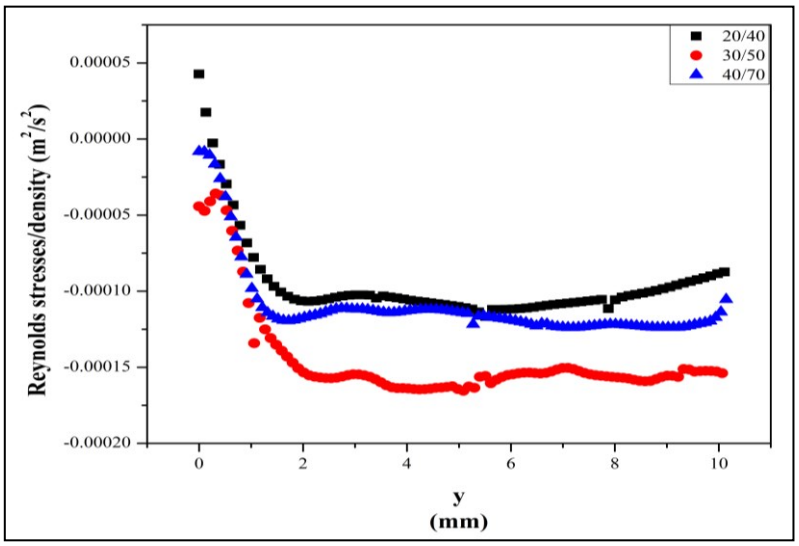

Figure 3-8 Normalized Reynolds stress profiles for the flow of water over the sand beds of three different particle size range at sub-critical velocity of 0.25 m/s.

Figure 3-9 shows the comparison of the axial turbulence intensity (also called the normal Reynolds stress) observed during the flow of water over the untreated sand beds of three different particle size ranges at sub-critical velocity of 0.25 m/s. The definition of the axial turbulence intensity is given by the Equation. 3-8:

$$u_{rms} = \sqrt{\overline{u'u'}} \quad \text{..... (3-8)}$$

The axial turbulence intensity is critical in sand particle removal because it represents the level of velocity fluctuations. Recent studies have indicated the significance of turbulent velocity fluctuations in particle removal [16, 17]. Results shown in Figure 3-9 indicate that higher axial turbulence intensity was registered when the particle mesh size changed from 40/70 to 30/50, indicating that higher axial turbulence intensity was observed with the larger particle size range. However, when we use particle mesh size of 20/40 (largest particle size range within the group), the trend was reversed, and the axial turbulence intensity level dropped. This observation is also in line with the previous observations regarding the reduced frictional pressure drop and Reynolds stress with 20/40 mesh size particles.

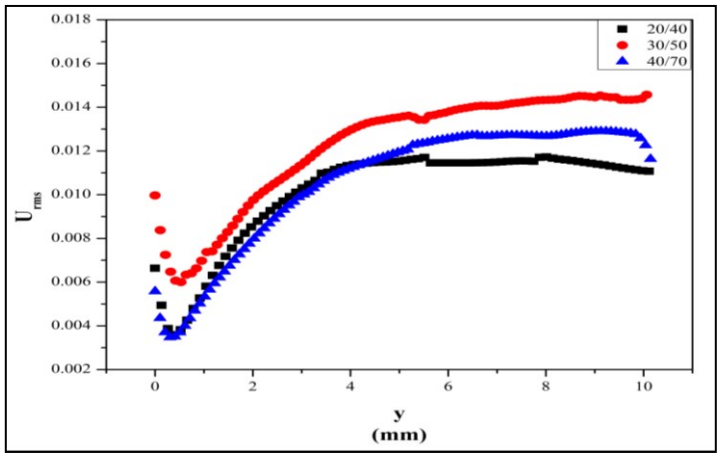

Figure 3-9 Axial turbulence intensity profiles for the flow of water over the sand beds of three different particle size range at sub-critical velocity of 0.25 m/s.

The radial component of turbulence intensity, v_{rms}, is of particular importance in solid transport and solid suspension. Kelessidis and Bandelis [18] based on the work of Davies [19] discussed the eddy fluctuation force, which is essential in keeping particles in suspension in turbulent flow. Davies [19] has shown that the eddy fluctuation force is proportional to radial velocity fluctuations. A higher level of radial velocity fluctuation results in a higher eddy fluctuation force. The definition of the radial turbulence intensity is given by the Equation 9:

$$v_{rms} = \sqrt{\overline{v'v'}} \qquad \text{..... (3-9)}$$

As shown in Figure 3-10, increasing radial turbulence intensity was observed with the changing particle mesh size from 40/70 to 30/50, indicating that higher turbulence was registered near the wall with the increasing particle size. This trend was reversed for the flow over the bed composed of particles with 20/40 mesh size. With the 20/40 mesh size particles, (the largest particle size range within the group tested), we registered the lowest radial turbulence intensity levels, again indicating like drag reduction type of behaviour.

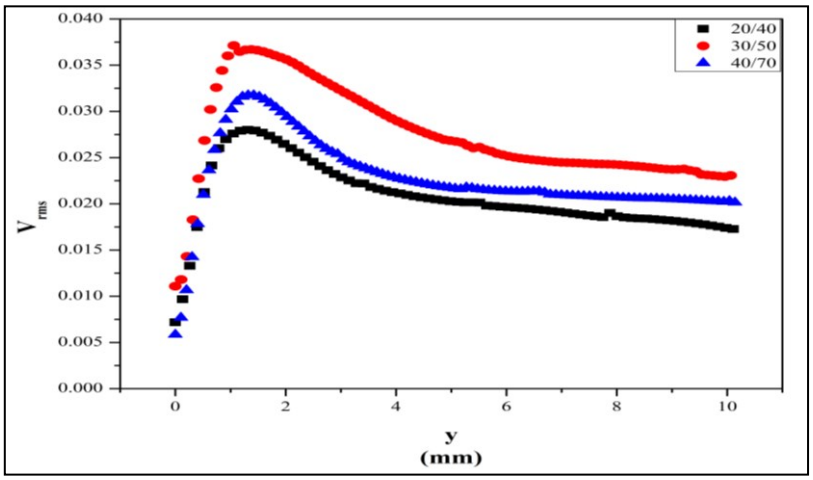

Figure 3-10 Radial turbulence intensity profiles for the flow of water over the sand beds of three different particle size range at sub-critical velocity of 0.25 m/s.

The friction velocity, u_τ, is directly related to the interfacial bed shear stress (Equation 3-5), therefore, it is an indirect measure of how the total frictional pressure loss in the system changes. The friction velocity values obtained from the PIV measured velocity data are shown in Figure 3-11.

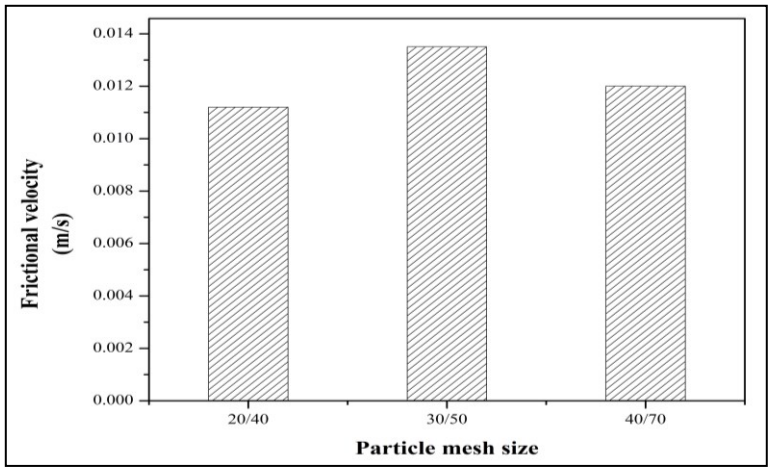

Figure 3-11 Friction velocity vs particle mesh size for experiments conducted at sub-critical velocity of 0.25 m/s.

Results of friction velocity measurements for the 3 subcritical flow experiments as shown in Figure 3-11 indicate that as the particle size range changes from 40/70 to 30/50 (i.e. with increasing particle size range) the friction velocity values also increase. With the change of particle mesh size from 30/50 to 20/40 (i.e. further increase in the particle size), however, the friction velocity decreased. The lowest friction velocity values were registered for the largest particle size range within the group of tested sands (i.e. 20/40). The unusual behaviour of 20/40 size range of particles is similar to the trend that was observed for the frictional pressure loss measurements. The friction velocity is directly related to the interfacial bed shear stress and thus the similarity of both results (i.e. lowest frictional pressure loss and friction velocity values were registered for 20/40 sands) are understandable. The friction velocity values were estimated by using the near wall velocity data obtained directly from PIV measurements, therefore, the results presented in Fig.3-11 provide confirmation of the trend that we

observed earlier on how the frictional pressure losses change as a function of the particle size range (presented in Table 3-2).

3.4.3. Critical Flow Rate Required for the Onset of Particle Removal

Table 3-3 provides summary of the flow rates (and velocities) and frictional pressure losses measured at the onset of the particle removal from the sand beds as a function of particle size range. We tried to keep the initial sand bed height constant in all three experiments. This was not a trivial task, nevertheless we were able to keep the bed height variation within 3-10% range. The slight variation in bed height would possibly influence the frictional pressure losses. However, as we have discussed in the section 3.1, the effect of slight change in bed height variation on the frictional pressure loss was minimal and for all practical purpose, we could say that change in critical velocity was mainly due to the change in particle size range for the experimental results reported here.

Data presented in Table 3-3 indicate that the critical velocity for the initiation of the bed erosion decreases with the increasing particle mesh size (i.e., decreasing particle size). The critical velocities were calculated by dividing the critical flow rates with their respective area available for the water flow and plotted against their particle mesh sizes.

Table 3-3 Summary of the test results at the onset of the untreated sand bed erosion

Sand particle mesh size	Bed height (cm)	Critical flow rate (lpm)	Critical velocity (m/s)	Critical pressure drop (Pa)
20/40	3.4	101	0.36	66
30/50	3.1	91.3	0.30	77.29
40/70	3.5	79.6	0.28	64.6
100	3.4	57.8	0.21	29.5

As also shown in Figure 3-12, the critical velocity decreases significantly with the increase in the particle mesh size. In other words, smaller particles are mobilized at lower values of fluid velocity, which is normally expected as the particle size decreases, the gravity and the frictional forces associated with it also decreases, therefore, it becomes easy to mobilize the particle. The similar observations were also reported by Ramadan et al. [13], though their test matrix was not as extensive as the one reported here.

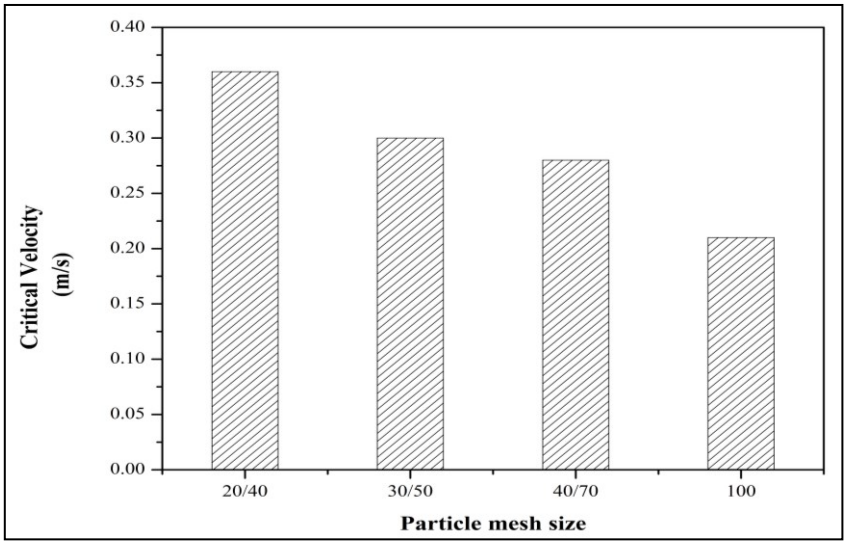

Figure 3-12 Critical velocity required for the onset of the untreated sand bed erosion versus the particle mesh size.

We have also recorded the critical pressure drop at the onset of bed erosion and plotted against the particles mesh size as shown in Figure 3-13. Except for the particle mesh size of 20/40, the critical pressure drop values decreased pronouncedly with the increasing particle mesh sizes (i.e. decreasing particle sizes). The critical pressure drop for particles of 20/40 mesh size was lower than that of the ones for 30/50 and 40/70 mesh size. Similar to what we have observed with untreated sands, largest (20/40 mesh) particle size in the treated sand group also shows some “drag reduction” effect.

The friction velocity values derived from the near wall velocity data obtained from PIV measurements are shown in Figure 3-14. Results of friction velocity measurements for the 4 critical flow rate experiments indicate that as the particle size range changes from 30/50 to 40/70 and to 100 mesh (i.e., with decreasing particle size range) the friction velocity values decrease, following the same trend observed in pressure loss measurements. The friction velocity value registered for the largest particle size range (20/40), however, was lower than the ones registered for 30/50 and 40/70 mesh sizes. The unusual behaviour of 20/40 size range of particles is similar to the trend that was observed for frictional pressure loss measurements. The friction velocity is directly related to the interfacial bed shear stress and thus this similarity of both results is reasonable.

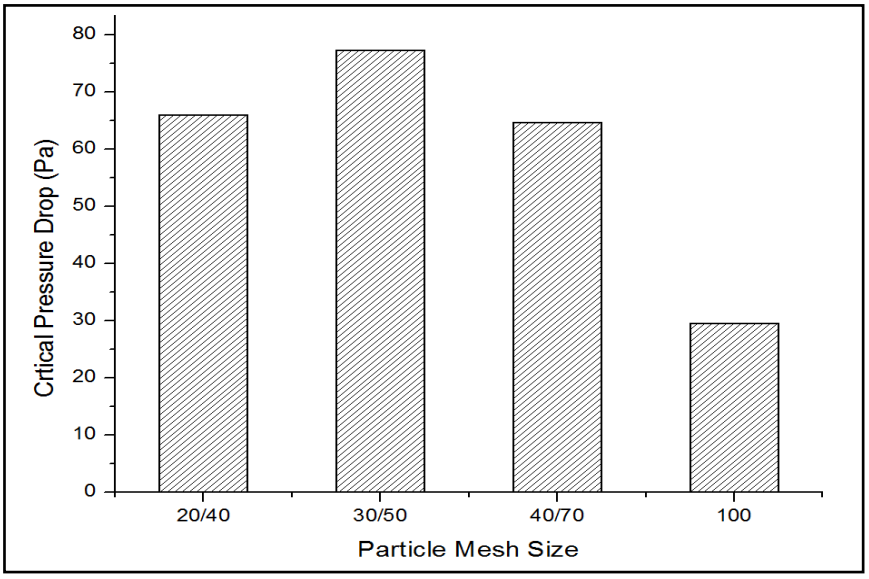

Figure 3-13 Critical pressure drop versus the particle mesh size measured at the onset of the untreated sand bed erosion

As the friction velocity values were estimated by using the near wall velocity data obtained directly from PIV measurements, the results presented in Figure 3-14 provide confirmation of the trend that we observed on how the frictional pressure loss changes as a function of the particle size range (presented in Table 3-3 and Figure 3-13).

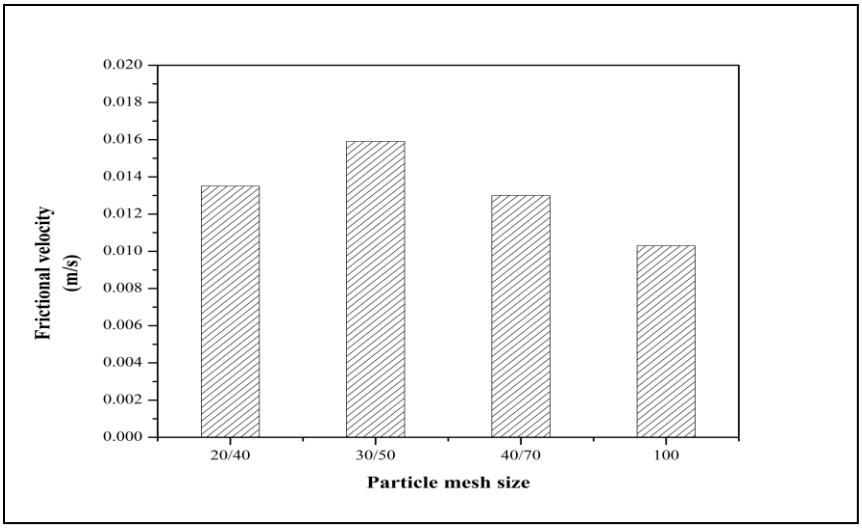

Figure 3-14 Friction velocity vs particle mesh size for experiments conducted at the critical velocity.

The results presented in this section are also in line with our earlier observations that water flow over the 20/40 mesh size sand bed resulted lower pressure drop than that of the beds with smaller particle size ranges (30/50 and 40/70 mesh size) at the same sub-critical flow rate. The difference in the latter case is even more dramatic as the lower pressure drop was registered with the 20/40 mesh size bed, even with the condition that the fluid velocity (i.e. critical velocity) was higher than all the other critical fluid velocities registered for the onset of the particle removal from sand beds with smaller particle size ranges.

3.5. RESULTS AND DISCUSSIONS – TURBULENT FLOW OF WATER OVER THE SURFACE TREATED SAND BED

3.5.1. Frictional Pressure Loss Measurements for the Flow of Water over the Treated Sand Beds of 4 Different Particle Size Range at Various Subcritical Flow Rates.

Table 3-4 summarizes the results of frictional pressure loss measurements and the normalized frictional pressure loss data for the flow of water over the sand beds of 3 different particle size ranges (i.e. 20/40, 30/50, 40/70 mesh sizes) at the sub-critical velocity of 0.16 m/s. Keeping the bed heights constant in all three experiments

was not an easy task especially due to increased mobility of treated sand particles, however difference in the bed height of each test is less than 5 %. To minimize the effect of the bed height variation on the frictional pressure losses, the flow rate is adjusted by considering the area above the bed open for flow such that the superficial velocity would be 0.16 m/s in each test. Note that the Reynolds number was around 1600 for these tests, indicating that flow regime was turbulent.

The results shown in Table 3-4 indicates that frictional pressure drops measured at the same fluid velocity (0.16 m/s) are almost the same for different mesh sizes of treated sand particles. We have also measured frictional pressure drops at different fluid velocities for the treated sand particles and the result are summarized in Figure 3-15. As shown in Figure 3-15, the frictional pressure drop vs velocity trend is similar for different particle mesh sizes within the flow rate ranges tested. The surface treatment of the sands might have caused dampening the effect of particle size on the pressure drop.

Table 3-4 Frictional Pressure Drop vs Treated Sand Particle Size Range Measured at 0.16 m/s.

Sand Particle Mesh Size	Bed Height (cm)	Flow Rate (lpm)	Frictional Pressure Loss (Pa)	Equivalent Diameter (m)	Normalized Frictional Pressure loss (Pa-m)
20/40	3.31	91.8	32	0.0789	2.525
30/50	3.45	66	35	0.0778	2.723
40/70	3.45	49	35	0.0778	2.723

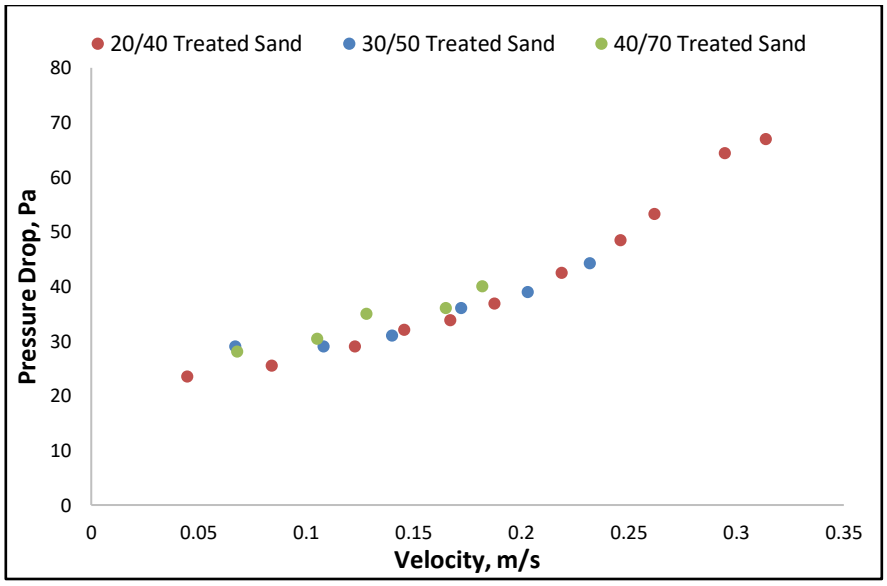

Figure 3-15 Frictional pressure drop measured for the flow of water over the treated sand beds at subcritical velocities.

3.5.2. Results of PIV Measurements at the Subcritical Flow Velocity of 0.16 m/s

100 mesh size of treated sand particles gathered on top of the horizontal pipe blocked the laser light during the flow experiments and this prevented measuring PIV for those treated sand particles. Therefore, PIV data were recorded only for 20/40, 30/50 and 40/70 treated sand particles. The subcritical velocity of 0.16 m/s was used as the common velocity to compare the PIV data recorded for 20/40, 30/50 and 40/70 treated sand particles. In all the figures of showing PIV measured data, the origin was set at the sand bed-water interface. The y-coordinate in these figures represent the distance from the bed in vertical direction (i.e. perpendicular to the flow direction) and y=0 represents the sand bed-water interface.

Figure 3-16 shows the near wall velocity profiles for the treated sand particles at the subcritical velocity of 0.16 m/s. Near wall velocity profiles follow the universal log law for the turbulent flow of water over the treated sand bed of 20/40, 30/50 and 40/70 mesh size.

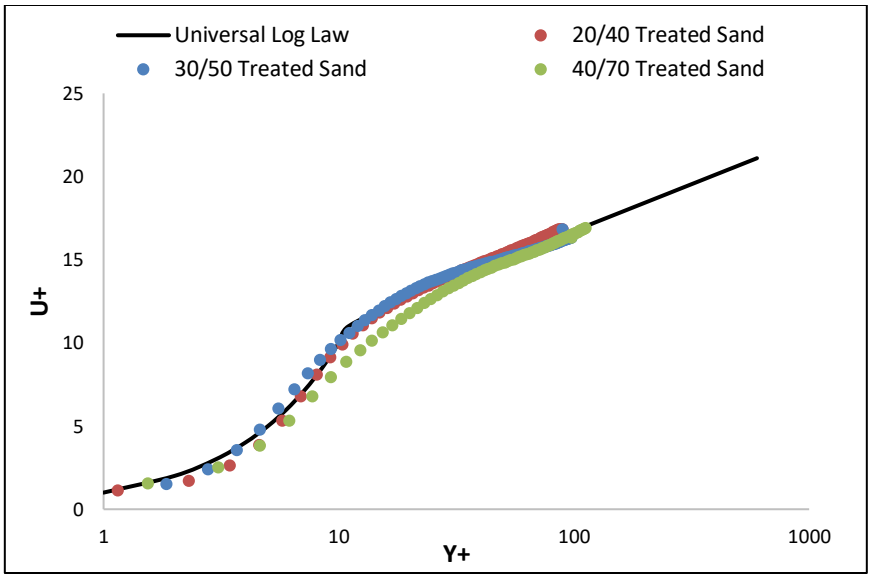

Figure 3-16 Dimensionless velocity profiles for 20/40, 30/50 and 40/70 mesh size of treated sand particles at the superficial velocity of 0.16 m/s.

Figure 3-17 shows the Reynolds stress profiles for the turbulent flow of water over the treated sand bed of 20/40, 30/50 and 40/70 mesh size. The Reynold stress accounts for the turbulent fluctuations in the fluid momentum. It can be also interpreted as the transport of fluid momentum to solids in the bed surface. Reynolds stress profiles did not show much difference near the wall, which was also in line with the fact that measured frictional pressure drops did not change significantly for the flow over these sands. Away from the fluid/bed interface, however, (similar to untreated sand case) the Reynolds stress profile for the flow over the sand bed of 30/50 mesh size was slightly higher than the other two treated sand sizes.

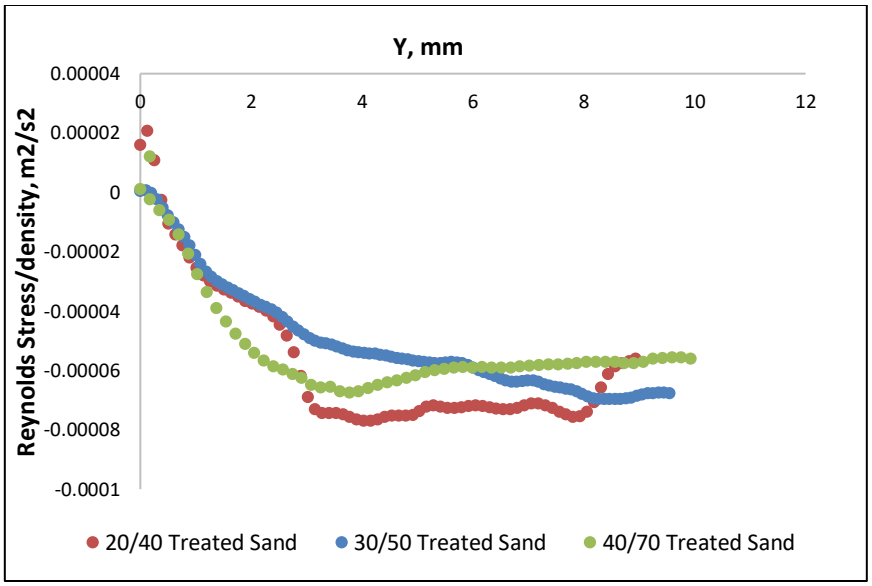

Figure 3-17 Reynolds stress profiles for the turbulent flow of water over the treated sand beds of 20/40, 30/50 and 40/70 mesh size at the mean fluid velocity of 0.16 m/s.

Figure 3-18 shows the axial turbulence intensity profiles for the turbulent flow of water over the treated sand beds of 20/40, 30/50 and 40/70 mesh size at the mean superficial fluid velocity of 0.16 m/s. The axial turbulence stress profiles did not show much difference near the wall. Away from the bed/fluid interface, however, the axial turbulence intensity profile for the flow over the 30/50 mesh size sand bed was slightly higher than that of 20/40 and 40/70 mesh size sand beds.

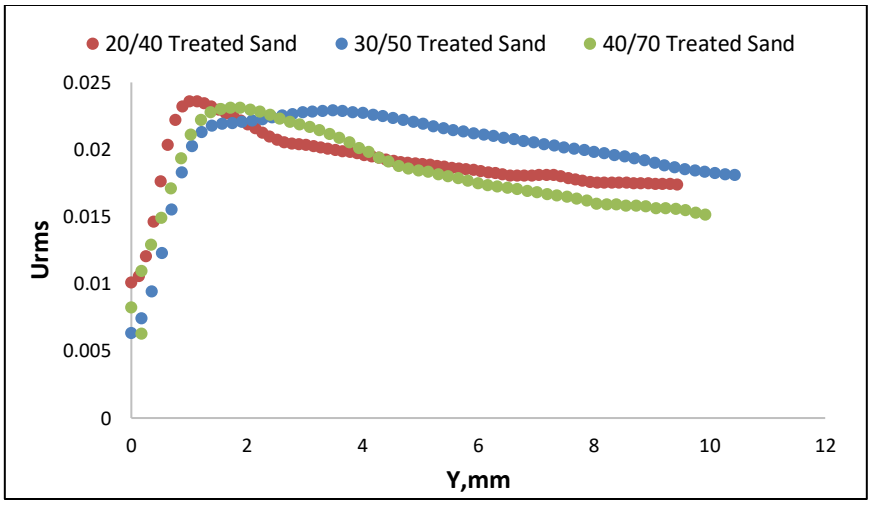

Figure 3-18 Axial turbulence intensity profiles for the turbulent flow of water over 20/40, 30/50 and 40/70 mesh size treated sand beds at the superficial velocity of 0.16 m/s.

Figure 3-19 shows the radial turbulence intensity profiles for the turbulent flow of water over the treated sand beds of 20/40, 30/50 and 40/70 mesh size at the mean superficial fluid velocity of 0.16 m/s. The radial turbulence stress profile for the flow over the 20/40 mesh size sand bed was the highest of the three cases near the wall, while the radial turbulence stress profile over the 30/50 mesh size sand bed was the lowest among the three. Away from the bed/fluid interface, however, the radial turbulence intensity profile for the flow over the 30/50 mesh size sand bed was slightly higher than that of 20/40 and 40/70 mesh size sand beds.

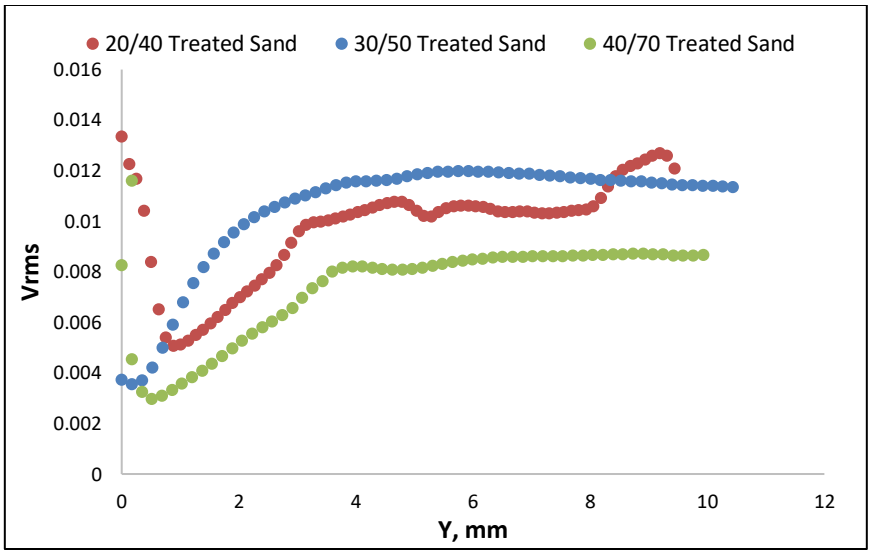

Figure 3-19 Radial turbulence intensity profiles for 20/40, 30/50 and 40/70 mesh size of treated sand particles at the superficial velocity of 0.16 m/s.

The friction velocity, u_τ, is directly related to the interfacial bed shear stress (Equation 3-5), therefore, it is an indirect measure of how the total frictional pressure loss in the system changes. The friction velocity values obtained from the PIV measurements at the subcritical velocity of 0.16 m/s are shown in Figure 3-20. The friction velocity values were similar for the flow over the all three treated sand beds. These results are well aligned with pressure drop measurements shown earlier (Table 3-4), which did not show much difference either for all three treated sand beds.

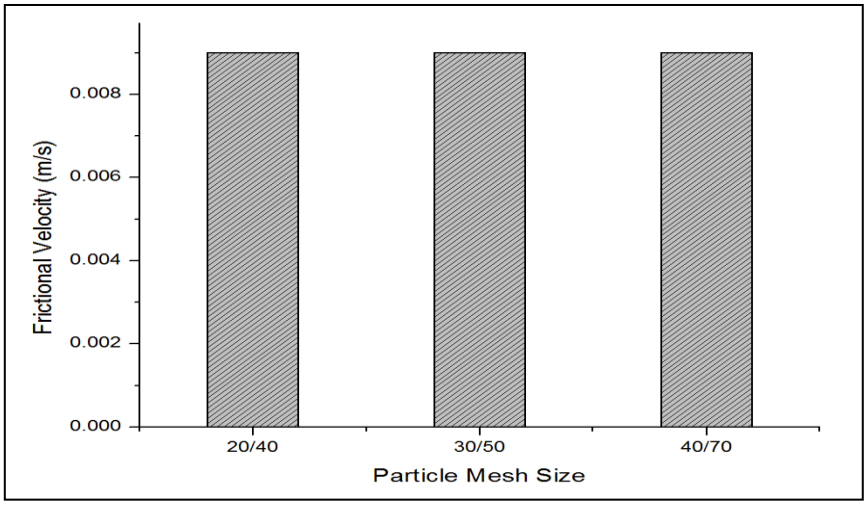

Figure 3-20 Frictional velocities for 20/40, 30/50 and 40/70 mesh size of treated sand particles at the superficial velocity of 0.16 m/s.

3.5.3. Critical Flow Rate Required for the Onset of Particle Removal from Treated Sand Bed Deposits

Critical velocities measured at the onset of particle removal from the treated sand beds in water flow are summarized in Table 3-5.

Table 3-5 Summary of the results of treated sand bed erosion experiments

Sand Particles Size	Bed Height (cm)	Flow Area (without bed) (cm^2)	Critical Flow Rate (lpm)	Critical Velocity (m/s)	Critical Pressure Drop (Pa)
20/40 Treated	3.31	48.91	91.8	0.31	66
30/50 Treated	3.45	47.59	66	0.23	44.3
40/70 Treated	3.45	47.59	49	0.17	36
100 Treated	3.31	48.91	41.8	0.14	23

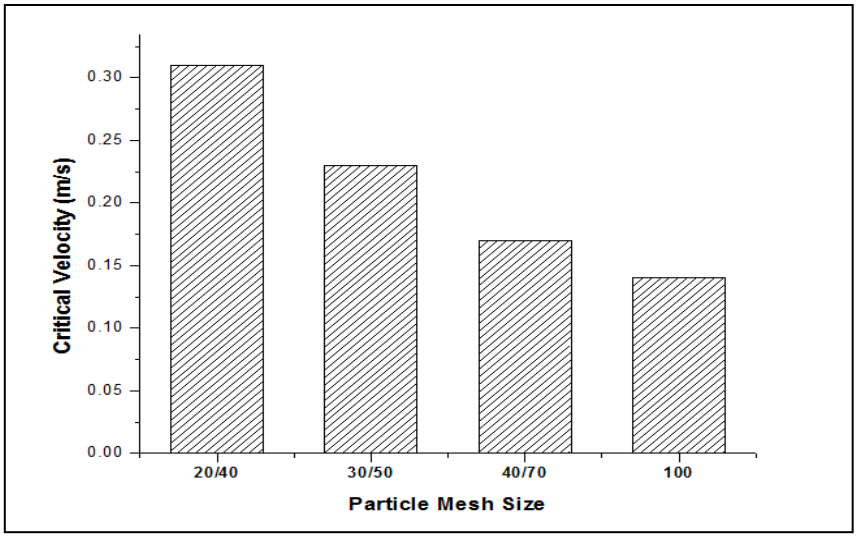

Figure 3-21 Critical velocities for treated sand particles.

Figure 3-21 shows the trend of critical velocities of sand particles with different sand particle mesh sizes. The critical velocity required for particle removal from the treated sand bedwith water also decreases as the sand-size decreases.

We have also recorded the critical pressure drop at the onset of the bed erosion and plotted against the particles mesh size as shown in Figure 3-22. The critical pressure drop values decreased pronouncedly with the increasing particle mesh sizes (i.e. decreasing particle size). The frictional velocity data presented in Figure 3-23 also show similar trend as the frictional pressure drop, confirming that the frictional pressure drop decreases with the decreasing particle size. As discussed earlier, we could not obtain PIV data (and hence could not calculate the frictional velocity) when conducting experiments with 100 mesh size sand bed because the laser light was blocked by the foamy froth collected at the high side of the pipe.

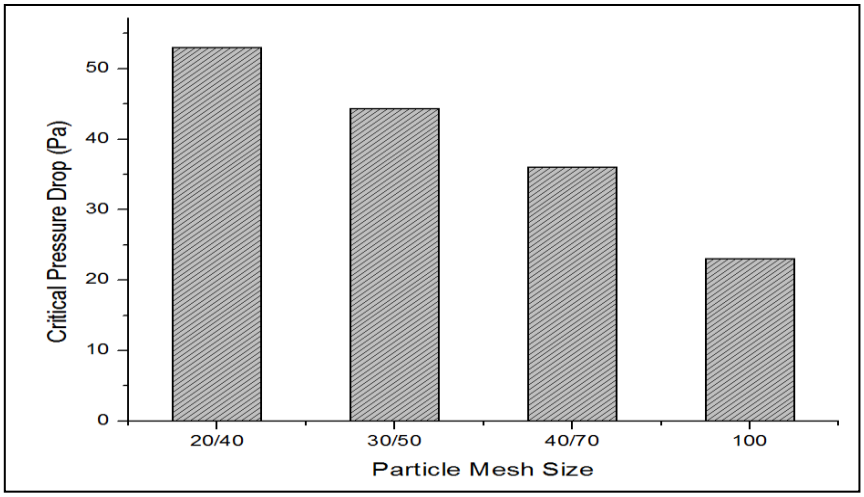

Figure 3-22 Critical pressure drop measured at the onset of the treated sand bed erosion with water.

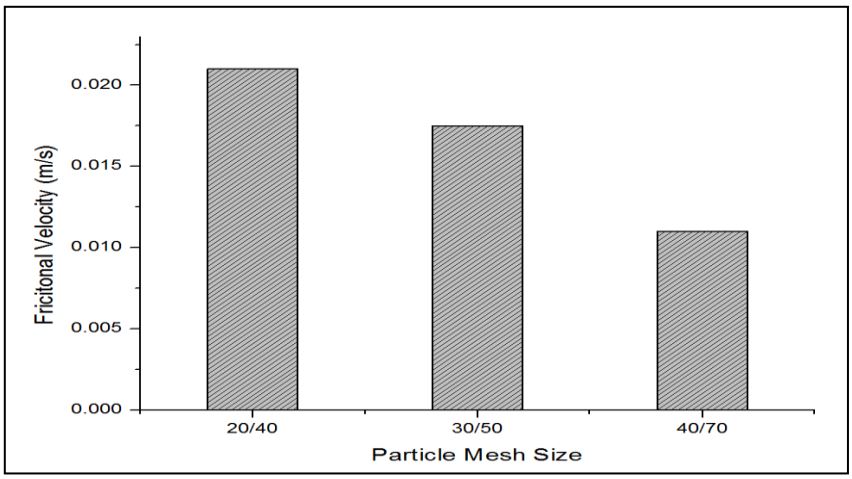

Figure 3-23 Frictional velocities obtained from PIV data measured at the onset of the treated sand bed erosion with water.

3.6. COMPARISON OF THE RESULTS OF TREATED VS. UNTREATED SAND BED EROSION TESTS

3.6.1. Comparison of Frictional Pressure Drop - Treated versus Untreated Sand Bed Erosion Tests

Frictional pressure drops for the flow of water over the treated and untreated sand beds were measured at several subcritical and critical flow rates. Comparisons of the frictional pressure drop measurements for treated and untreated sands were presented in Figures 3-24, 3-25, 3-26 and 3-27 for sand beds with particle mesh sizes of 20/40, 30/50, 40/70 and 100 respectively.

Turbulent flow of water over the treated sand bed registered slightly lower pressure drop values than that of over the untreated sand bed for all particle size ranges [20/40 mesh size (Fig.3-24), 30/50 mesh size (Fig.3-25), 40/70 mesh size (Fig.3-26) and 100 mesh size (Fig. 3-27)].

During these experiments, it was not easy to set the initial bed height same for all the tests, especially for the beds with treated sand particles where the sand particles were highly mobile due to the special surface treatment applied to them. We managed to keep the difference in bed heights less than 3% between all particle sizes of treated and untreated sand except for the 30/50 mesh size. For 30/50 mesh size of untreated sand particles, the bed height was 10 % higher than the same mesh size of the treated sand particles. However, this did not influence the general trend of the frictional pressure drop. Even though we considered these small variations in bed heights, the pressure drop trend for the flow of water over the untreated sand bed was still slightly higher than that of the treated sand bed.

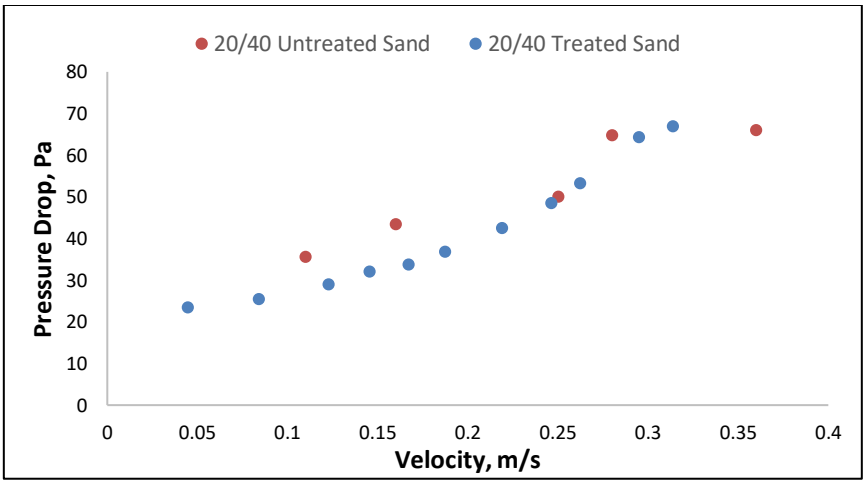

Figure 3-24 Comparison of the frictional pressure drop data measured at various velocities of water Flow over the 20/40 mesh size treated and untreated sand bed.

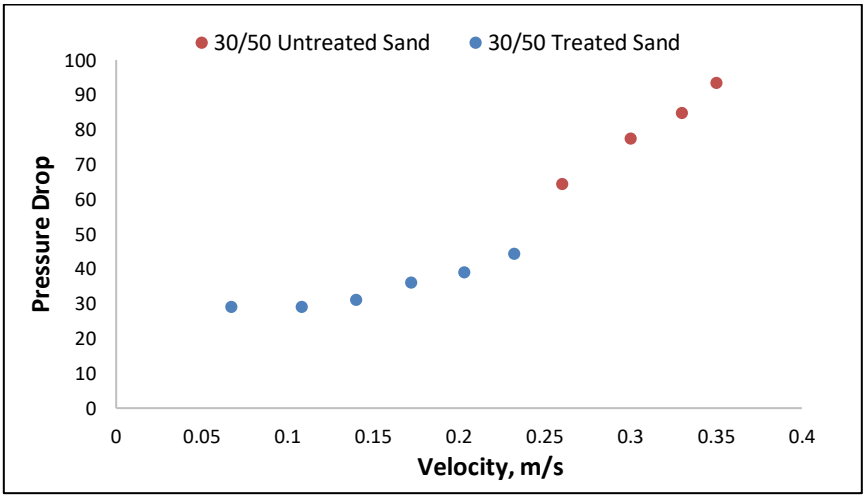

Figure 3-25 Comparison of the frictional pressure drop data measured at various velocities of water flow over the 30/50 mesh size treated and untreated sand bed.

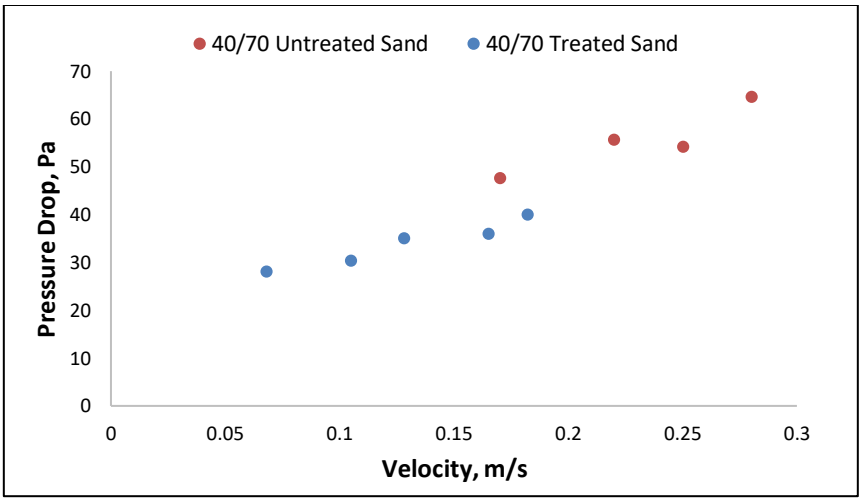

Figure 3-26 Comparison of the frictional pressure drop data measured at various velocities of water flow over the 40/70 mesh size treated and untreated sand bed.

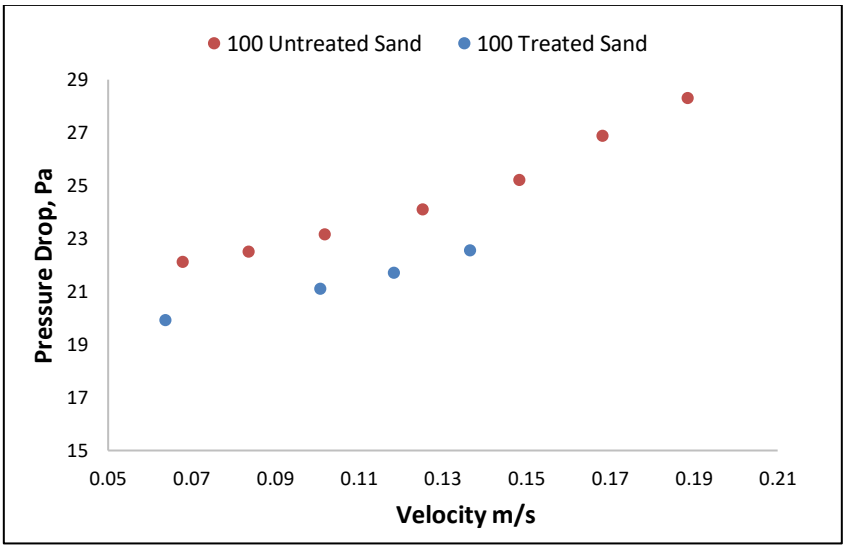

Figure 3-27 Comparison of the frictional pressure drop data measured at various velocities of water flow over the 100-mesh size treated and untreated sand bed.

3.6.2. Comparison of PIV Data Measured Over the Treated and the Untreated Sand Beds

Recording PIV data was not easy over the treated sand beds due to the increased mobility of the treated sand particles powered by their modified surface characteristics. Therefore, depending on the availability of good quality PIV data, comparison of the PIV test results could only be made at different fluid velocities for the flow over the treated and untreated sand bed of specific particle size.

For all the figures of PIV data comparisons given below, the origin (i.e., y=0) was set at the sand bed-water interface. The y-coordinate in the plots represents the vertical distance from the bed (in the direction perpendicular to the flow) and y=0 represents the sand bed-water interface.

Figure 3-28 presents the near wall velocity profiles for 0.25 m/s water flow over the treated and untreated sand bed of 20/40 mesh size particle.

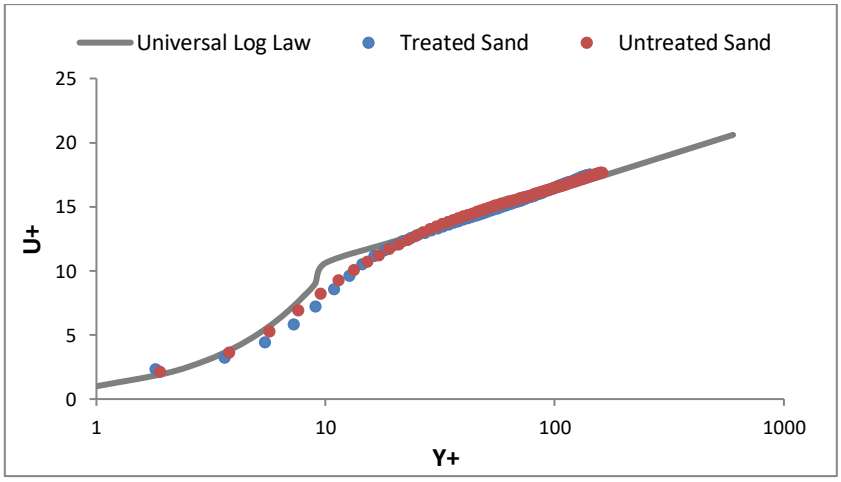

Figure 3-28 The near wall velocity profiles for 0.25 m/s water flow over the treated and untreated sand bed of 20/40 mesh size particles.

Figure 3-29 presents the near wall velocity profiles for 0.22 m/s water flow over the treated and untreated sand bed of 30/50 mesh size particles.

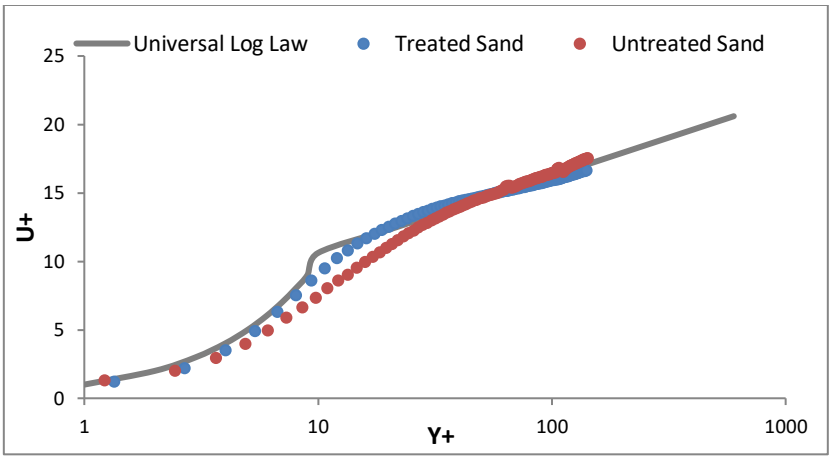

Figure 3-29 The near wall velocity profiles for 0.22 m/s water flow over the treated and untreated sand bed of 30/50 mesh size particles.

The dimensionless velocity profiles for water flow over the treated and the untreated sands beds of 20/40 (Fig.3-28) and 30/50 (Fig.3-29) mesh size particles follow the universal law within the log-law region (y+> 30), confirming that the flow in both cases were hydrodynamically smooth. However, slight downward shifts were observed in the viscous sub-layer region.

Figure 3-30 presents comparison of the normalized Reynolds shear stress profiles for 0.25 m/s water flow over the treated and untreated sand bed of 20/40 mesh size particles. The Reynolds shear stress profile for the flow over the 20/40 mesh size treated sand bed was lower than that of the case with 20/40 mesh size untreated sand bed.

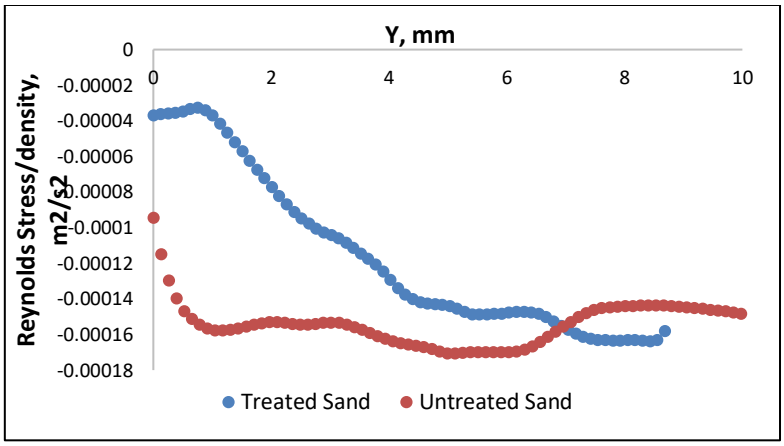

Figure 3-30 Reynolds shear stress profiles for 0.25 m/s water flow over the treated and untreated sand bed of 20/40 mesh size particles.

Figure 3-31 presents comparison of the normalized Reynolds shear stress profiles for 0.22 m/s water flow over the treated and untreated sand bed of 30/50 mesh size particles. The Reynolds shear stress profile for the flow over the 30/50 mesh size treated sand bed was lower than that of the case with 30/50 mesh size untreated sand bed.

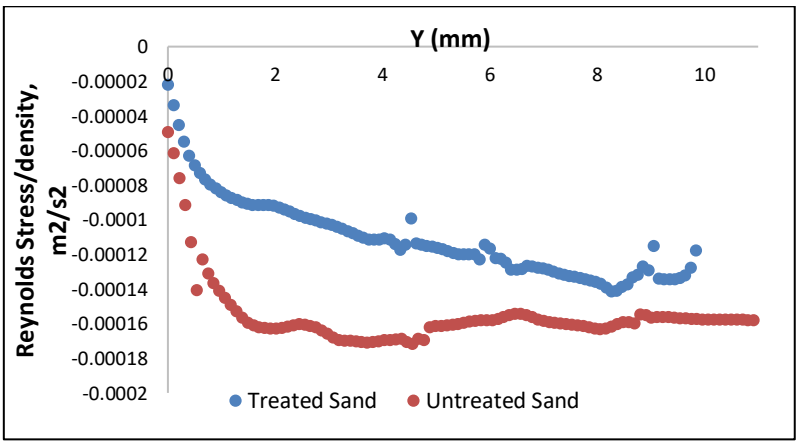

Figure 3-31 Comparison of the Reynolds shear stress profiles for 0.22 m/s water flow over the treated and untreated sand bed of 30/50 mesh size particles.

As shown in Figure 3-30 and 3-31, the Reynolds stress values for water flow over the treated sand particles are lower than that of the untreated sands for both 20/40 and 30/50 sand sizes. Reynolds stress in this case can be considered as a direct measure of the momentum transfer from the fluid to the sand bed. Lower Reynolds stress is analogous with lower energy dissipation through the flow over the treated sand bed, which can be attributed to the positive effect of the sand surface treatment. Lower Reynolds stress values observed for the flow over treated sand bed are in line with the lower frictional pressure drop recorded during the flow over the treated sand bed. It should be noted that the Reynolds stress profiles for flow over the treated and untreated sand bed becomes distinctively different especially far from the near wall region. It appears that the surface treated sand particles flowing (much like flying around) within the main stream of water flow away from the bed are also affecting the Reynolds stress generated by the water flow in this region significantly.

The axial turbulence intensity is critical in sand particle removal because it represents the level of velocity fluctuations in axial direction. Recent studies have shown that the turbulent velocity fluctuations may influence the particle removal significantly [16,17]. A comparison of the axial turbulence intensity profiles (also called the normal Reynolds stress) observed during the 0.25 m/s water flow over the untreated and treated sand beds of 20/40 mesh size particles is shown in Figure 3-32.

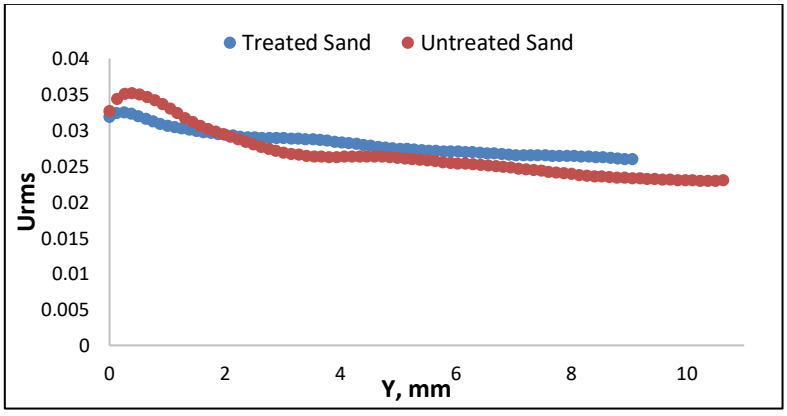

Figure 3-32 Comparison of the axial turbulence intensity profiles for 0.25 m/s water flow over the treated and untreated sand bed of 20/40 mesh size particles.

A comparison of the axial turbulence intensity profiles observed during the 0.22 m/s water flow over the untreated and treated sand beds of 30/50 mesh size sand particles is shown in Fig. 3-32.

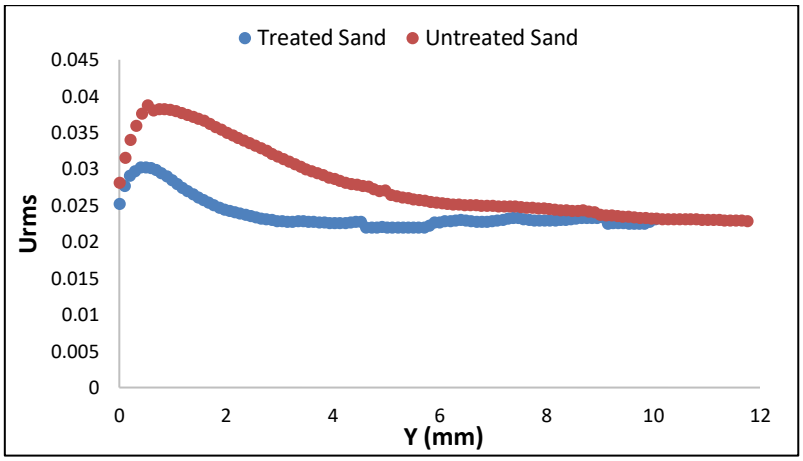

Figure 3-33 Comparison of the axial turbulence intensity profiles for 0.22 m/s water flow over the treated and untreated sand bed of 30/50 mesh size particles.

Results shown in Figure 3-32 and 3-33 indicate that the axial turbulence intensity observed near the wall was more or less the same for the treated and the untreated sands beds of 20/40 and 30/50 mesh sizes. Away from the sand bed/fluid interface, however, it was observed that the axial turbulent intensity for flow over the treated sand bed was lower than that of the untreated sand bed. The difference was more significant for the flow over the sand bed of 30/50 mesh size (smaller size of the two sands).

The radial component of turbulence intensity, v_{rms}, is of particular importance in solid transport and solid suspension. Kelessidis and Bandelis [18] based on the work of Davies [19] discussed the eddy fluctuation force and suggested that they were essential in keeping particles in suspension in turbulent flow. Davies [19] has shown that the eddy fluctuation force is proportional to radial velocity fluctuations. A higher level of radial velocity fluctuation results in a higher eddy fluctuation force.

Results shown in Fig.3-34 (20/40 mesh size sand) and Fig.3-35 (30/50 mesh size sand) indicate that the radial turbulence intensity profiles were more or less the same for the flow of water over treated and untreated sand bed.

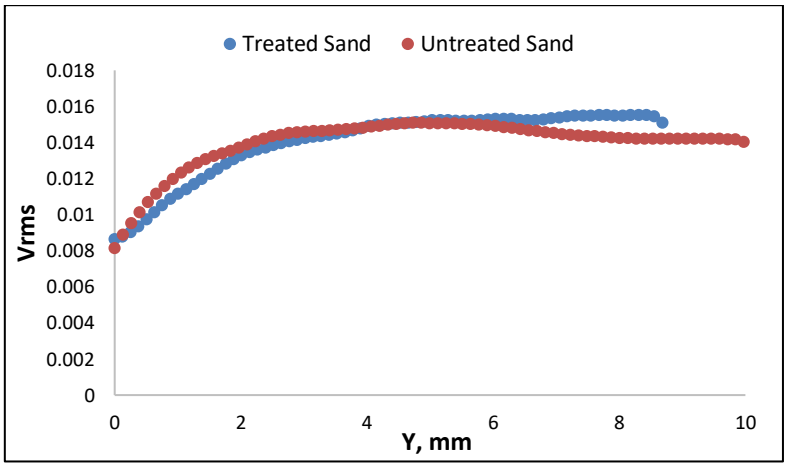

Figure 3-34 Radial turbulence intensity profiles for the flow of water over the treated and untreated sand beds of 20/40 mesh size particles at superficial velocity of 0.25 m/s.

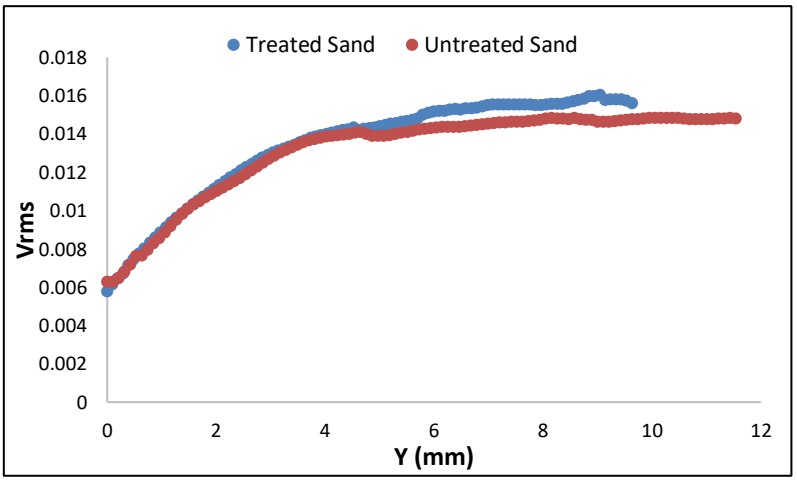

Figure 3-35 Radial turbulence intensity profiles for the flow of water over the treated and untreated sand beds of 30/50 mesh size particles at 0.22 m/s velocity.

3.6.3. Comparison of Critical Velocities Required for the Onset of Particle Removal from Treated and Untreated Sand Beds

Critical velocities required for the initiation of particle removal from treated and untreated sand beds of four different particle size ranges are summarised in Table 3-6 and also compared in Fig.3-36. Generally, the critical velocities required for the onset of the particle movement with water are significantly lower for the surface treated sands than the untreated sands. The most likely reason for observing lower critical velocities for treated sand particles is that the air bubbles seem to attach to the surface of the treated sand particles and, hence, enhance the buoyancy force acting on them. With the increased buoyancy force in place, it naturally becomes easier to mobilize treated sand particles than the untreated ones.

Table 3-6 Comparison of the critical velocity required for the onset of the particle removal from treated and untreated sand beds

Sand Particles Size	Bed Height (cm)	Flow Area (without bed) (cm^2)	Critical Flow Rate (lpm)	Critical Velocity (m/s)	Reduction in Critical Velocity (%)
20/40 Untreated	3.4	47.17	101	0.36	14
20/40 Treated	**3.31**	**48.91**	**91.8**	**0.31**	
30/50 Untreated	3.1	50.6	91.3	0.301	25
30/50 Treated	**3.45**	**47.59**	**66**	**0.23**	
40/70 Untreated	3.5	46.73	79.6	0.284	40
40/70 Treated	**3.45**	**47.59**	**49**	**0.17**	
100 Untreated	3.31	48.91	57.8	0.2	30
100 Treated	**3.31**	**48.91**	**41.8**	**0.14**	

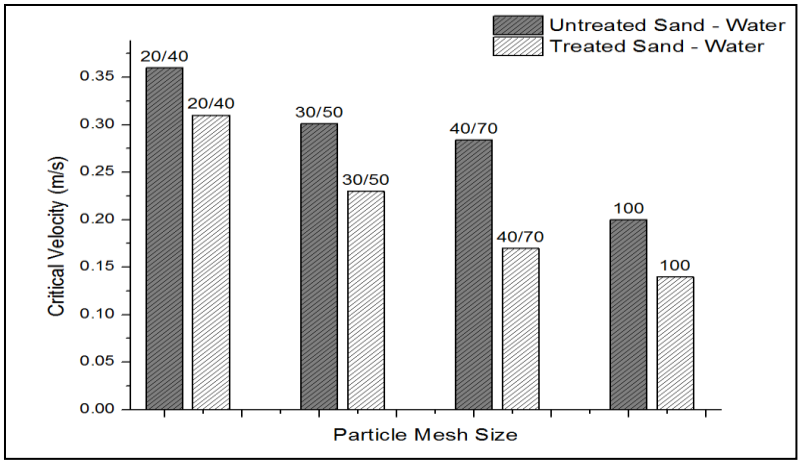

Figure 3-36 Comparison of the critical velocity required for the onset of the particle removal from treated and untreated sand bed.

3.7. CONCLUSIONS

An experimental study was conducted to investigate the turbulent flow of water over the sand bed deposited in a horizontal pipeline. The main objectives were: (a) to determine the near wall turbulence characteristics (i.e., near wall velocity profile, Reynolds shear stresses, axial and radial turbulent intensities) by using particle image velocity (PIV) technique; (b) to determine critical velocity for particle removal from bed deposits; (c) more specifically, to determine how the particle size and surface properties (i.e. wettability) would influence the critical velocity and near wall turbulence characteristics.

The critical velocity required for the onset of particle removal from sand bed decreases with decreasing sand particle for both treated and untreated sands. However, critical velocities for particle removal from treated sand beds were significantly lower than that of the untreated sand beds for all particle size ranges investigated.

It was observed that air bubbles were attached to the treated sand particles during the flow. It appears that the modified sand surface properties (i.e. changing from water wet to non-water wet) promote the air bubble attachment to the sand particles, which increases the buoyancy forces acting on these sand particles and, hence, causes the reduction of the critical velocity for particle removal. Moreover, the degree of reduction of the critical

velocity in this case varied depending on the particle size. For the sand sizes used in this study, the reduction in critical velocity was the highest (40%) for 40/70 mesh size of treated sand. As we decreased the sand size further to 100 mesh, however, the observed reduction of critical velocity due to surface treatment was only 30%, indicating that there exists a specific sand size where the reduction of the critical velocity becomes maximum.

For the flow of water over the untreated sand bed, frictional pressure loss varied depending on the particle size range. The frictional pressure loss for the flow of water over the 30/50 sand bed was higher than that of the case for 40/70 sand bed, indicating that frictional pressure loss decreases with the decreasing sand size. However, the trend was the opposite, when we used 20/40 mesh size (largest size sand particles within the group tested). The measured frictional pressure loss for the flow over the bed with 20/40 sand size range was lower than that of the flow over the beds with 30/50 and 40/70 sand size ranges. For the flow over the treated sand bed, however, frictional pressure loss values measured at the same fluid velocities were almost the same for all particle size ranges. It seemed like the surface treatment of the sands negated the effect of particle size on the frictional pressure drop.

The frictional pressure loss values measured for the water flow over the treated sand bed were slightly lower than that of the case with untreated sand bed for all particle size ranges. These results suggest that the modifications in surface characteristics of sand particles might have a positive (i.e., drag reduction effect) effect on frictional pressure losses for water flow over a sand deposit in a horizontal pipe.

The Reynolds stress values for water flow over the treated sand particles were lower than that of the untreated sands for both 20/40 and 30/50 sand sizes. Reynolds stress in this case can be considered as a direct measure of the momentum transfer from the fluid to the sand bed. Lower Reynolds stress is analogous with lower energy dissipation through the flow over the treated sand bed, which can be attributed to the positive effect of the sand surface treatment. Lower Reynolds stress values observed for the flow over treated sand bed are in line with the lower frictional pressure loss values recorded during the flow over the treated sand bed.

In summary, we can say that by applying special surface treatments on sand particles, more control over the bed erosion dynamics might be obtained. However, particle size is still a very important point to take into consideration for optimizing the effectiveness of the treatment. Such surface treatment of solids might be beneficial for the design of proppants that could possess more efficient transport properties and, hence, help improving the performance of hydraulic fracturing operations.

3.8. ACKNOWLEDGEMENTS

This research is financially supported by the funds available from the Natural Sciences and Engineering Research Council of Canada (NSERC EGP 515333-17 Kuru).

3.9. REFERENCES

1. Nazari, T., Hareland, G., Azar, J. J. (2010, May). Review of Cuttings Transport in Directional Well Drilling: Systematic Approach. SPE Western Regional Meeting Anaheim, California, USA, SPE-132372-MS, doi: 10.2118/132372-MS.
2. Li, J., Luft, B. (2014a, October). Overview of Solids Transport Studies and Applications in Oil and Gas Industry - Experimental Work. SPE Russian Oil and Gas Exploration & Production Technical Conference and Exhibition. Moscow, Russia, SPE-171285-MS, doi: 10.2118/171285-MS.
3. Li, J., Luft, B. (2014b, December). Overview Solids Transport Study and Application in Oil-Gas Industry-Theoretical Work. International Petroleum Technology Conference. Kuala Lumpur, Malaysia, IPTC-17832-MS, doi: 10.2523/IPTC-17832-MS.
4. Brown, N., Bern, P., Weaver, A. (1989). Cleaning Deviated Holes: New Experimental and Theoretical Studies. SPE/IADC Drilling Conf.
5. Adari, R., Miska, S., Kuru, E., Bern, P., Saasen, A. (2000, February). Cuttings Bed Erosion Curves Help Predict Optimum Circulation Time for Hole Cleaning. ETCE/ OMAE Joint Conference of ASME, New Orleans, LA.

6. Martins, A., Campos, W., Liporace, F., Wei, X., Van Riet, E. (1997). On the Erosion Velocity of a Cuttings Bed During the Circulation of Horizontal and Highly Inclined Wells. Latin American and Caribbean Petroleum Engineering Conference.

7. Rabenjafimanantsoa, A., Time, R. W., Saasen, A. (2007). Simultaneous Uvp and PIV Measurements Related to Bed Dunes Dynamics and Turbulence Structures in Circular Pipes. in 5th International Symposium on Ultrasonic Doppler Methods for Fluid Mechanics and Fluid Engineering, pp. 63-67.

8. Bizhani, M., Kuru, E. (2017). Particle Removal from Sandbed Deposits in Horizontal Annuli Using Viscoelastic Fluids. SPE Journal.

9. Bizhani, M. (2017). Experimental and Theoretical Investigations of Particle Removal from Sand Bed Deposits in Horizontal Wells Using Turbulent Flow of Water and Polymer Fluids. PhD Thesis, Civil and Environmental Engineering, University of Alberta, Edmonton, Canada.

10. Metzner, A.B., Reed, J.C. (1955). Flow of non-Newtonian fluids—correlation of the laminar, transition, and turbulent-flow regions. AICHE Journal,1(4), pp.434-440.

11. Raffel, M., Willert, C. E., Kompenhans, J. (2007). Particle Image Velocimetry: A Practical Guide: Springer Science & Business Media.

12. LaVision, Davis 8.3 Product Manual. ed, 2015.

13. Ramadan, A., Skalle, P., Johansen, S. T. (2003). A mechanistic model to determine the critical flow velocity required to initiate the movement of spherical bed particles in inclined channels. Chemical Engineering Science 58(10): 2153-2163 doi: 10.1016/S0009-2509(03)00061-7, Chem Eng Sci.

14. Duan, M. Q., Miska, S., Yu, M. J., Takach, N., Ahmed, R., Zettner, C. (2009). Critical Conditions for Effective Sand-Sized-Solids Transport in Horizontal and High-Angle Wells. SPE Drilling & Completion 24(2): 229-238, SPE Drill Completion, doi: 10.2118/104192-PA.

15. Kundu, P. K., Cohen, I. M., Dowling, D. R. (2012). Fluid Mechanics, 5th Edition. Amsterdam, Elsevier Science Bv.

16. Bizhani, M., Kuru, E. (2017). Critical Review of Mechanistic and Empirical (Semi- Mechanistic) Models for Particle Removal from Sand Bed Deposits in Horizontal Annuli by Using Water. SPE Journal, SPE-187948-PA, In press.

17. Diplas, P., Dancey, C. L., Celik, A. O., Valyrakis, M., Greer, K., Akar, T. (2008). The Role of Impulse on the Initiation of Particle Movement under Turbulent Flow Conditions. Science, vol. 322, pp. 717-720.

18. Kelessidis, V. C., Bandelis, G. E. (2004). Flow Patterns and Minimum Suspension Velocity for Efficient Cuttings Transport in Horizontal and Deviated Wells in Coiled-Tubing Drilling. SPE Drilling & Completion.

19. Davies, J. (1987). Calculation of Critical Velocities to Maintain Solids in Suspension in Horizontal Pipes. Chemical Eng.Sci., vol. 42, pp. 1667-1670.

4. EFFECT OF SAND PARTICLE SIZE AND SURFACE PROPERTIES ON THE NEAR WALL TURBULENCE CHARACTERISTICS OF THE POLYMER FLUID FLOW AND THE CRITICAL VELOCITY REQUIRED FOR THE PARTICLE REMOVAL FROM THE SAND BED DEPOSITED IN HORIZONTAL PIPELINES

4.1. ABSTRACT

An experimental study was conducted to investigate the turbulent flow of dilute polymer solution over a stationary sand bed deposited in a horizontal pipeline. The main objectives of the study were to determine effects of sand particle size and sand surface properties on the critical velocity required for the onset of the bed erosion and the near-wall turbulence characteristics of the polymer fluid flow over the sand bed.

Industrial sand particles having three different size ranges (20/40, 30/50, 40/70) with and without special surface treatment were used for the experiments.

The particle image velocimetry (PIV) technique was used to determine instantaneous local velocity distributions and near wall turbulence characteristics (such as Reynolds stress, axial and turbulence intensity profiles) of dilute polymer fluid flow over the stationary sand bed under turbulent flow conditions.

The critical velocity for the onset of the particle removal from a stationary sand bed using a polymer fluid flow is affected by the sand particle size and the surface characteristics. The effect, however, was varied depending on the relative comparison of the sand particle size with respect to the thickness of the viscous sublayer under turbulent flow condition.

4.2. INTRODUCTION

Deposition of drilled cuttings on the low side of the well is inevitable when drilling long horizontal or extended reach wells. If the cuttings are not cleaned sufficiently, operational problems such as slow drilling rate, excessive torque and drag, bridging, pack-off, hole fill, and a pipe stuck would occur [1-3]. Drilling needs to be interrupted

occasionally to clean the well from cuttings, however, this costs time and money. Also, circulating the drilling fluid at any rate may not be adequate to disturb the deposited sand bed unless a critical flow rate and a shear stress for bed erosion is exceeded [2,3]. There have been great advances in drilling methodology, drilling fluid technology and in field practices during the past 50 years as a result of intensive work done by researchers from both the academy and the industry, however hole cleaning is still a major problem when drilling highly inclined and horizontal wells [2,3].

Hole cleaning performance of water and some polymer-based fluids were studied by Brown et al. [4] through a set of experiments conducted by using a specially designed flow loop. Brown et.al [4] experiments presented a comprehensive picture of hole cleaning in oil-well drilling. Adari et al. [5] carried out extensive experiments to determine the effects of the drilling fluid flow rate and rheological properties on the cuttings bed erosion. Martins et al. [6] presented results of an extensive bed erosion tests conducted by using different polymeric suspensions in annular flow, at several values of flow rates, wellbore inclinations and drill pipe rotational speeds. Based on the experimental results, they have developed a method to quantify the volume of solids removed from the highly inclined and horizontal annulus with time.

Rabenjafimanantsoa et al. [7] studied the flow over the sand bed by using particle image velocimetry (PIV) and ultrasound velocity profile (UVP) techniques, which provided an improved understanding on the flow structure and its relationship to the sand bed. Recently Bizhani et al. [8] studied the effect of fluid viscoelasticity on the bed erosion dynamics in horizontal annuli by using PIV technique.

The particle size appears to be an important parameter in all models suggested to predict the critical velocity over a sand bed, regardless of a flow regime, the fluid type and the rheological properties. However, the main focus in most of the previous research on hole cleaning has always been either the flow regime or the fluid rheological properties. To fill this knowledge gap, we have conducted a series of bed erosion experiments to study

the effects of sand particle size and surface characteristics on the bed erosion performance of dilute polymer fluids.

4.3. MATERIALS AND METHODS

4.3.1. Sand Particles

Treated and untreated industrial quartz sand particles (SG =2.65) of three different mesh sizes of 20/40, 30/50 and 40/70 were used in this study. Table 4-1 summarizes the range of particles sizes in microns. We have conducted contact angle measurements for treated and untreated 20/40 mesh size sands. The contact angle for 20/40 mesh size treated sand was 139 degrees, indicating that treated sand was hydrophobic (Figure 4-1). A dilute (0.032 % w/w) water-based solution of Alcomer RD 110 polymer was used in these experiments. The rheological properties of the polymer fluid were determined by using a high resolution Bohlin C-VOR 150 rheometer. The rheogram (shear stress vs shear rate plot) of the polymer fluid is presented in Figure 4-2. The fluid shows pseudo plastic (power law) behaviour with consistency index (k) and flow behaviour index (n) values of 0.0055 (Pa-s^n) and 0.9093, respectively.

Table 4-1 Size Ranges of Sand Particles Used in the Experiments

Sand Particles Mesh Size	Sand Particles Size Range (microns)
20/40	420-840
30/50	297-590
40/70	210-420

Figure 4-1 Contact angle measurement for 20/40 mesh size sands: a-) Non-treated sand b-) Surface treated sand

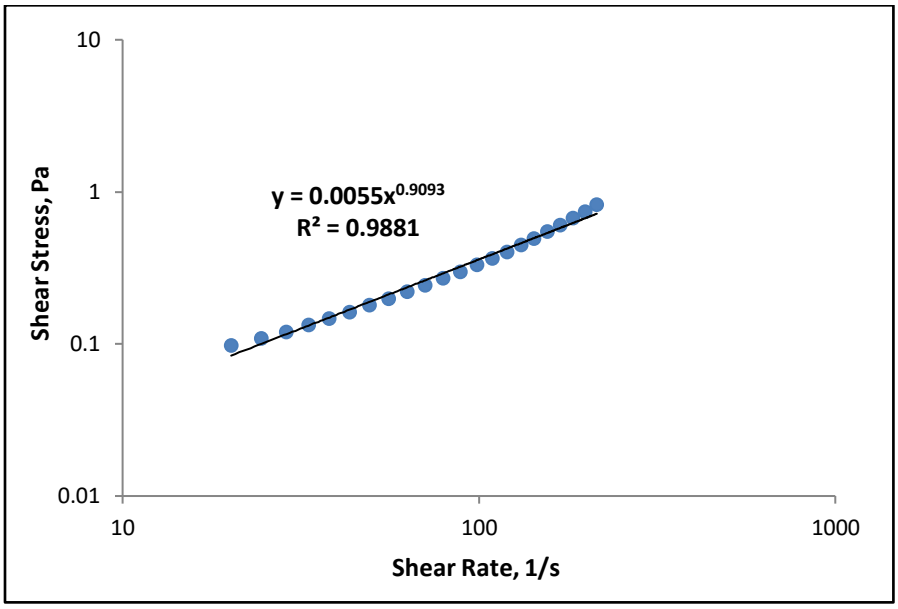

Figure 4-2 Rheogram of the polymer fluid used in the study

4.3.2. Experimental Flow Loop

A schematic view of the horizontal flow loop used in the bed erosion experiments is presented in Fig. 4-3.

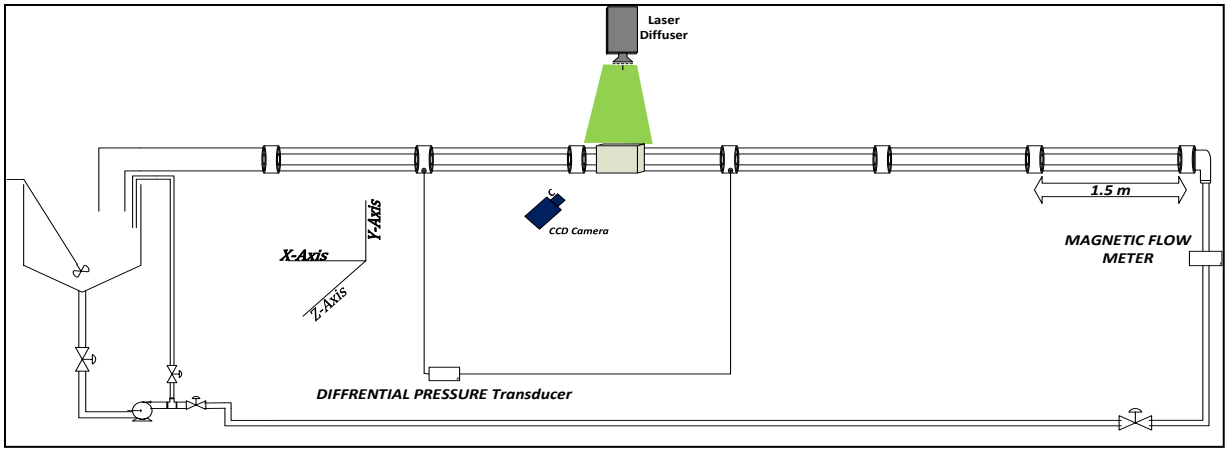

Figure 4-3 Schematic diagram of the experimental flow loop [9].

The main elements of the flow loop are; a 500-liter capacity mixing tank, a variable frequency drive centrifugal pump, differential pressure transducer, a magnetic flow meter, and several gate valves to control the fluid flow through the system and glass tubes.

The 9 m long test section consists of borosilicate glass pipes with 95 mm ID. The data acquisition system was operated by National Instrument`s Labview software. The flow rate was measured by OMEGA FMG607-R, magnetic flow meter with accuracy of ±0.5% that was installed at the test section inlet. A differential pressure transducer, OMEGA DPG409, with an accuracy of ±0.08% was used for measurement of frictional pressure drop over the 3.08 m long pipe section.

Figure 4-4 shows the camera – laser alignment and the main test section used for recording the Particle Image Velocimetry (PIV) data for all bed erosion experiments. In this section, the borosilicate glass pipe is inside a rectangular glass box filled with glycerol. This way measurement errors might arise from undesired refraction of the light passing through the circular pipe were eliminated, because glycerol and the borosilicate pipe have the same refractive indexes and so the light directly exposes to the fluid without any refraction.

PIV setup consists of a New Wave Research Solo III Nd: YAG laser, a Lavision Imager Intense CCD camera, Nikon 50 mm AF Nikkor lens of 1.4 mm aperture. The wavelength of the laser was 532 nm, and the Imager

Intense was a double framed camera with a 12-bit CCD sensor of having 1376 x 1040 pixels. All these components are monitored and synchronized by a commercial software, Davis 8.3. This software is also used to process and analyse the recorded data set.

In addition, the status of the sand bed at critical flow rates or at some subcritical flow rates was recorded by a Samsung digital camera - 8 MP, f/2.4, 31 mm, AF, 1080p @ 30fps.

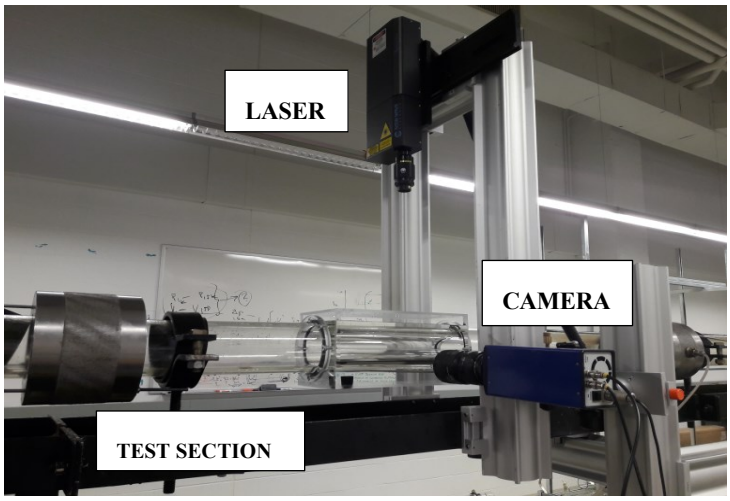

Figure 4-4 Image of the PIV setup and the test section

4.3.3. Experimental Procedure

The experimental procedure consisted of three main stages: i-) establishment of the sand particle bed; ii-) the second stage was polymer circulation through the sand particle bed, and the critical flow rate determination; and the third stage was iii-) PIV measurements at critical flow rate and at a particular subcritical flow rate. Prior to the bed erosion experiment, we have conducted calibration test to verify the accuracy of the pressure loss measurement. The method of verification of frictional pressure loss measurement and the experimental procedure for the three main stages are briefly explained below.

4.3.3.1.Verification of the Accuracy of the Frictional Pressure Loss Measurements

Frictional pressure drops for water (no sand bed) flow in the horizontal flow loop were measured and friction factors estimated from these measurements by using the Fanning friction equation (Eq.4-1) were compared with theoretical values calculated from conventional pipe flow correlation [10] for water to confirm the accuracy of the pressure measurements. Figure 5 shows the comparison of theoretical and experimental data.

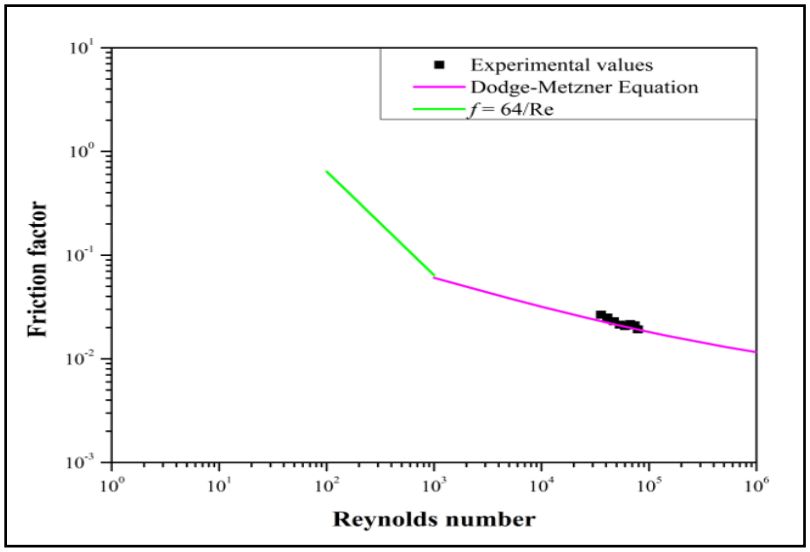

Figure 4-5 Comparison of experimental friction factor values estimated from water only flow tests against the ones calculated from Dodge and Metzner equation [10].

$$\Delta P = f\frac{\rho u^2}{d_e}\Delta L \quad \text{(4-1)}$$

Where ΔP is the frictional pressure drop, ΔL is the length of the pipe section over which the friction pressure loss was measured (3m in this case), ρ is the fluid density, u is the bulk velocity, f is the friction factor and, d_e is the equivalent diameter.

4.3.3.2. Sand Bed Establishment

Initially, the suction tank was filled with water. Then, water was circulated through the loop at the highest possible flow rate. Then the sand particles were added to the tank, while the water was still in circulation. Effort was spent to get the initial bed height same for all the experiments. The amount of sand needed to get the same bed height varied depending on the sand particle size. Depending on the particle mesh size range, the solid concentration used in the experiments changed from 5% to 8% wt/wt. When the sand bed was uniform everywhere in the flow loop, the pump was stopped, and the valves at the both end of the pipe section were closed. The fluid was kept in the flow loop under static condition over the night to make sure all sand particles in suspension to settle down and form a continuous bed.

4.3.3.3.Polymer Fluid Circulation and Measurement of Critical Flow Rate

After establishing a uniform bed, the suction tank was drained. In the mixing tank the dilute polymer solution was prepared and circulated through the flow loop starting with the low (subcritical) flow rate and gradually increasing it to the level at which the first couple of particles start moving. When the movement of the first couple of sand particles were observed (i.e., onset of the bed erosion), then the respective flow rate was recorded as the critical flow rate for bed erosion in that particular sand size range. Frictional pressure losses were also recorded at the critical and the various subcritical flow rates.

4.3.3.4. PIV Measurements

PIV is a non-intrusive laser based optical measurement technique commonly used to measure the instantaneous local (i.e. near wall) fluid velocities and analyse flow characteristics associated with the turbulent flow conditions [10]. In this technique, tracer particles sensitive to the light are exposed to the laser beam and their movements (i.e., velocity and direction) are recorded by using a double frame high speed CCD camera. The

recorded images are converted to velocity field data via a computer analysis, which requires use of a special software (LaVision Davis 8.3) allowing data processing by fast Fourier transformation (FFT) technique [11].

The PIV setup consisted of a light source and a recording device. A double pulse laser was used as the light source, and double frame CCD camera was used as the recording device. The camera view plane must be orthogonal to the laser light as shown in Figure 4-4. The tracer particles were added to the suction tank while maintaining the polymer circulation for a while to obtain a homogenous tracer distribution in the system. Hollow glass spheres with mean diameter of 10 microns were used as the tracer particles in the current study. Density of the tracer particles were similar to the density of the fluid, so tracers exactly follows the fluid flow. Since the flow was seeded with tracer particles, these tracer particles reflect the light when the laser light was impinged on them. The reflected light was then detected by the camera. Two successive images were captured by the camera in a very short time period. Figure 6a shows a typical PIV images acquired during the experiments. In this image, the cuttings bed is located at the bottom while the polymer fluid seeded with tracer particles (bright white dots) is flowing above the bed. These pictures were processed with appropriate algorithm to determine the instantaneous velocity field of the flow. PIV measurements at critical and subcritical flow rates were performed and recorded using the Davis 8.3 software. At least 1000 pair of images were acquired for each flow experiment, and the velocity values were averaged out to ensure higher accuracy in the measurements.

4.3.4. Data Processing and Analysis

Data processing and analysis consisted of two parts. In the first part, we have determined the critical flow rate. Fluid flow over the stationary sand bed at various flow rates were recorded by the video camera. The fluid flow rate was gradually increased from very low subcritical flow rates to the critical flow rate where the first movement of particles were observed. The critical flow rate was determined visually.

The second part was involved in the PIV data processing and analysis. The initially added light sensitive tracer particles following the fluid flow were seen as the bright spots in each pair of captured PIV images (Fig. 4-6a), and they were detected by the Davis 8.3 software.

By cross correlating these pair of images, the displacement (Δx and Δy) of particles between the two images was determined [12]. Since the time interval between the two images was known, the instantaneous velocities were calculated for all detected points by using the particle displacement (Δx and Δy) and time interval (Δt) as follows:

$$\begin{cases} \hat{u} = \frac{\Delta x}{\Delta t} \\ \hat{v} = \frac{\Delta y}{\Delta t} \end{cases} \qquad \text{..... (4-2)}$$

In order to find out the displacement of detected bright spots in x and y direction, Davis 8.3 software applied an FFT based cross correlation method [12]. First, both images were segmented into small interrogation windows and those windows in two images were compared to recognize the cross correlation [12]. The exact displacement was determined by identification of the highest peak of the correlation. A multi-pass approach starting from window size of 64 x 64 down to 24 x 24 including 32 x 32 size in between was used in PIV image processing with overlap of 50%. The recorded data with those settings were exported to excel files for further data analysis. Figure 4-6b shows the final velocity vector field for the flow over the cuttings bed.

In order to find out the displacement of detected bright spots in x and y direction, Davis 8.3 software applied an FFT based cross correlation method [12]. First, both images were partitioned into small interrogation windows and corresponding windows in two images were cross correlated [12]. The correlation resulting in the highest peak value indicated the exact displacement. A multi-pass approach was used in PIV image processing. The window size decreased from 64 x 64 down to 24 x 24 including 32 x 32 size in between in analysis with an overlap

of 50%. The data processed with those settings were exported to excel files for further analysis. Figure 4-6b shows the final velocity vector field for the flow over the cuttings bed obtained from all analysis.

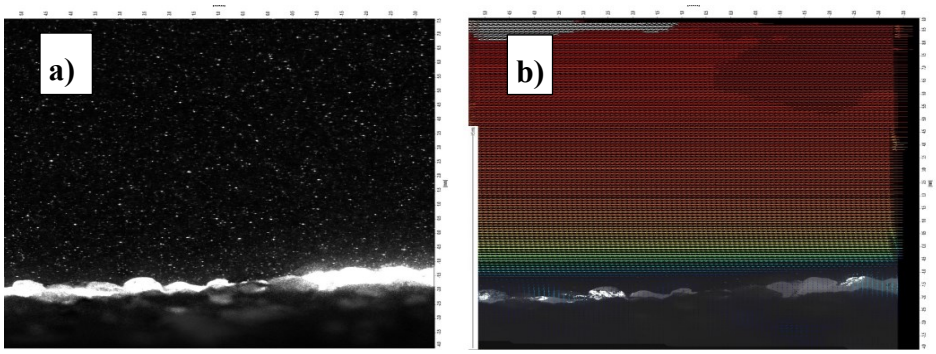

Figure 4-6 Typical PIV image acquired during the tests, b) resultant velocity field.

Four main features, Reynolds stresses, axial turbulence intensities, radial turbulence intensities and near wall dimensionless velocities, were further analysed and compared for all cases to detect the difference in the turbulent characteristics of the fluid flow over the sand bed. The Davis 8.3 software calculates all these features based on the governing equations for those using the velocities and velocity fluctuations measured in x and y directions for each pair of images taken.

The near wall velocity profiles were presented in terms of dimensionless distance (y^+) and dimensionless velocity units (u^+) as defined by equations 4-3 and 4-4, respectively.

$$y^+ = \frac{\rho y u_\tau}{\mu} \quad \text{..... (4-3)}$$

$$u^+ = \frac{u}{u_\tau} \quad \text{..... (4-4)}$$

$$u_\tau = \sqrt{\frac{\tau_b}{\rho}} \quad \text{..... (4-5)}$$

Where u_τ is the friction (shear) velocity, τ_b is the interfacial bed shear stress (i.e., shear stress at the fluid/sand bed interface), and ρ is the fluid density. The interfacial bed shear stress, τ_b, cannot be deduced accurately from

frictional pressure loss data because more than one surface is involved in the flow (i.e. pipe, wall and the bed surface). Therefore, the friction velocity, u_τ, cannot be directly estimated by using the bed shear stress. In this study, we have determined the friction velocity, u_τ, by using the plot of velocity versus vertical distance from the surface of the sand bed. These data were obtained directly from PIV measurements. The detailed procedure for determining the friction velocity from the PIV measured velocity data is given elsewhere [9].

The universal law of the wall states that the near wall velocity profiles generally consists of three regions depending upon the dimensionless distance from the bed: Viscous sub-layer y^+ <5, buffer region 5< y^+<30 and log-law region y^+> 30. The universal plot of a velocity profile for a hydrodynamically smooth flow condition is given by Equation 6 [13].

$$u^+ = \begin{cases} y^+ & y^+ < 10 \\ 2.44ln(y^+) + 5.5 & y^+ > 30 \end{cases}. \quad \text{..... (4-6)}$$

The Reynolds shear stress (or turbulent stress) is a direct function of the velocity fluctuations (u' and v') in the turbulent flow as defined by the Equation 7:

$$\tau_R = -\rho\overline{u'v'} \quad \text{..... (4-7)}$$

The axial turbulence intensity is defined by the Equation 8:

$$u_{rms} = \sqrt{\overline{u'u'}} \quad \text{..... (4-8)}$$

The radial turbulence intensity is defined by the Equation 9:

$$v_{rms} = \sqrt{\overline{v'v'}} \quad \text{..... (4-9)}$$

4.4. RESULTS AND DISCUSSIONS – BED EROSION EXPERIMENTS USING UNTREATED SANDS

4.4.1. Frictional Pressure Drops Measured for the Polymer Fluid Flow over the Untreated Sand Bed

Table 4-2 summarizes the frictional pressure loss measurements for the flow of the dilute polymer solution over the sand beds of 3 different particle size ranges (i.e. 20/40, 30/50, 40/70 mesh sizes) of untreated sand particles at the sub-critical velocity of 0.25 m/s. There are slight differences between the initial bed heights of each particle size range, which might affect the measured frictional pressure drops. To minimize the effect of slight variation in initial bed height, flow rates were adjusted to have the same superficial velocity of 0.25 m/s for each test. Adjustment in the flow rates were made by considering the area open to the fluid flow above the sand bed. At the subcritical fluid velocity of 0.25 m/s, the Reynolds number was 4800. The critical Reynolds number in this case was 2113. Therefore, the flow regime was determined as turbulent.

The equivalent diameter was calculated by assuming the area open for flow above the cuttings bed as a circle. The normalized frictional pressure loss was estimated by multiplying measured frictional loss values with the calculated equivalent diameter. The measured frictional pressure loss, equivalent diameter and the normalized frictional pressure loss data are all shown in the Table 4-2.

Table 4-2 Frictional Pressure Drop Over Untreated Sand Bed Measured at 0.25 m/s.

Sand Particle Mesh Size	Bed Height (cm)	Flow Rate (lpm)	Frictional Pressure Loss (Pa)	Equivalent Diameter (m)	Normalized Frictional Pressure loss (Pa-m)
20/40	3.65	70.3	43	0.0767	3.29
30/50	3.1	76	35.42	0.0802	2.84
40/70	3.31	74.7	48.95	0.0789	3.86

Figure 4-7 summarizes all the frictional pressure loss values measured over the stationary bed of untreated sands using multiple flow rates. The measured frictional pressure loss values for the flow over the 20/40 and 40/70 mesh size of untreated sand particles were close to each other at all fluid velocities. The frictional pressure loss measurements over the bed of 30/50 mesh size (intermediate size of three tested sands) range particles, however, were distinctly lower than that of the flow over the bed of 20/40 and 40/70 particle mesh size ranges. Clearly, the polymer fluid flow over the 30/50 mesh size sands presents a "drag reduction effect". We don't have any clear explanation of what causes the "drag reduction effect" in this case.

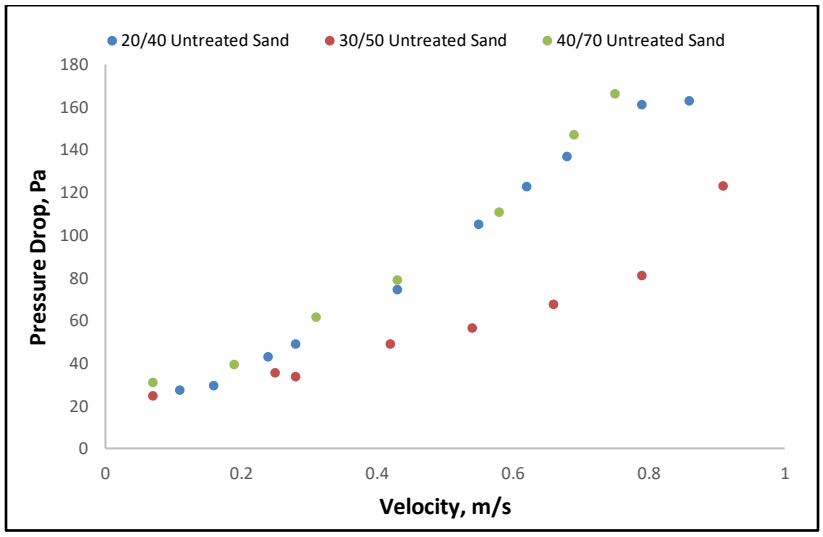

Figure 4-7 Frictional pressure drop measured for the flow of polymer fluid over the untreated sand bed of 3 different particle size ranges.

4.4.2. Turbulent Flow Characteristics of Polymer Fluid Flow over the Untreated Sand Bed

We have compared turbulent flow characteristics of polymer fluid flow over the sand bed of three different particle sizes using PIV measurements conducted at 0.25 m/s superficial fluid velocity.

In all the turbulent flow characteristics plots (Fig. 4-8 to 4-10), the y-coordinate represents the vertical distance from the bed (in the direction perpendicular to the flow) and y=0 represents the sand bed-water interface.

Figure 4-8 summarizes the near wall velocity profiles (presented in terms of dimensionless units). The near wall velocity profile for the flow over the 40/70 mesh size untreated sand particles follow the universal law within the log-law region ($y^+ > 30$), indicating that flow is hydrodynamically smooth in this case. The near wall velocity profiles for the flow of polymer fluid over the 20/40 and 30/50 mesh size sand bed were shifted up from the universal log-law trend line, indicating that the drag reduction effect prevails in these two cases. The drag reduction effect was more significant for the polymer fluid flow over the 30/50 mesh size sand. These results are in line with the direct measurement of frictional pressure losses presented earlier, where the lowest pressure drop was observed for the flow of polymer fluid over the 30/50 mesh size sand bed.

Figure 4-9 presents comparison of the normalized Reynolds shear stress profiles for the polymer flow over the 20/40, 30/50 and 40/70 mesh size untreated sand bed at the superficial velocity of 0.25 m/s. Near wall Reynolds stress profiles for all three sands were very similar. Away from the wall, however, slightly different Reynold stresses were registered depending on the particle size. The highest Reynolds stress was observed for the flow over the 30/50 mesh size sand bed. The Reynolds stress for the flow over the 40/70 mesh size sand bed was the intermediate, and the lowest Reynolds stress was registered for the flow over the 20/40 mesh size sand bed.

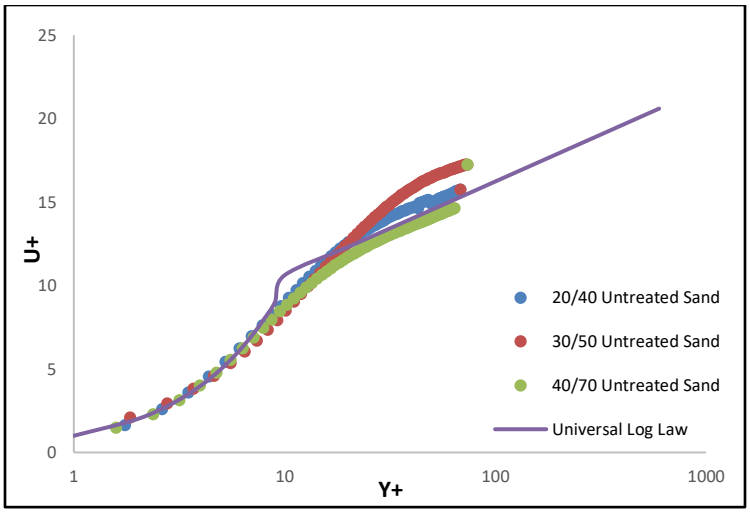

Figure 4-8 Dimensionless velocity profiles for flow of polymer fluid over untreated sand bed at the superficial velocity of 0.25 m/s.

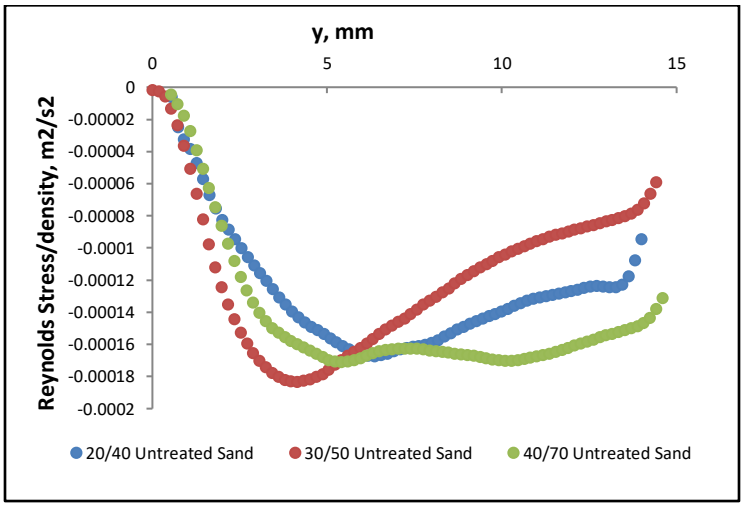

Figure 4-9 Reynolds stress profiles for flow of polymer fluid over untreated sand bed at the superficial velocity of 0.25 m/s.

Figures 4-10 shows the axial turbulence intensity profiles (also called the normal Reynolds stress) for the polymer fluid flow over the sand beds with three different mesh sizes of untreated sands at the superficial velocity of 0.25 m/s. There is no notable difference in the recorded axial turbulence intensity profiles in this case.

The radial component of turbulence intensity, v_{rms}, is particularly important in terms of solid transport and solid suspension capability of a fluid. Kelessidis and Bandelis [14] referring to the work of Davies [15] discussed the eddy fluctuation force, which is essential in keeping particles in suspension in turbulent flow. Davies [15] has shown that the eddy fluctuation force is proportional to radial velocity fluctuations. A higher level of radial velocity fluctuation results in a higher eddy fluctuation force. Figure 4-11 presents a comparison of the radial turbulent intensity profiles for the polymer fluid flow over the untreated sand beds of 3 different particle size ranges at the superficial liquid velocity of 0.25 m/s. The lowest radial turbulent intensity was registered for the flow over the sand bed with particles of 30/50 mesh size range, which indicates that for the flow over 30/50 mesh size sands turbulent eddies are in a more stable state (i.e. lower turbulence energy level). If the eddies are in a more stable state, this would reduce the frictional pressure losses due to decreased turbulent energy and momentum transfer in the radial direction. These results are in line with observation of lowest pressure drop for the flow over the 30/50 mesh size sand bed.

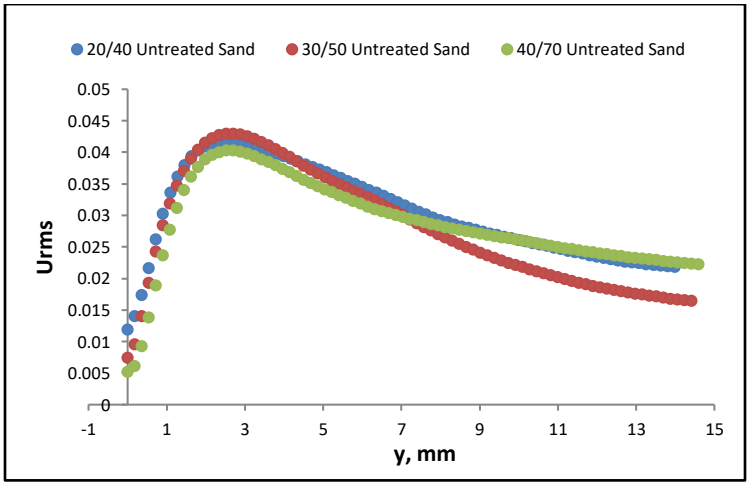

Figure 4-10 Axial turbulence intensity profiles for flow of polymer fluid over untreated sand bed at the superficial velocity of 0.25 m/s.

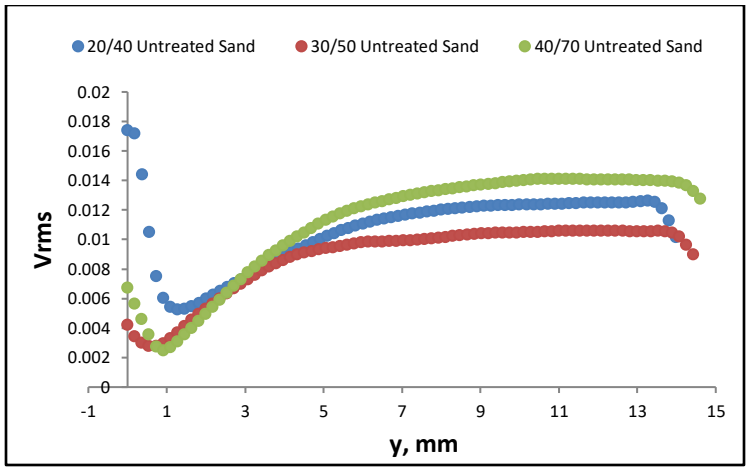

Figure 4-11 The radial turbulence intensity profile for the flow of polymer fluid over the untreated sand bed at the subcritical velocity of 0.25 m/s.

The frictional velocity is generally determined by analysing the near wall velocity data obtained from PIV measurements [9]. It is directly related to the interfacial bed shear stress (Eq.4-5). The interfacial bed shear stress is also an indirect measure of the total frictional pressure losses in the system. Therefore, the measured frictional pressure losses and the PIV derived frictional velocities are expected to correlate well with each other. The variations of the frictional velocities with sand particle size (as shown in Fig.4-12) are very much in line with that of the measured frictional pressure drop (shown in Table 4-2).

The lowest frictional pressure drop at the superficial velocity of 0.25 m/s was measured for the flow over the 30/50 mesh size untreated sand bed. Similarly, the lowest frictional velocity value was derived from the analyses of the near wall velocity data obtained from PIV measurements during the polymer fluid flow over the 30/50 mesh size sand bed. The highest frictional pressure drop was measured for the flow over the 40/70 mesh size untreated sand bed. The highest frictional velocity value was derived from the analyses of the near wall velocity data obtained by PIV measurements during the flow of polymer fluid over the 40/70 mesh size sand bed.

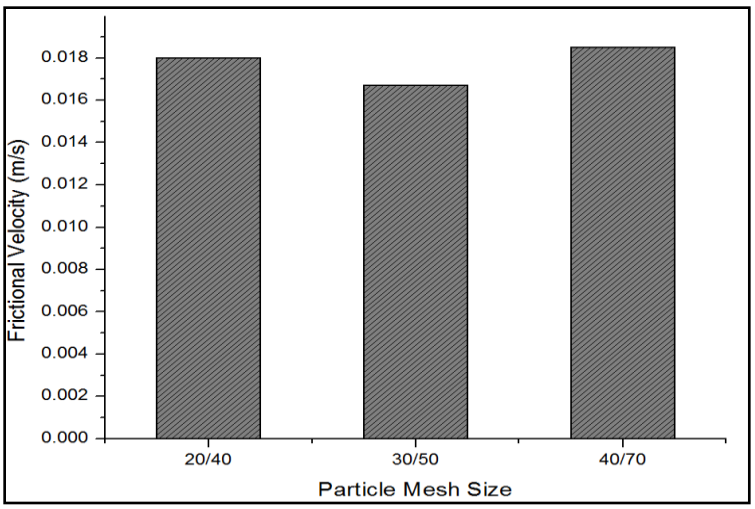

Figure 4-12 Friction velocity vs particle mesh size for experiments conducted at sub-critical velocity of 0.25 m/s.

4.4.3. Critical Velocity Required for the Particle Removal from Untreated Sand Bed

Table 4-3 and Fig.4-13 summarizes the critical velocities required for the onset of the particle removal from untreated sand bed using polymer fluid. The lowest critical velocity was observed for the flow over the sand bed with the largest particle size, i.e., 20/40 mesh. For the flow over the sand bed with 30/50 and 40/70 mesh size particles, the critical velocity decreased with decreasing sand size.

Table 4-3 Results of untreated sand bed erosion experiments using polymer fluid.

Sand Mesh Size	Bed Height (cm)	Area Open for Flow (cm^2)	Critical Flow Rate (lpm)	Critical Velocity (m/s)	Critical Pressure Drop (Pa)
20/40	3.65	45.8	183.5	0.67	122.61
30/50	3.1	50.6	271.6	0.895	123.12
40/70	3.31	48.9	218.3	0.744	166.2

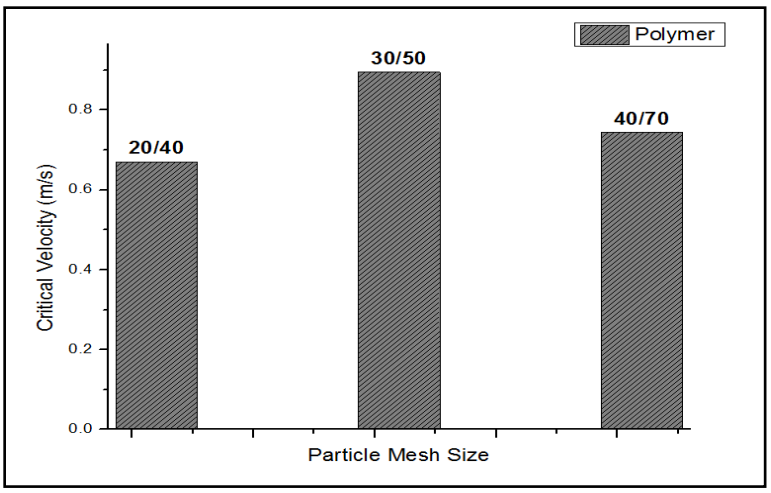

Figure 4-13 Critical velocity for the onset of the particle removal from untreated sand bed using polymer fluid.

The fluid drag and lift forces are the major forces responsible for the particle movement. However, it was shown that the drag forces are generally order of magnitude higher than the lift forces [16]. In our analyses of the particle movement, therefore, we will only consider the drag force as the main force responsible for the particle movement. In this study, we have determined the drag force exerted by the flowing fluid to sand particles at the onset of bed movement by using equation 4-10 [16].

$$F_D = \frac{1}{2}\rho A_p C_D u^2, \quad \text{..... (4-10)}$$

Where F_D is the drag force, ρ is the fluid density, u is the local instantaneous fluid velocity, A_p is the projected area of sand particles and C_D is the drag coefficient.

The drag coefficient, C_D, is generally given as a function of the particle Reynolds number, Re_p. The particle Reynolds number for pseudo plastic (power law) type fluids can be determined by using Eq.4-11. In this study, the correlations (Eqns. 12-14) suggested by Duan et al. [17] were used to determine C_D values.

$$Re_p = \frac{\rho u^{2-n} {d_p}^n}{K}. \quad \text{..... (4-11)}$$

$$C_D = \frac{24}{Re_p}(2-n),\ Re_p < 0.2(2^n). \quad \text{..... (4-12)}$$

$$C_D = \frac{37}{\left(\frac{Re_p}{2^n}\right)^{1.03}} + n\left[1 - \frac{20.9}{\left(\frac{Re_p}{2^n}\right)^{1.11}}\right],\ 0.2(2^n) < Re_p < 24(2^n). \quad \text{..... (4-13)}$$

$$C_D = \frac{37}{\left(\frac{Re_p}{2^n}\right)^{1.03}} + 0.25 + 0.36n,\ 0.2(2^n) < Re_p < 100(2^n). \quad \text{..... (4-14)}$$

Where Re_p is the particle Reynolds number, d_p is the particle diameter, K is the consistency index, n is the flow behaviour index, u is the local instantaneous flow velocity, ρ is fluid density and C_D is drag coefficient.

The drag force (Eq.4-10) is a direct function of the local instantaneous velocity, u. It was shown that the instantaneous local velocity (fluid velocity at the particle/fluid interface) could be significantly different than average fluid velocity [16]. We have used PIV measurements to determine the instantaneous local (near wall) velocity values. In order to calculate the drag force, we have used the largest particle size within a given particle mesh size range.

In our analyses of particle movement, we considered the buoyed weight of the particle, F_B (i.e., the difference between the force of gravity, F_g, and the buoyancy force, F_b) as the main force resisting the particle movement (i.e. neglect the friction forces and van der Vaals forces). The buoyed weight of the particle, F_B, can be estimated using Eq.4-15.

$$\boldsymbol{F}_B = \boldsymbol{F}_g - \boldsymbol{F}_b = \mathbf{1/6}\ \boldsymbol{\pi d_p^3 g}\ (\boldsymbol{\rho_s - \rho_f}) \quad \text{..... (4-15)}$$

Where d_p is the particle size, g is the gravitational acceleration, ρ_s is the solid density, ρ_f is the fluid density.

The net force, F_N, acting on the particle can be approximated by the difference between F_D and F_B. Hence, the particle movement can be initiated when the net force becomes greater than zero.

A summary of the forces acting on a single untreated sand particle at critical velocity is provided in Table-4. For 40/70 mesh size of untreated sand particles the drag force could not be calculated due to lack of PIV data at the critical velocity.

Table 4-4 Forces acting on a single untreated sand particle at critical velocity

Particle Mesh Size	Particle Size	Critical Velocity	Near Bed Velocity	Drag Coefficient	Drag Force	Buoyed Weight	Net Force
	Micron	m/s	m/s		N	N	N
20/40	840	0.67	0.03824	5.3312128	4.10E-06	4.05E-06	4.35E-08
30/50	590	0.895	0.036459	7.06577566	2.57E-06	1.40E-06	1.16E-06
40/70	420	0.744	-	-	-	5.07E-07	-

Results shown in Table 4-4 indicate that although the critical velocity (calculated using the average flow rate measured at the onset of the particle removal from the bed) for 20/40 untreated sand is lower than that of the 30/50 mesh size sand, the near wall velocity (measured by using PIV) for 20/40 mesh size sand was actually higher than that of the case with 30/50 mesh size. The drag force (Eqn.10) acting on the particle is controlled by the near wall velocity, not by the average velocity. Although the critical velocity was the lowest for onset of the 20/40 mesh size particle movement, the corresponding drag force was the highest in this case. The non-zero net force (= Drag Force-Buoyed Weight) also confirms that the drag force was sufficiently high to mobilize the 20/40 particles at this lower critical velocity (0.67 m/s).

We also calculated forces acting on a single sand particle at sub-critical velocities and the results were summarized in Table 4-5. The net forces were negative in all cases, confirming that sand particles could not be mobilized at these sub-critical velocities.

Table 4-5 Forces acting on a single untreated sand particle at sub-critical velocity

Particle Mesh Size	Particle Size	Superficial Velocity	Near Bed Velocity	Drag Coefficient	Drag Force	Buoyed Weight	Net Force
	Micron	m/s	m/s		N	N	N
20/40	840	0.6	0.02387	7.955	2.51E-06	4.05E-06	-1.54E-06
30/50	590	0.778	0.01358	18.094	9.12E-07	1.40E-06	-4.92E-07
40/70	420	0.436	0.01026	31.578	4.60E-07	5.07E-07	-4.64E-08

As shown by the results presented in Table 4-5, the 30/50 mesh size sands were not mobilized at the superficial velocity of 0.778 m/s, which was actually higher than the critical velocity observed for 20/40 mesh size sands (0.67 m/s). When we compared the near bed velocities for these two cases, we saw that although critical velocity for 20/40 mesh size sand (0.67 m/s) was lower than the sub-critical velocity (0.778 m/s) for 30/50 mesh size sand, the near bed velocity measured in the former case (0.03824 m/s) was higher than that of the latter (0.01358 m/s). These results also confirm that near bed velocities (controlling the drag forces) very much depend on the relative size and position of the sand particle with respect to viscous boundary layer thickness.

The lowest critical velocity observed for 20/40 mesh size particles can be explained by the effective drag forces acting on the particles, which may vary significantly depending on the relative positions of this size particles (420-840 micron) with respect to viscous boundary layer thickness, δ_v (Eqn. 4-16).

$$\delta_v = \frac{5\mu_w}{\rho u_\tau} \quad \text{(4-16)}$$

Where δ_v is the boundary layer thickness, μ_w is the fluid viscosity at the wall, ρ is the fluid density, and u_τ is the friction velocity. Viscous sublayer thickness estimated for the polymer fluid flow over the three different mesh size untreated sand beds at the corresponding critical flow rates are presented in Table 4-6.

Table 4-6 Viscous sublayer thickness for polymer fluid flow over the untreated sand bed at their corresponding critical flow rates

	20/40 Untreated Sand	30/50 Untreated Sand	40/70 Untreated Sand
Particle Mesh Size (micron)	840 - 420	590 - 297	420 – 210
Viscous Sublayer Thickness (micron)	765	811	797

The estimated boundary layer thickness at the critical velocity of 20/40 mesh size particles (0.67 m/s) was 765 microns. It was smaller than the largest particle size in the group (i.e. 840 micron), therefore, we may expect that some of the particles within 20/40 mesh size range sticks out of the boundary layer and, hence, could be exposed to higher local velocities (as opposed the ones positioned completely within the boundary layer). This was exactly what we observed as shown by the PIV data measured near the wall (Table 4-4). As a result, higher effective drag forces will be active on these particles, which can mobilize the particles at lower average superficial velocities (Table 4-4).

Note that the estimated viscous boundary layer thickness (i.e., 765 micron) at the critical velocity of 20/40 mesh size particles (i.e., 0.67 m/s), was higher than the largest size particles within the group of 30/50 mesh size (i.e., 590 micron) and 40/70 mesh size (i.e., 420 micron) particles. That means that 30/50 and 40/70 mesh size particles were all located within the viscous boundary layer at the critical velocity, which was able to erode 20/40 mesh size sand bed. Therefore, the effective velocity (and the drag force) acting on 30/50 and 40/70 mesh size particles might not be high enough to mobilize these particles at this velocity.

Figure 4-14 presents the critical pressure drop values measured at the onset of the particle removal from untreated sand beds of different mesh size particles. The highest critical pressure drop was measured for the flow over the 40/70 mesh size sand bed. Critical pressure drop values for the flow over the 20/40 and 30/50 mesh size sand beds were similar. This was rather unexpected result. However, the frictional velocity values for 20/40 and 30/50 mesh size sand were also very similar as shown in Fig.4-15. Frictional velocity values were directly related to frictional pressure loss in the system, however, they were estimated using the analyses of the PIV data (independent from direct pressure loss measurement). The fact that both data from direct pressure loss measurement and the PIV analyses show similar trend indicates that data quality in this case was not an issue.

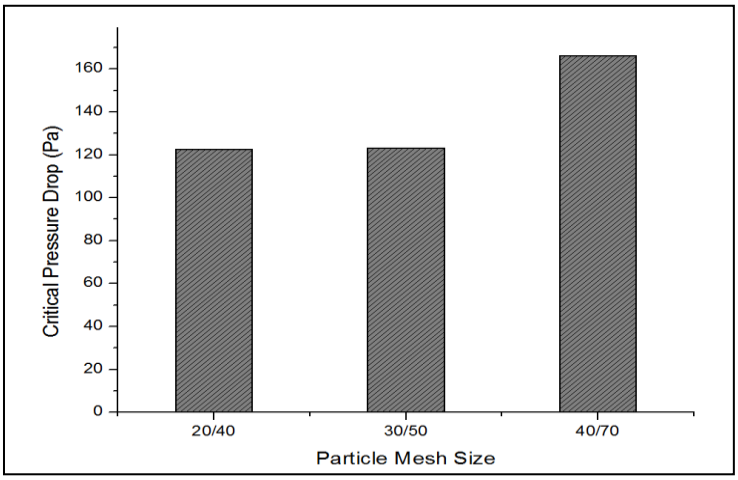

Figure 4-14 Critical velocity for the onset of the particle removal from untreated sand bed using polymer fluid.

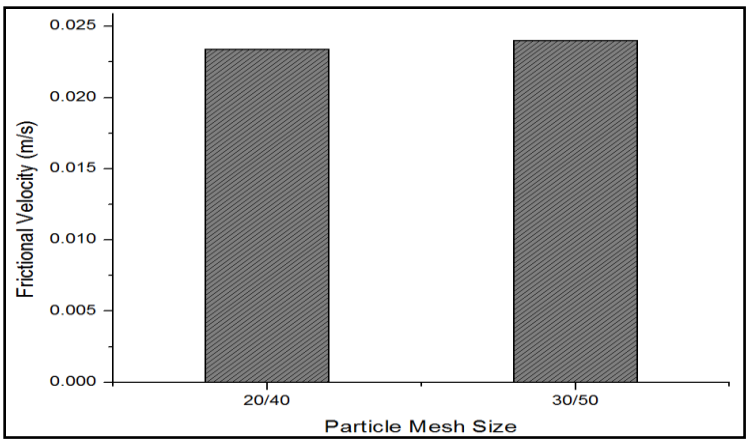

Figure 4-15 Friction velocity vs particle mesh size for experiments conducted at the critical velocity.

4.5. RESULTS AND DISCUSSIONS – BED EROSION TESTS WITH TREATED SANDS

4.5.1. Frictional Pressure Drops Measured for the Polymer Fluid Flow over the Treated Sand Bed

Table 4-7 summarizes the frictional pressure losses measured for the flow of polymer fluid over the treated sand beds of 20/40, 30/50 and 40/70 mesh size particles at a subcritical velocity of 0.25 m/s. The normalized frictional pressure losses for treated sand particles were calculated by multiplying equivalent dimeter by frictional pressure loss.

Table 4-7 Frictional Pressure Drop vs Mesh Size of Treated Sand Measured at 0.25 m/s.

Sand Particle Mesh Size	Bed Height (cm)	Flow Rate (lpm)	Frictional Pressure Loss (Pa)	Equivalent Diameter (m)	Normalized Frictional Pressure loss (Pa-m)
20/40	3.31	74.5	43	0.0789	3.39
30/50	3.22	76.5	60.27	0.0796	4.80
40/70	3.31	74.6	40.38	0.0789	3.19

Pressure drop values recorded at various subcritical and critical flow rates are summarized in Figure 4-16. For the flow over the 20/40 and 40/70 mesh size treated sand beds pressure drop values did not show significant

difference. Pressure drop values for the flow over the 30/50 mesh size treated sand bed, however, were notably higher than that of the flow over the 20/40 and 40/70 mesh size treated sand beds.

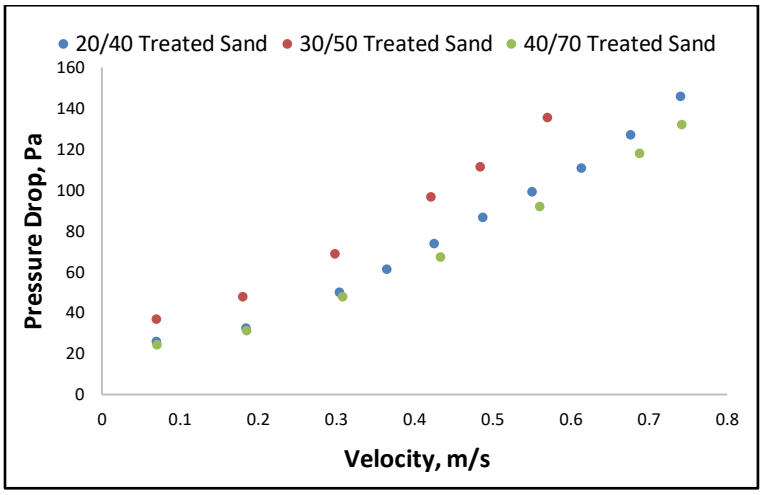

Figure 4-16 Frictional pressure drop for the flow of polymer fluid over the treated sand bed.

4.5.2. Turbulent Flow Characteristics of Polymer Fluid Flow over the Treated Sand Bed.

We have compared turbulent flow characteristics of polymer fluid flow over the treated sand bed of three different particle sizes using PIV measurements conducted at 0.25 m/s superficial fluid velocity.

In all the turbulent flow characteristics plots (Figs. 4-17 to 4-20), the y-coordinate represents the vertical distance from the bed (in the direction perpendicular to the flow) and y=0 represents the sand bed-water interface.

Figure 4-17 presents the near wall velocity profiles for the flow of the dilute polymer solution over the sand beds of three different particle size ranges of treated sand particles at the superficial velocity of 0.25 m/s. As seen in Figure 4-17, the dimensionless velocity profiles for the flow of polymer over the sand beds of 20/40 and 30/50 mesh sizes of treated sand particles follow the universal law within the log-law region ($y^+ > 30$), indicating that the flow in all these cases are hydrodynamically smooth. However, for 40/70 mesh size of treated sand particles there is a strong upshift in the dimensionless velocity profile showing the drag reduction effect by the flow of

dilute polymer solution over the sand bed of 40/70 mesh size range. This also correlates well with the lowest frictional pressure loss measured for the flow over 40/70 mesh size sand bed.

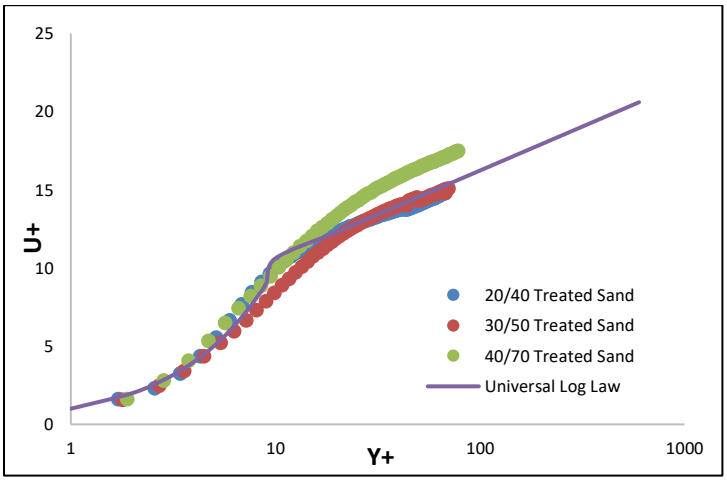

Figure 4-17 Dimensionless velocity profiles for polymer fluid flow over the treated sand bed at the superficial velocity of 0.25 m/s.

Figure 4-18 presents comparison of the normalized Reynolds stress profiles for the flow of polymer fluid over the treated sand beds of three different particle size ranges at the superficial velocity of 0.25 m/s. Reynolds stress profiles for 20/40 and 40/70 mesh size treated sands were similar, but they were lower than that of the one observed from 30/50 mesh size of treated sand bed. Lower Reynolds stress indicates less energy and momentum transfer from the fluid to sand bed. Therefore, lower levels of Reynolds stress are in line with the lower pressure drop values observed in this case (i.e. pressure drop for the flow over 20/40 and 40/70 mesh size particles were lower than that of 30/50 mesh size particles).

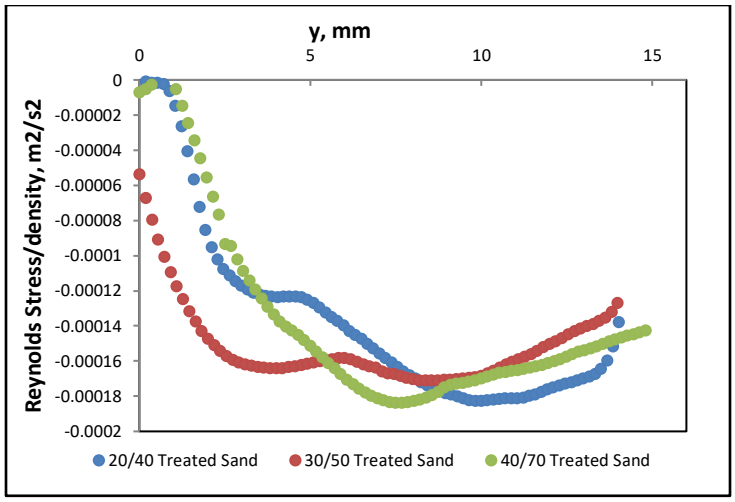

Figure 4-18 Reynolds stress profiles for polymer fluid flow over the treated sand bed at the superficial velocity of 0.25 m/s.

Figure 4-19 shows the comparison of the axial turbulence intensity profiles observed during the flow of polymer over the sand beds of three different particle size range for treated sand particles at the superficial velocity of 0.25 m/s. The axial turbulence intensity is critical in sand particle removal because it represents the level of velocity fluctuations. Recent studies have indicated the significance of turbulent velocity fluctuations in particle removal [16, 18]. The axial turbulence intensities were similar for 20/40 and 40/70 mesh sizes of treated sand particles (Fig.4-19), but it was higher at the near wall region of 30/50 mesh size sand bed. Higher axial turbulence intensity recorded for the flow over the 30/50 mesh size treated sand bed also indicates that the higher turbulent energy was spent in this case (also correlates well with the higher frictional pressure losses observed for 30/50 mesh size sand).

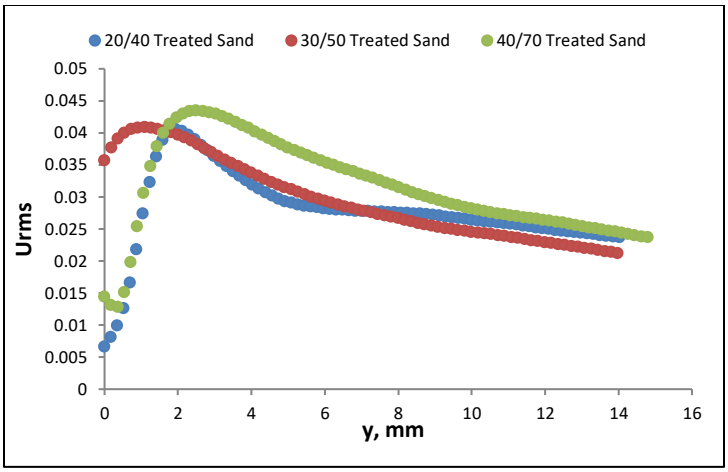

Figure 4-19 Axial turbulence intensity profiles for polymer fluid flow over the treated sand bed at the superficial velocity of 0.25 m/s.

The radial component of turbulence intensity, v_{rms}, is of particular importance in solid transport and solid suspension. A higher level of radial velocity fluctuation results in higher eddy fluctuation forces. Similar radial turbulence intensity profiles were observed with all three treated sands (Fig.4-20). The radial turbulence intensity near the wall of 40/70 mesh size sand bed was slightly higher than that of other two sand size bed.

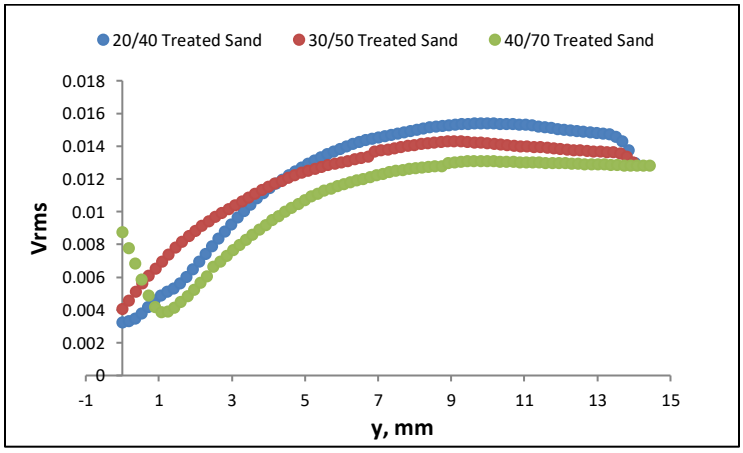

Figure 4-20 Radial turbulence intensity profiles for polymer fluid flow over the treated sand bed at the superficial velocity of 0.25 m/s.

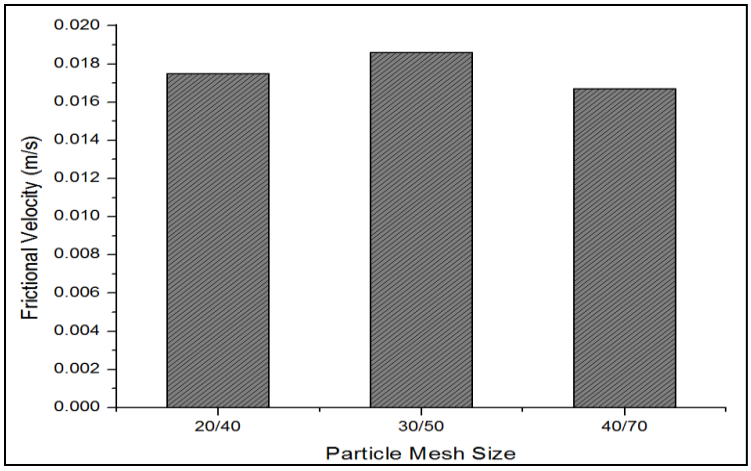

Figure 4-21 Friction velocity vs treated sand particle mesh size for experiments conducted at sub-critical velocity of 0.25 m/s.

Frictional velocities determined from PIV measurements at the superficial velocity of 0.25 m/s are shown in Figure 4-21. The frictional velocity was the highest for the flow over the 30/50 mesh size treated sand bed. The frictional velocities for the flow over the 20/40 and 40/70 mesh size treated sand beds were almost the same. Similarly, the measured pressure drop at the superficial velocity of 0.25 m/s was the highest for the flow over the 30/50 mesh size treated sand particles. The measured pressure drops for the flow over 20/40 and 40/70 mesh size treated sand beds were more or less the same. Thus, the results from the frictional velocities obtained from PIV data and the directly measured frictional pressure drops were in line.

4.5.3. Critical Velocities for Particle Removal from the Treated Sand Beds

Critical velocities for the particle removal from three different size treated sand bed are summarized in Table-8 and plotted in Fig.4-22. The lowest critical velocity was observed for the particle removal from 30/50 mesh size sand bed. The highest critical velocity rate was recorded for the particle removal from 40/70 mesh size sand bed, which was the smallest among tested three sands.

Table 4-8 Results of treated sand bed erosion experiments using polymer fluid.

Sand Mesh Size	Bed Height (cm)	Area Open for Flow (cm^2)	Critical Flow Rate (lpm)	Critical Velocity (m/s)	Critical Pressure Drop (Pa)
20/40	3.31	48.9	198.2	0.68	122.61
30/50	3.22	49.8	170	0.57	135.55
40/70	3.31	48.9	217.6	0.74	132.1

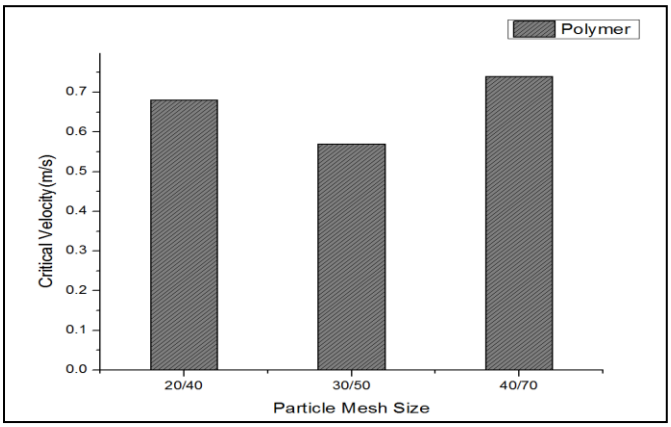

Figure 4-22 Critical velocity for the onset of the particle removal from the treated sand bed using polymer fluid.

A summary of the forces acting on a single treated sand particle at a critical velocity is provided in Table 4-9.

Table 4-9 Forces acting on a single treated sand particle at critical velocity

Particle Mesh Size	Particle Size	Critical Velocity	Near Bed Velocity	Drag Coefficient	Drag Force	Buoyed Weight	Net Force
	Micron	m/s	m/s		N	N	N
20/40	840	0.68	0.040745	4.932467725	4.54E-06	4.05E-06	4.84E-07
30/50	590	0.57	0.036241	7.104524707	2.55E-06	1.40E-06	1.15E-06
40/70	420	0.74	0.020999	15.58833985	9.52E-07	5.07E-07	4.46E-07

Results shown in Table 4-9 indicate that although the critical velocity (0.57 m/s) for 30/50 untreated sand is lower than that of the 40/70 mesh size sand, the near wall velocity (measured by using PIV) for 30/50 mesh size sand was actually higher than that of the case with 40/70 mesh size. The drag force (Eqn.4-10) acting on the particle is controlled by the near wall velocity, not by the average velocity. Therefore, although the critical velocity was the lowest for onset of the 30/50 mesh size particle movement, the corresponding drag force was not the lowest in this case. The non-zero net force (= Drag Force-Buoyed Weight) also confirms that the drag force was sufficiently high to mobilize the 30/50 particles at this lower critical velocity (0.57 m/s).

We also calculated forces acting on a single treated sand particle at sub-critical velocities and the results were summarized in Table 4-10. The net forces were negative in all cases, confirming that sand particles could not be mobilized at these sub-critical velocities.

Table 4-10 Forces acting on a single treated sand particle at sub-critical velocity

Particle Mesh Size	Particle Size	Superficial Velocity	Near Bed Velocity	Drag Coefficient	Drag Force	Buoyed Weight	Net Force
	Micron	m/s	m/s		N	N	N
20/40	840	0.625	0.025212	7.563518161	2.66E-06	4.05E-06	-1.39E-06
30/50	590	0.483	0.014086	17.45720186	9.47E-07	1.40E-06	-4.58E-07
40/70	420	0.56	0.009973	32.47307113	4.47E-07	5.07E-07	-5.93E-08

As shown by the results presented in Table 4-10, the 40/70 mesh size sands were not mobilized at the superficial velocity of 0.56 m/s, which was actually very close to the critical velocity observed for 30/50 mesh size sands (0.57 m/s). When we compared the near bed velocities for these two cases, we saw that although critical velocity for 30/50 mesh size sand (0.57 m/s) was very close to the sub-critical velocity (0.56 m/s) for 40/70 mesh size sand, the near bed velocity measured in the former case (0.01408 m/s) was higher than that of the latter

(0.009973 m/s). These results also confirm that near bed velocities (controlling the drag forces) very much depend on the relative size and position of the sand particle with respect to viscous boundary layer thickness.

It is expected that the surface characteristic (i.e. treated vs. untreated sand) of the sand, absolute value of the particle size and the relative position of particle with respect to viscous sublayer thickness (i.e., how the particle size compares with the viscous sublayer thickness) all affect the critical velocity. Viscous sublayer thickness estimated (Eqn. 4-15) for the polymer fluid flow over the three different mesh size treated sand beds at the corresponding critical flow rates are shown in Table 4-11. It appears that the boundary layer thickness did not vary significantly for flow over the sand bed of three different particle size range at their corresponding critical flow rates.

Table 4-11 Viscous sublayer thickness for polymer fluid flow over the treated sand bed at critical flow rates

	20/40 Treated Sand	30/50 Treated Sand	40/70 Treated Sand
Particle Size (micron)	840 - 420	590 - 297	420 – 210
Viscous Sublayer Thickness (micron)	819	755	785

The estimated boundary layer thickness at the (lowest) critical velocity recorded for 30/50 mesh size particles (0.57 m/s) was 755 microns. It was smaller than the largest particle size in the group 20/40 mesh size sand (i.e. 840 micron),therefore, we may expect that some of the particles within 20/40 mesh size range sticks out of the boundary layer and, hence, could be exposed to higher local velocities (as opposed the ones positioned completely within the boundary layer) but the effective drag force at this velocity was not sufficiently high to start the bed erosion. Note that at 0.57 m/s average fluid velocity boundary layer thickness (755 microns) was higher than the largest particle size within the 30/50 mesh size group (590 micron). So, theoretically all the particles in 30/50

mesh size range were expected to be submerged into the boundary layer at the critical velocity, yet the drag forces were high enough to initiate the bed erosion.

The largest size particle (420 micron) within the 40/70 mesh size range was smaller than the boundary layer thickness measured at the lowest critical velocity (755 micron @ 0.57 m/s). It was expected that particles in 40/70 mesh size range would be exposed to lower near wall velocities (Table 4-9). Consequently, the drag forces would be on the low side and most likely would not be high enough to initiate the bed erosion for this size of the treated sand bed.

It seemed like there was no clear-cut correlation between critical velocity and particle size in this case. We do not have a clear explanation of why the 30/50 mesh size sand particles were mobilized at the lowest critical velocity. During the bed erosion experiments, it was commonly observed that air bubbles were attached to the sand particles. It is possible that attached air bubbles to sand particles make the effective sand size bigger for 30/50 mesh size sand such that the sand particles stick out of the viscous boundary layer and, hence, they are exposed to higher local velocities (Table 4-9).

Figure 4-23 shows the critical frictional pressure drops (i.e. frictional pressure drops measured at the onset of the bed erosion) as a function of the treated sand particle mesh size. The lowest critical pressure drop was recorded for the flow over the 20/40 mesh size treated sand bed. The critical pressure drop data measured for the erosion of 30/50 and 40/70 mesh size treated sand bed were almost the same.

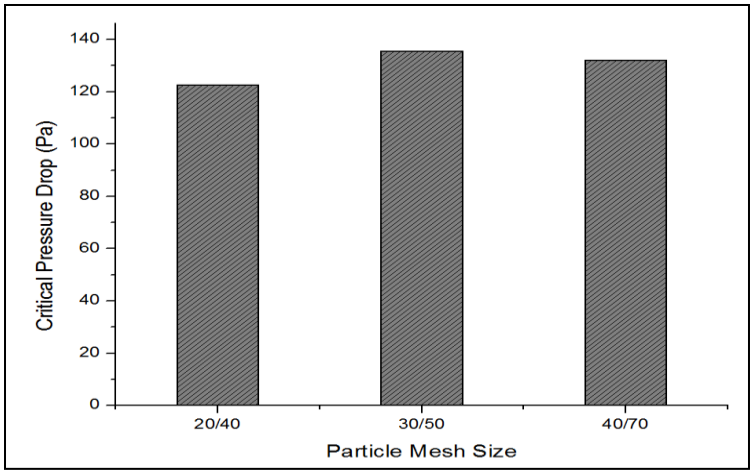

Figure 4-23 Critical pressure drop versus the treated sand particle mesh size

Figure 4-24 shows the frictional velocities obtained from PIV measurements at the onset of the particle removal from 20/40, 30/50 and 40/70 mesh size treated sand bed. The lowest frictional velocity value was recorded for 20/40 sand mesh size sand bed. The frictional velocity values for 30/50 and 40/70 treated sand bed were almost the same. The frictional velocity values and the measured frictional pressure drops correlate well at critical velocities.

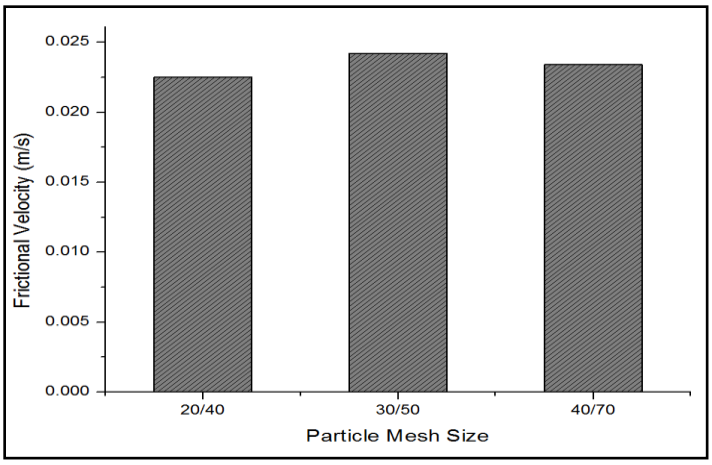

Figure 4-24 Friction velocity vs treated sand particle mesh size for the experiments conducted at the critical velocity.

4.6. RESULTS AND DISCUSSIONS – COMPARISON OF THE RESULTS FOR THE FLOW OF POLYMER FLUID OVER THE TREATED AND UNTREATED SAND BED

4.6.1. Comparison of Frictional Pressure Drops Measured for the Polymer Fluid Flow over the Treated and Untreated Sand Bed

For polymer fluid flow over the 20/40 mesh size untreated and treated sand beds, there was no notable difference in the measured frictional pressure drops (Fig. 4-25).

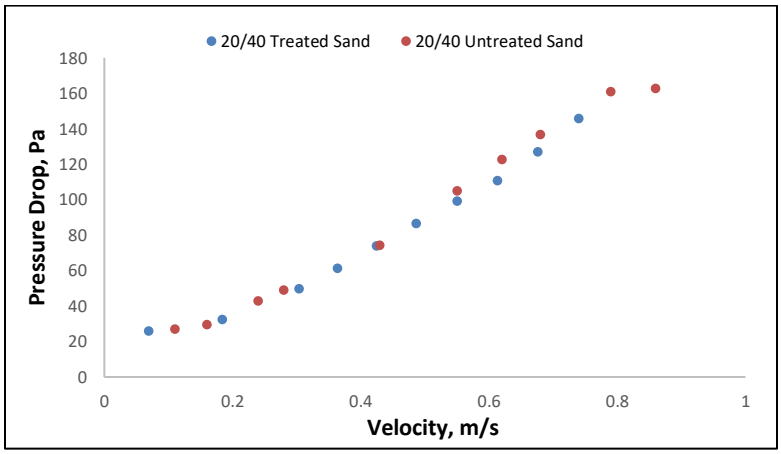

Figure 4-25 Comparison of frictional pressure drop data for the polymer fluid flow over the 20/40 mesh size treated and untreated sand beds.

Frictional pressure drop for the flow of polymer fluid over the 30/50 mesh size treated sand was significantly higher than that of the untreated sand (Fig.4-26). The difference between the frictional pressure drop for the flow over the 30/50 mesh size treated and untreated sand bed increased with the increasing fluid velocity.

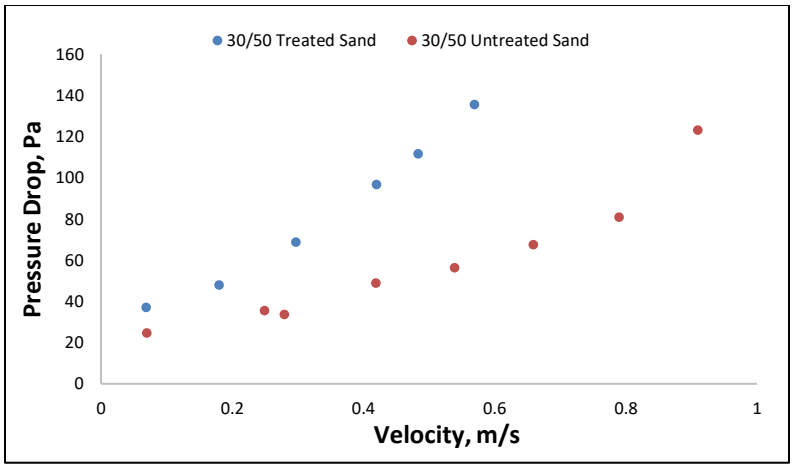

Figure 4-26 Comparison of frictional pressure drop data for the polymer fluid flow over the 30/50 mesh size treated and untreated sand beds.

For flow over the 40/70 mesh size sand bed, the frictional pressure over the untreated sand bed was slightly higher than that of the treated sand bed (Fig.4-27).

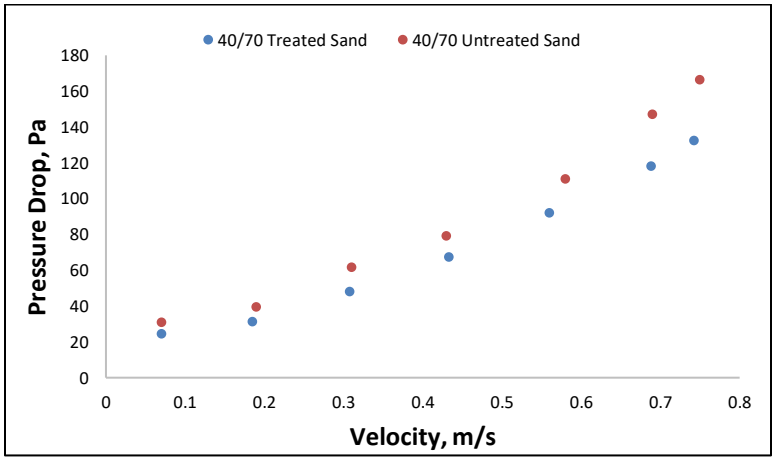

Figure 4-27 Comparison of frictional pressure drop data for the polymer fluid flow over the 40/70 mesh size treated and untreated sand beds.

It appears that the measured frictional pressure drop trend varies depending on the particle size range. However, it was not clear at this point why the frictional pressure drop values were so distinctly different for

intermediate size (30/50 mesh size) particles, while we did not see any significant difference for the largest (20/40 mesh size) and the smallest size (40/70) particles tested.

4.6.2. Comparison of the Turbulence Characteristics of Polymer Fluid Flow over the Treated and Untreated Sand Bed

We have compared the turbulence characteristics of polymer fluid flow over the treated and untreated sand bed at the same sub-critical velocity of 0.25 m/s. The near wall velocity profiles of the polymer fluid flow over the treated and untreated 20/40 mesh size sand bed are shown in Fig.4-28.

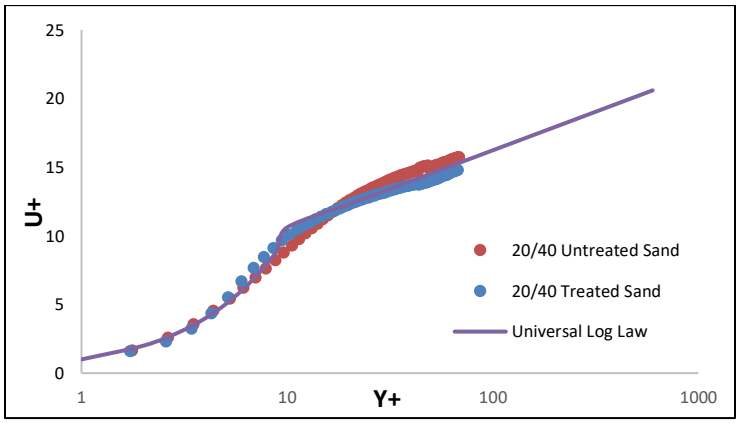

Figure 4-28 Dimensionless near wall velocity profiles for the flow of polymer fluid over the 20/40 mesh size treated and untreated sand bed at the superficial velocity of 0.25 m/s.

The near wall velocity profile for the flow over the both treated and untreated sand bed followed the universal log law trend, indicating that the flow was hydrodynamically smooth over 20/40 mesh size treated and untreated sand beds. These results are in line with the pressure loss measurements where there was no significant difference between the pressure drop for the flow over the 20/40 mesh size treated and untreated sand bed observed (Fig.4-25).

The near wall velocity profiles of the polymer fluid flow over the 30/50 mesh size treated and untreated sand beds are shown in Fig.4-29.

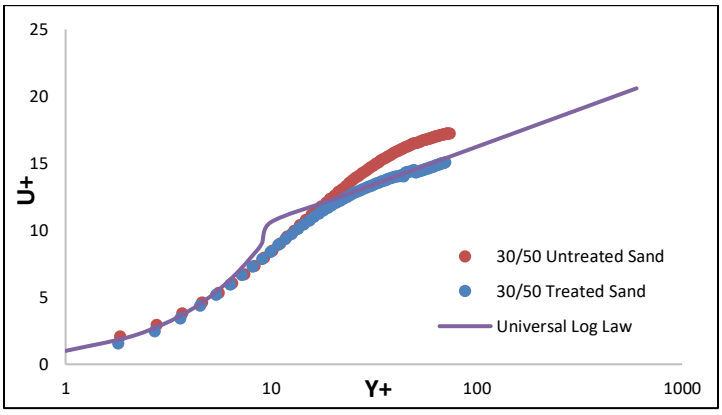

Figure 4-29 Dimensionless near wall velocity profiles for the flow of polymer fluid over the 30/50 mesh size treated and untreated sand bed at the superficial velocity of 0.25 m/s.

The near wall velocity profile for the flow over the 30/50 mesh size treated sand bed follows the universal log law trend, indicating that the flow was hydrodynamically smooth in this case. The near wall velocity profile for the polymer fluid flow over the 30/50 mesh size untreated sand bed, however, shifted up from the log law trend, indicating the presence of drag reduction effect in this case. These results are also in line with the pressure loss measurements where the recorded frictional pressure drop for the flow over the 30/50 mesh size untreated sand bed was lower than that of the case with treated sand bed (Fig. 4-26).

The near wall velocity profiles of the polymer fluid flow over 40/70 mesh size treated and untreated sand beds are shown in Fig.30.

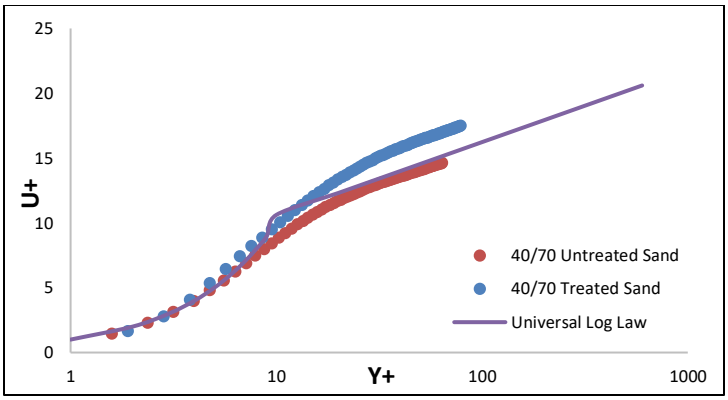

Figure 4-30 Dimensionless near wall velocity profiles for the flow of polymer fluid over the 40/70 mesh size treated and untreated sand bed at the superficial velocity of 0.25 m/s.

The near wall velocity profile for the flow over the 40/70 mesh size untreated sand bed followed the universal log law trend, indicating that the flow was hydrodynamically smooth in this case. The near wall velocity profile for the polymer fluid flow over the 40/70 mesh size treated sand bed, however, shifted up from the log law trend, indicating the presence of drag reduction effect in this case. These results are also in line with the pressure loss measurements where the recorded frictional pressure drop for the flow over the 40/70 mesh size treated sand bed was slightly lower than that of the case with untreated sand bed (Fig. 4-27).

The results shown in Figs. 4-28 to 4-30 indicate that the near wall velocity profile varies depending on the particle size and the surface characteristics. However, there was no general trend on how the surface characteristics would affect the near wall velocity trend. In one case surface treated sand created drag reduction effect (40/70 mesh size). In another case, the surface treated sand bed resulted hydraulically smooth flow (30/50 mesh size and 20/40 mesh size). We do not have a clear explanation of this complex behaviour. One possible reason would be that the relative size of the sand particle with respect to viscous sublayer thickness. Depending on whether they are fully immersed in the boundary layer or partially stick out, sand particles might have been exposed to different near wall velocities (Tables 4-4 and 4-9).

The Reynolds stress is a measure of how much momentum is transferred from fluid to sand bed under certain flow conditions (i.e. fluid velocity, particle size and surface characteristics, geometry of the flow conduit, bed height thickness, etc.). Lower Reynolds stress generally translates into a lower turbulent energy dissipated under that particular flow conditions. Therefore, it is expected that the Reynolds stress values obtained from PIV data analyses should correlate well with the results from direct frictional pressure loss measurements.

Figure 4-31 presents the Reynolds stress profiles for the polymer fluid flow over the 20/40 mesh size untreated and treated sand beds. The Reynolds stress profiles were more or less the same in this case. These results are also in line with the frictional pressure loss measurements in this case. As shown in Fig.4-25, there was no significant difference between the frictional pressure losses measured for the flow over the 20/40 mesh size treated and untreated sand beds.

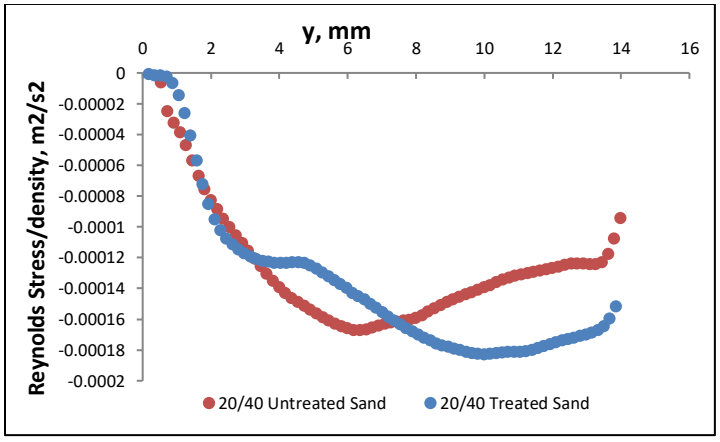

Figure 4-31 Reynolds stress profiles for the flow of polymer fluid over the 20/40 mesh size treated and untreated sand bed at the superficial velocity of 0.25 m/s.

The Reynolds stress profiles for the polymer fluid flow over the 30/50 mesh size untreated and treated sand beds are shown in Fig. 4-32. The Reynolds stress profile for the flow over the 30/50 mesh size untreated sand bed was significantly lower than that of the treated sand bed. These results also correlate well with the measured

frictional pressure losses, where the observed frictional pressure losses for the flow over the 30/50 mesh size untreated sand bed were significantly lower than that of the treated sand bed (Fig.4-26).

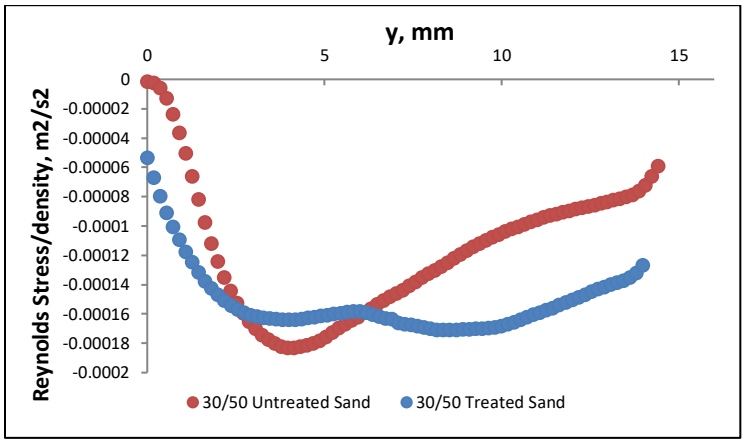

Figure 4-32 Reynolds stress profile for the flow of polymer fluid over the 30/50 mesh size treated and untreated sand bed at the superficial velocity of 0.25 m/s.

Figure 4-33 presents the Reynolds stress profiles registered for the flow over the 40/70 mesh size treated and untreated sand beds. The Reynolds stress profiles for the flow over the treated and untreated sand beds were very similar in this case. These results were also supported by frictional pressure loss measurements, where the recorded pressure loss values were not significantly different from each other for the flow over the 40/70 mesh size treated and untreated sand bed (Fig.4-27).

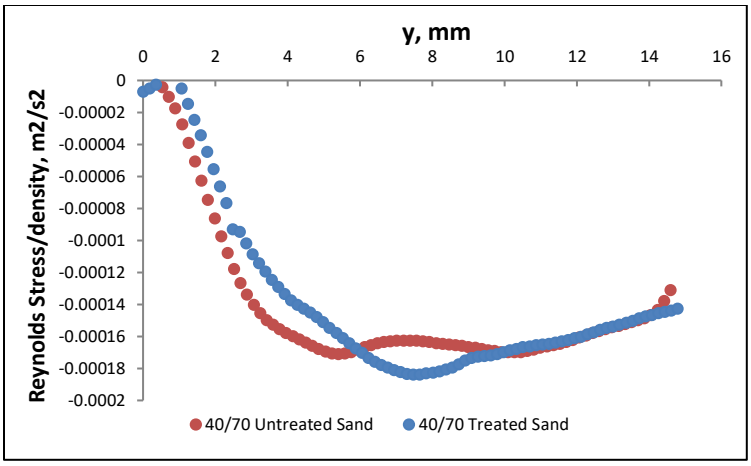

Figure 4-33 Reynolds stress profiles for the flow of polymer fluid over the 40/70 mesh size treated and untreated sand bed at the superficial velocity of 0.25 m/s.

Figures 4-34 to 4-36 show the comparisons of the axial turbulence intensity (also called the normal Reynolds stress) observed during the flow of polymer fluid over the treated and untreated sand beds of three different particle size ranges at the same superficial velocity of 0.25 m/s. For flow over the 20/40 mesh size treated and untreated sand beds, the axial turbulence intensity profiles were very similar (Fig.4-34). The axial turbulent intensity very near the wall was slightly higher for the flow over the untreated sand bed than that of the case with treated sand bed.

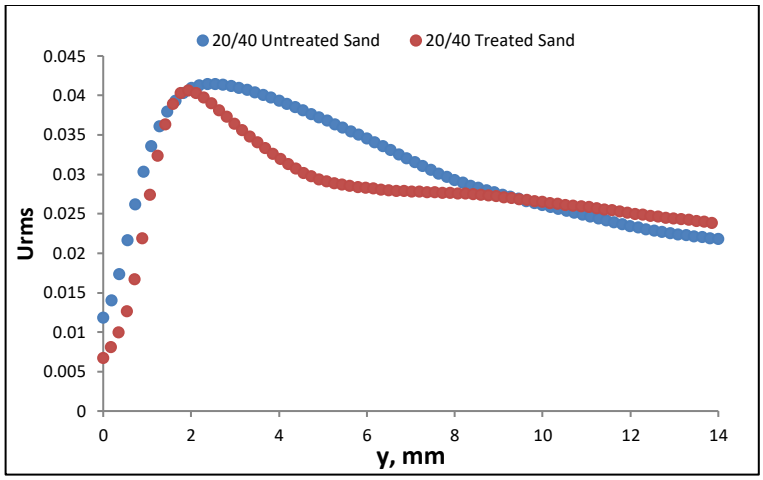

Figure 4-34 Axial turbulence intensity profiles for the flow of polymer fluid over the 20/40 mesh size treated and untreated sand bed at the superficial velocity of 0.25 m/s.

For flow over the 30/50 mesh size treated and untreated sand beds, however, axial turbulence intensity near the wall was significantly higher for the flow over the treated sand bed than that of the case with untreated sand bed (Fig.4-35).

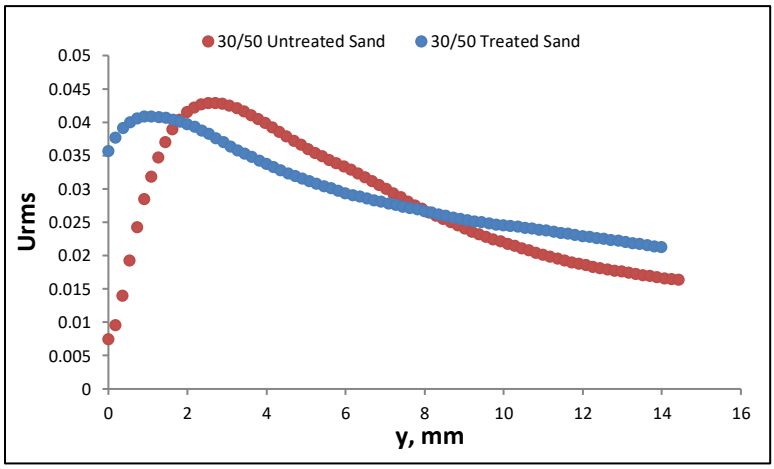

Figure 4-35 Axial turbulence intensity profiles for the flow of polymer fluid over 30/50 mesh size treated and untreated sand bed at the superficial velocity of 0.25 m/s.

The axial turbulence intensity profiles for flow over the 40/70 mesh size treated and untreated sand beds were also similar to each other (Fig.4-36). The axial turbulent intensity very near the wall was slightly higher for the flow over the treated sand bed than that of the case with untreated sand bed.

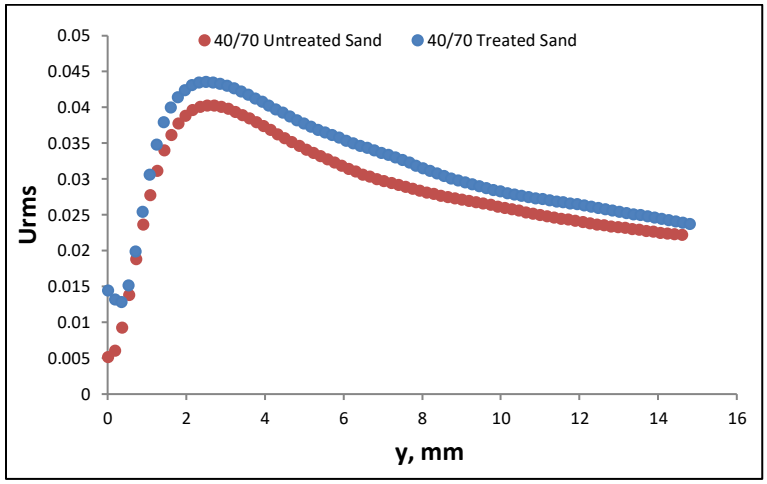

Figure 4-36 Axial turbulence intensity profiles for the flow of polymer fluid over 40/70 mesh size treated and untreated sand bed at the superficial velocity of 0.25 m/s.

The radial turbulence intensity profiles for all three mesh sizes of treated and untreated sand beds are shown in Figs. 4-37 to 4-39. The radial turbulence intensity very close to the wall for flow over the 20/40 mesh size treated sand bed was significantly lower than that of the flow over the untreated sand bed (Fig.4-37). Away from the wall, however, the radial intensity trend was reversed, and higher radial intensity was recorded for the flow over the untreated sand bed. The radial turbulence intensity for flow over the 30/50 mesh size untreated bed was consistently higher than that of the flow over the treated sand bed (Fig.4-38). Radial turbulence intensity profiles for the flow of polymer fluid over 40/70 mesh size treated and untreated sand bed were very similar as well (Fig.4-39). Radial turbulence intensity very close to well was slightly higher for the flow over the untreated sand bed than that of the case with treated sand bed.

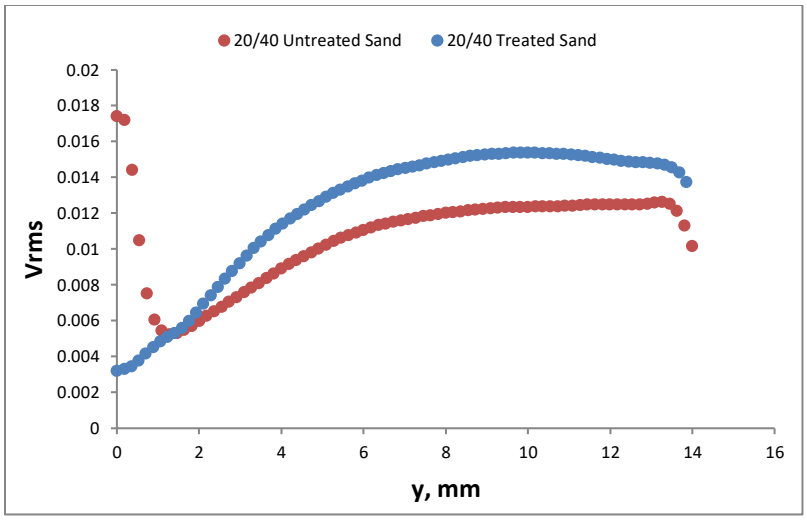

Figure 4-37 Radial turbulence intensity profiles for the flow of polymer fluid over 20/40 mesh size treated and untreated sand bed at the superficial velocity of 0.25 m/s.

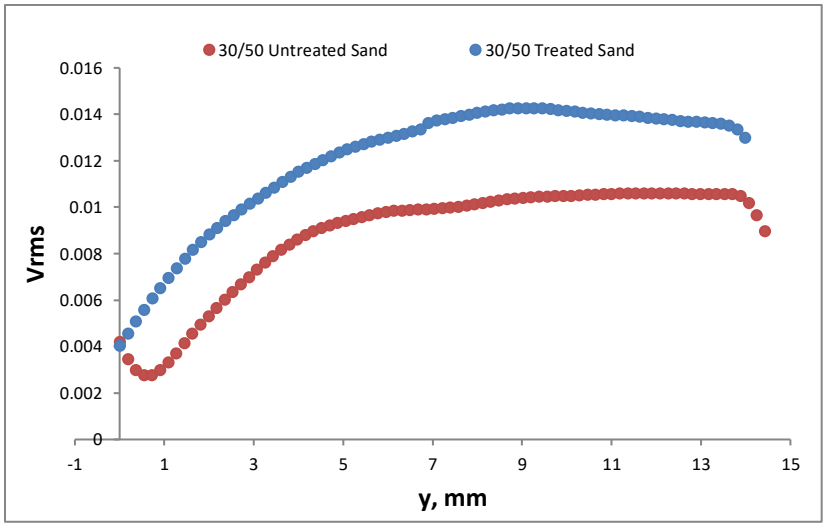

Figure 4-38 Radial turbulence intensity profiles for the flow of polymer fluid over 30/50 mesh size treated and untreated sand bed at the superficial velocity of 0.25 m/s.

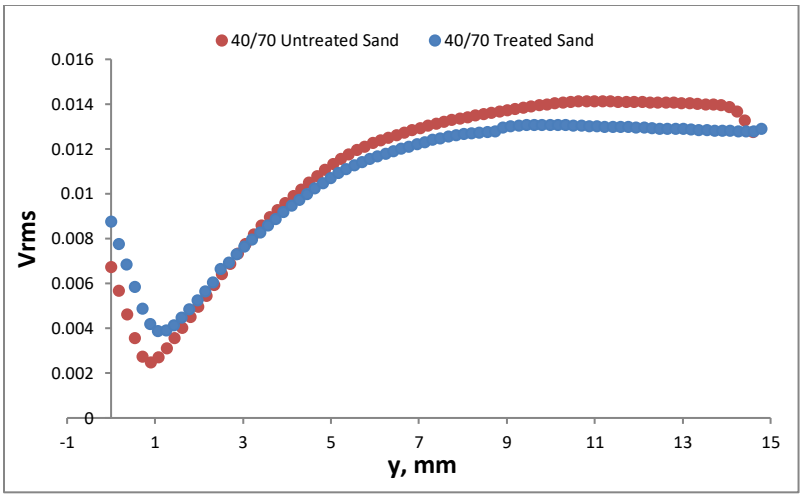

Figure 4-39 Radial turbulence intensity profiles for the flow of polymer fluid over 40/70 mesh size treated and untreated sand bed at the superficial velocity of 0.25 m/s.

4.6.3. Comparison of Critical Velocities Required for Particle Removal from the Treated and Untreated Sand Bed

Table 4-12 summarizes the results of the bed erosion tests and the observed critical velocities required for the onset of particle removal from 20/40, 30/50, 40/70 mesh size untreated and treated sand beds. Comparisons of the critical velocities in this case are also provided in Fig.4-40. Critical velocities for particle removal from both 20/40 mesh size and 40/70 mesh size treated and untreated sand beds were almost the same. However, the critical velocity for particle removal from 30/50 mesh size of treated sand was 36% lower than that of the untreated sand bed. It seems like the surface characteristic (i.e. treated vs. untreated sand) of the sand and the absolute value of the particle size are not the only factors affecting the critical velocity with polymer fluid flow. When we use a polymer fluid for transport, critical velocity also varies depending on the relative position of the sand particle with respect to viscous sublayer thickness (i.e., how the particle size compares with the viscous sublayer thickness). If the particle size is bigger than the viscous sublayer thickness, then the sand particle is more likely to be exposed to higher near wall velocity at a given superficial fluid velocity condition (Tables 4-5 and 4-9).

Therefore, a sand particle sticking out of the viscous sublayer will be removed from the bed at a critical (superficial) velocity lower than that of the one, which is completely submerged into the viscous boundary layer.

Table 4-12 Comparisons of the critical velocities - Treated vs Untreated sand

Sand Particles Mesh Size	Bed Height (cm)	Flow Area (without bed) (cm^2)	Critical Flow Rate (lpm)	Critical Velocity (m/s)	Reduction (%)
20/40 Untreated Sand	3.65	45.8	183.5	**0.670**	**0**
20/40 Treated Sand	3.31	48.9	198.2	**0.675**	
30/50 Untreated Sand	3.10	50.6	271.6	**0.895**	**36**
30/50 Treated Sand	3.22	49.8	170.0	**0.570**	
40/70 Untreated Sand	3.31	48.9	218.3	**0.744**	**0**
40/70 Treated Sand	3.31	48.9	217.6	**0.742**	

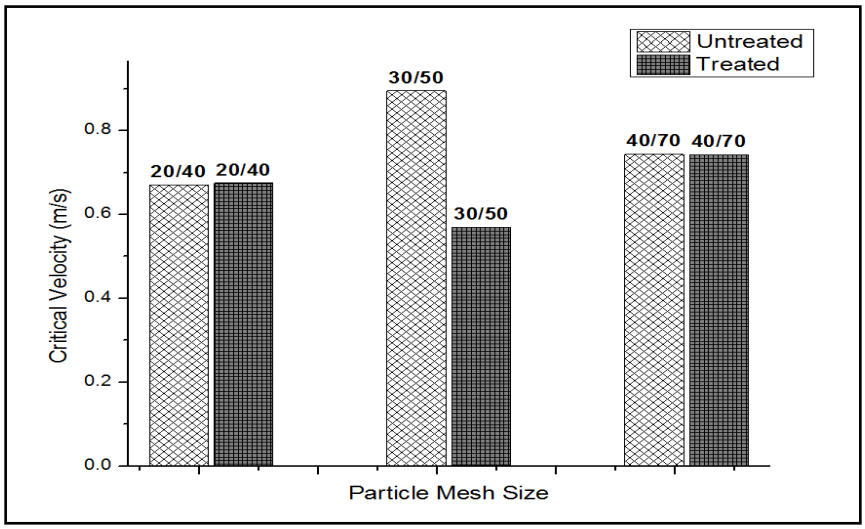

Figure 4-40 Comparisons of the critical velocities - Treated vs Untreated sand.

4.7. CONCLUSIONS

An experimental study was conducted to investigate the possible effects of sand particle size and surface properties on the critical velocity, the frictional pressure drops and the turbulent characteristics of the polymer

fluid flow over a sand bed deposit in a horizontal pipe. In particular, we have used PIV measurements to determine the effects of the surface treatment and/or the particle size on the turbulent characteristics of the polymer fluid flow over a sand bed.

For untreated sand particles, the lowest critical velocity was observed for the flow over the bed the with the largest particle size range (i.e., 20/40 mesh size of sand). For the treated sand particles, however, the lowest critical velocity was observed for the flow over the sand bed with intermediate particle size range (i.e., 30/50 mesh size).

It seems like when a polymer fluid is used for solids transport, the critical velocity not only depends on the surface characteristic (i.e. treated vs. untreated sand) of the sand and the absolute value of the particle size but also on the relative position of the sand particle with respect to viscous sublayer thickness (i.e., how the particle size compares with the viscous sublayer thickness).

Frictional pressure drops measured during the polymer fluid flow over the 20/40 and 40/70 mesh size of untreated and treated sand beds were similar. However, frictional pressure drop for the flow of polymer fluid over the 30/50 mesh size treated sand was significantly higher than that of the untreated sand. Moreover, the difference between the frictional pressure drop for the flow over the 30/50 mesh size treated and untreated sand bed increased with the increasing fluid velocity. The frictional velocity (function of interfacial bed shear stress) values obtained from the PIV measurements (conducted at the fluid/sand bed interface) also confirmed the trends of the frictional pressure drop measured during the polymer fluid flow over the both treated and untreated sand bed.

Reynolds stress profiles were found to be very much in line with the frictional pressure drops measured during the flow over the same mesh size of the treated and untreated sand bed. Generally, we can say that there is not a significant difference in Reynolds stress profiles for treated and untreated sand particles if the critical velocity is similar for both cases. However, if there is a reduction in the critical velocity due to the surface treatment or if there is a change in near wall characteristics due to surface treatment, then this causes an increase in Reynolds stress profile. When the Reynolds stress comparison was done only based on the particle size, we did not see a

direct correlation between the Reynolds stress profile and the particle size. A difference in Reynolds stress was only observed between 30/50 mesh size of treated and untreated sand.

Surface treatment did not seem to have any significant effect on the axial turbulence intensity profiles for the flow over the 20/40 and 40/70 mesh size sand beds. However, for flow over the 30/50 mesh size sand bed, the surface treatment increased the mobility of sand particles and increase in mobility could be seen as an increase in recorded axial turbulence intensity profiles for treated sand particles especially close to near wall area. Particle size did not affect the axial turbulent intensity profiles for the flow over the both treated and untreated sand beds.

The difference in radial turbulence intensity profiles was negligibly small for the flow over the 20/40 and 40/70 mesh size sand beds. However, even the difference was negligibly small, the measured values were higher for the flow over the untreated sand beds. Radial turbulence intensity profiles were considerably higher for the flow over the 30/50 mesh size treated sand beds than that of 30/50 mesh size untreated sand bed. Again, here we may say that if the surface treatment reduces the critical velocity or changes the near wall characteristics, then this would increase the radial turbulence intensity profiles. There was no significant difference in radial turbulence intensity profiles recorded for the flow over treated sand beds of different particle size. For flow over the untreated sand beds, 30/50 mesh size untreated sand particles have lower radial turbulence intensity values. While the radial turbulent intensities for the flow over the 20/40 and 40/70 mesh size untreated sand beds were almost the same. Generally, it was not possible to establish a correlation between particle size and radial turbulence intensity profiles for treated and untreated sand particles.

In summary, we can say that by applying special surface treatments on the sand particles, more control over the bed erosion dynamics of the dilute polymer fluid flow might be obtained. Although it is case specific, such surface treatment of solids might be beneficial for the design of proppants that could possess more efficient transport properties and, hence, help improving the performance of the hydraulic fracturing operations.

4.8. ACKNOWLEDGEMENTS

This research is financially supported by the funds available from the Natural Sciences and Engineering Research Council of Canada (NSERC EGP 515333-17 Kuru).

4.9. REFERENCES

1. Nazari, T., Hareland, G. and Azar, J. J. (2010, May). Review of Cuttings Transport in Directional Well Drilling: Systematic Approach. SPE Western Regional Meeting Anaheim, California, USA, SPE-132372-MS, doi: 10.2118/132372-MS.
2. Li, J., Luft, B. (2014a, October). Overview of Solids Transport Studies and Applications in Oil and Gas Industry - Experimental Work. SPE Russian Oil and Gas Exploration & Production Technical Conference and Exhibition. Moscow, Russia, SPE-171285-MS, doi: 10.2118/171285-MS.
3. Li, J., Luft, B. (2014b, December). Overview Solids Transport Study and Application in Oil-Gas Industry-Theoretical Work. International Petroleum Technology Conference. Kuala Lumpur, Malaysia, IPTC-17832-MS, doi: 10.2523/IPTC-17832-MS.
4. Brown, N., Bern, P., Weaver, A. (1989). Cleaning Deviated Holes: New Experimental and Theoretical Studies. SPE/IADC Drilling Conf.
6. Adari, R., Miska, S., Kuru, E., Bern, P., Saasen, A. (2000, February). Cuttings Bed Erosion Curves Help Predict Optimum Circulation Time for Hole Cleaning. ETCE/ OMAE Joint Conference of ASME, New Orleans, LA.
6. Martins, A., Campos, W., Liporace, F., Wei, X., Van Riet, E. (1997). On the Erosion Velocity of a Cuttings Bed During the Circulation of Horizontal and Highly Inclined Wells. Latin American and Caribbean Petroleum Engineering Conference.
7. Rabenjafimanantsoa, A., Time, R. W., Saasen, A. (2007). Simultaneous Uvp and PIV Measurements Related to Bed Dunes Dynamics and Turbulence Structures in Circular Pipes. 5th International Symposium on Ultrasonic Doppler Methods for Fluid Mechanics and Fluid Engineering, pp. 63-67.
8. Bizhani, M., Kuru, E. (2017). Particle Removal from Sandbed Deposits in Horizontal Annuli Using Viscoelastic Fluids. SPE Journal.

9. Bizhani, M. (2017). Experimental and Theoretical Investigations of Particle Removal from Sand Bed Deposits in Horizontal Wells Using Turbulent Flow of Water and Polymer Fluids, PhD Thesis, Civil and Environmental Engineering, University of Alberta, Edmonton, Canada.

10. Metzner, A.B., Reed, J.C. (1955). Flow of non-Newtonian fluids—correlation of the laminar, transition, and turbulent-flow regions. AICHE Journal,1(4), pp.434-440.

11. Raffel, M., Willert, C. E., Kompenhans, J. (2007). Particle Image Velocimetry: A Practical Guide: Springer Science & Business Media.

12. LaVision, Davis 8.3 Product Manual. ed, 2015.

13. Kundu, P. K., Cohen, I. M., Dowling, D. R. (2012). Fluid Mechanics, 5th Edition. Amsterdam, Elsevier Science Bv.

14. Kelessidis, V. C., Bandelis, G. E. (2004). Flow Patterns and Minimum Suspension Velocity for Efficient Cuttings Transport in Horizontal and Deviated Wells in Coiled-Tubing Drilling. SPE Drilling & Completion.

15. Davies, J. (1987). Calculation of Critical Velocities to Maintain Solids in Suspension in Horizontal Pipes. Chemical Eng.Sci., vol. 42, pp. 1667-1670.

16. Bizhani, M., Kuru, E. (2018, April). Critical Review of Mechanistic and Empirical (Semi-mechanistic) Models for Particle Removal from Sandbed Deposits in Horizontal Annuli with Water. SPE Journal, Vol.23, Issue.02, pp.237-255, doi:10.2118/187948-PA.

17. Duan, M., Miska, S. Z., Yu, M., Takach, N. E., Ahmed, R. M., Zettner, C. M. (2009). Critical Conditions for Effective Sand-Sized Solids Transport in Horizontal and High-Angle Wells. Society of Petroleum Engineers. doi:10.2118/106707-PA

18. Diplas, P., Dancey, C. L., Celik, A. O., Valyrakis, M., Greer, K., Akar, T. (2008). The Role of Impulse on the Initiation of Particle Movement under Turbulent Flow Conditions. Science, vol. 322, pp. 717-720.

5. EFFECT OF POLYMER FLUID VISCOELASTIC PROPERTIES ON THE EARLY TRANSITION TO TURBULENT FLOW AND THE DRAG REDUCTION IN THE FLOW THROUGH HORIZONTAL PIPE

5.1. ABSTRACT

In this study, we have investigated the flow of viscoelastic fluids through horizontal pipeline. The main objective of the research was to determine the effect of the fluid elasticity on the drag reduction and the onset of the turbulence in horizontal pipe flow.

A 9m long horizontal flow loop (ID: 95 mm) equipped with particle image velocimetry (PIV) system was used for the experiments. The velocity field data obtained by using PIV technique were analysed to determine the turbulent characteristics of the viscoelastic polymer fluid flow.

The fluids were prepared by mixing three different grades (i.e. $5x10^5$, $8x10^6$, $20x10^6$ g/gmol) of partially hydrolysed polyacrylamide (HPAM) polymer. Three different dilute polymer fluids (i.e. polymer concentration; 0.095 %wt/wt, 0.100 %wt/wt, 0.135 %wt/wt), having the same shear viscosity but different elasticity, were used for the experiments. By preparing the fluids in such manner, we were able to investigate the effect of the fluid elasticity (independent from the fluid shear viscosity) on the drag reduction and the onset of the turbulence in horizontal pipe flow.

Results have shown that that drag reduction effect associated with the pipe flow of a dilute polymer fluid was enhanced by the increasing the fluid elasticity. Moreover, the fluid elasticity was effective in controlling the onset of the turbulent flow. An earlier transition to turbulent flow regime (as compared to water flow) was only observed during the flow of the viscoelastic fluid, which had the highest elasticity among the three fluids.

The initiation of the drag reduction effect and the highest drag reduction value were found to be strongly dependent on the characteristic Weissenberg number. The drag reduction started to be effective at a Weissenberg

number around 2 and it reached a peak value at a Weissenberg number around 5 for all the fluids used in these experiments.

Results of this study highlighted the importance of the fluid elastic properties on the turbulence characteristics of the dilute polymer fluid flow in pipes. Better understanding of the fluid elasticity effect would allow improved hydraulic design of the transport problems associated with these types of fluids such has hole cleaning/cuttings transport in oil and gas well drilling, proppant transport in hydraulic fracturing operations. Field efforts to find the solutions of the problems caused by excessive dynamic pressures encountered in drilling horizontal or extended reach wells or to increase effectiveness of hydrocarbon transportation through pipelines might benefit from the findings of these and other similar research.

5.2. INTRODUCTION

Drag reducing effect of dilute polymer fluids was first discovered through the experiments conducted by Toms in 1948 [1]. Savins [2] claimed that the drag reduction is directly related to viscoelastic properties of fluids. Savins [2] also highlighted that while all high molecular weight polymer fluids do not have a drag reduction effect, some fluids in colloidal form having viscoelastic properties show drag reduction. Walsh [3] explained that the drag reduction occurs as the energy stored by molecules strained in viscous sublayer is transferred to the center of the flow and he used linear viscoelastic theory of Rouse [4] to calculate the stored strain energy. Based on their experimental work, Elata et al. [5] concluded that for drag reducing polymer fluids, the laminar viscous sublayer thickness increases, and this increase causes the drag reduction. Later, Virk [6] suggested an elastic sublayer model to explain the drag reduction phenomena, his explanations were somehow similar to explanations of Elata et al. [5], however in his model, in addition to viscous sublayer, an elastic sublayer was defined by Virk. Lumley [7] claimed that increasing effective viscosity by the expansion of the molecules in the flow, stabilizes the turbulent eddies by thickening the viscous sublayer and this optimizes the energy transferred in the flow direction. When the optical measurement techniques became available, Achia et al. [8] used such techniques to further

analyse the drag reduction of dilute polymer solutions and their experimental results confirmed the existence of a stabilized wall layer (claimed previously in the literature) and this stabilization was linked with elongational viscosities developed during the flow. Massah et al. [9] studied the drag reducing effect of dilute polymer solutions with FENE-P (Finitely extensible nonlinear elastic) model. Their work showed that the polymer chains deformed by high shear in flow produces some extra stresses and these extra stresses cause the drag reduction by modifying the structure of eddies producing Reynolds stresses [9]. While studying the effect of rheological properties on the drag reduction with direct numerical simulations, Dimitropoulos et al. [10] highlighted the role of elongational viscosities in drag reduction phenomena and they stated that there was a certain Weissenberg number associated with the onset of the drag reduction and elongational viscosity development. Pinho et al. [11] modified the GNF (Generalized Newtonian Fluid) model to include the effect of elongational viscosity and they considered the elongational viscosity among the most important parameters causing the drag reduction. Bonn [12] experimentally showed the direct connection between the elongational viscosity and the drag reduction of dilute polymer solutions. All these works from the literature clearly show the direct relationship between elongational viscosities developed by the polymer chains in solution and the drag reducing effect of dilute polymer solutions.

In addition to the drag reducing effect, dilute polymer solutions might also exhibit early transition to turbulent flow regime. Groisman et al. [13] suggested that polymer fluids with sufficiently high elastic properties would start chaotic flow at low velocities and this might stimulate the effectiveness of mixing polymers by leading an elastic turbulence. Early turbulence phenomena for flow in conduits was initially reported for the flow of dilute polymer solutions in capillary tubes [14]. The occurrence of early turbulence for flow through larger diameter pipes was only a hypothesis until Hansen et al. [14] and Forame et al. [15] experimentally showed that early turbulence might occur for the flow of dilute polymer fluids in pipes having larger diameters, (i.e. 0.553 cm and 0.660 cm). Early turbulence was also reported by Hoyt [16] for flow of dilute polymer solutions in a water tunnel. Hansen et al. [14], Forame et al. [15] and Hoyt [16] related the occurrence of the early turbulence with drag

reduction phenomena solely. Dubief et al. [17] showed that the elasto-inertial turbulence (EIT) – which occurs as a result of developed elongational viscosities by the stretch of long polymer chains during the flow - causes earlier transition to turbulent state in channel flow for dilute polymer solutions with the direct numerical simulation method. Samanta et al. [18] mentioned that rather than Reynolds number, the elasto-inertial turbulence depends on the shear rate. Their flow experiments in pipes having diameters of 2 mm and 10 mm showed that earlier transition to turbulent regime occurred for 500 ppm polyacrylamide (i.e. molecular weight $5x10^6$ g/gmol) solution. However, they claimed that the early turbulence might not occur for larger diameter pipes as the shear rates will be much lower. In the current study, we have shown that early turbulence might also occur for flow in large diameter pipes (i.e. 9.5 cm) and beside shear rate or drag reduction also elastic properties of the dilute polymer fluids are significant for the early turbulence phenomena. In order to see the direct influence of the fluid viscoelasticity on the drag reduction and the early turbulence phenomena, we have investigated the flow of three dilute polymer fluids having the same shear viscosities but different elastic properties through a 9m long horizontal pipeline with a 95 mm inner diameter. The turbulent characteristics of the flow such as Reynolds stresses, axial and radial turbulence intensity profiles were also determined by analysing the velocity field data collected by using PIV technique. Earlier transition to turbulence was observed only during the flow of fluid with the highest elasticity (among the three tested fluids) while, on the other hand, all the three fluids showed significant drag reducing behaviour. Lowest frictional pressure drops were measured during the flow of the most elastic fluid.

5.3. MATERIALS AND METHODS

5.3.1. Polymer Fluids

Three different dilute polymer fluids having the same shear viscosity, but different elastic properties were used for the experiments. Three different grades of HPAM (Partially Hydrolysed Polyacrylamide) were used in

preparation of these fluids. Molecular weight and the specific names of those three polymer grades are given in Table 5-1. All these polymer grades are water soluble with a degree of hydrolysis of around 30 %.

Table 5-1 HPAM different grades molecular weight data

Polymer Name	Molecular Weight (g/gmol)
HPAM AB 005V	$5x10^5$
HPAM 3330S	$8x10^6$
HPAM 3630S	$20x10^6$

Shear viscosity of a polymer fluid is a function of the average molecular weight of the polymer mix used for the preparation of the fluid [19]. Equation 5-1 defines the average molecular weight of the polymer mix of different grades. In order to have the same shear viscosities for each fluid, Equation 5-1 was used to arrange the composition of each mixture. The elastic properties of a polymer fluid are a function of the molecular weight distribution (MWD) of the polymer mix used for preparation of the fluid. The polydispersity index, I (defined by Equation 5-2) can be used as a measure of the MWD of a polymer blend [19]. In order to create polymer blends of different MWD, we have used the polydispersity index as a measure and calculated I values of the three polymer blends by using Equation 5-2. The Fluid A was prepared by mixing HPAM AB 005V and HPAM 3630S grade polymers as the most elastic solution. Fluid B was prepared by mixing only HPAM 3330S grade as the least elastic solution. Fluid C was prepared by mixing three different grades altogether as the solution having an elasticity in between among these three dilute solutions. Concentrations giving the same viscosity for each mixture were determined based on the mixing experience of those mixtures in the suction tank. Table 5-2 presents compositions and concentrations used for Fluid A, Fluid B and Fluid C based on the Equation 5-1, Equation 5-2 and the mixing experience.

$$M_{w,B} = \prod_{i=1}^{n} M_{w,i}^{\omega_i} \quad \text{..... (5-1)}$$

$$I = \frac{M_w}{M_n} = \left(\sum_{i=1}^{n} \omega_i M_{w,i} \right) \times \left(\sum_{i=1}^{n} \frac{\omega_i}{M_{w,i}} \right) \quad \text{..... (5-2)}$$

In Equations 5-1 and 5-2; M_{wB} is the average molecular weight of the polymer blend, ω_i is the weight fraction of the polymer grade i, $M_{w,i}$ is the molecular weight of polymer grade i, M_w is the weighted average molecular weight, M_n is the number average molecular weight and I is the polydispersity index.

Table 5-2 Compositions and concentrations of Fluids A, B and C

Mixture	Concentration (%wt/wt)	HPAM AB005V (w%)	HPAM 3330S (w%)	HPAM 3630S (w%)	Average Molecular Weight	Polydispersity Index
Fluid A	0.135	24.2	0	75.8	$8x10^6$	8.05
Fluid B	0.095	0	100	0	$8x10^6$	1
Fluid C	0.100	42.95	43.95	13.92	$8x10^6$	4.26

Bohlin C-VOR 150, a high-resolution rheometer, was used for measurements of rheological properties of these fluids. Basic rheological measurements done for these fluids were frequency sweep and viscosity tests. The relaxation times of these fluids were determined by using frequency sweep tests. The shear stress – shear rate characteristics of these fluids were obtained from viscometer tests. To ensure the repeatability and validity of the measurements, each test was repeated at least two times at the beginning and at the end of each experiment. Samples for the tests were collected from the suction tank.

5.3.2. Experimental Flow Loop

A schematic of the horizontal flow loop used for experiments is shown in Figure 5-1. Major components of the flow loop include a suction tank of 500 litres capacity, a variable frequency (VFD) driven centrifugal pump, suction and discharge lines, a differential pressure transducer, a magnetic flow meter, and several gate valves (used for isolating the flow when needed) and glass tubes.

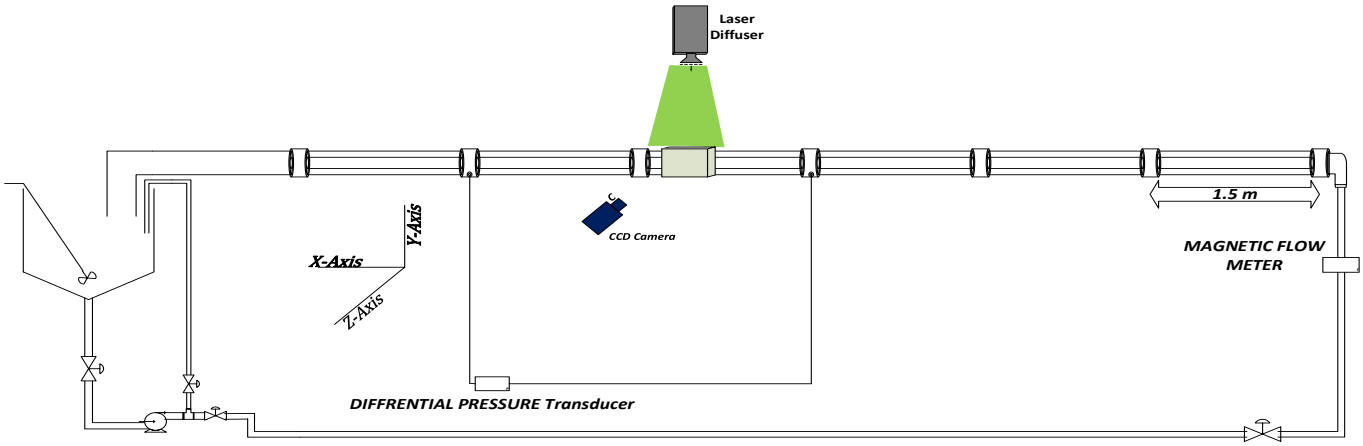

Figure 5-1 Schematic diagram of the experimental flow loop [20].

The horizontal test section is composed of 9m long 95 mm inner diameter borosilicate glass pipes. The electric motor driving the centrifugal pump was linked to a variable frequency drive (VFD) unit and the flow rate in the loop was controlled through National Instrument's Labview software by changing the rotational speed of the electric motor. A magnetic flow meter (OMEGA FMG607-R; accuracy ±0.5%) installed at the inlet of the flow loop was used to measure the flow rate. A differential pressure transducer (OMEGA DPG409, accuracy ±0.08% of full scale) was used to measure the frictional pressure drop across 3.08 m long section.

PIV measurements of the velocity field data were conducted over the pipe section, which was located inside a rectangular glass box. This test section is shown in Figure 5-2. The glass box was filled with glycerol, which has the similar refractive index as the borosilicate glass pipe. This arrangement was necessary to minimize

measurement errors due to a possible refraction that might occur when the light passes through the circular surface of the glass pipe and make sure that the light reaches the flowing fluid without any significant refraction.

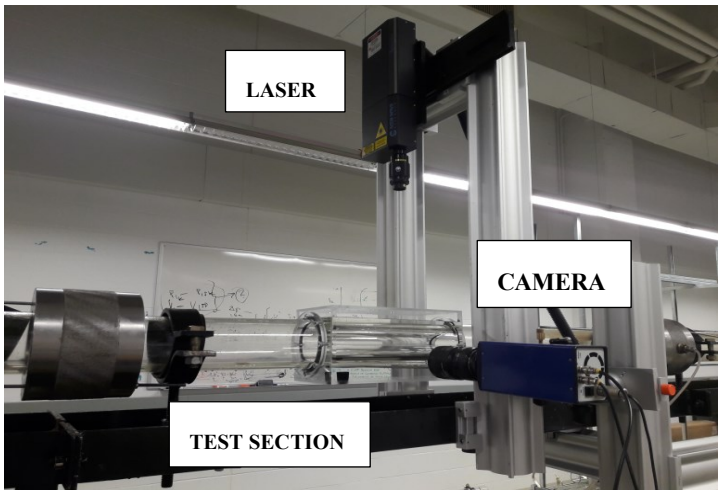

Figure 5-2 Image of the PIV setup and the test section

A New Wave Research Solo III Nd: YAG laser, a Lavision Imager Intense CCD camera, Nikon 50 mm AF Nikkor lens of 1.4 mm aperture were the main elements of the PIV setup. The wavelength of the laser light was 532 nm. The Imager Intense CCD camera was a double framed camera with a 12-bit CCD sensor of having 1376 x 1040 pixels. Davis 8.3 software was used to establish the communication between all these components. Analysis and processing of the recorded images were done by using Davis 8.3.

5.3.3. Experimental Procedure

The experimental procedure was composed of two main stages. The first stage was preparation of the dilute polymer fluid and circulating it in the horizontal flow loop while measuring frictional pressure drops at several flow rates; and the second stage was PIV measurements at several flow rates. The procedure followed in these experiments are briefly explained below.

2.3.1. Polymer fluid circulation and pressure drop measurements

To confirm the accuracy of the frictional pressure loss measurements, the theoretical friction factor values determined from Dodge and Metzner model [21] and experimental friction factor values measured during the pipe flow of water were compared. The results of the comparisons are presented in Figure 5-3.

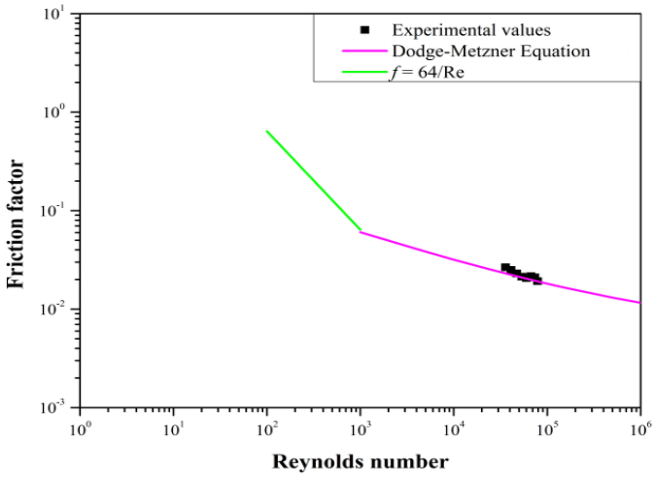

Figure 5-3 Comparison of experimental friction factor values estimated from water only flow tests against the ones calculated from Dodge and Metzner equation [21].

The suction tank was isolated from the system and it was filled with 500 litres of water. Then, based on the predetermined concentrations and compositions of the polymer blends, dilute polymer fluids were mixed in the suction tank by using the air operated mixer. The rotational speed of the air mixer was kept below 300 rpm. When the dilute polymer fluid was ready, the circulation was started across the flow loop. After ensuring the rheological properties of the fluids were within desired range, the frictional pressure losses were measured at several flow rates and recorded using Lab view software.

2.3.2. PIV measurements

PIV is a non-intrusive optical measurement technique used to measure instantaneous velocity field of fluid flow [22]. This technique requires addition of light sensitive tracer particles to the flow. The light sensitive tracer particles perfectly reflect the light. The flow was then illuminated with the laser light and movement of the tracer particles in the flow were recorded by a double frame high speed CCD camera. In this method, it is assumed that tracer particles directly follow the fluid motion, so there is no difference between fluid motion and motion of tracer particles [22]. The recorded images were converted to velocity fields by using fast Fourier transformation (FFT) technique [22].

As shown in Figure 5-2, a double pulse laser was used as the light source and a double frame camera was the recording device in the PIV setup. The light source and the camera view were orthogonal. To get a homogenous distribution in the flow, tracer particles were added in advance to start recording PIV. Tracer particles were hollow glass spheres having a mean diameter of 10 microns. The fluid in flow and the tracer particles have the similar density, so the gravity had no effect on the movement of tracers in the flow and, hence, the tracers directly follows the fluid motion. In the recorded images these tracer particles were detected as bright spots and the analysis of the successive image pairs with the appropriate code allowed to determine the instantaneous velocities for each fluid element in the flow. For the analysis and recording Davis 8.3. software was used. In order to optimize the accuracy of the recorded data at least 1000 pair of images were captured and analysed for each flow rate.

5.3.4. Data Processing and Analysis

Data processing and analysis comprised of two parts. In the first part, the frictional pressure losses were measured at various flow rates. Processing and analysis of the recorded PIV data was the second part. First, all the captured image pairs were cross correlated by using the Davis 8.3 software. The FFT cross correlation technique provided the displacement of the detected particles in these images [23]. Instantaneous velocities were

simply calculated by dividing the measured particle displacements in vertical and horizontal directions (Δx and Δy) with the elapsed time (Δt) between two consecutive image recording. The elapsed time interval was adjusted by the user for each recording. Therefore, velocities parallel and perpendicular to the flow direction were estimated by using the following pair of equations (Equations 5.3).

$$\begin{cases} \hat{u} = \frac{\Delta x}{\Delta t} \\ \hat{v} = \frac{\Delta y}{\Delta t} \end{cases} \qquad \text{..... (5-3)}$$

To cross correlate each pair of captured images, each image was first divided into small interrogation windows and interrogation windows in those sequential images were cross correlated with an FFT based algorithm included in Davis 8.3. [23] and this way instantaneous velocities were determined [23]. A multi-pass approach was used to increase the accuracy of the analysis. Used interrogation window sizes were 64 x 64, 32 x 32 and 24 x 24 with a standard overlap of 50%. We continued doing further analysis by exporting the processed data to excel files.

Reynolds stresses, axial turbulence intensities, radial turbulence intensities and near wall dimensionless velocities were further analysed and compared to detect the similarities and differences in the turbulent characteristics of flow of each polymer fluid in the horizontal loop. Davis 8.3 calculates Reynolds stresses, axial and radial turbulence intensities based on the basic equations, which uses measured velocities and velocity fluctuations in x and y directions for each pair of images taken.

The near wall velocity profiles were presented in terms of dimensionless distance (y^+) and dimensionless velocity units (u^+) as defined by equations 5-4 and 5-5, respectively.

$$y^+ = \frac{\rho y u_\tau}{\mu} \qquad \text{..... (5-4)}$$

$$u^+ = \frac{u}{u_\tau} \qquad \text{..... (5-5)}$$

$$u_\tau = \sqrt{\frac{\tau_b}{\rho}} \qquad \text{..... (5-6)}$$

Where u_τ is the friction (shear) velocity, τ_b is the interfacial bed shear stress (i.e., shear stress at the fluid/pipe wall interface), and ρ is the fluid density. The interfacial bed shear stress, τ_b, can be deduced accurately from frictional pressure loss data, so the friction velocity, u_τ, directly estimated this way.

The universal law of the wall states that the near wall velocity profile generally consists of three regions depending upon the dimensionless distance from the wall: Viscous sub-layer y^+ <5, buffer region 5< y^+<30 and log-law region y^+> 30. The universal plot of a velocity profile for a hydrodynamically smooth flow condition is given by Equation 5-7 [24].

$$u^+ = \begin{cases} y^+ & y^+ < 10 \\ 2.44ln(y^+) + 5.5 & y^+ > 30 \end{cases} \quad \text{..... (5-7)}$$

Virk's asymptote, which is the upper limit for maximum pressure reduction is defined by Equation 5-8 [25].

$$u^+ = 11.7\ln(y^+) - 17 \quad \text{..... (5-8)}$$

The Reynolds shear stress (or turbulent stress) is direct function of velocity fluctuations (u' and v') in the turbulent flow as defined by the Equation 5-9:

$$\tau_R = -\rho\overline{u'v'} \quad \text{..... (5-9)}$$

The axial turbulence intensity is determined by using the Equation. 5-10:

$$u_{rms} = \sqrt{\overline{u'u'}} \quad \text{..... (5-10)}$$

The radial turbulence intensity is determined by using the Equation 5-11:

$$v_{rms} = \sqrt{\overline{v'v'}} \quad \text{..... (5-11)}$$

5.4. RESULTS AND DISCUSSIONS

5.4.1. Rheological Properties of Fluids

As the shear stress versus shear rate data shown in Figure 5-3 indicate, the fluids A, B and C can be rheologically described as power law type fluids and be formulated by equation 12. K and n values for these fluids are given in Table 5-3. The minimum and the maximum velocities practically achievable in this horizontal flow loop are around 0.05 m/s and 1.5 m/s respectively. The wall shear rates corresponding to these minimum and maximum flow velocities are calculated by using equation 5-13 as 5 1/s and 150 1/s, respectively [26]. We also determined the minimum and maximum wall shear rates for the flow of these fluids using velocity profiles obtained from PIV measurements. The wall shear rate values obtained from PIV measurements varied from 40 1/s to 220 1/s. As shown in Figure 5-4, within the practical ranges of shear rates applicable to our flow loop, these three fluids have the same shear viscosity. Similar K and n values (Table 5-3) of these fluids also confirm that shear viscosities of these fluids are almost the same. The value of n was around 0.61 for each fluid indicating that these dilute polymer fluids were moderately non-Newtonian.

$$\tau = K\gamma^{n} \qquad \text{(5-12)}$$

$$\gamma_w = \frac{3n+1}{4n}\frac{8V}{D} \qquad \text{(5-13)}$$

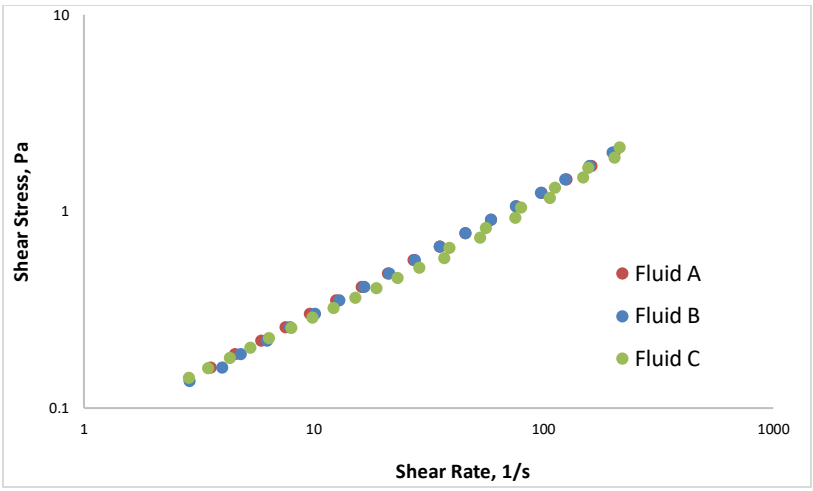

Figure 5-4 Shear stress vs. shear rate plots for Fluids A, B and C

In order to characterize the viscoelastic properties of the polymer fluids, frequency sweep tests were conducted. The frequency sweep test evaluates the storage and loss modulus of a matter at various angular frequencies. The storage modulus is the proportion of in-phase stress to strain and the loss modulus is the proportion of out-phase stress to strain. In-phase and out-phase terms accounts for the delay of a viscoelastic material's response as strain for an applied stress.

Loss modulus and storage modulus shows the extent of energy transmitted by the applied stress to a matter that is irreversible and reversible respectively [27]. While the strain by the in-phase stress is recoverable, the energy transmitted by the out-phase stress is lost as heat loss [27]. The inverse of the angular frequency value (measured by frequency sweep test) where the storage modulus and the loss modulus become equal is defined as the longest relaxation time. The longest relaxation time is commonly used as an indicator of the degree of fluid's elasticity (i.e., higher the longest relaxation time value, the more elastic would be the fluid). However, it should be kept in mind that the longest relaxation time is a complex concept and its value may be altered by strain and as Hatfield et al. [28] indicated that non-linear forces arise during the flow create transverse and longitudinal relaxation times. Figures 5-5, 5-6 and 5-7 present the results of frequency sweep tests for Fluids A, B and C, respectively. Table 4 shows the relaxation times and other rheological properties of fluids A, B and C. The Fluid

A is the most elastic one and Fluid B is the least elastic one, elasticity of the Fluid C is in between Fluid A and Fluid B.

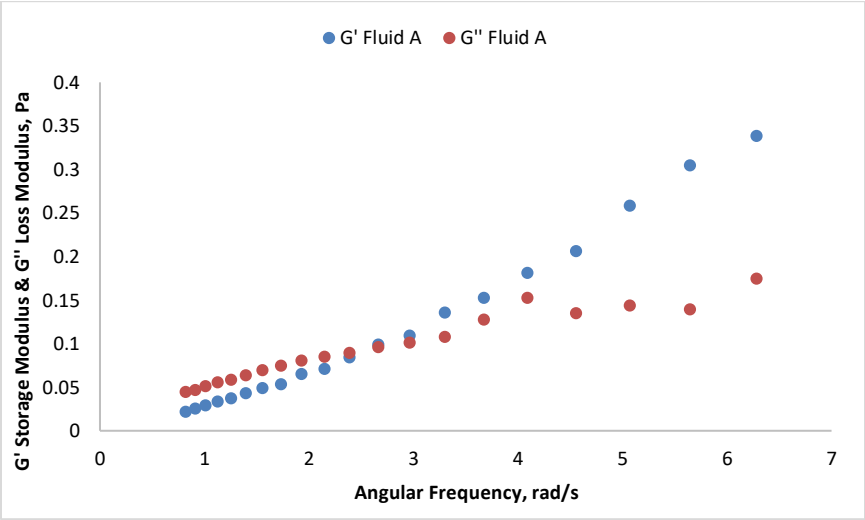

Figure 5-5 Frequency sweep test data for Fluid A

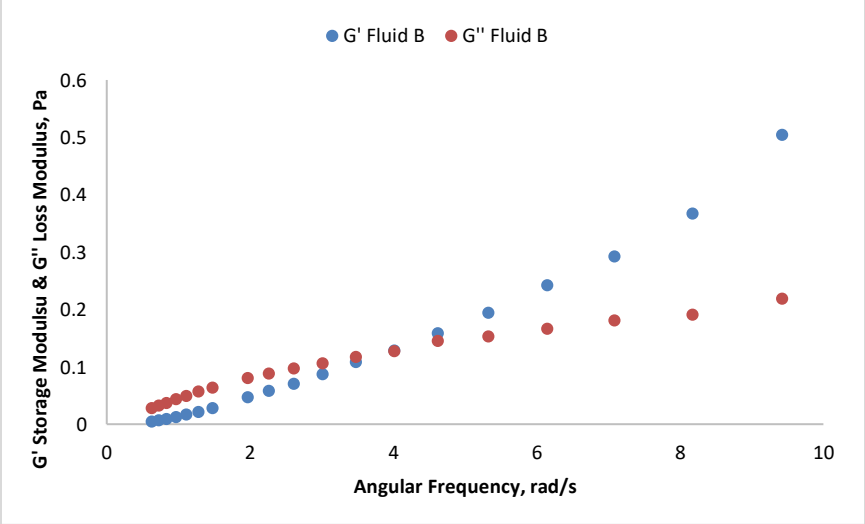

Figure 5-6 Frequency sweep test data for Fluid B

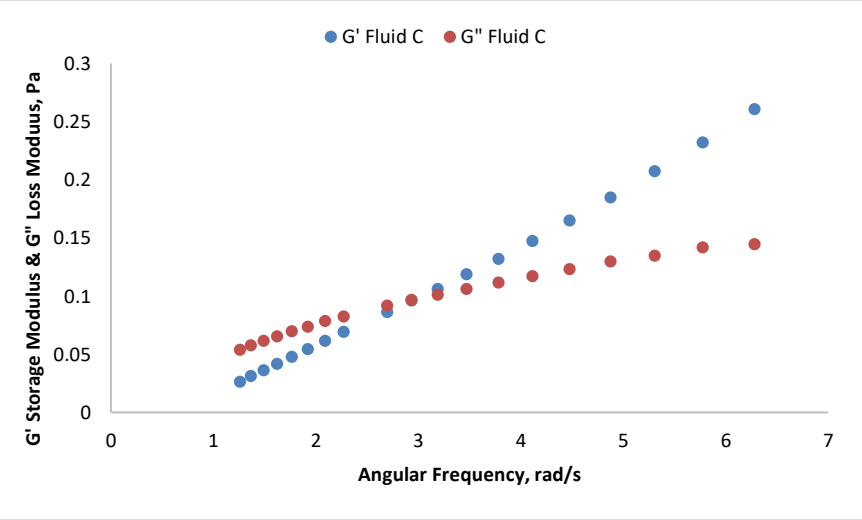

Figure 5-7 Frequency sweep test data for Fluid C

Table 5-3 Summary of the rheological properties of Fluids A, B and C

Mixture	Concentration (%wt/wt)	K (Pa.s^n)	n	Frequency Sweep Intersection (rad/s)	Longest Relaxation Time (s)
Fluid A	0.135	0.0752	0.5959	2.52	0.40
Fluid B	0.095	0.0683	0.6209	4	0.25
Fluid C	0.100	0.0714	0.6078	2.98	0.34

5.4.2. Frictional Pressure Drops and PIV Analysis

Figure 5-8 shows the frictional pressure drops measured during the flow of Fluids A, B and C in the horizontal flow loop. For Fluid C pressure drop measurements could be recorded up to a certain flow rate, because increasing the flow rate further caused some degradation of the fluid. Because of structural degradation of the fluid due to high shear rate, the recorded pressure loss data for Fluid C was limited as shown in Figure 5-8. The measured pressure drops were also converted to friction factors by using Fanning equation (Eq. 5-14). The friction factor vs Reynolds number data for Fluid A, B and C are shown in Figure 5-9. In Figure 5-9, friction factors for water

were estimated by using Blasius formula (Eq. 5-15) and the Virk's asymptote was determined by using the equation 5-16 [29].

$$f = \frac{2\tau}{\rho u^2} \quad \text{..... (5-14)}$$

$$f = 0.079 x Re^{-0.25} \quad \text{..... (5-15)}$$

$$f = 0.20 x Re^{-0.48} \quad \text{..... (5-16)}$$

Where f is Fanning friction factor, τ is shear stress calculated from measured pressure drops, ρ is the fluid density, u is the average flow velocity and Re is the Reynolds number.

The frictional pressure drops and friction factors of all polymer fluids were lower than that of water, indicating the drag reducing characteristics of these polymer fluids. The drag reduction upper limit was indicated by the Virk's asymptote. Despite Fluids A, B and C all have the same shear viscosities, Fluid A exhibited the lowest pressure drops while Fluid B exhibited the highest pressure drops. The frictional pressure drops measured for Fluid C was in between Fluid A and Fluid B. These results clearly show that beside viscometric properties, elastic properties of dilute polymer fluids also control the frictional pressure losses observed in pipe flow. Moreover, increasing fluid elasticity also increases the drag reduction effect of the dilute polymer fluids flowing through smooth circular pipe. After a certain flowrate (i.e. 400 lpm) difference in frictional pressure drops for these fluids becomes more substantial.

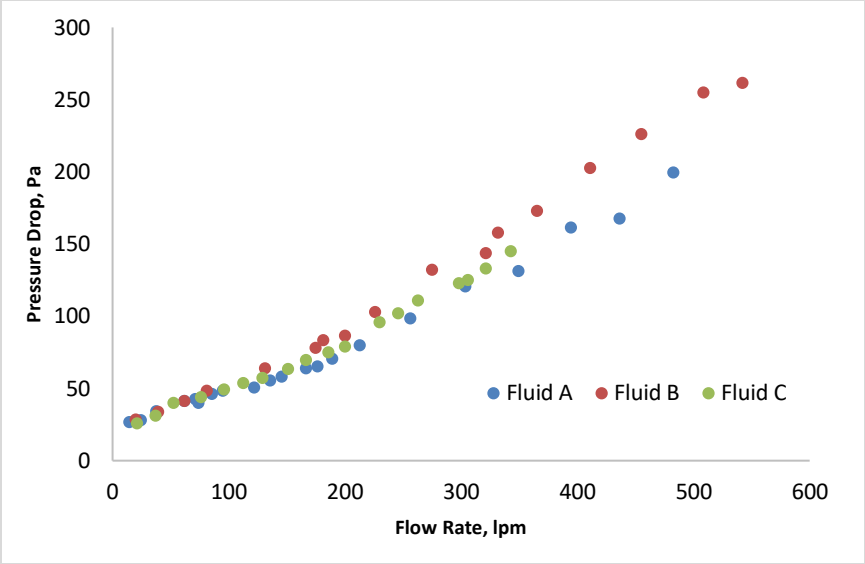

Figure 5-8 Frictional pressure drop measured during the flow of Fluids A, B and C in the horizontal pipe

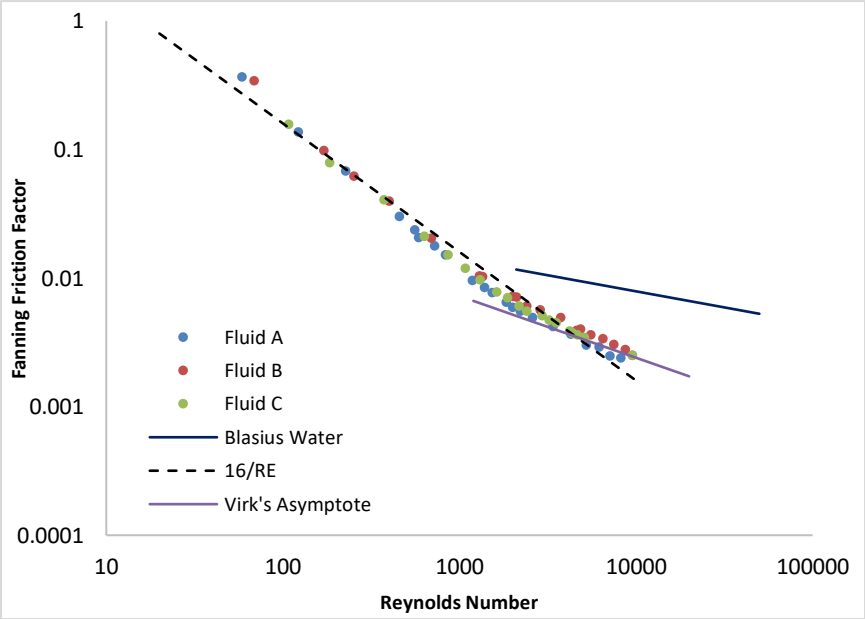

Figure 5-9 Friction factors vs. Reynolds number for the flow of Fluids A, B and C in horizontal pipe.

Bonn et al [12] experimentally showed that the drag reduction of dilute polymer fluids in flow directly depends on the elongational viscosities of the fluids. They claimed that there was a strong link between the drag reduction phenomena observed during the flow of dilute polymer solutions and the elongational viscosities of these fluids

developed during the flow. Increasing elongational viscosities also increases the effective viscosity for the flowing fluid [11]. Increased effective viscosity stabilizes the turbulent eddies in the near wall region by thickening the viscous sublayer as Lumley suggested [7]. In this study, we could not measure elongational viscosities of the fluids A, B, and C. Instead, we measured the first normal stress differences of Fluids A, B and C. The first normal stress difference and the elongational viscosities are directly related as shown in equation 5-17 [30]. At a given shear rate, higher first normal stress translates into the higher elongational viscosity of the fluid. The first normal stress is also function of the longest relaxation time as shown by Equation 5-18 [31].

$$N_1 = \sigma_{xx} - \sigma_{yy} = \bar{\eta}(\dot{\varepsilon})\frac{\partial u}{\partial x} \quad \text{(5-17)}$$

$$N_1 = -2Nk_BT\lambda^2\dot{\gamma}^2 \quad \text{(5-18)}$$

In equations 5-17 and 5-18; N_1 is first normal stress difference, σ_{xx} and σ_{yy} are normal stresses, $\bar{\eta}$ is elongational viscosity, $\dot{\varepsilon}$ is strain, $\frac{\partial u}{\partial x}$ is local shear rate, N is number of molecules per volume, k_B is the Boltzmann's constant, T is temperature, λ is relaxation time and $\dot{\gamma}$ is shear rate.

Figure 5-10 shows the first normal stress differences measured for Fluids A, B and C. The highest first normal stress differences were measured for the Fluid A, the most elastic fluid, and the lowest first normal stress differences were measured for the Fluid B, the least elastic fluid. The first normal stress differences measured for the Fluid C was in between.

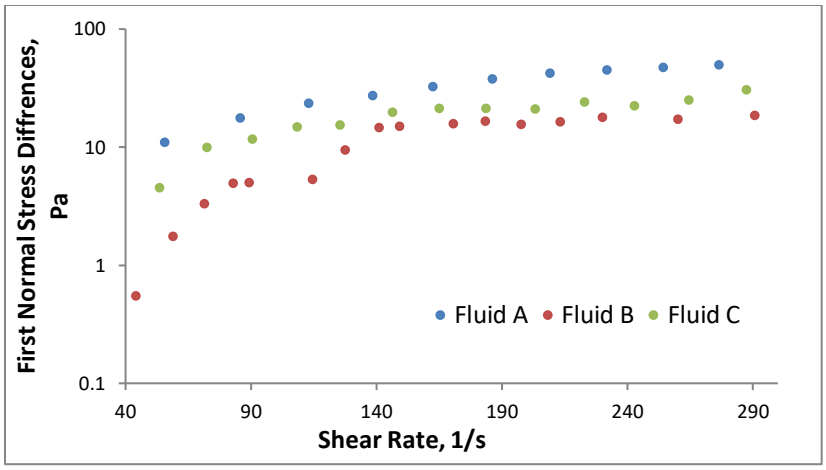

Figure 5-10 First normal stress differences of Fluids A, B and C

Based on the results of first normal stress difference and the longest relaxation time measurements, it can be concluded that the Fluid A had the highest elongational viscosity and the Fluid B had the lowest elongational viscosity and the elongational viscosity of the Fluid C was in between Fluids A and B.

The results of this study showing the increasing fluid elasticity enhancing the drag reduction are, therefore, in line with the conclusions of the previous studies by Bonn et al [12] and Lumley [7], where they suggested that there was a strong link between the drag reduction phenomena observed during the flow of dilute polymer fluids and their elongational viscosities.

5.4.3. Analyses of the Turbulent Flow Characteristics Using Data Obtained by PIV Measurements

Flow rates of 221.5 lpm (i.e. Reynolds number; 2971) and 316 lpm (i.e. Reynolds number; 4903) were selected to conduct PIV measurements. The results from PIV data analyses were then used to determine the effect of the fluid elasticity on the turbulent flow characteristics of polymer fluid flow in pipe.

The average flow velocities corresponding 221.5 and 316 lpm were 0.52 and 0.74 m/s respectively, however, higher peak velocities were measured with PIV for each fluid at these rates despite the flow rates were the same for all fluids. Therefore, in Figures 5-11 and 5-12 full velocity profiles are shown in terms of the normalized

velocities. The normalized velocity was defined as the ratio of the measured local velocity to the average flow velocity. Oldaker et al. [32] mentioned that larger differences between velocity of the fluid at the center of the pipe and the velocity near the wall might be possible for drag reducing polymer fluid flow. So, considering Oldaker et al's [32] comments, observing the highest peak velocity for the flow of the most elastic fluid, Fluid A, which is also the most drag reducing one is not unexpected.

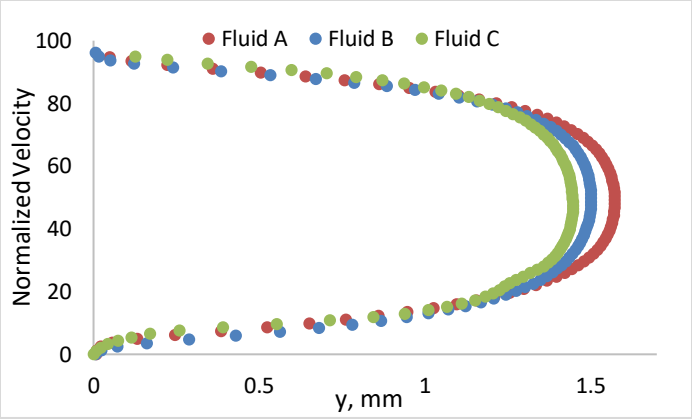

Figure 5-11 Full velocity profiles at the flow rate of 221.5 lpm.

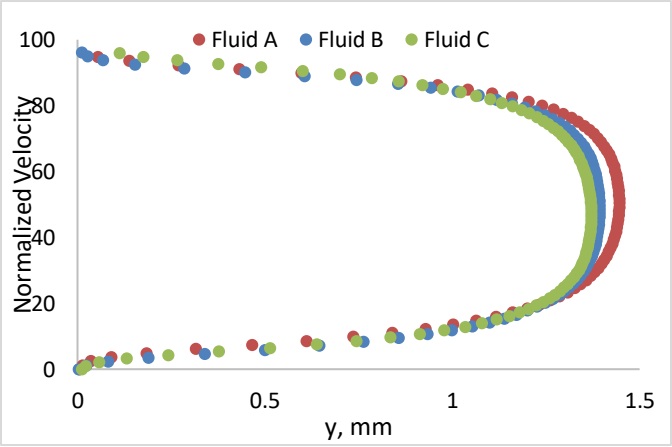

Figure 5-12 Full velocity profiles at the flow rate of 316 lpm.

Figures 5-13 and 5-14 show the dimensionless near wall velocity profiles for Fluids A, B and C at flow rates of 221.5 and 316 lpm, respectively. The near wall velocity profiles for the three fluids were bounded by an envelope that was constrained by the Virk's asymptote above and the universal log law below. The dimensionless velocity profile of the Fluid A was closer to the Virk's asymptote and this means that the drag reducing effect for Fluid A was stronger than that of the Fluid B and Fluid C. The dimensionless velocity profile of the Fluid C was in the middle and the Fluid B was the furthest from the Virk's asymptote among these fluids. These results also confirm the trends of the frictional pressure loss values measured during the flow of these fluids.

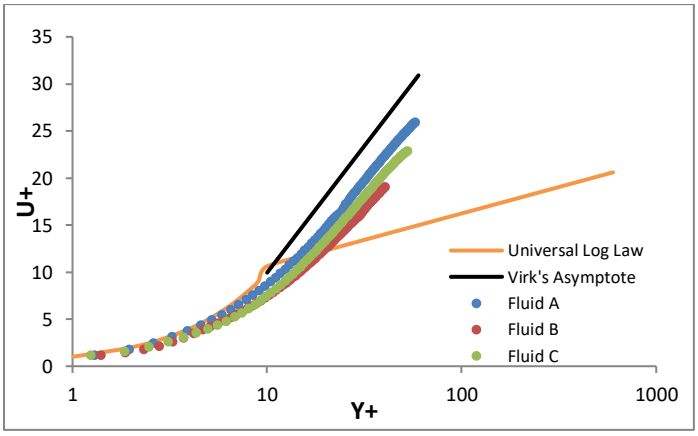

Figure 5-13 Dimensionless velocity profiles of Fluids A, B, and C at the flowrate of 221.5 lpm

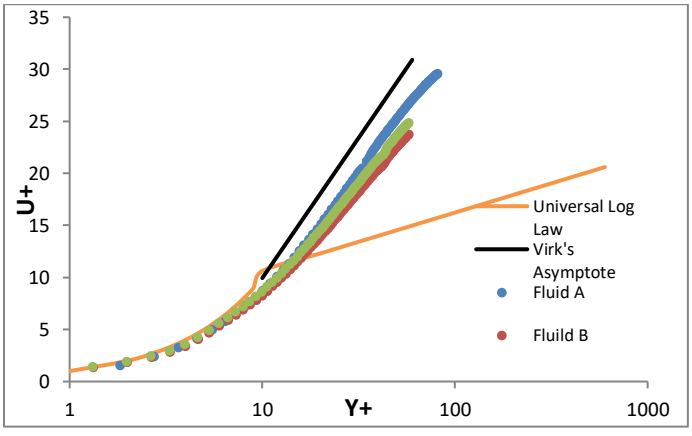

Figure 5-14 Dimensionless velocity profiles of Fluids A and Fluid B at the flowrate of 316 lpm.

Reynolds stress profiles of Fluids A, B and C at flow rates of 221.5 and 316 lpm are shown in Figures 5-15 and 5-16. At both flow rates, low Reynolds stress profiles were observed for Fluid A, Fluid B and Fluid C. Flow orientated vortices are important contributors for Reynolds stress production in turbulent flow [33]. Also, viscous sublayer thickness is effective on level of Reynold stresses produced [34]. Observing low Reynold stress profiles for these fluids can be associated with thickened viscous sublayers of these drag reducing fluids, because increase in viscous sublayer lowers the Reynolds stresses by supressing the turbulent vortices and other similar turbulent structures formed in the flow. However, despite the Reynolds stresses recorded for these fluids at these flow rates are very low, the Reynolds stresses recorded for these fluids are slightly higher at 316 lpm than 221.5 lpm as a result of increased inertial forces.

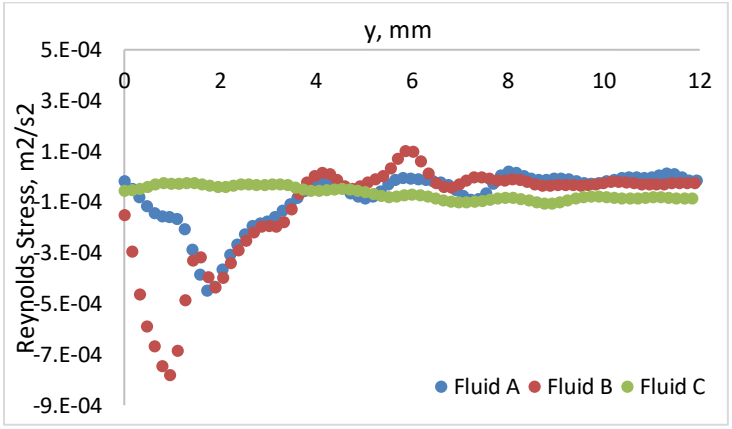

Figure 5-15 Reynolds stress profiles at the flowrate of 221.5 lpm.

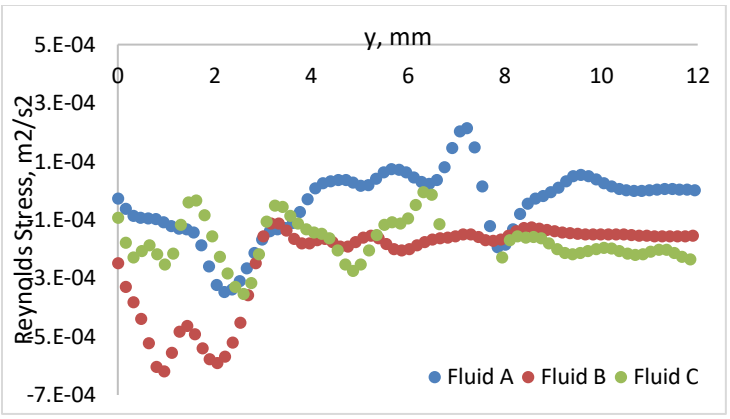

Figure 5-16 Reynolds stress profiles at the flowrate of 316 lpm.

The axial turbulence intensity profiles of Fluids A, B and C measured at flow rates of 221.5 and 316 lpm are shown in Figures 5-17 and 5-18, respectively. The axial turbulence intensity profiles recorded were similar for Fluids A, B and C except the near wall region. At the flow rate of 221.5 lpm, Fluid C has the lowest axial turbulence intensity profile and Fluid B has the highest axial turbulence intensity profile around the near wall region. At the flow rate of 316 lpm, Fluid A has the lowest axial turbulence intensity profile and Fluid B has the highest axial turbulence intensity profile.

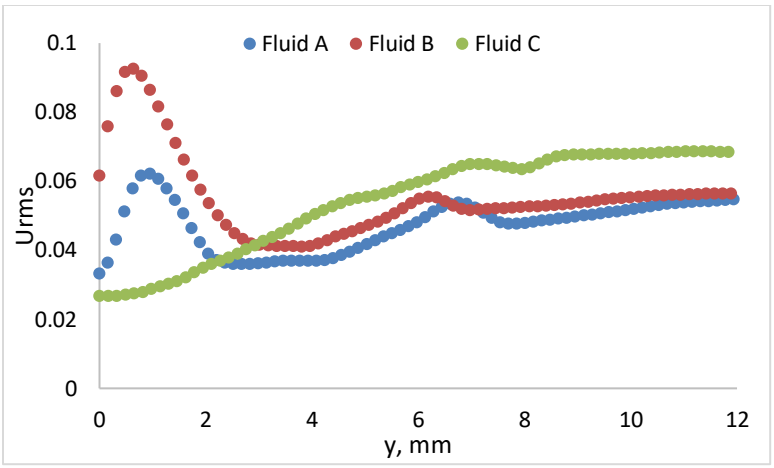

Figure 5-17 Axial turbulence intensity profiles at the flowrate of 221.5 lpm.

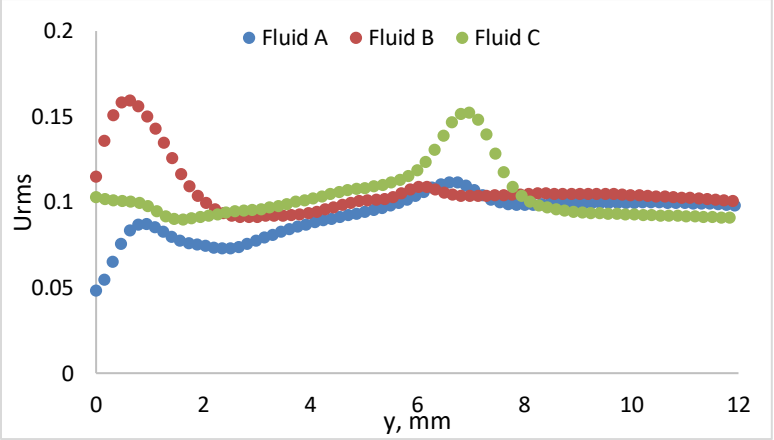

Figure 5-18 Axial turbulence intensity profiles at the flowrate of 316 lpm.

Figure 5-19 and Figure 5-20 show the radial turbulence intensity profiles of Fluids A, B and C at flow rates of 221.5 lpm and 316 lpm, respectively. At each flow rate, the lowest radial turbulence intensities were recorded for Fluid A and highest radial turbulence intensities were recorded for Fluids B in the near wall region. The radial turbulence intensity profiles were in line with the near wall effective viscosities. Fluid A was expected to have the highest near wall effective viscosity (as a consequence of the fact that Fluid A had highest elasticity and the resulting extensional viscosity values. So, the velocity fluctuations in radial direction were dampened most for the Fluid A and, as a result, the lowest radial turbulence intensity profiles were observed for this fluid. Similarly,

the highest radial turbulence intensity profiles were observed for the Fluid B because the Fluid B was expected to have the lowest near wall effective viscosity due to the fact that it had the lowest elasticity and the extensional viscosity among the three fluids.

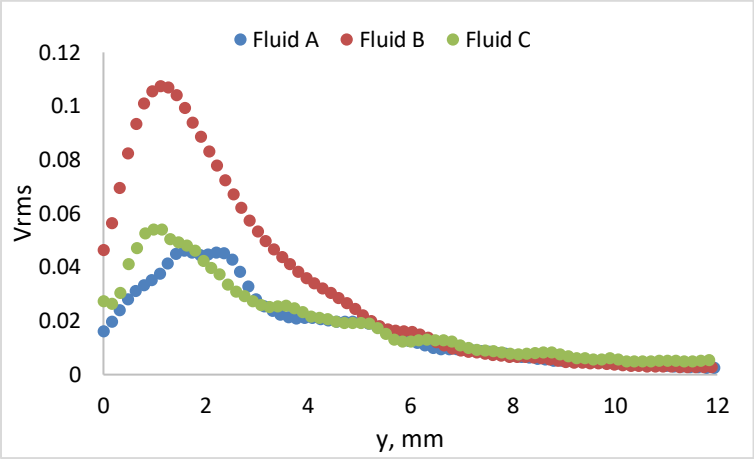

Figure 5-19 Radial turbulence intensity profiles at the flowrate of 221.5 lpm.

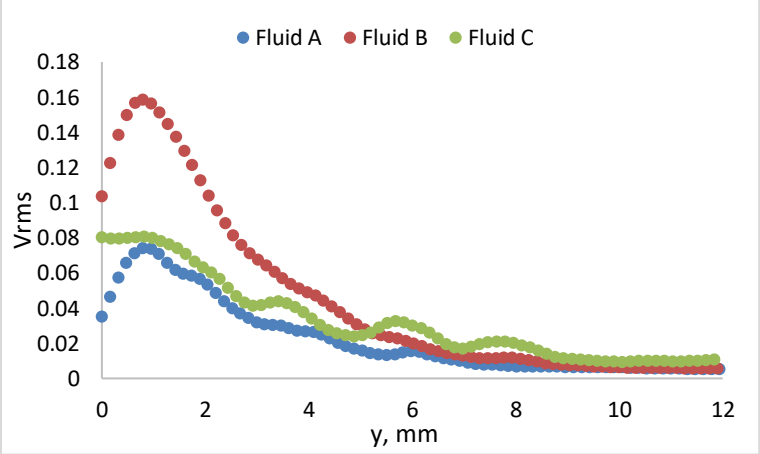

Figure 5-20 Radial turbulence intensity profiles at the flowrate of 316 lpm.

5.4.4. Analyses of the Early Onset of the Turbulence

As explained by the Reiner [35], the structural turbulence is different than the Reynolds' turbulence. In Reynolds' turbulence there is a critical Reynolds number that must be exceeded before the start of the turbulence

in the flow. However, in the structural turbulence, a certain critical shear stress value is required to be exceeded for the start of the turbulent state. According to Ram et al. [35] structural turbulence is more likely to occur for dilute polymer solutions because the structural turbulence occurs as a result of the deformation of polymer chains in solution and in a dilute solution, polymer chains are freer to elongate and extend under the shear force. Flexibility and deformability of polymer chains is so important that the applied shear stress might not be enough to deform the polymer chains, therefore for polymers like Carbopol or Carboxy Methyl Cellulose structural turbulence might not be observed [35].

In this study, we wanted to see whether the structural turbulence for fluids A, B and C occurs or not. First, friction factors vs. Reynolds number plots for each fluid were given a detailed look. Figures 5-21, 5-22 and 5-23 show the friction factors vs. Reynolds number plots for fluids A, B and C, respectively. In these plots, any observed change in the trend of friction factor vs Reynold number can be used to identify the transition (i.e. critical Reynolds number) from laminar to turbulent flow regime. The equation 5-19 defines the critical Reynolds number for power law type fluids [36,37,38]. Critical Reynolds number for Fluid A, B and C were determined by using Equation 5-19 as 2361, 2388 and 2349 respectively. However, the analyses of the friction factor versus Reynolds number plots for these fluids indicate that the critical Reynolds numbers for Fluid A, B and C were around 1844, 2414 and 2388, respectively. So, it seems that for Fluid B and Fluid C transition from laminar to turbulent flow regime occurs on time, but for the Fluid A, an earlier transition from laminar to turbulent flow was observed at Reynolds number of 1844.

$$Re_c = 2100\frac{(4n+2)(5n+3)}{3(3n+1)^2} \quad \text{..... (5-19)}$$

Where Re_c is the critical Reynolds number, n is the power law flow behaviour index.

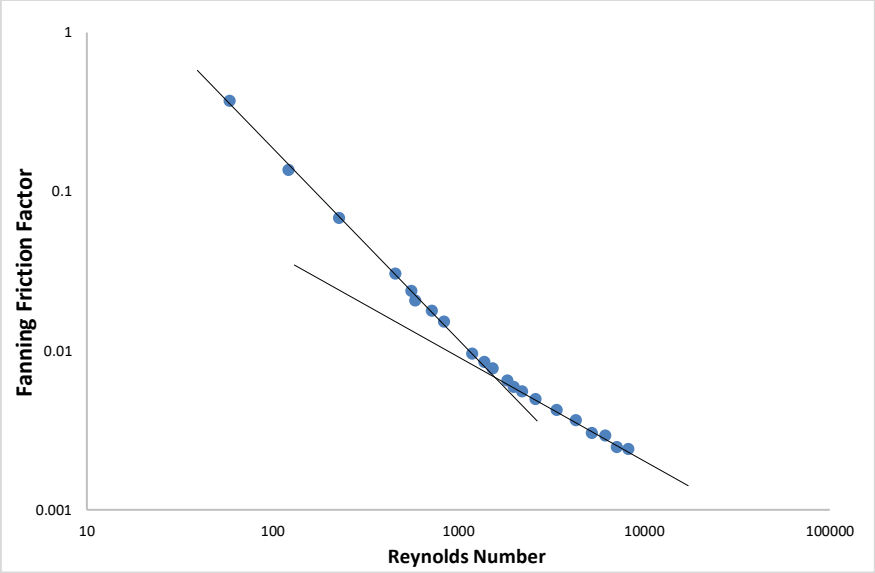

Figure 5-21 Friction factor vs Reynolds number plot of Fluid A.

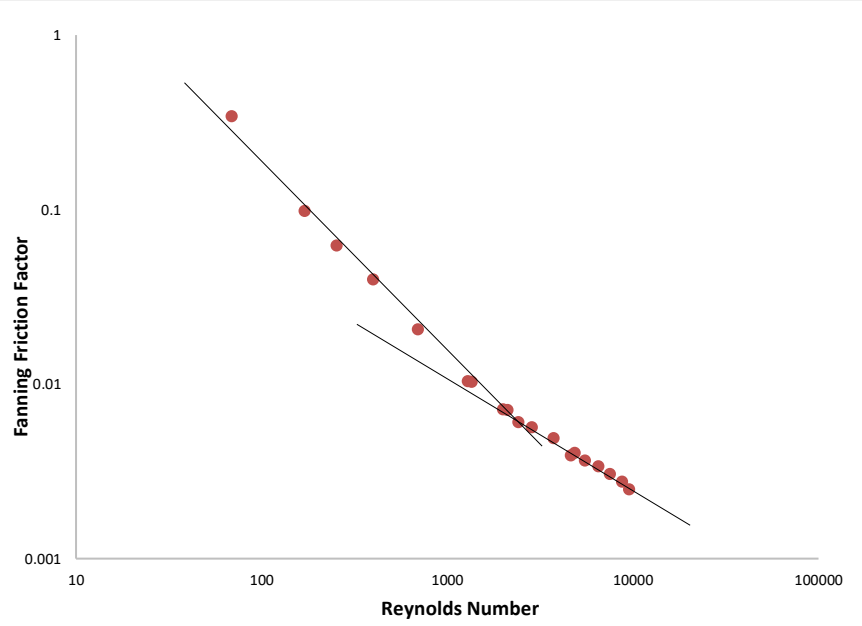

Figure 5-22 Friction factor vs. Reynolds number plot of Fluid B.

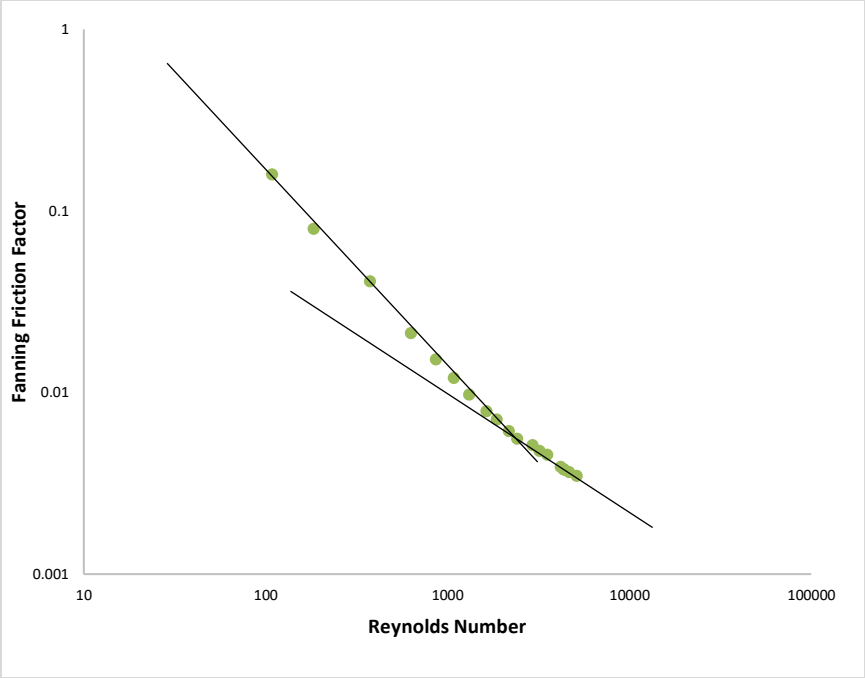

Figure 5-23 Friction factor vs. Reynolds number plot of Fluid C

Forame et al. [15] used flow rate and wall shear stress data in the same plot for dilute solutions of Polyox to detect the transition point from laminar to turbulent regime. We also used a similar approach to verify the estimated transition Reynolds numbers for Fluid A, B and C. Flow rate vs wall shear stress plots of fluids A, B and C are presented in Figure 5-24, Figure 5-25 and Figure 5-26, respectively. In order to be consistent with the analysis of Forame et al. [15], cc/sec was used as the unit for flow rate and dyne/cm^2 was used as the unit for the wall shear stress. For Fluid A, the flow rate after which the deviation from laminar flow regime started was around 170 lpm and the Reynolds number corresponding to 170 lpm in this horizontal loop for Fluid A was around 1900. For the Fluid B the deviation from laminar flow regime starts around 200 lpm and the Reynolds number corresponding to 200 lpm for the Fluid B was 2414. For the Fluid C the deviation from laminar flow regime started around 195 lpm and the Reynolds number corresponding to 195 lpm was 2349. So, for these three dilute polymer solutions, both analyses resulted similar transition Reynolds numbers. Therefore, we concluded that an early turbulence for the pipe flow of Fluid A occurs at a Reynolds number around the range of 1844 to 1900.

However, for Fluids B and C, transition from laminar to turbulent flow occurs at the Reynolds number of 2414 and 2359 respectively. Higher fluid elasticity values might have caused an early turbulence for Fluid A. The early onset of the turbulence might have been caused by the structural turbulence generated by the deformation of the long polymer chains under the shear force of the flow in a circular pipe. In this process, the flexibility or deformability of the polymer molecules forming the solution is crucial.

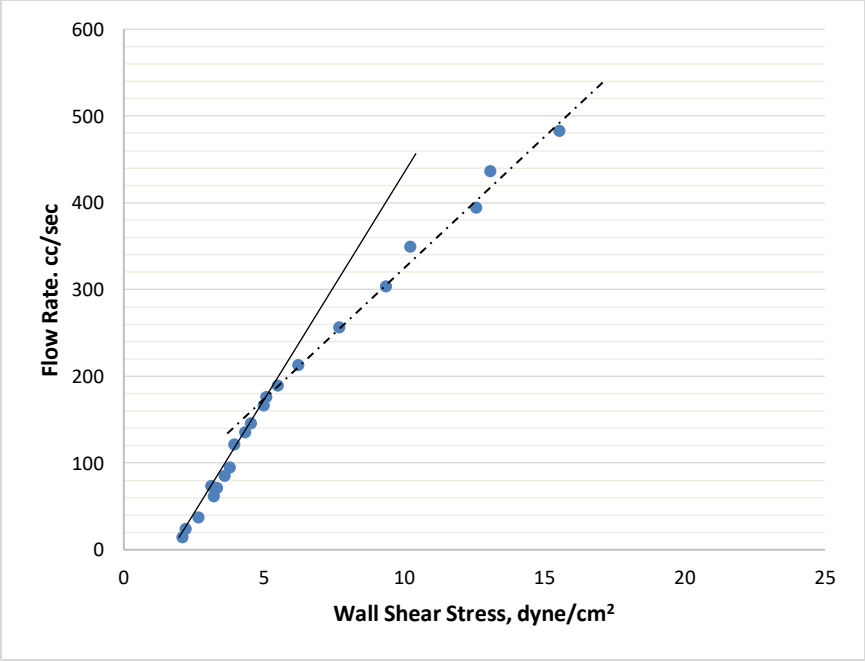

Figure 5-24 Flowrate vs. wall shear stress plot for Fluid A.

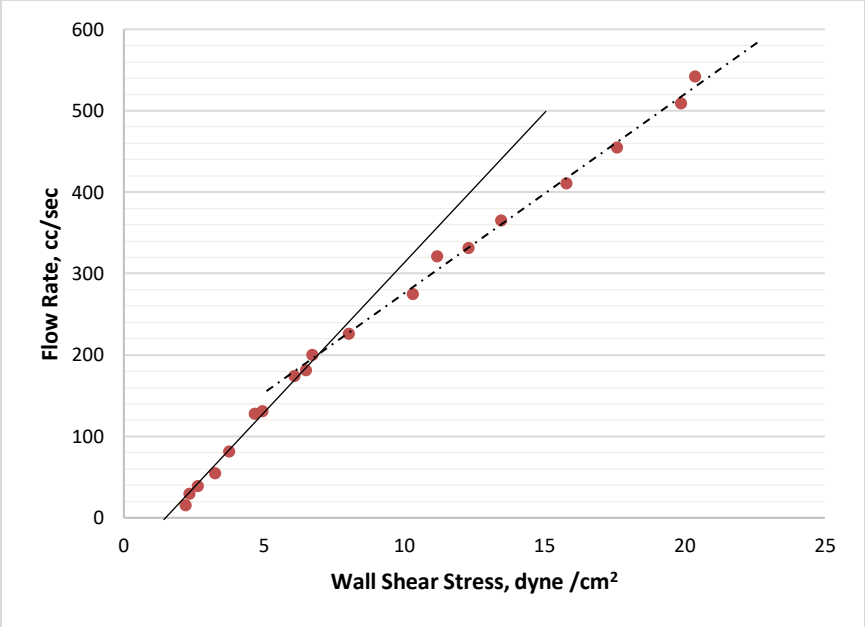

Figure 5-25 Flowrate vs. wall shear stress plot for Fluid B.

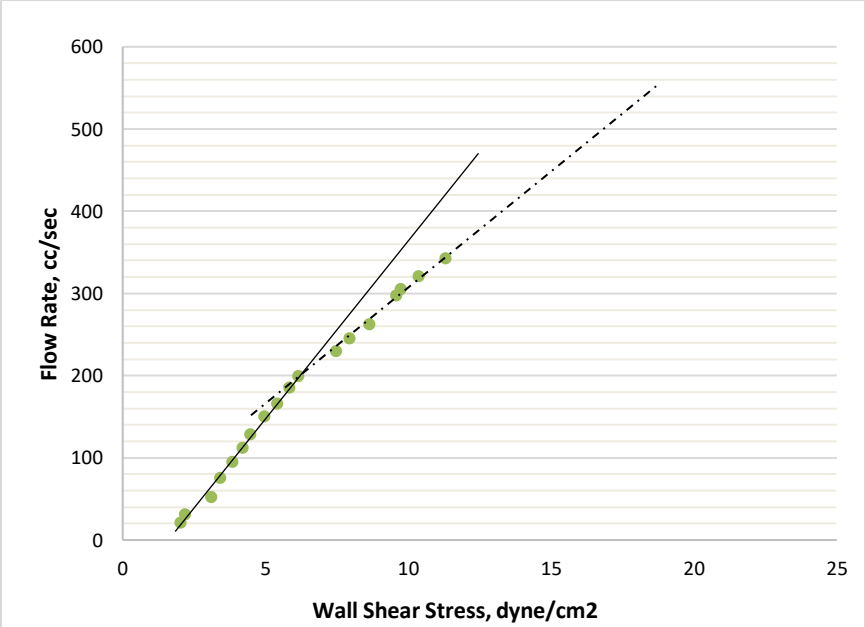

Figure 5-26 Flowrate vs. wall shear stress plot for Fluid C.

5.4.5. Critical Conditions for the Onset of the Drag Reduction and the Maximum Drag Reduction

Bayode et al. [39] conducted a series of flow experiments with dilute polymer solutions of polyacrylamide at different concentrations using different flow geometries including a circular pipe. The concentrations of the polyacrylamide solutions used in their experiments were 5 times lower than the ones used in this study [39]. They found out that drag reducing effect of the polymer solutions were observed after a critical Weissenberg number of 0.5. The drag reduction reached a maximum level at a Weissenberg number of 5 identically for all polyacrylamide-based solutions tested in all geometries [39]. We used a similar approach to analyse our experimental data. The Figure 5-27 shows the drag reduction observed during the flow of Fluids A, B and C versus the Weissenberg number, which is a product of the longest relaxation time and the average shear rate. The drag reductions for these fluids (as compared to water flow) were calculated by using equation 5-20 [39]. In Figure 5-27, it can be seen that the drag reduction for Fluid A, B and C starts after a Weissenberg number around 2. Drag reduction for these fluids increase with increasing Weissenberg number, however drag reduction reaches the MDR (Maximum drag reduction asymptote) around a Weissenberg number of 3 to 4 for Fluid A and Fluid B.

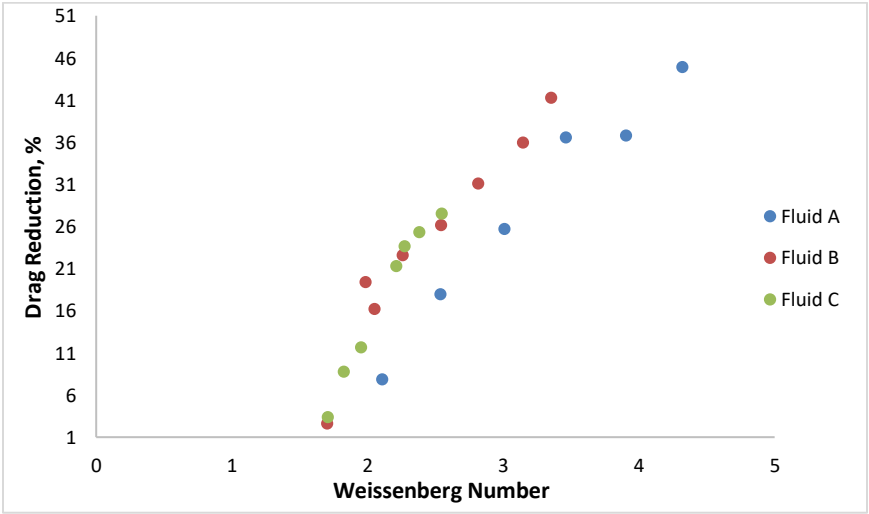

Figure 5-27 Drag reduction in percentage vs Weissenberg number.

$$DR = \frac{\Delta P_N - \Delta P_v}{\Delta P_N} \times 100 \ldots\ldots\ldots\ldots\ldots\ldots \text{(5-20)}$$

Where DR is the drag reduction in percentage, ΔP_N pressure drop for Newtonian fluid (water), ΔP_v is pressure drop for viscoelastic fluid.

For dilute polymer solutions of certain polymer types, existence of a global Weissenberg number for the start of the drag reduction could be claimed. Elongational viscosities developed by the dilute polymer solutions during the flow is the main reason causing the drag reduction as we explained earlier. Elongational viscosity develops as a result of the strain hardening of polymer chains. The development of the elongational viscosity is directly proportional to the Weissenberg number. However, after a certain Weissenberg number, development of the elongational viscosity becomes independent from the increase in strain rate and the Weissenberg number [40]. Gupta et al. [40] also reported that after a certain Weissenberg number, elongational viscosities decrease with increasing strain rate. In their work, this Weissenberg number for the polystyrene solutions they used was determined as 10 [40]. This might explain why drag reduction effect disappears for some dilute polymer solutions after reaching a high strain rate, which was also discussed in details by Walsh [3]. After a certain high strain rate, instead of an increase, a decrease in elongational viscosity is observed and this could be the main reason for the disappear of drag reduction effect for some dilute polymer solutions. We wanted to find out whether this happens for our dilute polymer fluids or not. However, unfortunately, the flow rate range of the horizontal flow loop was not sufficiently high to test this.

5.5. CONCLUSIONS

The experimental study conducted provided valuable information about the effects of elasticity on the frictional pressure losses and the turbulent flow characteristics of the polymer fluid flow in pipe.

Results have shown that viscoelastic properties and the chain length of polymer molecules composing the dilute solution are interrelated and a complete understanding of the flow dynamics of dilute polymer fluids in a horizontal pipe is not possible without considering the effects of the fluid viscoelasticity.

Chain length of polymer molecules basically depends on the molecular weight of the polymer. In dilute polymer solutions intensive deformation abilities of long polymer chains causes each chain to extend in the flow direction and generate significant elongational viscosities especially close to the pipe wall where the shear rate is the highest during the flow. The development of elongational viscosity maximizes the energy transferred in the flow direction by stabilizing the turbulent eddies in the near wall region. As a result, a drag reduction is observed during the flow when even a small amount of high molecular weight polymer is added into a Newtonian solvent. This experimental study showed that more elastic solutions develop higher first normal stresses (and, hence, higher elongational viscosities), and they exhibit lower frictional pressure drops during the flow in a smooth walled circular pipe. Although Fluids A, B and C all have the same viscometric properties (i.e. shear viscosity), the Fluid A, which has the highest elasticity among the three, exhibited the lowest frictional pressure drops. These results were also confirmed by the analyses of the PIV data.

The dimensionless near wall velocity profiles of the Fluid A was the closest to the Virk's asymptote. Also, as the viscous sublayer thickens due to elastic effects, low Reynolds stresses were recorded for each drag reducing fluid.

The lowest radial turbulent intensity profiles were recorded for the flow of the fluid with the highest elasticity in the near wall region. This is mainly due to the stabilized turbulent eddies resulting from the highest elongational viscosities generated by the flow of the most elastic fluid in a smooth walled circular pipe.

In this experimental study, the existence of the early onset of the turbulence during the flow of the three polymer fluids was also investigated. Initially the friction factors vs. Reynolds number plots of these fluids were used to detect the transition from laminar to turbulent regime. These plots showed that early turbulence only

occurs for the most elastic fluid among the three. In order to verify this, another approach suggested by Forame et al. [15] was applied to experimental data and similar transition Reynolds numbers were obtained for each solution and the early turbulence was confirmed to happen once again only during the flow of the most elastic fluid. Therefore, results from this experimental study showed that early turbulence phenomena for dilute polymer solutions can also occur in large diameter pipes (i.e. 95 mm) and the occurrence of the early turbulence is directly related to elastic properties of a solution. If the elasticity of a solution and the deformability of the polymer chains forming the solution are high enough, an earlier turbulence might be triggered as the deformed polymer chains would cause a structural turbulence.

Also, these experiments gave us an opportunity to discuss the conditions required for the onset of the drag reduction and reaching maximum drag reduction for a dilute polymer solution. Based on the results of these experiments and similar studies in the literature, we concluded that a certain Weissenberg number could be suggested as the critical Weissenberg number for the onset of drag reduction of dilute solutions of certain polymers. This is also valid for reaching the maximum drag reduction level. Elongational viscosity does not increase anymore with the increasing strain rate after a certain Weissenberg number and, therefore, at a certain Weissenberg number or strain rate the drag reduction reaches the MDR. Also, the decrease in elongational viscosity starts after a certain shear rate or Weissenberg number could be the main reason causing drag reduction effect to disappear at high shear rates for dilute polymer solutions.

In conclusion, viscoelasticity is crucial to understand the flow of dilute polymer solutions in a horizontal pipe. The frictional pressure drops, turbulent flow characteristics, transition of the flow regime from laminar to turbulent are all affected by viscoelastic properties of dilute polymer solutions. Weissenberg number and the relaxation times might be used as influential parameters to monitor the effect of viscoelasticity for the flow of dilute polymer solutions in horizontal pipes. Manipulation of viscoelastic properties while designing drilling and

hydraulic fracturing fluid systems may bring radical solutions to problems associated to the horizontal and extended reach well drilling, hydraulic fracturing as well as the transportation of hydrocarbons through pipelines.

5.6. ACKNOWLEDGEMENTS

This research is financially supported by the funds available from Natural Sciences and Engineering Research Council of Canada (NSERC RGPIN-2016-04647 KURU).

5.7. REFERENCES

1. Toms, B. A. (1948). Some observations on the flow of linear polymer solutions through straight tubes at large Reynolds numbers. In Proceedings of the 1st International Congress on Rheology, vol. 2, pp. 135–141. North-Holland.
2. Savins, J. G. (1966). A Stress-Controlled Drag-Reduction Phenomenon. Society of Petroleum Engineers. doi:10.2118/1724-MS
3. Walsh, M. (1967). On the Turbulent Flow of Dilute Polymer Solutions 11, Ph.D. Thesis, Calif. Inst. Tech., Pasadena, Calif.
4. Rouse, E. P. (1953). A Theory of the Linear Viscoelastic Properties of Dilute Solution of Coiling Polymers. The Journal of Chemical Physics. 21. 1272-1280. doi:10.1063/1.1699180.
5. Elata, C., J. Lehrer and A. Kahanovitz (1966). Turbulent Shear Flow of Polymer Solutions. Israel Journal of Technology, Vol. 4, No. 1, 1966, pp. 87-95.
6. Virk, P. (1971). An elastic sublayer model for drag reduction by dilute solutions of linear macromolecules. Journal of Fluid Mechanics, 45(3), 417-440. doi:10.1017/S0022112071000120
7. Lumley, J. (1973). Drag Reduction in Turbulent Flow by Polymer Additives. Journal of Polymer Science: Macromolecular Reviews. 7. 263 - 290. doi:10.1002/pol.1973.230070104.
8. Achia, B., Thompson, D. (1977). Structure of the turbulent boundary in drag-reducing pipe flow. Journal of Fluid Mechanics, 81(3), 439-464. doi:10.1017/S002211207700216X
9. Massah, H., Hanratty, T. (1997). Added stresses because of the presence of FENE-P bead–spring chains in a random velocity field. Journal of Fluid Mechanics, 337, 67-101. doi:10.1017/S0022112097004916

10. Dimitropoulos, C., Sureshkumar, R., Beris, A. (1998). Direct numerical simulation of viscoelastic turbulent channel flow exhibiting drag reduction: Effect of the variation of rheological parameters. Journal of Non-Newtonian Fluid Mechanics. 79. 433-468. doi:10.1016/S0377-0257(98)00115-3.

11. Pinho, F. (2003). A GNF framework for turbulent flow models of drag reducing fluids and proposal for a k-type closure. J. Non-Newtonian Fluid Mech. 114. 149-184. doi:10.1016/S0377-0257(03)00120-4.

12. Bonn, D., Amarouchene, Y., Wagner, C., Douady, S., Cadot, O. (2005). Turbulent drag reduction by polymers. Journal of Physics: Condensed Matter. 17. S1195. doi:10.1088/0953-8984/17/14/008.

13. Groisman, A., Steinberg, V. (2004). Elastic turbulence in curvilinear flows of polymer solutions. New Journal of Physics. 6–29. doi:10.1088/1367-2630/6/1/029.

14. Hansen, R. J., Little R. C. (1974). Early turbulence and drag reduction phenomena in larger pipes. Nature. doi:10.1038/252690a0, 252, 5485, (690-690)

15. Forame, P. C., Hansen, R. J., Little, R. C. (1972). Observations of early turbulence in the pipe flow of drag reducing polymer solutions. AIChE J., 18: 213-217. doi:10.1002/aic.690180139

16. W. Hoyt, J. (1977). Laminar-turbulent transition in polymer solutions. Nature. 270. 508-509. doi:10.1038/270508a0.

17. Dubief, Y., Terrapon, V., Soria, J. (2013). On the mechanism of elasto-inertial turbulence. Physics of fluids (Woodbury, N.Y.: 1994). 25. 110817. doi:10.1063/1.4820142.

18. Samanta, D., Dubief, Y., Holzner, M., Schäfer, C., Morozov, A., Wagner, C., Hof, B. (2013). Elasto-inertial turbulence. Proceedings of the National Academy of Sciences of the United States of America. 110. doi:10.1073/pnas.1219666110.

19. Arnipally, S. K., Kuru, E. (2018). Settling Velocity of Particles in Viscoelastic Fluids: A Comparison of the Shear-Viscosity and Elasticity Effects. Society of Petroleum Engineers. doi:10.2118/187255-PA

20. Bizhani, M. (2017). Experimental and Theoretical Investigations of Particle Removal from Sand Bed Deposits in Horizontal Wells Using Turbulent Flow of Water and Polymer Fluids. PhD Thesis, Civil and Environmental Engineering, University of Alberta, Edmonton, Canada.

21. Metzner, A.B., Reed, J.C. (1955). Flow of non-Newtonian fluids—correlation of the laminar, transition, and turbulent-flow regions. AICHE Journal,1(4), pp.434-440.

22. Raffel, M., Willert, C. E., Kompenhans, J. (2007). Particle Image Velocimetry: A Practical Guide: Springer Science & Business Media.

23. LaVision, Davis 8.3 Product Manual. ed, 2015.

24. Kundu, P. K., Cohen, I. M., Dowling, D. R. (2012). Fluid Mechanics, 5th Edition. Amsterdam, Elsevier Science Bv.

25. Virk, P. S. (1975). Drag reduction fundamentals. AIChE J., 21: 625-656. doi:10.1002/aic.690210402

26. Skelland, A. H. P. (1967). Non-Newtonian flow and heat transfer. Wiley, New York.

27. Roylance, D., (2001). Engineering Viscoelasticity. Department of Materials Science and Engineering Massachusetts Institute of Technology Cambridge, MA 02139

    Retrieved from http://web.mit.edu/course/3/3.11/www/modules/visco.pdf

28. Hatfield, J. W., Quake, S. R. (1999). Dynamic Properties of an Extended Polymer in Solution. Physical Review Letters, 82 (17). pp. 3548-3551. ISSN 0031-9007.

29. Xiao, Q., Wang, A., Tao, W. (1996). Experimental study for pressure drop of viscoelastic fluids through periodically sudden converging-diverging tube. Journal of Thermal Science. 5. doi:19-23. 10.1007/BF02663727.

30. Gyr, A., Bewersdorff, H. (1995). Drag Reduction of Turbulent Flows by Additives. Springer, Dordrecht

31. Zell, A., Gier, S., Rafai, S., Wagner, C. (2009). Is there a Relationship between the Elongational Viscosity and the First Normal Stress Difference in Polymer Solutions?

32. Oldaker, K. D., Tiederman, G. W. (1977). Spatial structure of the viscous sublayer in drag-reducing channel flows. Physics of Fluids - PHYS FLUIDS. 20. doi:10.1063/1.861722.

33. Massah, H., Hanratty, T. (1997). Added stresses because of the presence of FENE-P bead–spring chains in a random velocity field. Journal of Fluid Mechanics, 337, 67-101. doi:10.1017/S0022112097004916

34. Flierl, G., Ferrari, R. 12.820 Turbulence in the Ocean and Atmosphere. Spring 2007. Massachusetts Institute of Technology: MIT OpenCourseWare, https://ocw.mit.edu. License: Creative Commons BY-NC-SA.

35. Ram, A., Tamir, A. (1964). Structural turbulence in polymer solutions. J. Appl. Polym. Sci., 8: 2751-2762. doi:10.1002/app.1964.070080621.

36. Mishra, P., Tripathi, G. (1971). Transition from laminar to turbulent flow of purely viscous non-Newtonian fluids in tubes. Chemical Engineering Science, 26, 915-921

37. Mishra, P., Tripathi, G. (1973). Heat and Momentum-Transfer to Purely Viscous Non-Newtonian Fluids Flowing Through Tubes. Transactions of The Institution of Chemical Engineers, 51, 141-150

38. Trinh, T. (2010). On the Critical Reynolds Number for Transition from Laminar to Turbulent Flow.

39. Bayode, E. O., Dennis, D., Poole, R. (2017). Turbulent drag reduction by polymer additives in parallel-shear flows. Journal of Fluid Mechanics. 827. doi:10.1017/jfm.2017.544.

40. Gupta, R. K., Nguyen, D. A., Sridhar, T. (2000). Extensional viscosity of dilute polystyrene solutions: Effect of concentration and molecular weight. Physics of Fluids 2000 12:6, 1296-1318. doi: 10.1063/1.870383

6. EFFECT OF FLUID ELASTIC PROPERTIES ON THE BED EROSION DYNAMICS OF A SAND BED DEPOSITED IN A HORIZONTAL PIPELINE

6.1. ABSTRACT

An experimental study was conducted to investigate how the fluid elastic properties would influence, the frictional pressure drops, the critical velocity for the onset of the bed erosion, and turbulent flow characteristics (i.e. Reynolds stress, axial and radial turbulence intensity profiles) of the polymer fluid flow over the stationary sand bed deposited in horizontal pipeline.

A 9m long horizontal flow loop (pipe ID: 95 mm) equipped with particle image velocimetry (PIV) system was used for the experiments. The polymer fluids, which had almost identical shear viscosity characteristics while showing significantly different elastic properties (quantified in terms of relaxation time) were used together with 30/50 mesh size industrial sands in the bed erosion experiments. Polymer fluids were prepared by mixing three different grades (i.e. $5x10^5$, $8x10^6$, $20x10^6$ g/gmol) of partially hydrolysed polyacrylamide (HPAM) polymer.

After determining the critical velocities for the onset of the bed erosion using both fluids, the frictional pressure drops at critical and several subcritical velocities were recorded for both fluids. Additionally, instantaneous near bed velocities were measured by using the PIV technique. Further analyses of the velocity data obtained by PIV technique, we were able to determine the turbulent flow features such as Reynolds stress, axial and radial turbulence intensity profiles.

Results showed that the fluid elasticity affects the bed erosion dynamics significantly. Generally, frictional pressure drops, and critical velocities for the bed erosion all increased with the increasing fluid elasticity.

This paper presents results of an experimental study where the PIV technique was used to investigate the bed erosion dynamics due to the turbulent flow of elastic polymer fluid over the stationary sand beds. Fluids were prepared using a special technique, which allowed us to alter the fluid elastic properties while keeping the

shear viscosity constant. By conducting experiments under controlled conditions, for the first time in drilling literature, we were able to quantify the individual effect of the fluid elasticity (independent from shear viscosity) on the critical flow rate for bed erosion and the turbulent flow characteristics of polymer fluid flow over the stationary sand bed.

6.2. INTRODUCTION

Effective transportation of the drilled cuttings to the surface is an important operational concern in oil and gas well drilling. Bilgesu et al. [1] stated that hole cleaning and cutting transport becomes difficult in deviated wells as the hole angle increases and even becomes more challenging for a horizontal or extended reach well. If well-established and properly-designed hole cleaning practices are not followed, then the drilled cuttings deposited on the lower side of the well might cause serious operational problems such as excessive torque and drag, slow drilling rate, pack-off, bridging, hole fill and a pipe stuck as the worst-case scenario [2,3,4]. Therefore, the hole cleaning and its optimization in horizontal and extended reach wells has become a very important research area in petroleum engineering and majority of these studies have been focusing on the effects of the drilling fluids.

The fluid rheological properties and circulation rates are the two main operational variables significantly affecting the hole cleaning performance. Adari et al. [5] investigated the effect of fluid rheological properties and flow rates on cuttings bed erosion through a broad set of experiments. Rabenjafimanantsoa et al. [6] and Bizhani et al. [7] reported the delay in onset of particle movement in bed erosion tests conducted by using polymer fluids. Walker et al. [8], on the other hand, concluded that polymer-based fluids had higher cutting carrying capacity. Based on the field practices from North Sea operations, Saasen and Loklingholm [9] discussed the hole cleaning performance of polymer-based drilling fluids in detail and they concluded that the gel forming as a result of the interaction of cuttings bed and polymer-based drilling fluid is an important factor undermining hole cleaning performance of polymer-based fluids. Therefore, Saasen and Loklingholm [9] suggested the use of high molecular weight polymers only to prevent barite sag [9]. Duan et al., [10] recommended the use of polymer-based fluids

while drilling continues to effectively remove the small particles from the well, but for post-drilling cleanout operations they indicated that use of low viscosity fluids would be more effective. In all these works mainly, viscometric properties of polymer-based fluids were considered and analysed in terms of hole cleaning. However, most of the drilling fluids possess not only viscous but also elastic properties, which might also influence the flow dynamics and interactions of those fluids with the drill cuttings. Powell et al. [11] related the elasticity with the gel-like behaviour and their analysis showed that elasticity enhanced the suspension ability of the biopolymer fluids. Similarly, Zamora et al. [12] mentioned that elasticity enhances the hole cleaning in laminar flow and increases the suspension ability for the biopolymer-based fluids. Cuttings transport experiments conducted by Sayindla et al., [13] and the follow up study by Werner et al. [14] have shown that oil-based fluids had a superior cutting transport ability comparing to water-based fluids despite having the similar viscometric properties. Werner et al. [14] also reported that the water-based drilling fluid used in their study had no yield stress and a 50–100% higher elasticity than the oil-based drilling fluids.

Results from all these previous laboratory tests and field experience indicate that fluid elastic properties play important role in cuttings transport and should be given due consideration together with fluid viscous properties in order to have more realistic assessment of the cuttings transport ability of a drilling fluid. However, there are not many studies in the literature investigating the individual (as well as combined) effects of drilling fluid viscometric properties (i.e., shear viscosity, yield stress) and the elastic properties on the hole cleaning [14].

Recently, Bizhani and Kuru [15] studied the effect of viscoelasticity on the particle removal from a stationary sand bed deposited in horizontal pipeline. They reported that the delay in particle movement was observed when they used fluid with higher elasticity for bed erosion experiments. Bizhani and Kuru [15] concluded that elastic normal forces arising from the normal stress differences due to the variation of the fluid elastic properties were responsible for this behaviour. One of the limitations in Bizhani and Kuru [15] study was that the fluids used in their study had different elastic properties as well as different shear viscosity values. Therefore, the difference in

hole cleaning performance of these two fluids could be affected by the change in both the elastic properties and shear viscosities. In this study, we removed this limitation by formulating two fluids, which had almost identical shear viscosity characteristics while showing significantly different elastic properties (quantified in terms of the longest relaxation time). We then conducted bed erosion experiments using these two fluids under controlled conditions and, for the first time in drilling literature, we were able to quantify the individual effect of the fluid elasticity (independent from shear viscosity) on the critical flow rate for bed erosion and the turbulent flow characteristics of polymer fluid flow over the stationary sand bed.

6.3. MATERIALS AND METHODS

6.3.1. Sand Particles

30/50 mesh size (297-590 microns) industrial quartz sand particles (SG =2.65) were used in this study.

6.3.2. Polymer Fluids

Two dilute polymer fluids having the same shear viscosity, but different elastic properties were used as the transport fluid in the bed erosion tests. These fluids were prepared by mixing three different grades of HPAM (Partially Hydrolysed Polyacrylamide). Information such as molecular weight, material name for those three grades are summarized in Table 6-1. All these grades of HPAM are water soluble with a degree of hydrolysis of around 30 %.

Table 6-1 Molecular weight of different HPAM polymer grades

Polymer Name	Molecular Weight (g/gmol)
HPAM AB 005V	$5x10^5$
HPAM 3330S	$8x10^6$
HPAM 3630S	$20x10^6$

The average molecular weight of a polymer mix of multiple components can be determined by using the Equation 6-1 [16].

$$M_{w,B} = \prod_{i=1}^{n} M_{w,i}^{\omega_i} \quad \text{..... (6-1)}$$

In Equation 6-1, $M_{w,B}$ is the average molecular weight of the polymer blend, ω_i is the weight fraction of the polymer grade i, $M_{w,i}$ is the molecular weight of polymer grade i. Polymer fluids prepared by using polymer mix of the same average molecular weight would have the similar shear viscosity [16]. Polymer compositions and concentrations used for formulations of Fluids A and B are summarized in Table 6-2. Although the molecular weight distribution was different, the average molecular weight of the polymer mixes used in Fluid A and B were the same. Therefore, these two fluids are expected to show the same shear viscosity behaviour as it will be shown later in section 3.1. Polymer concentrations for both fluids were adjusted to make sure that fluids prepared in the mixing tank would have the similar shear viscosity characteristics. Elastic properties of the polymer fluids strongly depend on molecular weight of the individual polymer present in the polymer mix as well as the molecular weight distribution (MWD) of the polymer mix. The polydispersity index defined by Equation 6-2 can be used as an indicator of the MWD. Fluids prepared by using polymer mix of higher polydispersity index would generally show higher elasticity [16].

$$I = \frac{M_w}{M_n} = \left(\sum_{i=1}^{n} \omega_i M_{w,i} \right) \times \left(\sum_{i=1}^{n} \frac{\omega_i}{M_{w,i}} \right) \quad \text{..... (6-2)}$$

In Equation 6-2; I is the polydispersity index, M_w is the weighted average molecular weight, M_n is the number average molecular weight, ω_i is the weight fraction of the polymer grade i, $M_{w,i}$ is the molecular weight of polymer grade i.

In order to prepare two fluids having distinctly different elastic properties, the polymers mix used for formulation of these fluids should be prepared in such a way that the difference in polydispersity indexes (I) of two mixtures would be as high as possible. Therefore, Fluid A was prepared by mixing HPAM AB 005V and HPAM 3630S grade polymers (I=8.05), while the Fluid B was only composed of HPAM 3330S grade (I=1.0). Table2 summarizes compositions and concentrations used for Fluid A and Fluid B based on Equation 6-1, Equation 6-2 and the mixing experience.

Table 6-2 Polymer compositions and concentrations of Fluid A and Fluid B

Mixture	Concentration	HPAM AB005V (w%)	HPAM 3330S (w%)	HPAM 3630S (w%)	Average Molecular Weight	Polydispersity Index
Fluid A	0.135	24.2	0	75.8	$8x10^6$	8.05
Fluid B	0.095	0	100	0	$8x10^6$	1

Frequency sweep tests were used to determine the elastic properties. The longest relaxation time was used as a measure of the fluid elasticity in this case. Viscometer tests were carried out to determine shear stress vs. shear rate behaviour. All the rheological characterization measurements were carried out by using a high-resolution rheometer, Bohlin C-VOR 150. Samples were collected from the suction tank after mixing the fluids just before the flow loop experiments conducted. Each measurement was repeated at least two times to check the repeatability of the results. Rheometer measurements were also conducted by using the samples collected from mixing tank

after finishing the flow loop experiments. These later tests were carried out to see if there was any change in the fluid rheological properties due to any possible degradation that might have occurred as a result of time lapse or applied high shear rates during the experiments.

6.3.3. Experimental Setup

Figure 6-1 shows the schematic of the horizontal flow loop used in the experimental study. Main components of the flow loop are a suction tank of 500 litres capacity, a variable frequency drive centrifugal pump, differential pressure transducers, a magnetic flow meter, and several gate valves for flow control in the system.

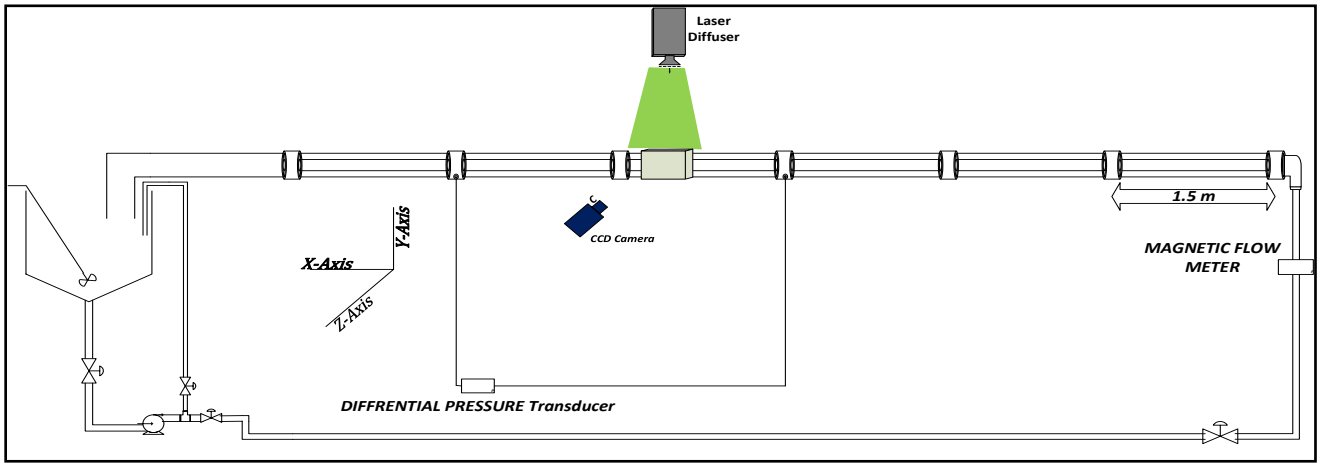

Figure 6-1 Schematic diagram of the experimental flow loop [17].

The main flowline is composed of 9 m long horizontal pipeline (ID=95 mm). The pipeline is made out of borosilicate glass pipes. A variable frequency drive (VFD) system allows controlling the circulation rate through the flow loop by changing the rpm of the electric pump via National Instrument's Labview software. OMEGA FMG607-R magnetic flow meter measures the flow rate at the inlet of the test section with an error margin of ±0.5%. OMEGA DPG409 differential pressure transducer measures the frictional pressure drop across 3.08 m long pipe section with an error margin of ±0.08% in the horizontal flow loop.

The flow loop is also equipped with particle image velocimetry (PIV) system used for velocity field measurement within the designated test section. Figure 6-2 shows the section, where all the Particle Image Velocimetry (PIV) data are recorded and the camera and laser arrangement for the tests run. As shown in Figure 6-2, the glass pipe is positioned inside a rectangular glass box filled with glycerol. Glycerol and the glass pipe have the similar refractive index, so this arrangement allows the laser light to be impinged upon the fluid orthogonally and minimize the measurement errors arising from the circular shape of the glass pipe causing refraction of the laser light.

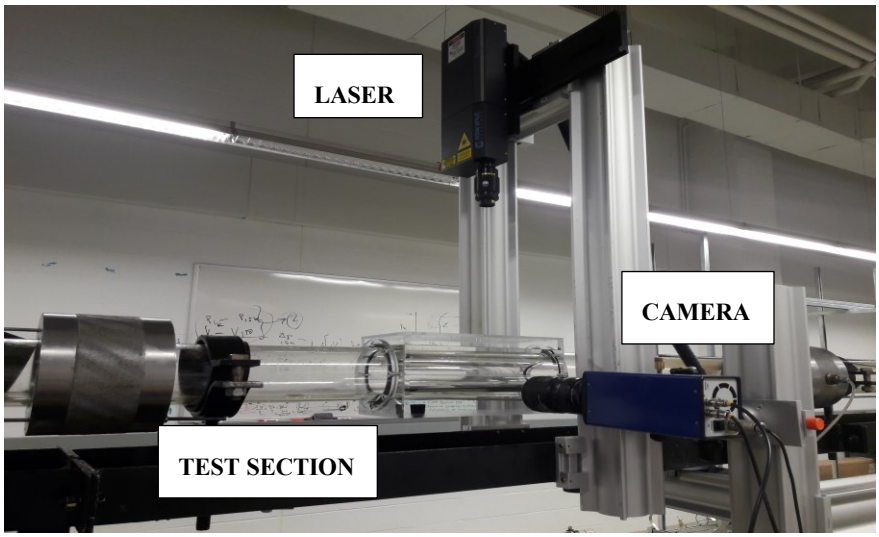

Figure 6-2 Image of the PIV setup and the test section

The PIV system is composed of a double pulsed Laser (New Wave Research Solo III Nd: YAG), a high-speed camera (Lavision Imager Intense CCD camera) and a lens (Nikon 50 mm AF Nikkor lens of 1.4 mm aperture). A commercial software Davis 8.3 was used to record and process the PIV data. The wavelength of the laser light was 532 nm. The camera was a double framed camera with a 12-bit CCD sensor of having 1376 x 1040 pixels.

In addition, videos were recorded at the critical flow rates of the fluids tested showing the onset of sand particle movement. A Samsung digital camera - 8 MP, f/2.4, 31 mm, AF, 1080p @ 30fps - was used to record these videos.

6.3.4. Experimental Procedure

The experimental procedure consisted of three main stages. The first stage was establishment of the sand particle bed; the second stage was polymer the fluid preparation and circulation over the stationary sand bed and the determination of the critical flow rate; and the third stage was PIV measurements at selected subcritical flow rates and at the critical flow rate. All the three steps are briefly explained below.

6.3.4.1.Sand Bed Establishment

Firstly, the suction tank was filled with water. Then, while keeping water in circulation at the highest possible flow rate through the horizontal loop, the sand particles were added slowly to the tank. The amount of sand added is crucial to get the same bed height for different sand size range. When the sand bed was uniform along the flow loop, circulation was stopped and valves on the both end of horizontal section were closed. Water in the flow loop was kept under static condition over the night to allow all sand particles in the suspension to settle down and form a continuous bed.

6.3.4.2.Polymer Fluid Circulation, Calibration of Pressure Transducer, and Measurement of Critical Flow Rates

After allowing all the sand particles to settle down and establishing the uniform bed, the water in the flow loop was drained completely. Then, the mixing tank was isolated from the rest of the loop and filled with 500 litres water. The necessary amount of polymer blend based on the concentrations and compositions determined previously were slowly added to the tank while the air mixer was on with a rotational speed around 300 rpm. The fluid was mixed in the suction tank till a homogeneous solution was obtained. When the mixture was ready, the fluid was circulated through the flow loop starting from low flow rates. The flow rate was then gradually increased in a sequence. When the first movement of the sand particles were observed (i.e., onset of the bed erosion), then the respective flow rate was recorded as the critical flow rate for that particular sand size range. The Lab view

software was used to record critical and subcritical flow rates and the corresponding frictional pressure losses. To check the accuracy of measured frictional pressure drops, the experimental friction factor values measured for water only (no sand bed) in the horizontal flow loop were compared with theoretical ones calculated from the conventional pipe flow correlation given for water flow [18] as shown in Figure 3.

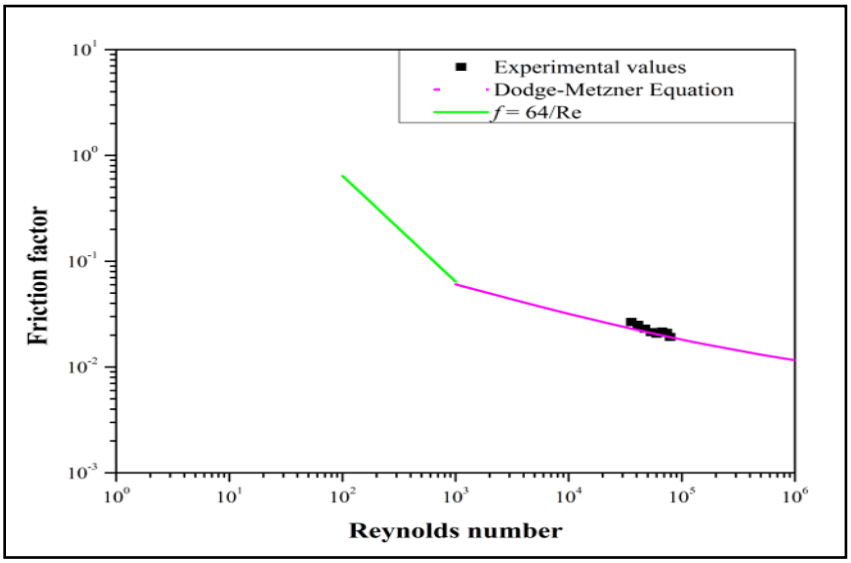

Figure 6-3 Comparison of experimental friction factor values estimated from water only flow tests against the ones calculated from Dodge and Metzner equation [18]

6.3.4.3. PIV Measurements

PIV is a non-intrusive optical measurement technique extensively used to measure the instantaneous velocities in various fluid flows and for further analysis of the flow phenomena [19]. In this technique, the flow is seeded by tracer particles sensitive to the light and flow is recorded by a double frame high speed CCD camera while the fluid is exposed to the laser beam. The images taken are processed by a commercial software or a specially designed fast Fourier transformation (FFT) code and finally, the detailed description of the flow field (i.e. velocity and direction) is obtained [19].

A double pulse laser (as the light source) and a double frame CCD camera (as the recording device) were the basic components of the PIV setup used in these experiments. The camera view must be orthogonal to the laser light as shown in Figure 6-2. The tracer particles were added to the system and circulation was maintained for a while to obtain a homogenous tracer distribution before recording the data. The tracer particles are hollow glass spheres with a mean diameter of 10 microns and density of those particles were similar to the density of the transport fluid so that the particles in the fluid can float freely and follow the fluid motion during the flow. Due to presence of tracer particles in the fluid, exposed light is reflected to the camera. This reflected light was then detected as bright spots in the two successive images captured by the camera. An example of a typical PIV image taken during the experiments is shown in Figure 6-4a. In this image, the cuttings bed is seen as located at the bottom while the polymer fluid is flowing over the top. The bright spots are the tracer particles reflecting the laser light exposed on them. These pictures were processed by Davis 8.3 software by using the proper settings to determine the instantaneous velocity field of the flow. To optimize the accuracy of the measurements at least 1000 pair of images were captured analysed for each flow experiment.

6.3.5. Data Processing and Analysis

Data processing and analysis has two parts. In the first part, we determine the critical velocity. The status of the bed at various flow rates were observed and recorded by a video camera. When the particle or sand bed movement was first detected visually, the flow rate was recorded as the critical flow rate for that particular mesh size of sand particles.

In the second part, we recorded the PIV data and analysed the recorded data set. The light sensitive tracer particles following the fluid flow were seen as the bright spots in each pair of captured PIV images, and they were detected by the Davis 8.3 software.

By cross correlating these pair of images, the displacement of particles between the two images was determined [20]. Since the time interval between the images was known, the instantaneous velocities were calculated for all flow field by using the particle displacement (Δx and Δy) and time interval (Δt) as follows:

$$\begin{cases} \hat{u} = \frac{\Delta x}{\Delta t} \\ \hat{v} = \frac{\Delta y}{\Delta t} \end{cases} \qquad \text{..... (6-3)}$$

In order to find out the displacement of detected bright spots in x and y direction, Davis 8.3 software applied an FFT based cross correlation method [20]. Firstly, both images were divided into small interrogation windows. These windows in two images were then directly cross correlated one by one [20]. The highest peak value for the correlation gave the exact displacement for the particle group detected. A multi-pass approach starting from window size of 64 x 64 down to 24 x 24 including 32 x 32 size in between was used in PIV image processing with overlap of 50%. The data obtained at the end of processing were extracted to excel files for further data analysis. An example of the final velocity vector field for the flow over the cuttings bed is shown in Figure 4b.

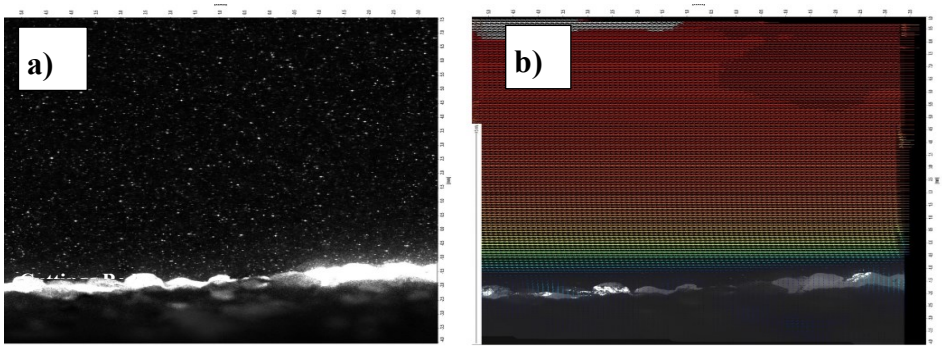

Figure 6-4 a) Typical PIV image acquired during the tests, b) resultant velocity field.

Four main turbulent features; Reynolds stresses, axial turbulence intensities, radial turbulence intensities and near wall dimensionless velocities were given a closer look and compared for the flow over sand particle beds to detect the similarities and differences in the turbulent characteristics of the flow. The software, Davis 8.3,

estimates all these turbulent features based on the defining equations for those terms using the velocities and velocity fluctuations measured in x and y directions by analysing the image set captured.

The near wall velocity profiles were presented in terms of dimensionless distance (y+) and dimensionless velocity units (u^+) as defined by equations 6-4 and 6-5, respectively.

$$y^+ = \frac{\rho y u_\tau}{\mu} \quad \text{..... (6-4)}$$

$$u^+ = \frac{u}{u_\tau} \quad \text{..... (6-5)}$$

$$u_\tau = \sqrt{\frac{\tau_b}{\rho}} \quad \text{..... (6-6)}$$

Where u_τ is the friction (shear) velocity, τ_b is the interfacial bed shear stress (i.e., shear stress at the fluid/sand bed interface), and ρ is the fluid density. The interfacial bed shear stress, τ_b, cannot be deduced accurately from frictional pressure loss data because more than one surface is involved in the flow (i.e., pipe wall and the bed surface). Therefore, the friction velocity, u_τ, cannot be directly estimated by using the bed shear stress. In this study, we have determined the friction velocity, u_τ, by using the plot of velocity versus vertical distance from the surface of the sand bed. These data were obtained directly from PIV measurements. The detailed procedure for determining the friction velocity from the PIV measured velocity data is given elsewhere [17].

The universal law of the wall states that the near wall velocity profiles generally consists of three regions depending upon the dimensionless distance from the bed: Viscous sub-layer $y^+ < 5$, buffer region $5 < y^+ < 30$ and log-law region $y^+ > 30$. The universal velocity profile for a hydrodynamically smooth flow condition is defined by Equation 6-7 [21].

$$u^+ = \begin{cases} y^+ & y^+ < 10 \\ 2.44 ln(y^+) + 5.5 & y^+ > 30 \end{cases} \quad \text{..... (6-7)}$$

Virk's asymptote which is the upper limit for maximum pressure reduction is defined by Equation 6-8 [22].

$$u^+ = 11.7\ln(y^+) - 17 \quad \text{..... (6-8)}$$

The Reynolds shear stress (or turbulent shear stress) is a direct function of the velocity fluctuations (u' and v') in the turbulent flow as defined by the Equation 6-9:

$$\tau_R = -\rho\overline{u'v'} \quad \text{..... (6-9)}$$

The axial turbulence intensity is defined by the Equation 6-10:

$$u_{rms} = \sqrt{\overline{u'u'}} \quad \text{..... (6-10)}$$

The radial turbulence intensity is defined by the Equation 6-11:

$$v_{rms} = \sqrt{\overline{v'v'}} \quad \text{..... (6-11)}$$

6.4. RESULTS AND DISCUSSIONS

6.4.1. Rheological Properties of Polymer Fluids

The shear stress versus shear rate diagram of the Fluids A and B are presented in Figure 6-5. The viscometer data shown in Figure 6-5 confirm that both fluids can be characterized as pseudo-plastic (power law) type of fluids. The rheological model describing pseudo-plastic behaviour is given by equation 6-12.

$$\tau = K\gamma^n \quad \text{..... (6-12)}$$

Where τ is the shear stress, γ is the shear rate, K and n are the consistency index and the flow behaviour index, respectively.

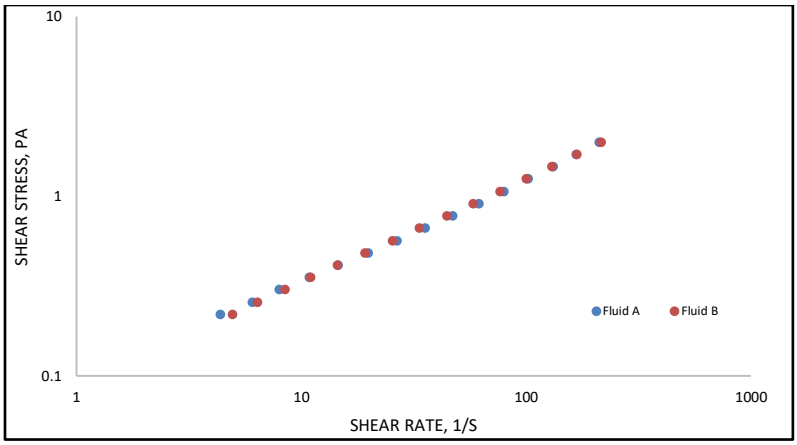

Figure 6-5 Shear stress vs. shear rate diagram of Fluid A and Fluid B

The nominal wall shear rate for the flow of power law type fluid in a pipe can be approximated by using Equation 6-13 [23].

$$\gamma_w = \frac{3n+1}{4n}\frac{8V}{D} \quad \text{..... (6-13)}$$

The minimum and the maximum average fluid velocities that could be reached in the horizontal flow loop are around 0.05 m/s and 2 m/s, respectively when the bed height of the existing sand deposit is 2.3 cm. So, the nominal wall shear rates corresponding these minimum and maximum average velocities achievable in the horizontal flow loop were calculated by using the hydraulic diameter (considering the area open for flow above the sand bed) in Equation 6-13 as 6 1/s and 230 1/s, respectively. We have also estimated wall shear rate by taking the derivative of the near bed velocity profiles measured by the PIV at the minimum and maximum test flow rates used in the flow loop experiments. The shear rate at the sand bed varied from 80 1/s to 210 1/s. The viscometer data shown in Figure 6-5 indicate that the Fluid A and Fluid B have the similar shear viscosity within the approximated operational shear rate range of the horizontal flow loop. The K and n values of the Fluids A and B are summarized in Table 6-3. The K and n values of the Fluids A and B were similar, which also confirmed that shear viscosities of these fluids were almost the same. The value of n, which was around 0.57, for both fluids indicated that these two dilute polymer fluids were moderately non-Newtonian.

Table 6-3 Summary of the rheological properties of Fluid A and Fluid B

Mixture	Concentration	K (Pa.s^n)	n	Frequency Sweep Intersection (rad/s)	Relaxation Time (s)
Fluid A	0.135	0.0918	0.5646	2.8	0.36
Fluid B	0.095	0.0877	0.5783	3.7	0.27

In order to determine the elastic properties of the polymer fluids, frequency sweep tests were conducted. Frequency sweep test measures the storage and loss modulus values of a material at different angular frequencies. The storage modulus (G') is the ratio of in-phase stress to strain and the loss modulus (G") is the ratio of out-phase stress to strain. In-phase and out-phase terms refers to the delay in the reaction of a viscoelastic material (measured as the strain) to an applied stress.

The loss and storage moduli also represent the extent of the irreversible and the reversible energy, which is transferred to the material by the applied stress, respectively [24]. While the strain caused by in phase stress – defining the storage modulus – can be reversible, the energy transferred to the matter by the out-phase stress – defining the loss modulus – is irreversible as a heat loss [24]. In frequency sweep test, the angular frequency where the storage modulus and the loss modulus are equal, is a characteristic point for dilute polymer fluids. The inverse of the characteristics angular frequency is known as the longest relaxation time, which is commonly used for comparison of the different viscoelastic fluids. When two viscoelastic fluids are compared, the fluid having a longer relaxation time is considered to be the more elastic fluid. Figure 6-6 and Figure 6-7 show the results of frequency sweep tests for Fluid A and Fluid B, respectively. The longest relaxation times of Fluid A and Fluid B estimated from these measurements are listed in Table 6-3. The longest relaxation time of Fluid A (0.36 s) is higher than that of the Fluid B 0.27). Therefore, the Fluid A is more elastic than the Fluid B.

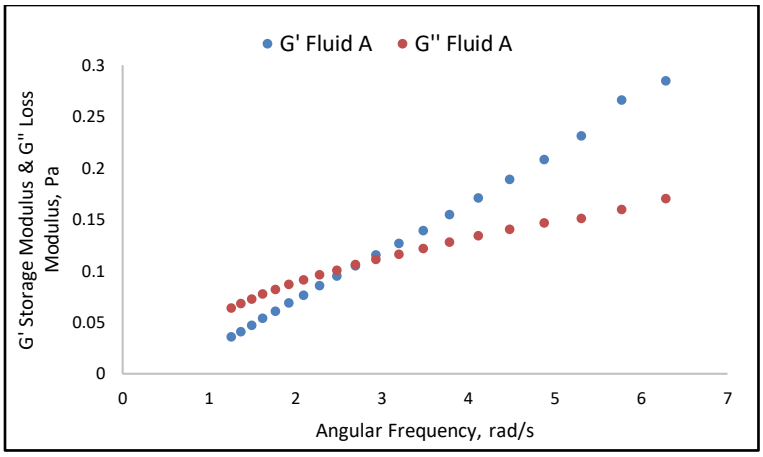

Figure 6-6 Frequency sweep test data for Fluid A

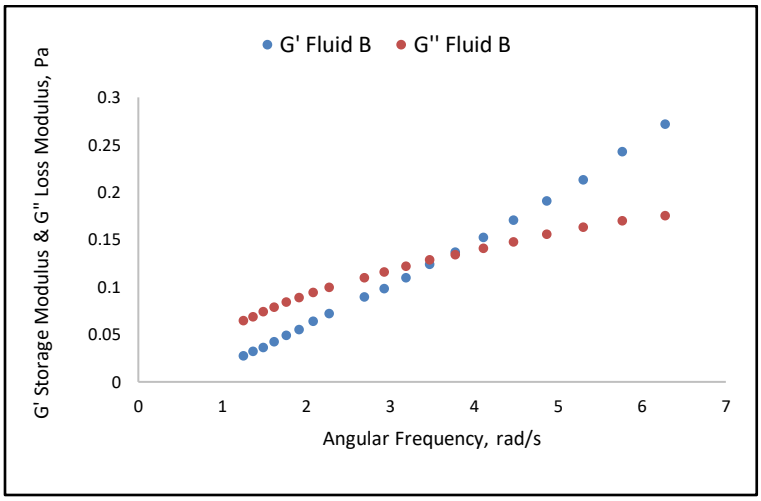

Figure 6-7 Frequency sweep test data for Fluid B

6.4.2. Critical Velocities for 30/50 Mesh Size of Sand Particles in Fluid A and Fluid B

Table 6-4 summarizes the critical velocities recorded at the onset of 30/50 mesh size sand bed erosion using Fluid A and Fluid B.

Table 6-4 Details of bed erosion experiments for Fluid A and Fluid B

Sand Particles Size	Bed Height (cm)	Flow Area (without bed) (cm^2)	Critical Flow Rate (lpm)	Critical Velocity (m/s)
30/50 Sand Particles – Fluid A	**2.3**	**57.6**	**424.5**	**1.24**
30/50 Sand Particles – Fluid B	**2.3**	**57.6**	**321**	**0.94**

The critical velocity recorded when using the Fluid A was significantly (32%) higher than the Fluid B. The results indicate that the bed erosion was delayed when we used fluid with higher elasticity (Fluid A). Similar results were also reported by previous researchers [15]. Discussing the bed erosion performance of viscoelastic fluids in their experimental work similar to ours, Bizhani and Kuru [15] concluded that higher fluid elasticity reduces the effectiveness of the bed erosion performance of a fluid due to the normal forces (resulting from the normal stress differences) exerted on the particles.

The polymers, which are in a coil form when they are at rest, can be stretched under the shear force applied to the fluid during the flow. Therefore, the relaxation time and the elastic properties of the dilute polymer solutions may be altered under dynamic conditions as the stretch of polymer molecules in the solution causes strain anisotropy with the resultant non-linear forces acting on the polymer molecules [25]. According to Hatfield et al. [25] non-linear forces arising from the strain anisotropy produces transverse and longitudinal relaxation times. As Bird et al. [26] and Gyre et al. [27] explained, the main effect of high shear on polymer molecules is the elongation of the polymer molecules or chains, which produces anisotropy in the internal structure of the flow and as a result creates non-zero normal stress differences (an effect which does not appear in inelastic fluids) together with a significant elongational viscosity for dilute polymer solutions.

The definition of the first normal stress is given by the Equation 6-14, which indicates that the first normal stress difference, N_1, is a function of the elongational viscosity and the shear rate in the flow direction [26].

$$N_1 = \sigma_{xx} - \sigma_{yy} = \bar{\eta}(\dot{\varepsilon})\frac{\partial u}{\partial x} \quad \text{(6-14)}$$

The first normal stress difference, N_1, can also be expressed as a function of the relaxation time and shear rate as shown in Equation 6-15 [28].

$$N_1 = -2Nk_BT\lambda^2\dot{\gamma}^2 \quad \text{(6-15)}$$

In equation 6-14 and 6-15; N_1 is first normal stress difference, σ_{xx} and σ_{yy} are normal stresses, $\bar{\eta}$ is elongational viscosity, $\dot{\varepsilon}$ is strain, $\frac{\partial u}{\partial x}$ is local shear rate, N is number of molecules per volume, k_B is the Boltzmann's constant, T is temperature, λ is relaxation time and $\dot{\gamma}$ is shear rate.

As shown in Equation 6-15, as the longest relaxation time increases (i.e. as the fluid becomes more elastic) the first normal stress would also increase. We have determined the first normal stress differences for Fluid A and Fluid B. As shown in Figure 6-8, the first normal stress difference, N_1, for Fluid A is higher than that of Fluid B.

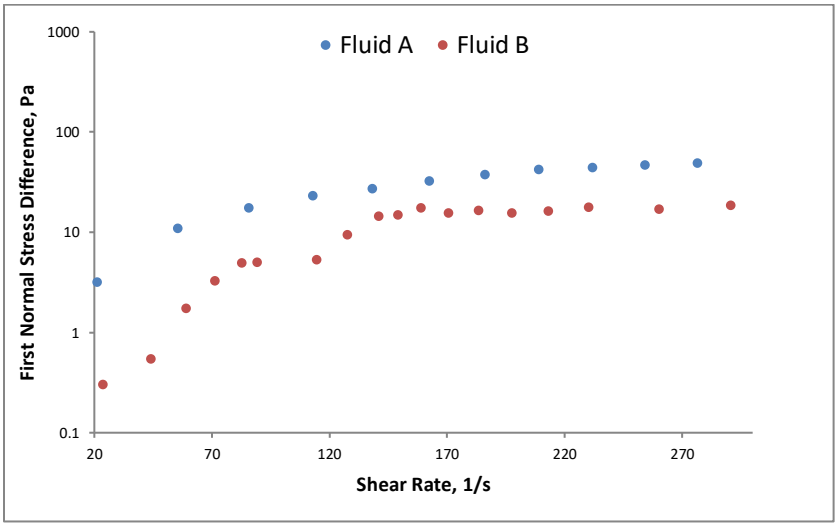

Figure 6-8 First normal stress differences measured for Fluid A and Fluid B.

Bird et al. [26] stated that the non-zero normal stress difference, which is a characteristic of viscoelastic fluids, can be considered as a source of an additional normal force acting perpendicular to the flow direction. Tropea et al. [29] has shown that the total normal force, F_N, exerted by the flowing viscoelastic fluid on the free surface of a spherical shape can be estimated by using the Equation 6-16.

$$F_N = N_1 \frac{\pi}{8} d_p^2 \quad \text{(6-16)}$$

Hence, by using the measured values of first normal stresses (Fig.6-8) and the average diameter of the sand particles (i.e., 444 micron) used in our experiments and assuming a projected area in the direction of the elastic normal force equal to the area of a circle with diameter equal to 444 microns, we have determined the normal (elastic) forces as a function of shear rate. Calculated normal forces within the operational shear rate range of the experiments – from 80 1/s to 210 1/s -are shown in Figure 9.

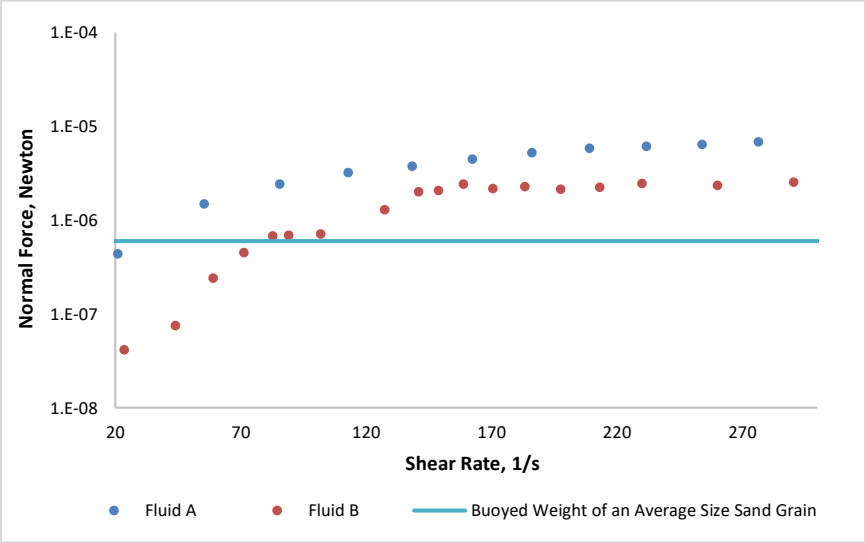

Figure 6-9 Normal forces calculated from measured first normal stress differences.

As shown in Figure 6-9, more elastic fluid (Fluid A) yields higher normal forces than less elastic fluid (Fluid B). Moreover, magnitude of the elastic forces is comparable to the magnitude of the gravity force (due to buoyed

weight of the particle). These elastic forces are expected to behave like additional holding forces acting on the particles laying at the sand bed, and, therefore, delay the onset of the particle movement (i.e., bed erosion).

In a recent study, Hirpa et al. [30] have shown that when a polymer fluid is used for solids transport, the critical velocity depends on not only the particle size but also the relative position of the sand particle with respect to viscous sublayer thickness (i.e., how the particle size compares with the viscous sublayer thickness). The viscous boundary layer thickness, δ_v , is defined by Equation 6-17.

$$\delta_v = \frac{5\mu_w}{\rho u_\tau} \quad \text{(6-17)}$$

Where δ_v is the boundary layer thickness, μ_w is the fluid viscosity at the wall, ρ is the fluid density, and u_τ is the friction velocity.

One other reason for the observed higher critical velocity with more elastic fluid could be the increased thickness of the viscous sublayer due to the higher effective viscosities (due to additional effect of higher elongational viscosities) of the more elastic fluid near the sand bed region. Viscoelastic dilute polymer solutions may develop elongational viscosities significantly higher than the solvent viscosity during the flow [31]. Considering the contribution of the elongational viscosities, Pinto [32] showed that an effective molecular viscosity of the viscoelastic fluids could be significantly higher than that of the shear viscosity of the same fluid. Therefore, we can expect that the more elastic fluids would have higher effective viscosities near the sand bed region and a thicker viscous sublayer as also explained by Lumley [33].

If a particle size is less than the boundary layer thickness, that particle would essentially lay within the viscous boundary layer, and, therefore, be exposed to relatively lower effective fluid velocities. As a result, it would be more difficult to mobilize the particle (essentially much higher average fluid velocities will be required to reach the critical shear stress level) by using more elastic fluid as we observed in our bed erosion experiments.

6.4.3. Frictional Pressure Drop Due to Flow Polymer Fluids in Pipe

Figure 6-10 shows the measured frictional pressure drop data obtained during the flow of Fluid A and Fluid B through the horizontal flow loop without the presence of solids in the system. The fluid with higher elasticity (Fluid A) exhibits significantly lower pressure drop than the fluid with lower elasticity (Fluid B). The difference is particularly notable at the higher flow rates. Bonn [34] showed experimentally that the drag reduction observed during the flow of dilute polymer solutions is directly related to the elongational viscosities of these fluids. Drag reducing dilute polymer solutions develops significant elongational viscosities under high shear and this increases effective viscosity for them. As Lumley [33] explained the increase in effective viscosity of the solution thickens the viscous sublayer and this stabilizes the turbulent eddies in the near wall region and reduces the observed frictional pressure drops by increasing the efficiency of momentum transfer in the direction of the flow. So, this effect is stronger for the more elastic fluid as it develops higher elongational viscosities. As a result, lower frictional pressure drops were recorded for the more elastic fluid.

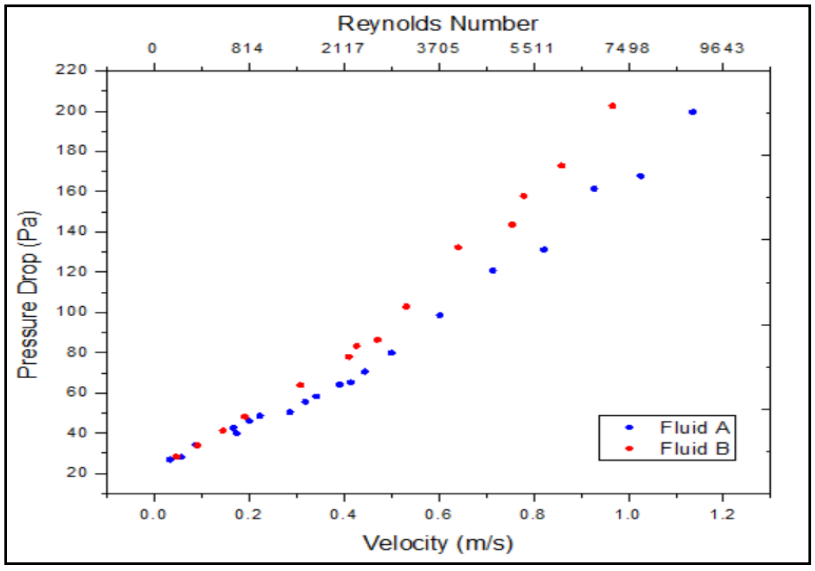

Figure 6-10 Frictional pressure drops for Fluid A and Fluid B without a sand bed.

6.4.4. Frictional Pressure Losses Due to Flow of Polymer Fluids Over the 30/50 Mesh Size Sand Bed

We measured the frictional pressure drops during the flow of Fluid A and Fluid B over the 30/50 mesh size sand bed. Figure 6-11 shows the measured frictional pressure drops for the flow of the Fluid A and the Fluid B over the 30/50 mesh size sand bed. Frictional pressure drops measured for the flow of both Fluid A and B were almost the same in this case. The difference we observed for the pipe flow of Fluid A and B diminished when there was a sand bed in the pipe. Therefore, the presence of the sand bed changed the flow dynamics significantly. Bewersdorff et al. [22] carried out the flow tests for drag reducing surfactant and polymer solutions in rough pipes and they reported that rough surfaces decrease the drag reduction effect. The negative effect of rough surfaces on drag reducing polymer solutions seems stronger for more elastic dilute polymer solutions. When there is a sand bed deposit in the horizontal pipe, two different interfaces were involved in the flow; glass pipe/fluid (smooth interface) and sand bed/fluid (rough interface). Flow of low elasticity fluid (Fluid B) over the relatively smooth pipe wall results higher frictional losses than that of the high elasticity fluid (Fig.6-10). When there was a sand bed involved in the flow, however, difference in frictional losses between Fluid A and B diminished (Fig.6-11). Therefore, the flow of high elasticity fluid (Fluid A) over the relatively rough sand surface might have yielded higher frictional pressure loss than that of the low elasticity fluid (Fluid B) to make up the difference in this case.

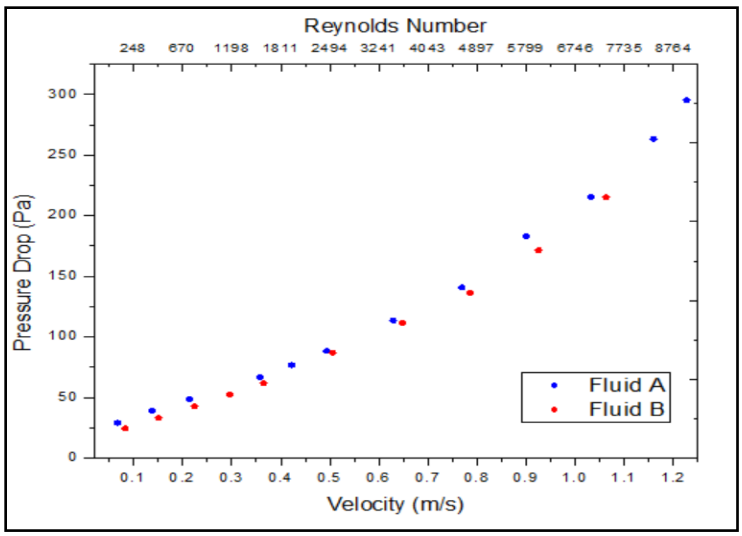

Figure 6-11 Frictional pressure drops for Fluid A and fluid B over the sand bed.

6.4.5. PIV Data for 30/50 Mesh Size of Sand Particles in Fluid A and Fluid B

In order to see the effect of fluid elasticity on the characteristics of the turbulent flow of viscoelastic fluid over a sand bed, PIV measurements were carried out by using Fluid A and Fluid B at two common flow rates of 225 lpm and 274 lpm. The y-coordinate of the figures 6-12 to 6-20 show the vertical distance from the bed (in the direction perpendicular to the flow) in physical form or dimensionless units and y=0 is the sand bed-fluid interface.

Full scale velocity profiles associated with the flow of Fluids A and B through the annular space between the sand bed and pipe wall were recorded by using PIV at the flow rates of 225 lpm (Fig.6-12) and 274 lpm (Fig.6-13). The normalized velocity profiles shown in these plots were calculated by dividing the measured local velocity with the superficial velocity. Full scale velocity profiles of the Fluid A and the Fluid B over the sand bed were almost the same at both flow rates. The peak velocity of the Fluid A was slightly higher than that of the Fluid B. It seems that the difference in the peak velocities increases with the increasing average fluid velocity.

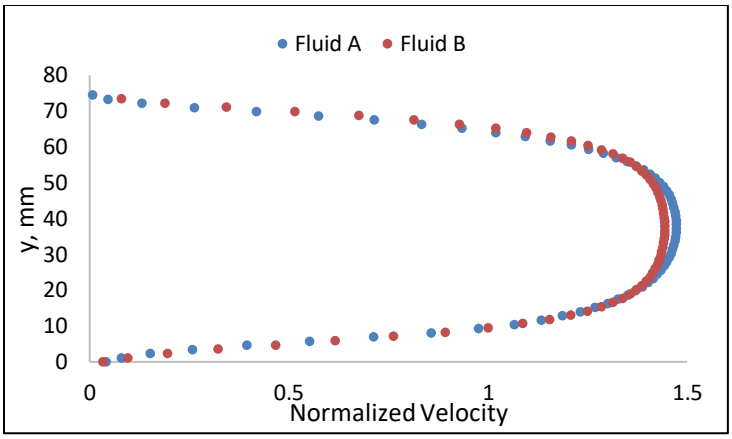

Figure 6-12 Velocity profiles in the annulus between the sand bed and the pipe wall measured at flow rate of 225 lpm

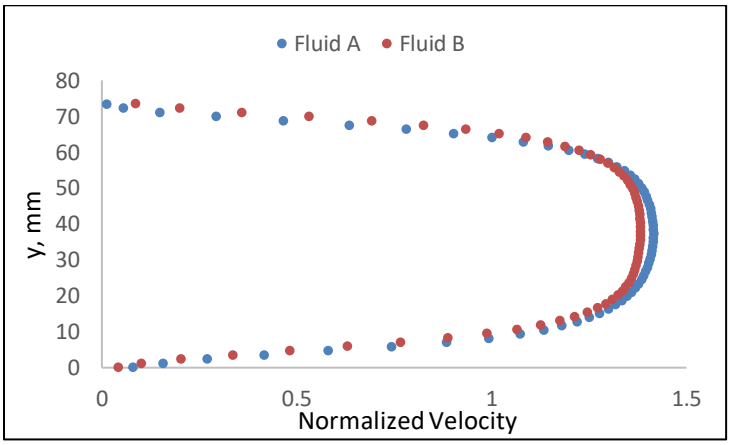

Figure 6-13 Velocity profiles in the annulus between the sand bed and the pipe wall measured at flow rate of 274 lpm

Figures 6-14 and 6-15 present the dimensionless near wall velocity profiles for the flow of Fluid A and Fluid B over 30/50 mesh size of sand bed in the horizontal pipe measured at flow rates of 225 lpm and 274 lpm, respectively. Dimensionless velocity profiles for both Fluid A and Fluid B deviated from the universal law within log-law region indicating that both fluids had a drag reducing effect. In both cases, near wall velocity profiles stayed inside an envelope bounded by the universal log law below and by the Virk's asymptote above. The Fluid

B has a more drag reducing effect than the Fluid A, because the near wall velocity profiles of the Fluid B are closer to the limiting Virk's asymptote.

These results also support the discussion we had regarding the reversal of the frictional pressure losses observed during the flow of the Fluid A and B for the cases with and without the presence of sand bed in the pipe flow. The flow of fluid A (more elastic fluid of the two) over the sand bed yielded higher frictional pressure losses, which was also supported by the lower drag reduction effect (i.e. relatively higher frictional pressure loss) observed from the near wall velocity of the fluid A.

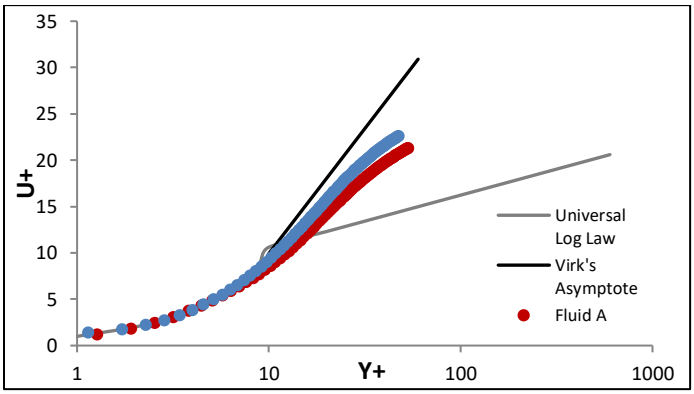

Figure 6-14 Dimensionless velocity profiles for Fluid A and Fluid B at 225 lpm

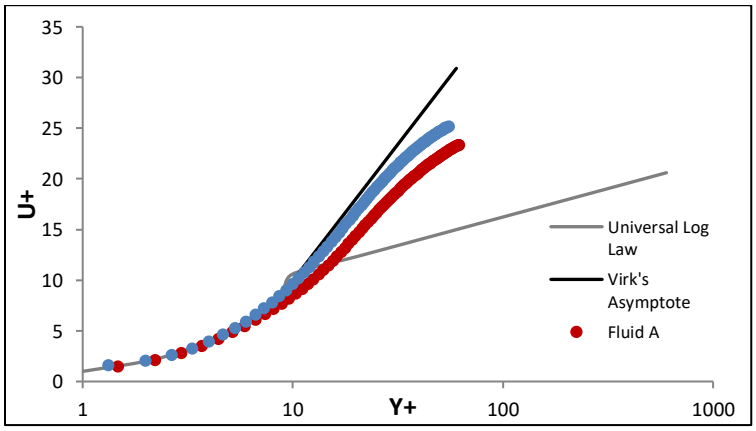

Figure 6-15 Dimensionless velocity profiles of Fluid A and Fluid B at 274 lpm

Figures 6-16 and 6-17 compares the Reynolds shear stress profiles for Fluid A and Fluid B at flow rates of 225 lpm and 275 lpm, respectively. Reynolds shear stress profile is expected to correlate with observed frictional pressure drops, so it is good to compare Reynolds stress profiles for these fluids at similar superficial velocities in order to double check the frictional pressure drop behaviour. However, as shown in Figures 6-16 and 6-17, the Reynolds stress values are lower for more elastic fluid - Fluid A - exhibiting higher frictional pressure drops. Here, it is not unusual that we do not see the direct effect of difference in the frictional pressure drops on Reynolds stress profiles recorded, because the main cause of difference in observed pressure drops for flow of these fluids over the sand bed is the interaction of the flowing fluid and the rough sand surface resulting in entanglements of long polymer chains in the flow. There are two kind of stresses generated in boundary-layer flows; these are viscous stresses and Reynolds stresses [35]. Viscosity is dominant close to the boundary and viscous stress near the boundary is generated by viscous forces, but away from the boundary, viscosity becomes insignificant and Reynolds stress is generated by turbulence [35]. Viscous sublayer thickness is controlled by Reynolds stresses and viscous stresses [35]. So, Reynolds stresses recorded for Fluid A and Fluid B indicates that the viscous sublayer is thicker for the more elastic fluid, as the recorded Reynolds stresses are lower for the more elastic fluid.

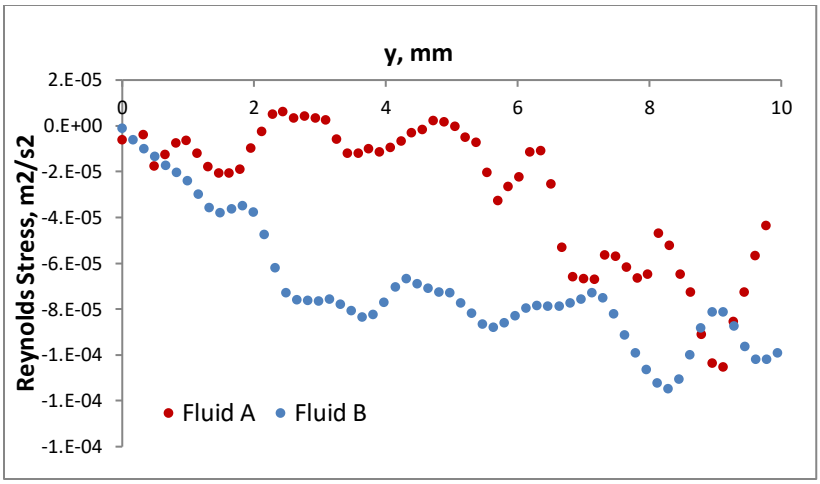

Figure 6-16 Reynolds stress profiles for Fluid A and Fluid B at 225 lpm

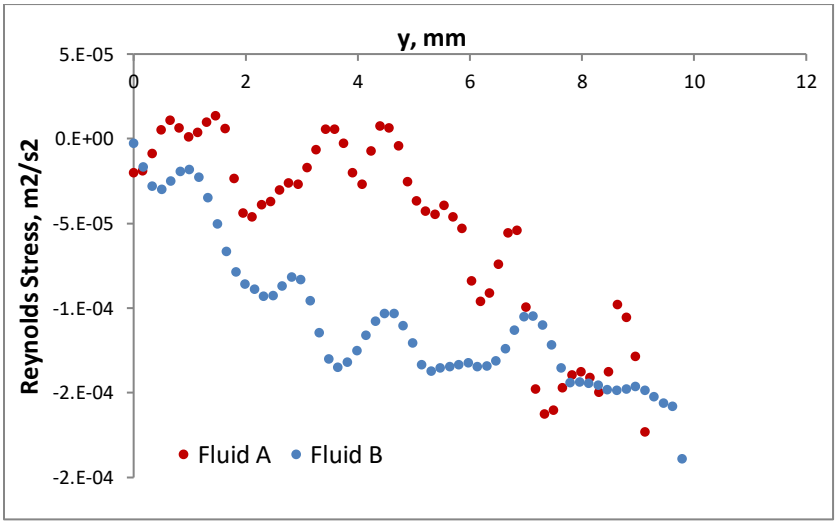

Figure 6-17 Reynolds stress profiles for Fluid A and Fluid B at 274 lpm

Figures 6-18 and 6-19 show the axial turbulence intensity profiles (also called the normal Reynolds stress) of the Fluid A and the Fluid B at the flow rates of 225 lpm and 274 lpm, respectively. There is a significant difference in the axial turbulence intensity profiles of Fluid A and Fluid B near the sand bed. Away from the sand – fluid interface, however, the difference becomes insignificant. In the near wall region, the Fluid B (lower elasticity fluid of the two) has higher axial turbulence intensity values than that of the Fluid A. These results suggest that the intensity of the axial turbulence decreases with the increasing elasticity (i.e.; longer polymer chains,

characteristics of high molecular weight, higher elasticity polymer fluids) creates dampening effect on the turbulent fluctuation velocities in axial direction).

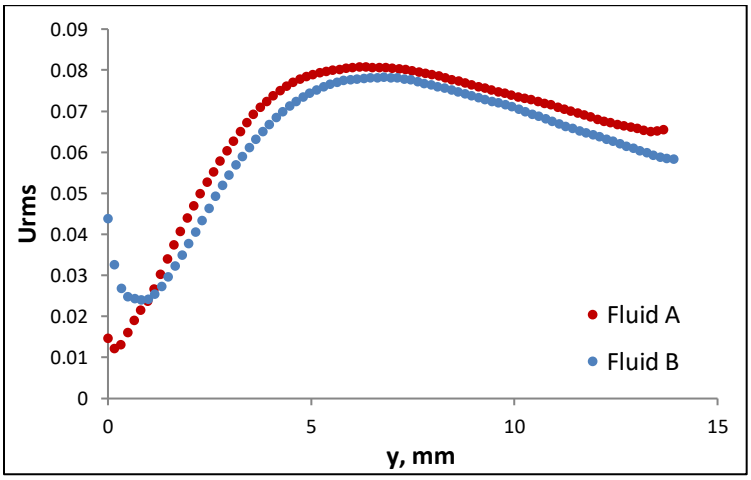

Figure 6-18 Axial turbulence intensity profiles for Fluid A and Fluid B at 225 lpm

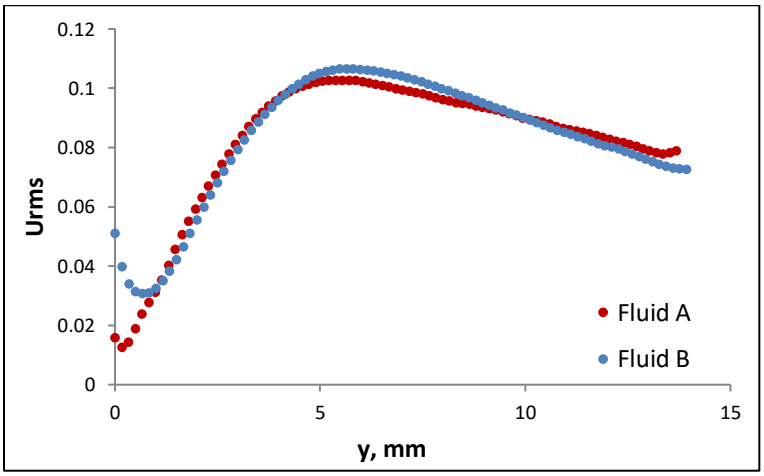

Figure 6-19 Axial turbulence intensity profiles for Fluid A and Fluid B at 274 lpm

The radial turbulence intensity, v_{rms}, is of particular importance in solid transport and solid suspension. Davies [36] has shown that the eddy fluctuation forces are proportional to radial velocity fluctuations. A higher level of radial velocity fluctuations corresponds to a higher eddy fluctuation force. Figures 6-20 and 6-21 show the radial turbulence intensity profiles of the Fluid A and the Fluid B at flow rates of 225 lpm and 274 lpm, respectively.

Radial turbulence intensity profiles of the Fluid A (higher elasticity fluid of the two) were lower than that of the Fluid B. Higher elongational viscosities developed by the more elastic fluid dampens the velocity fluctuations in vertical direction and this produces lower radial turbulence intensity profiles for the more elastic fluid. The radial turbulence intensity profiles peak around the near wall region for both fluids. We calculated the ratio of the maximum radial turbulence intensity to minimum radial turbulence intensity for both fluids at each flow rate. The calculated ratios for the Fluid A are 3.45 and 2.65 and the calculated ratios for the Fluid B is 4.1 and 3.13 at flow rates of 225 lpm and 274 lpm, respectively. Rationally the peaks are lower for the more elastic fluid and the lower peaks observed might be the indicator of stronger entanglements of the longer polymer chains included in the more elastic dilute polymer solution.

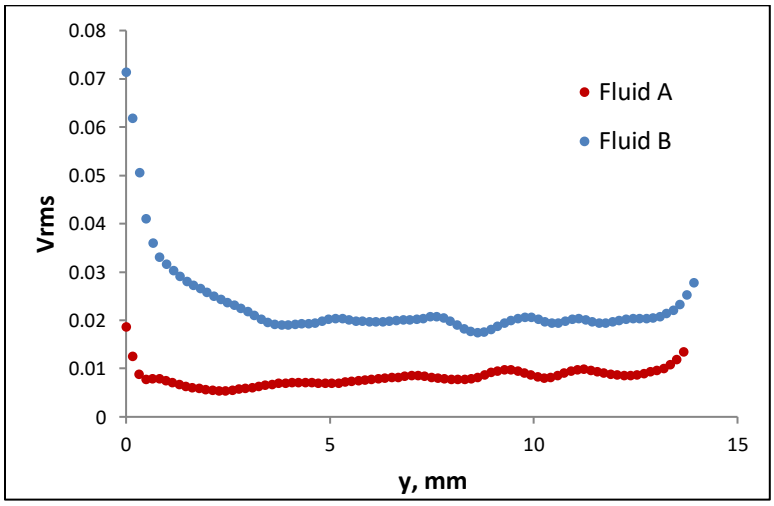

Figure 6-20 Radial turbulence intensity profiles for Fluid A and Fluid B at 225 lpm.

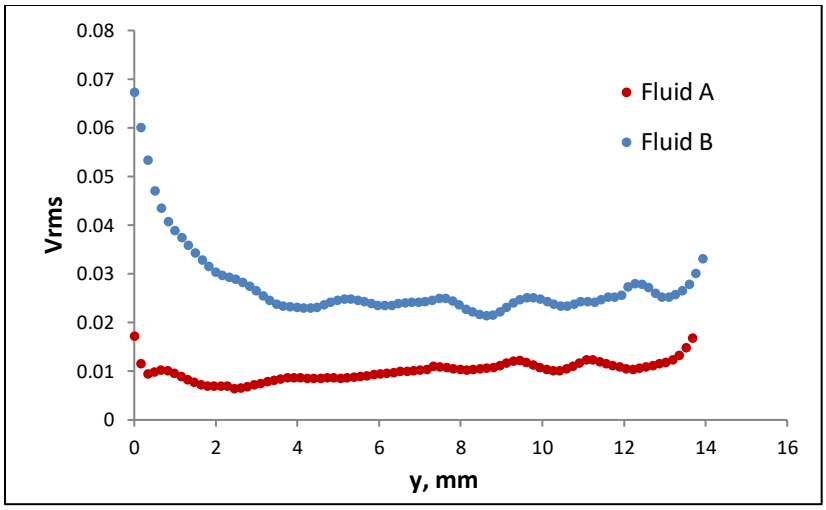

Figure 6-21 Radial turbulence intensity profile for Fluid A and Fluid B at 274 lpm.

6.5. CONCLUSIONS

An experimental study was conducted to find out the influence of fluid elastic properties on the critical velocity, frictional pressure drops and the turbulent flow characteristics of a polymer fluid flow over a sand bed deposited in a horizontal pipe.

For fluid only flow (no sand bed deposit) in pipe, more elastic fluid exhibited lower frictional pressure drop than that of the less elastic fluid. However, if there was a sand bed inside the pipe, then higher frictional pressure drops were measured for the flow of more elastic fluid than that of the less elastic one. The elongational viscosity developed in the near wall region due to extension of polymer chains under shear force enhances the stabilization of turbulent eddies by thickening the viscous sublayer. This causes a drag reduction for dilute polymer solutions by optimizing the efficiency of energy transfer in the flow direction. In fluid only pipe flow (no sand), this effect is stronger for the more elastic fluid - as it develops higher elongational viscosities – therefore, we observed lower frictional pressure drops for the flow of more elastic fluid. In the case where there is a sand bed in the horizontal pipe, polymer chains in flow extends and develops elongational viscosities similarly, however, this time the flow over a rough surface leads long chain polymer molecule to entangle each other. These entanglements increase the

friction between the fluid and the sand bed undermining the drag reduction effect of dilute polymer solutions. The entanglements are stronger for the more elastic fluid, therefore decrease in drag reduction is higher for the more elastic fluid and higher frictional pressure drops were measured for the more elastic fluid in this case.

Results also showed that higher critical velocities were required for the onset of the bed erosion with the use of more elastic fluid. Fluid with higher elasticity – longer polymer chains – develops higher normal stress difference and higher elongational viscosity under the shear during the flow. In the pipe flow with or without a sand bed the highest shear rate exists in the near wall or near fluid – sand bed interface region, so during the flow highest elongational viscosities and normal stress differences are observed in those regions. Higher normal stress difference results in greater normal force acting on the sand particles as an additional holding force and, as a result, more elastic polymer fluid delays the onset of sand movement as compared to less elastic polymer fluid or water. Moreover, higher elongational viscosities developed by more elastic fluid increases the effective viscosity and thickness of the viscous sublayer significantly, which also contributes to the delay of the onset of particle movement.

Analyses of the turbulent flow characteristics of the polymer fluids (based on the PIV measurements) also confirmed the findings and conclusions about the observed critical velocities and frictional pressure losses. The full velocity profiles were quite similar for both fluids, but the peak velocity was higher for the more elastic fluid. Dimensionless velocity profiles indicated that the fluid with lower elasticity had more drag reducing effect than the one with higher elasticity during the flow over the sand bed. These results were in line with the frictional pressure losses measured directly during the flow of both fluids.

The Reynolds stress profile obtained for the more elastic fluid flow was lower than the less elastic one. The viscosity is very dominant inside the viscous sublayer and viscous effects supresses the Reynolds stresses generated. Therefore, the reason for observing lower Reynolds stress profiles for the more elastic fluid is the higher effective viscosity of the higher elasticity fluid in the near wall region. Also, the lower Reynolds stresses

recorded for the more elastic fluid indicates that viscous sublayer for the more elastic fluid is thicker. The thicker viscous sublayer is one of the main reasons delaying the onset of particle movement for the more elastic fluid.

Axial turbulence intensity profiles were quite similar for both fluids except the near wall region. In the near wall region observed higher axial turbulence intensity profiles for the less elastic fluid might be the reason or the result of the increased mobility of sand particles in the flow of less elastic fluid.

The lower radial turbulence intensity profiles recorded for the more viscoelastic fluid than the less elastic one soundly supports the claims on elongational viscosities developed by these fluids. Higher elongational viscosities developed by the more elastic fluid dampened the velocity fluctuations in vertical direction and, therefore, lower the radial turbulence intensity profiles.

In conclusion, viscoelastic properties of the dilute polymer fluids are very important and should be given due consideration when these fluids are used for hole cleaning and/or solids transport in drilling and hydraulic fracturing operations.

6.6. ACKNOWLEDGEMENTS

This research is financially supported by the funds available from Natural Sciences and Engineering Research Council of Canada (NSERC RGPIN-2016-04647 KURU).

6.7. REFERENCES

1. Bilgesu, H. I., Mishra, N., & Ameri, S. (2007). Understanding the Effect of Drilling Parameters on Hole Cleaning in Horizontal and Deviated Wellbores Using Computational Fluid Dynamics. Society of Petroleum Engineers. doi:10.2118/111208-MS
2. Nazari, T., Hareland, G. and Azar, J. J. (2010, May). Review of Cuttings Transport in Directional Well Drilling: Systematic Approach. SPE Western Regional Meeting Anaheim, California, USA, SPE-132372-MS, doi: 10.2118/132372-MS.

3. Li, J., Luft, B. (2014a, October). Overview of Solids Transport Studies and Applications in Oil and Gas Industry - Experimental Work. SPE Russian Oil and Gas Exploration & Production Technical Conference and Exhibition. Moscow, Russia, SPE-171285-MS, doi: 10.2118/171285-MS.

4. Li, J., Luft, B. (2014b, December). Overview Solids Transport Study and Application in Oil-Gas Industry-Theoretical Work. International Petroleum Technology Conference. Kuala Lumpur, Malaysia, IPTC-17832-MS, doi: 10.2523/IPTC-17832-MS.

5. Adari, R., Miska, S., Kuru, E., Bern, P., Saasen, A. (2000) Cuttings Bed Erosion Curves Help Predict Optimum Circulation Time for Hole Cleaning. ETCE/ OMAE Joint Conference of ASME, February 14-17, 2000, New Orleans, LA.

6. Rabenjafimanantsoa, H. A., Rune, W. T., Saasen, A. (2005). Flow regimes over particle beds experimental studies of particle transport in horizontal pipes Annual Transactions of the Nordic Rheology Society, 13.

7. Bizhani, M., Corredor, F. E. R., Kuru, E. (2016). Quantitative Evaluation of Critical Conditions Required for Effective Hole Cleaning in Coiled-Tubing Drilling of Horizontal Wells. SPE Drilling & Completion 31(3): 188-199, doi: 10.2118/174404-PA.

8. Walker, S., Li, J. (2000, April). The Effects of Particle Size, Fluid Rheology, and Pipe Eccentricity on Cuttings Transport. g2000 SPE/ICoTA Coiled Tubing Roundtable. Houston, TX, SPE-60755-MS, doi: 10.2118/60755-MS.

9. Saasen, A., Løklingholm, G. (2002, February). The Effect of Drilling Fluid Rheological Properties on Hole Cleaning. IADC/SPE Drilling Conference. Dallas, Texas, SPE-74558-MS, doi: 10.2118/74558-MS.

10. Duan, M., Miska, S. Z., Yu, M. et al. (2007, April). Critical Conditions for Effective Sand-Sized Solids Transport in Horizontal and High-Angle Wells. SPE Production and Operations Symposium Oklahoma City, Oklahoma, USA, SPE-106707-MS, doi: 10.2118/106707-MS.

11. Powell, J. W., Parks, C. F., Seheult, J. M. (1991). Xanthan and Welan: The Effects of Critical Polymer Concentration on Rheology and Fluid Performance. Society of Petroleum Engineers. doi:10.2118/22066-MS

12. Zamora, M., Jefferson, D. T., Powell, J. W. (1993). Hole-Cleaning Study of Polymer-Based Drilling Fluids. Society of Petroleum Engineers. doi:10.2118/26329-MS

13. Sayindla, S., Lund, B., Ytrehus, J.D., et al., (2017, November). Hole-cleaning performance comparison of oil-based and water-based drilling fluids. J. Pet. Sci. Eng., Volume 159, Pages 49-57. doi: 10.1016/ j.petrol. 2017.08.069.

14. Werner, B., Myrseth, V., Saasen, A. (2017). Viscoelastic properties of drilling fluids and their influence on cuttings transport. Journal of Petroleum Science and Engineering, Volume 156, Pages 845-851, ISSN 0920-4105, doi:10.1016/j.petrol.2017.06.063.

15. Bizhani, M., Kuru, E. (2018). Particle Removal from Sandbed Deposits in Horizontal Annuli Using Viscoelastic Fluids. SPE Journal, Vol.23, Issue.02, pp.256-273, doi:10.2118/189443-PA

16. Arnipally, S., Kuru, E. (2018). Settling Velocity of Particles in Viscoelastic Fluids: A Comparison of the Shear Viscosity and Elasticity Effect. SPE Journal, Online Preprint, doi: 10.2118/ 187255-PA

17. Bizhani, M. (2017). Experimental and Theoretical Investigations of Particle Removal from Sand Bed Deposits in Horizontal Wells Using Turbulent Flow of Water and Polymer Fluids. PhD Thesis, Civil and Environmental Engineering, University of Alberta, Edmonton, Canada.

18. Metzner, A.B., Reed, J.C. (1955). Flow of non-Newtonian fluids—correlation of the laminar, transition, and turbulent-flow regions. AICHE Journal,1(4), pp.434-440.

19. Raffel, M., Willert, C. E., Kompenhans, J. (2007). Particle Image Velocimetry: A Practical Guide: Springer Science & Business Media.

20. LaVision, Davis 8.3 Product Manual. ed, 2015.

21. Kundu, P. K., Cohen, I. M., Dowling, D. R. (2012). Fluid Mechanics, 5th Edition. Amsterdam, Elsevier Science Bv.

22. Bewersdorff, H., Thiel, H. (1993). Turbulence Structure of Dilute Polymer and Surfactant Solutions in Artificially Roughened Pipes. Applied Scientific Research. 50. 347-368. doi:10.1007/BF00850566.

23. Skelland, A. H. P. (1967). Non-Newtonian flow and heat transfer. Wiley, New York.

24. Roylance, D., (2001). Engineering Viscoelasticity. Department of Materials Science and Engineering Massachusetts Institute of Technology Cambridge, MA 02139

    Retrieved from http://web.mit.edu/course/3/3.11/www/modules/visco.pdf

25. Hatfield, J. W., Quake, S. R. (1999). Dynamic Properties of an Extended Polymer in Solution. Physical Review Letters, 82 (17). pp. 3548-3551. ISSN 0031-9007.

26. Bird RB, Armstrong RC, Hassager O. (1987). Dynamics of Polymeric Liquids, vol 1. Wiley, New York

27. Gyr, A., Bewersdorff, H. (1995). Drag Reduction of Turbulent Flows by Additives. Springer, Dordrecht

28. Zell, A, Gier, S, Rafai, S., Wagner, C. (2009). Is there a Relationship between the Elongational Viscosity and the First Normal Stress Difference in Polymer Solutions?

29. Tropea, C., Yarin, A. L., Foss, J. (2007). Springer Handbook of Experimental Fluid Mechanics. doi:10.1007/978-3-540-30299-5.

30. Hirpa, M.M., Arnipally, S.K., Kuru, E. et al. (2018). Effect of Sand Particle Size and Surface Properties on the Near Wall Turbulence Characteristics of the Polymer Fluid Flow and the Critical Velocity Required for the Particle Removal from the Sand Bed Deposited in Horizontal Pipelines. Submitted to SPE Journal, under review.

31. Sunthar, P. (2010). Polymer Rheology. Rheology of Complex Fluids. 171-191. doi:10.1007/978-1-4419-6494-6_8.

32. Pinho, F. (2003). A GNF framework for turbulent flow models of drag reducing fluids and proposal for a k-type closure. J. Non-Newtonian Fluid Mech. 114. 149-184. doi:10.1016/S0377-0257(03)00120-4.

33. Lumley, J. (1973). Drag Reduction in Turbulent Flow by Polymer Additives. Journal of Polymer Science: Macromolecular Reviews. 7. 263 - 290. doi:10.1002/pol.1973.230070104.

34. Bonn, D., Amarouchene, Y., Wagner, C., Douady, S., Cadot, O. (2005). Turbulent drag reduction by polymers. Journal of Physics: Condensed Matter. 17. S1195. doi:10.1088/0953-8984/17/14/008.

35. Flierl, G., Ferrari, R. 12.820 Turbulence in the Ocean and Atmosphere. Spring 2007. Massachusetts Institute of Technology: MIT OpenCourseWare, https://ocw.mit.edu. License: Creative Commons BY-NC-SA.

36. Davies, J. (1987). Calculation of Critical Velocities to Maintain Solids in Suspension in Horizontal Pipes. Chemical Eng.Sci., vol. 42, pp. 1667-1670.

7. CONCLUSIONS AND RECOMMENDATIONS FOR FUTURE WORK

7.1. CONCLUSIONS

In this chapter, main conclusions of the all work done in this thesis will be covered briefly. A detailed discussion and interpretation of the results of each experimental study have been already given in separate chapters. Here a summary of all findings from individual papers will be presented and the importance of each specific research topics will be highlighted. First, the major conclusions from all experimental work will be presented. Then, an executive summary of conclusions from individual chapters will be provided.

7.1.1. Major conclusions

- All bed erosion experiments in this study showed that rather than average flow velocity, the local velocity at the sand bed surface is effective for particle removal.
- It is clearly seen that water erodes a deposited bed at lower flow velocities than a polymeric fluid regardless of sand particle size or surface treatment.
- For water, the main parameter controlling the bed erosion dynamics is the particle size forming the sand deposit in a horizontal pipeline. Critical velocity to mobilize the sand particles increases with increasing particle size.
- For polymeric fluids, the particle size forming the sand deposit is an important parameter controlling the bed erosion dynamics, however, this is not the absolute one and particle position with respect to viscous sublayer is also significant.
- It is observed that sand particles bigger than the viscous sublayer thickness in size are easier to mobilize with polymeric fluids, and lower critical velocities were reported for the particles sticking out the viscous sublayer in bed erosion tests included in this work.

- If the particles are inside or outside the viscous sublayer, then particle size becomes the only factor controlling the critical velocity. Smaller particle requires lower critical velocity among two particles outside the viscous sublayer. This is valid and the same for the particles inside the viscous sublayer.
- Surface treatment of sand particles soundly increase the bed erosion performance of water in horizontal pipelines. In these experiments, it is observed that the surface treatment stimulated the bed erosion performance more strongly for smaller particles.
- Effect of surface treatment of sand particles on bed erosion dynamics is not straightforward for polymeric solutions. Only for one sand size, surface treatment enhanced the bed erosion performance.
- This study showed that elasticity negatively affects the bed erosion dynamics and delays the onset of particle movement.
- A Thicker viscous sublayer and existence of higher normal forces arising from higher normal stress differences for the more elastic fluid were the main reasons for the delay of onset of particle movement for more elastic fluid.
- Higher elasticity negatively affects the frictional pressure drops over a rough surface. The more elastic fluid exhibited higher frictional pressure drops than the less elastic one over the sand deposit.
- Higher elasticity stimulated the drag reduction effect and lower frictional pressure drops were observed for a more elastic fluid than the less elastic one having the same shear viscosity in pipe flow over a smooth walled surface.
- This study showed that certain Weissenberg numbers are associated with the initiation and the optimization of drag reduction in pipe flow of dilute polymer fluids.
- It is shown that elastic properties of a polymeric fluid are also crucial for transition from laminar to turbulent flow regime. Among fluids tested in horizontal flow loop, earlier transition to turbulence was observed only for the most elastic fluid in pipe flow.

7.1.2. Conclusions from individual chapters

Results of this study provided new knowledge regarding the impacts of the particle size, surface characteristics and fluid elastic properties on the dynamics of the bed erosion process. Beside significant contributions to understanding of the bed erosion dynamics, results of this study also provided new knowledge on how elastic properties of dilute polymer fluids would influence the onset of the drag the reduction and its magnitude and the critical condition for the initiation of the transition from laminar to turbulent regime. An executive summary of conclusions from each chapter is presented in the following sections.

7.1.2.1. Chapter 3 - Effect of particle size and surface properties on the near wall turbulence characteristics and the critical velocity required for the particles removal from the sand bed deposited in horizontal pipelines

The critical velocity required for the onset of particle removal from sand bed decreases with decreasing sand particle for both treated and untreated sands in water flow. However, critical velocities for particle removal from treated sand beds were significantly lower than that of the untreated sand beds for all particle size ranges investigated in these experiments where the transport fluid was water.

It was observed that air bubbles were attached to the treated sand particles during the flow. It appears that the modified sand surface properties (i.e. changing from water wet to non-water wet) promote the air bubble attachment to the sand particles, which increases the buoyancy forces acting on these sand particles and, hence, causes the reduction of the critical velocity for particle removal. Moreover, the degree of reduction of the critical velocity in this case varied depending on the particle size. For the sand sizes used in this study, the reduction in critical velocity was the highest (40%) for 40/70 mesh size of treated sand. As we decreased the sand size further to 100 mesh, however, the observed reduction of critical velocity due to surface treatment was only 30%, indicating that there exists a specific sand size where the reduction of the critical velocity becomes maximum.

For the flow of water over the untreated sand bed, frictional pressure loss varied depending on the particle size range. The frictional pressure loss for the flow of water over the 30/50 sand bed was higher than that of the case for 40/70 sand bed, indicating that frictional pressure loss decreases with the decreasing sand size. However, the trend was the opposite, when we used 20/40 mesh size (largest size sand particles within the group tested). The measured frictional pressure loss for the flow over the bed with 20/40 sand size range was lower than that of the flow over the beds with 30/50 and 40/70 sand size ranges. For the flow over the treated sand bed, however, frictional pressure loss values measured at the same fluid velocities were almost the same for all particle size ranges. It seemed like the surface treatment of the sands negated the effect of particle size on the frictional pressure drop.

The frictional pressure loss values measured for the water flow over the treated sand bed were slightly lower than that of the case with untreated sand bed for all particle size ranges. These results suggest that the modifications in surface characteristics of sand particles might have a positive (i.e., drag reduction effect) effect on frictional pressure losses for water flow over a sand deposit in a horizontal pipe.

7.1.2.2. Chapter 4 - Effect of sand particle size and surface properties on the near wall turbulence characteristics of the polymer fluid flow and the critical velocity required for the particle removal from the sand bed deposited in horizontal pipelines

For untreated sand particles, the lowest critical velocity was observed for the flow over the bed with the largest particle size range (i.e., 20/40 mesh size of sand). For the treated sand particles, however, the lowest critical velocity was observed for the flow over the sand bed with intermediate particle size range (i.e., 30/50 mesh size).

It seems like when a polymer fluid is used for solids transport, the critical velocity not only depends on the surface characteristic (i.e. treated vs. untreated sand) of the sand and the absolute value of the particle size but also on the relative position of the sand particle with respect to viscous sublayer thickness (i.e., how the particle size compares with the viscous sublayer thickness).

Frictional pressure drops measured during the polymer fluid flow over the 20/40 and 40/70 mesh size of untreated and treated sand beds were similar. However, frictional pressure drop for the flow of polymer fluid over the 30/50 mesh size treated sand was significantly higher than that of the untreated sand. Moreover, the difference between the frictional pressure drop for the flow over the 30/50 mesh size treated and untreated sand bed increased with the increasing fluid velocity. The frictional velocity (function of interfacial bed shear stress) values obtained from the PIV measurements (conducted at the fluid/sand bed interface) also confirmed the trends of the frictional pressure drop measured during the polymer fluid flow over the both treated and untreated sand bed.

Reynolds stress profiles were found to be very much in line with the frictional pressure drops measured during the flow over the same mesh size of the treated and untreated sand bed. Generally, we can say that there is not a significant difference in Reynolds stress profiles for treated and untreated sand particles if the critical velocity is similar for both cases. However, if there is a reduction in the critical velocity due to the surface treatment or if there is a change in near wall characteristics due to surface treatment, then this causes an increase in Reynolds stress profile. When the Reynolds stress comparison was done only based on the particle size, we did not see a direct correlation between the Reynolds stress profile and the particle size. A difference in Reynolds stress was only observed between 30/50 mesh size of treated and untreated sand.

Surface treatment did not seem to have any significant effect on the axial turbulence intensity profiles for the flow over the 20/40 and 40/70 mesh size sand beds. However, for flow over the 30/50 mesh size sand bed, the surface treatment increased the mobility of sand particles and increase in mobility could be seen as an increase in recorded axial turbulence intensity profiles for treated sand particles especially close to near wall area. Particle size did not affect the axial turbulent intensity profiles for the flow over the both treated and untreated sand beds.

The difference in radial turbulence intensity profiles was negligibly small for the flow over the 20/40 and 40/70 mesh size sand beds. However, even the difference was negligibly small, the measured values were higher for the flow over the untreated sand beds. Radial turbulence intensity profiles were considerably higher for the

flow over the 30/50 mesh size treated sand beds than that of 30/50 mesh size untreated sand bed. Again, here we may say that if the surface treatment reduces the critical velocity or changes the near wall characteristics, then this would increase the radial turbulence intensity profiles. There was no significant difference in radial turbulence intensity profiles recorded for the flow over treated sand beds of different particle size. For flow over the untreated sand beds, 30/50 mesh size untreated sand particles have lower radial turbulence intensity values. While the radial turbulent intensities for the flow over the 20/40 and 40/70 mesh size untreated sand beds were almost the same. Generally, it was not possible to establish a correlation between particle size and radial turbulence intensity profiles for treated and untreated sand particles.

7.1.2.3. Chapter 5 - Effect of polymer fluid viscoelastic properties on the early transition to turbulent flow and the drag reduction in the flow through horizontal pipe

Chain length of polymer molecules basically depends on the molecular weight of the polymer. In dilute polymer solutions intensive deformation abilities of long polymer chains causes each chain to extend in the flow direction and generate significant elongational viscosities especially close to the pipe wall where the shear rate is the highest during the flow. Elongational viscosities generated optimizes the energy transferred into the flow direction by stabilizing the turbulent eddies in the near wall region. As a result, a drag reduction is observed during the flow when even a small amount of high molecular weight polymer is added into a Newtonian solvent. This experimental study showed that more elastic solutions develop higher elongational viscosities, and they exhibit lower frictional pressure drops during the flow in a smooth walled circular pipe. Fluid A, Fluid B and Fluid C have the same viscometric properties, however Fluid A, which is the most elastic solution, exhibited the lowest frictional pressure drops. These measurements were also approved by PIV recordings for these fluids. The dimensionless velocity profile for Fluid A was the closest to the Virk's asymptote. Also, as viscous sublayer thickens due to elastic effects, low Reynolds stresses were recorded for each drag reducing fluid. Lowest radial turbulent intensity profiles recorded for the most elastic solution in the near wall region due to stabilized turbulent

eddies as a result of highest elongational viscosities generated by the most elastic fluid in a smooth walled circular pipe.

In this experimental study, the existence of early turbulence for these fluids was also investigated. Initially the friction factors vs. Reynolds number plots of these fluids were used to detect the transition from laminar to turbulent regime. Those plots showed that early turbulence only occurs for the most elastic solution. In order to verify this, another approach by Forame et al. was applied to experimental data and similar transition Reynolds numbers were obtained for each solution and the early turbulence was confirmed once again only for the most elastic fluid.

Also, these experiments gave us an opportunity to discuss the conditions required for the onset of the drag reduction and reaching maximum drag reduction for a dilute polymer solution. Based on the results of these experiments and similar studies in the literature, we concluded that a certain Weissenberg number could be suggested as the critical Weissenberg number for the onset of drag reduction of dilute solutions of certain polymers. This is also valid for reaching the maximum drag reduction level. Elongational viscosity does not increase anymore with the increasing strain rate after a certain Weissenberg number and, therefore, at a certain Weissenberg number or strain rate the drag reduction reaches the MDR. Also, the decrease in elongational viscosity starts after a certain shear rate or Weissenberg number could be the main reason causing drag reduction effect to disappear at high shear rates for dilute polymer solutions.

7.1.2.4. Chapter 6 - Effect of fluid elastic properties on the bed erosion dynamics of a sand deposited in a horizontal pipeline

For fluid only flow (no sand bed deposit) in pipe, more elastic fluid exhibited lower frictional pressure drop than that of the less elastic fluid. However, if there was a sand bed inside the pipe, then higher frictional pressure drops were measured for the flow of more elastic fluid than that of the less elastic one. The elongational viscosity developed in the near wall region due to extension of polymer chains under shear force enhances the stabilization

of turbulent eddies by thickening the viscous sublayer. This causes a drag reduction for dilute polymer solutions by optimizing the efficiency of energy transfer in the flow direction. In fluid only pipe flow (no sand), this effect is stronger for the more elastic fluid - as it develops higher elongational viscosities – therefore, we observed lower frictional pressure drops for the flow of more elastic fluid. In the case where there is a sand bed in the horizontal pipe, polymer chains in flow extends and develops elongational viscosities similarly, however, this time the flow over a rough surface leads long chain polymer molecule to entangle each other. These entanglements increase the friction between the fluid and the sand bed undermining the drag reduction effect of dilute polymer solutions. The entanglements are stronger for the more elastic fluid, therefore decrease in drag reduction is higher for the more elastic fluid and higher frictional pressure drops were measured for the more elastic fluid in this case.

Results also showed that higher critical velocities were required for the onset of the bed erosion with the use of more elastic fluid. Fluid with higher elasticity – longer polymer chains – develops higher normal stress difference and higher elongational viscosity under the shear during the flow. In the pipe flow with or without a sand bed the highest shear rate exists in the near wall or near fluid – sand bed interface region, so during the flow highest elongational viscosities and normal stress differences are observed in those regions. Higher normal stress difference results in greater normal force acting on the sand particles as an additional holding force and, as a result, more elastic polymer fluid delays the onset of sand movement as compared to less elastic polymer fluid or water. Moreover, higher elongational viscosities developed by more elastic fluid increases the effective viscosity and thickness of the viscous sublayer significantly, which also contributes to the delay of the onset of particle movement.

Analyses of the turbulent flow characteristics of the polymer fluids (based on the PIV measurements) also confirmed the findings and conclusions about the observed critical velocities and frictional pressure losses. The full velocity profiles were quite similar for both fluids, but the peak velocity was higher for the more elastic fluid. Dimensionless velocity profiles indicated that the fluid with lower elasticity had more drag reducing effect than

the one with higher elasticity during the flow over the sand bed. These results were in line with the frictional pressure losses measured directly during the flow of both fluids.

The Reynolds stress profile obtained for the more elastic fluid flow was lower than the less elastic one. The viscosity is very dominant inside the viscous sublayer and viscous effects supresses the Reynolds stresses generated. Therefore, the reason for observing lower Reynolds stress profiles for the more elastic fluid is the higher effective viscosity of the higher elasticity fluid in the near wall region. Also, the lower Reynolds stresses recorded for the more elastic fluid indicates that viscous sublayer for the more elastic fluid is thicker. The thicker viscous sublayer is one of the main reasons delaying the onset of particle movement for the more elastic fluid.

Axial turbulence intensity profiles were quite similar for both fluids except the near wall region. In the near wall region observed higher axial turbulence intensity profiles for the less elastic fluid might be the reason or the result of the increased mobility of sand particles in the flow of less elastic fluid.

The lower radial turbulence intensity profiles recorded for the more viscoelastic fluid than the less elastic one soundly supports the claims on elongational viscosities developed by these fluids. Higher elongational viscosities developed by the more elastic fluid dampened the velocity fluctuations in vertical direction and, therefore, lower the radial turbulence intensity profiles.

7.2. RECOMMENDATIONS FOR FUTURE WORK

I have learnt a lot from the mistakes and the achievements I had in the past two years while studying bed erosion dynamics of Newtonian and non-Newtonian fluids over an unconsolidated sand bed with sand particles having different size and surface characteristics and also investigating the direct effect of elastic properties of dilute polymer fluids on the bed erosion and pipe flow dynamics. Therefore, based on my observations and experience I would like to provide some recommendations for future work that might be carried out as a follow up to this study.

- Our experiments showed that viscous sublayer thickness is very effective in bed erosion dynamics and a particle bigger than viscous sublayer is mobilized easier. However, rather than a single size, the sand particles we used in our experiments had a size range, therefore the relation we found out between particle size and viscous sublayer thickness in terms of bed erosion must be further investigated by conducting bed erosion experiments for single size sand particles with dilute polymer fluids.
- In our study we studied the effect of viscoelastic properties on bed erosion dynamics in terms of critical flow velocities and frictional pressure drops, However, solids carrying capacity of the drilling fluids is also very important and at this point it would be good to investigate the effect of viscoelasticity on carrying capacity of polymer fluids in terms of critical deposition velocity (average velocity required to prevent the formation of stationary bed), cuttings transport ratio and effective hole cleaning time.
- In this study, we observed an early transition to turbulent state for the most elastic fluid we tested in pipe flow. Now, a more elastic fluid might be prepared and it can be tested in the horizontal flow loop to see whether an earlier transition to turbulent state would be observed or not. If HPAM would be used for this purpose, the dilute polymer solution might be prepared by using only the polymer grade having $20x10^6$ g/gmol molecular weight. The dilute polymer solution can be prepared in different concentrations, so this way the effect of concentration on early transition to turbulent state might be investigated.
- In the literature, elastic turbulence is mentioned by some researchers for highly viscous and viscoelastic fluids. Also, by conducting some experiments with such fluids in the horizontal flow loop, the occurrence of elastic turbulence might be tested.
- Elongational viscosity is the main feature causing drag reduction for dilute polymer fluids. In the literature, it is highlighted that elongational viscosity decreases after a certain Weissenberg number. Therefore, the drag reduction effect of a dilute polymer solution should disappear after a certain

Weissenberg number as the elongational viscosity decreases. A dilute polymer solution with proper rheological properties must be prepared and it should be tested in the horizontal flow loop to see whether drag reduction effect would disappear or not.

BIBLIOGRAPHY

Achia, B., Thompson, D. (1977). Structure of the turbulent boundary in drag-reducing pipe flow. Journal of Fluid Mechanics, 81(3), 439-464. doi:10.1017/S002211207700216X

Adari, R., Miska, S., Kuru, E., Bern, P., Saasen, A. (2000, February). Cuttings Bed Erosion Curves Help Predict Optimum Circulation Time for Hole Cleaning. ETCE/ OMAE Joint Conference of ASME, New Orleans, LA.

Arnipally, S. K., Kuru, E. (2018). Settling Velocity of Particles in Viscoelastic Fluids: A Comparison of the Shear-Viscosity and Elasticity Effects. Society of Petroleum Engineers. doi:10.2118/187255-PA

Arnipally, S., Kuru, E. (2018). Settling Velocity of Particles in Viscoelastic Fluids: A Comparison of the Shear Viscosity and Elasticity Effect. SPE Journal, Online Preprint, doi:10.2118/ 187255-PA

Bayode, E. O., Dennis, D., Poole, R. (2017). Turbulent drag reduction by polymer additives in parallel-shear flows. Journal of Fluid Mechanics. 827. doi:10.1017/jfm.2017.544.

Bewersdorff, H., Thiel, H. (1993). Turbulence Structure of Dilute Polymer and Surfactant Solutions in Artificially Roughened Pipes. Applied Scientific Research. 50. 347-368. doi:10.1007/BF00850566.

Bilgesu, H. I., Mishra, N., Ameri, S. (2007). Understanding the Effect of Drilling Parameters on Hole Cleaning in Horizontal and Deviated Wellbores Using Computational Fluid Dynamics. Society of Petroleum Engineers. doi:10.2118/111208-MS

Bird, R. B., Armstrong, R. C., Hassager, O. (1987) Dynamics of Polymeric Liquids, vol 1. Wiley, New York

Bizhani, M., (2017). Experimental and Theoretical Investigations of Particle Removal from Sand Bed Deposits in Horizontal Wells Using Turbulent Flow of Water and Polymer Fluids. PhD Thesis, Civil and Environmental Engineering, University of Alberta, Edmonton, Canada.

Bizhani, M., Corredor, F. E. R., Kuru, E. (2016). Quantitative Evaluation of Critical Conditions Required for Effective Hole Cleaning in Coiled-Tubing Drilling of Horizontal Wells. SPE Drilling & Completion 31(3): 188-199, doi: 10.2118/174404-PA.

Bizhani, M., Kuru, E. (2017). Critical Review of Mechanistic and Empirical (Semi- Mechanistic) Models for Particle Removal from Sand Bed Deposits in Horizontal Annuli by Using Water. SPE Journal, SPE-187948-PA, In press.

Bizhani, M., Kuru, E. (2017). Particle Removal from Sandbed Deposits in Horizontal Annuli Using Viscoelastic Fluids. SPE Journal.

Bizhani, M., Kuru, E. (2018). Critical Review of Mechanistic and Empirical (Semi-mechanistic) Models for Particle Removal from Sandbed Deposits in Horizontal Annuli with Water. SPE Journal, Vol.23, Issue.02, pp.237-255, doi:10.2118/187948-PA.

Bizhani, M., Kuru, E. (2018). Particle Removal from Sandbed Deposits in Horizontal Annuli Using Viscoelastic Fluids. SPE Journal, Vol.23, Issue.02, pp.256-273, doi:10.2118/189443-PA

Bonn, D., Amarouchene, Y., Wagner, C., Douady, S., Cadot, O. (2005). Turbulent drag reduction by polymers. Journal of Physics: Condensed Matter. 17. S1195. doi:10.1088/0953-8984/17/14/008.

Brown, N., Bern, P., Weaver, A. (1989). Cleaning Deviated Holes: New Experimental and Theoretical Studies. SPE/IADC Drilling Conf.

Cameron, C. (2001). Drilling Fluids Design and Management for Extended Reach Drilling. Society of Petroleum Engineers. doi:10.2118/72290-MS

Davies, J. (1987). Calculation of Critical Velocities to Maintain Solids in Suspension in Horizontal Pipes. Chemical Eng.Sci., vol. 42, pp. 1667-1670.

Dimitropoulos, C., Sureshkumar, R., Beris, Antony. (1998). Direct numerical simulation of viscoelastic turbulent channel flow exhibiting drag reduction: Effect of the variation of rheological parameters. Journal of Non-Newtonian Fluid Mechanics. 79. 433-468. doi:10.1016/S0377-0257(98)00115-3.

Diplas, P., Dancey, C. L., Celik, A. O., Valyrakis, M., Greer, K., Akar, T. (2008). The Role of Impulse on the Initiation of Particle Movement under Turbulent Flow Conditions. Science, vol. 322, pp. 717-720.

Duan, M. Q., Miska, S., Yu, M. J., Takach, N., Ahmed, R., Zettner, C. (2009). Critical Conditions for Effective Sand-Sized-Solids Transport in Horizontal and High-Angle Wells. SPE Drilling & Completion 24(2): 229-238, SPE Drill Completion, doi: 10.2118/104192-PA.

Dubief, Y., Terrapon, V., Soria, J. (2013). On the mechanism of elasto-inertial turbulence. Physics of fluids (Woodbury, N.Y.: 1994). 25. 110817. doi:10.1063/1.4820142.

Elata, C., J. Lehrer, Kahanovitz, A. (1966). Turbulent Shear Flow of Polymer Solutions. Israel Journal of Technology, Vol. 4, No. 1, pp. 87-95.

Flierl, G., Ferrari, R. 12.820 Turbulence in the Ocean and Atmosphere. Spring 2007. Massachusetts Institute of Technology: MIT OpenCourseWare, https://ocw.mit.edu. License: Creative Commons BY-NC-SA.

Forame, P. C., Hansen, R. J., Little, R. C. (1972). Observations of early turbulence in the pipe flow of drag reducing polymer solutions. AIChE J., 18: 213-217. doi:10.1002/aic.690180139

Groisman, A., Steinberg, V. (2004). Elastic turbulence in curvilinear flows of polymer solutions. New Journal of Physics. 6–29. doi:10.1088/1367-2630/6/1/029.

Gupta, R. K., Nguyen, D.A., Sridhar, T. (2000). Extensional viscosity of dilute polystyrene solutions: Effect of concentration and molecular weight. Physics of Fluids 2000 12:6, 1296-1318. doi: 10.1063/1.870383

Gyr, A., Bewersdorff, H. (1995). Drag Reduction of Turbulent Flows by Additives. Springer, Dordrecht

Hansen, R. J., Little, R. C. (1974). Early turbulence and drag reduction phenomena in larger pipes. Nature, 10.1038/252690a0, 252, 5485, (690-690).

Hatfield, J. W., Quake, S. R. (1999). Dynamic Properties of an Extended Polymer in Solution. Physical Review Letters, 82 (17). pp. 3548-3551. ISSN 0031-9007.

Hirpa, M. M., Arnipally, S. K., Kuru, E. et al. (2018). Effect of Sand Particle Size and Surface Properties on the Near Wall Turbulence Characteristics of the Polymer Fluid Flow and the Critical Velocity Required for the Particle Removal from the Sand Bed Deposited in Horizontal Pipelines. Submitted to SPE Journal, under review.

Hoyt, J. W. (1977). Laminar-turbulent transition in polymer solutions. Nature. 270. 508-509. doi:10.1038/270508a0.

Kelessidis, V. C., Bandelis, G. E. (2004). Flow Patterns and Minimum Suspension Velocity for Efficient Cuttings Transport in Horizontal and Deviated Wells in Coiled-Tubing Drilling. SPE Drilling & Completion.

Kundu, P. K., Cohen, I. M., Dowling, D. R. (2012). Fluid Mechanics, 5th Edition. Amsterdam, Elsevier Science Bv.

Lakes, R. (2009). Introduction: Phenomena. In Viscoelastic Materials (pp. 1-13). Cambridge: Cambridge University Press. doi:10.1017/CBO9780511626722.002

LaVision, Davis 8.3 Product Manual. ed, 2015

Li, J., Luft, B. (2014a, October). Overview of Solids Transport Studies and Applications in Oil and Gas Industry - Experimental Work. SPE Russian Oil and Gas Exploration & Production Technical Conference and Exhibition. Moscow, Russia, SPE-171285-MS, doi: 10.2118/171285-MS.

Li, J., Luft, B. (2014b, December). Overview Solids Transport Study and Application in Oil-Gas Industry-Theoretical Work. International Petroleum Technology Conference. Kuala Lumpur, Malaysia, IPTC-17832-MS, doi: 10.2523/IPTC-17832-MS.

Lumley, J. (1973). Drag Reduction in Turbulent Flow by Polymer Additives. Journal of Polymer Science: Macromolecular Reviews. 7. 263 - 290. doi:10.1002/pol.1973.230070104.

Martins, A., Campos, W., Liporace, F., Wei, X., Van Riet, E., (1997). On the Erosion Velocity of a Cuttings Bed During the Circulation of Horizontal and Highly Inclined Wells. Latin American and Caribbean Petroleum Engineering Conference.

Massah, H., Hanratty, T. (1997). Added stresses because of the presence of FENE-P bead–spring chains in a random velocity field. Journal of Fluid Mechanics, 337, 67-101. doi:10.1017/S0022112097004916

McCabe, W.L., Smith, J.C., Harriott, P. (2004). Unit Operations of Chemical Engineering, New York: McGraw-Hill.

Metzner, A.B., Reed, J.C. (1955). Flow of non-Newtonian fluids—correlation of the laminar, transition, and turbulent-flow regions. AICHE Journal,1(4), pp.434-440.

Mishra, P., Tripathi, G. (1971). Transition from laminar to turbulent flow of purely viscous non-Newtonian fluids in tubes. Chemical Engineering Science, 26, 915-921

Mishra, P., Tripathi, G. (1973). Heat and Momentum-Transfer to Purely Viscous Non-Newtonian Fluids Flowing Through Tubes. Transactions of the Institution of Chemical Engineers, 51, 141-150

Nazari, T., Hareland, G., Azar, J. J. (2010, May). Review of Cuttings Transport in Directional Well Drilling: Systematic Approach. SPE Western Regional Meeting Anaheim, California, USA, SPE-132372-MS, doi: 10.2118/132372-MS.

Oldaker, K. D., Tiederman, G. W. (1977). Spatial structure of the viscous sublayer in drag-reducing channel flows. Physics of Fluids - PHYS FLUIDS. 20. doi:10.1063/1.861722.

Pinho, F. (2003). A GNF framework for turbulent flow models of drag reducing fluids and proposal for a k-type closure. J. Non-Newtonian Fluid Mech. 114. 149-184. doi:10.1016/S0377-0257(03)00120-4.

Powell, J. W., Parks, C. F., Seheult, J. M. (1991). Xanthan and Welan: The Effects of Critical Polymer Concentration on Rheology and Fluid Performance. Society of Petroleum Engineers. doi:10.2118/22066-MS

Rabenjafimanantsoa, A., Time, R. W., Saasen, A. (2007). Simultaneous Uvp and PIV Measurements Related to Bed Dunes Dynamics and Turbulence Structures in Circular Pipes. in 5th International Symposium on Ultrasonic Doppler Methods for Fluid Mechanics and Fluid Engineering, pp. 63-67.

Rabenjafimanantsoa, H. A., Rune, W. T., Saasen, A. (2005). Flow regimes over particle beds experimental studies of particle transport in horizontal pipes Annual Transactions of the Nordic Rheology Society, 13.

Raffel, M., Willert, C. E., Kompenhans, J. (2007). Particle Image Velocimetry: A Practical Guide: Springer Science & Business Media.

Ram, A., Tamir, A. (1964). Structural turbulence in polymer solutions. J. Appl. Polym. Sci., 8: 2751-2762. doi:10.1002/app.1964.070080621.

Ramadan, A., Skalle, P., Johansen, S. T. (2003). A mechanistic model to determine the critical flow velocity required to initiate the movement of spherical bed particles in inclined channels. Chemical Engineering Science 58(10): 2153-2163 doi:10.1016/S0009-2509(03)00061-7, Chem Eng Sci.

Rouse, E. P. (1953). A Theory of the Linear Viscoelastic Properties of Dilute Solution of Coiling Polymers. The Journal of Chemical Physics. 21. 1272-1280. doi:10.1063/1.1699180.

Roylance, D., (2001). Engineering Viscoelasticity. Department of Materials Science and Engineering Massachusetts Institute of Technology Cambridge, MA 02139 Retrieved from http://web.mit.edu/course/3/3.11/www/modules/visco.pdf

Saasen, A., Løklingholm, G. (2002, February). The Effect of Drilling Fluid Rheological Properties on Hole Cleaning. IADC/SPE Drilling Conference. Dallas, Texas, SPE-74558-MS, doi: 10.2118/74558-MS.

Samanta, D., Dubief, Y., Holzner, M., Schäfer, C., Morozov, A., Wagner, C., Hof, B. (2013). Elasto-inertial turbulence. Proceedings of the National Academy of Sciences of the United States of America. 110. doi:10.1073/pnas.1219666110.

Savins, J. G. (1966). A Stress-Controlled Drag-Reduction Phenomenon. Society of Petroleum Engineers. doi:10.2118/1724-MS

Sayindla, S., Lund, B., Ytrehus, J. D., et al., (2017). Hole-cleaning performance comparison of oil-based and water-based drilling fluids. J. Pet. Sci. Eng., Volume 159, Pages 49-57. doi:10.1016/ j.petrol. 2017.08.069.

Skelland, A. H. P. (1967). Non-Newtonian flow and heat transfer. Wiley, New York.

Sunthar, P. (2010). Polymer Rheology. Rheology of Complex Fluids. 171-191. doi:10.1007/978-1-4419-6494-6_8.

Toms, B. A. (1948). Some observations on the flow of linear polymer solutions through straight tubes at large Reynolds numbers. In Proceedings of the 1st International Congress on Rheology, vol. 2, pp. 135–141. North-Holland.

Trinh, T. (2010). On the Critical Reynolds Number for Transition from Laminar to Turbulent Flow.

Tropea, C., Yarin, A. L., Foss, J. (2007). Springer Handbook of Experimental Fluid Mechanics. doi:10.1007/978-3-540-30299-5.

Virk, P. (1971). An elastic sublayer model for drag reduction by dilute solutions of linear macromolecules. Journal of Fluid Mechanics, 45(3), 417-440. doi:10.1017/S0022112071000120

Virk, P. S. (1975). Drag reduction fundamentals. AIChE J., 21: 625-656. doi:10.1002/aic.690210402

Walker, S., Li, J. (2000, April). The Effects of Particle Size, Fluid Rheology, and Pipe Eccentricity on Cuttings Transport. g2000 SPE/ICoTA Coiled Tubing Roundtable. Houston, TX, SPE-60755-MS, DOI: 10.2118/60755-MS.

Walsh, M. (1967). On the Turbulent Flow of Dilute Polymer Solutions. 11, Ph.D. Thesis, Calif. Inst. Tech., Pasadena, Calif.

Werner B., Myrseth V., Saasen, A. (2017). Viscoelastic properties of drilling fluids and their influence on cuttings transport, Journal of Petroleum Science and Engineering, Volume 156, Pages 845-851, ISSN 0920-4105, doi:10.1016/j.petrol.2017.06.063.

Xiao, Q, Wang, A., Tao, W. (1996). Experimental study for pressure drop of viscoelastic fluids through periodically sudden converging-diverging tube. Journal of Thermal Science. 5. 19-23. doi:10.1007/BF02663727.

Zamora, M., Jefferson, D. T., Powell, J. W. (1993). Hole-Cleaning Study of Polymer-Based Drilling Fluids. Society of Petroleum Engineers. doi:10.2118/26329-MS

Zell, A., Gier, S., Rafai, S., Wagner, C. (2009). Is there a Relationship between the Elongational Viscosity and the First Normal Stress Difference in Polymer Solutions?